UNIVERSITY OF SOUTHAMPTON

FACULTY OF SOCIAL AND HUMAN SCIENCES

Geography and Environment

Uncertainty Associated with Scaling Spectral Indices of Carbon Fluxes at Various Spatial and Temporal Scales

by

Seyed Hossein Kia

Thesis for the degree of Doctor of Philosophy

October 2017

UNIVERSITY OF SOUTHAMPTON

ABSTRACT

FACULTY OF SOCIAL AND HUMAN SCIENCES

Geography and Environment

Thesis for the degree of Doctor of Philosophy

Uncertainty Associated with Scaling Spectral Indices of Carbon Fluxes at Various Spatial and Temporal Scales

Seyed Hossein Kia

Measurements from the global network of micrometeorological tower sites (FLUXNET) provide essential information on the ecosystems productivity (i.e. a key component for the study of the carbon cycle). However, the area sampled by instruments on a flux tower is poorly defined and varies with weather conditions. Additionally, gaps in the FLUXNET record are common, either due to unsuitable measurement conditions or instrument failure. Hence, remote sensing (RS) has been proposed as a way to enhance the FLUXNET database, as it provides complete spatial coverage and frequent repeat observations. In practice, the use of RS for this task is challenging. The integration of spatially-explicit ecosystem models, RS observations and eddy covariance (EC) flux measurements with environmental variables have facilitated the quantification of carbon cycling dynamics across multiple spatial and temporal scales. In this regard, process-based models with the aim of simulation of carbon dynamics in forest ecosystems are increasingly being used besides other tools to predict the effects of environmental factors on the forest carbon pool and forest productivity. However, despite this, decision makers must be aware of the limitations of these models by uncertainty analyses to make the process-based models more robust and to optimize them for estimating productivity at landscape level. There is a need to address various sources of uncertainty associated with such quantification, including sensor limitations in terms of support size defined by spatial and temporal resolutions; spatial heterogeneity of land surface properties; pre-processing calibration; and the structure of the model proposed and its parameterization.

This research investigated the sources of uncertainty mentioned across three domains of interest: spectral, spatial and temporal. The present research deals with this need using a combination of tower-based EC flux measurements and RS data from both airborne and satellite RS systems at a range of temporal and spatial scales. It incorporates multiple remote sensing data sets (Airborne LiDAR, Airborne Imaging Spectrometry, DMC, and MODIS) to derive indices related to canopy structure (nCHM), plant cover (NDVI) and photosynthesis processes (PRI), and attempts to relate these to the data measured by instruments on flux towers in two locations: Wytham Woods, southern England, and Chequamegon Nicolet National Forest in northern Wisconsin, USA.

In terms of the spectral domain, the research adds to the evidence that NDVI alone is insufficient to fully characterize the primary productivity of plant canopies, specifically across heterogeneous landscape. The study also demonstrates the magnitude and variability of extraneous parameters (e.g. optical geometry, shadow fraction, soil background and aerosol) in RS observations of the mixed forest of Wytham Woods using a 3D forest light simulation model (FLIGHT model). The results reveal that the observed vegetation indices (NDVI and PRI) form the mixed forest is highly sensitive to variation in solar and view zenith angles and soil background, while the indices are relatively robust to aerosol scattering.

In the temporal domain, the research makes use of a unique time-series of ten multispectral images acquired during a single growing season by the DMC satellite sensors. The heterogeneity of canopy cover has greatest impact on the DMC data early in the season, and this highlights the importance of understanding how the flux tower footprint varies with weather conditions. As the canopy began to green-up, the precision of temporal sampling became more important. Based on explicit representation of the time-varying flux tower footprint, prediction of flux tower measurements directly from space-borne coarse spatial resolution imagery is challenging and leads to a low predictive ability.

In order to use the global FLUXNET EC dataset and RS observations to estimate the ecosystem productivity at regional and global scales, this research deals with an up-scaling approach that it involves flux footprint climatology modelling and RS-based light use efficiency (LUE) model fusion. In this aspect, a large correlation is found between satellite-based PRI and the EC-based LUE of a homogeneous deciduous forest. However, estimating the regional level LUE of a heterogeneous landscape from space is still an uncertain process as the required spectral index (PRI) is affected by canopy-level variables as well as the geometry of illumination and view. Furthermore, the

sensitivity analysis of a simple Diagnostic Carbon Flux Model (DCFM) to seven input parameters (ε_{max}, α, β, R'_{ref}, γ, λ and E_0) using a five-years record of the EC data from four flux towers selected across various plant functional types (PFTs) in the Upper Midwest region of northern Wisconsin, is considered to optimize the RS-based LUE model for estimating regional productivity. The results confirm that empirical constants for the estimation of the fPAR absorbed by vegetation canopies (α and β) next to the maximum light use efficiency (ε_{max}) has little impact on the fluctuations of net carbon exchange within each PFT whereas DCFM model was very sensitive to γ so, the estimation of this factor, in comparison with the other parameters, plays the key role in the accuracy of NEE's predictions. Moreover, except for homogenous canopy cover, in other PFTs, interactions among the crucial eco-physiological parameters have minor contribution to uncertainty of NEE prediction by DCFM model.

In conclusion, the results demonstrated the potential combination of the satellite-based approach, flux footprint modelling and data-model fusion for improving the accuracy of regional/global productivity estimations. This approach includes four steps: (1) a RS-based LUE model for estimating productivity; (2) EC flux footprint analysis for the corresponding RS images; (3) using the footprint integration of RS-based ecosystem productivity to be comparable with the tower-based EC-derived productivity values, several key parameters of the RS-based LUE model can be optimized using the DCFM; and (4) The optimized RS-based LUE model can be applied for estimating regional productivity.

Table of Contents

List of Tables

List of Figures

DECLARATION OF AUTHORSHIP

I, Seyed Hossein Kia declare that the thesis entitled

Uncertainty Associated with Scaling Spectral Indices of Carbon Fluxes at Various Spatial and Temporal Scales and the work presented in the thesis are both my own, and have been generated by me as the result of my own original research. I confirm that:

- this work was done wholly or mainly while in candidature for a research degree at this University;
- where any part of this thesis has previously been submitted for a degree or any other qualification at this University or any other institution, this has been clearly stated;
- where I have consulted the published work of others, this is always clearly attributed;
- where I have quoted from the work of others, the source is always given. With the exception of such quotations, this thesis is entirely my own work;
- I have acknowledged all main sources of help;
- where the thesis is based on work done by myself jointly with others, I have made clear exactly what was done by others and what I have contributed myself;
- parts of this work have been published as:

Conference Proceeding

1. Kia, S.H., & Milton, E.J. (2015). *Hyper-temporal remote sensing for scaling between spectral indices and flux tower measurements.* Applied Ecology and Environmental Research, 13(2), 464-487

2. Kia, S. H. (2012) Temporal and spatial variability of Spectral Indices of CO2 flux around a UK's flux tower, Wytham Woods, Oxfordshire. In, Annual Conference of the Chequamegon Ecosystem Atmosphere Study. Observing and simulating carbon cycle impacts of forest management and climate variability in heterogeneous landscapes (*ChEAS 2012*), Wisconsin, USA, 26-30 June 2012.

3. Kia, S.H. and Milton, E.J. (2011). *What can a time series of remotely sensed measurements from a mixed broadleaf forest tell about net ecosystem exchange?* In, Annual Conference of the Remote Sensing and Photogrammetry Society. Earth Observation in a Changing World (*RSPSoc 2011*), Bournemouth, GB, 13-15 September 2011.

Signed: *S.H. Kia*

Date: 09/10/2017

Acknowledgements

I would like to thank Professor Edward J. Milton and Professor Peter Atkinson for their continuous supervision, support, advice, guidance and encouragement during my education period at the University of Southampton. I would also like to thank Dr Angela Harris for her input to the project, before her move to the University of Manchester.

I would like to thank Professor Kenneth J. Davis for his support through my visiting the Chequamengon Ecosystem-Atmosphere Study (ChEAS)-North American Carbon Program at the Pennsylvania State University, USA.

I also thank the University of Oxford for allowing access to Wytham Woods, and the following organisations which supported my work by providing data: NERC Centre for Ecology and Hydrology (CEH); NERC Airborne Research and Survey Facility (ARSF); British Atmospheric Data Centre (BADC) and NASA (MODIS). I am particularly grateful to Dr Stephen Mackin (DMCii/SSTL) for arranging for me to have data from the Disaster Monitoring Constellation (DMC);

I am grateful to the Erasmus Mundus programme of the European Union for providing me with a scholarship to study in the UK and to the Worldwide University Network (WUN) Research Mobility Program (RMP) for enabling my visit to Pennsylvania State University.

Finally, I would like to thank my family especially my parents who always bless and support me through life, and thank my wife who has supported me throughout my studies. Thanks to all my friends and colleagues who helped me get through difficulties.

1. Introduction

1.1 Environmental Change and Earth Observation

Rapid population growth and anthropogenic activities are putting increasing pressure on natural resources and are widely regarded as implicated in regional and global environmental changes, such as land cover change (Foody, 2010), climate change (IPCC, 2014; Walser and Nodvin, 2007) and biodiversity loss (Gitay et al., 2002). The Intergovernmental Panel on Climate Change (ICPP, 2014) reported that "human influence on the climate system is clear, and recent anthropogenic emissions of greenhouse gases are the highest in history". Recent climate change has widespread impacts on both human and natural systems and often alters ecosystem structure and function as a result of changes to the global carbon cycle. The IPCC Fourth Assessment Report in 2007 stated that the concentration of atmospheric carbon dioxide (CO_2) in 1750 before industrialization was approximately 280 ppm, and had increased to about 380 ppm in 2005. Increasing the atmospheric CO_2 concentration, mostly due to fossil fuel burning and land changes in the form of deforestation (IPCC, 2014), results in a phenomenon commonly referred to as global warming (IPCC, 2001; Walser and Nodvin 2007). Deforestation not only releases CO_2 into the atmosphere, but also reduces its uptake by photosynthetic organisms. In contrast, forest ecosystems, which cover approximately 30% of the Earth's land surface (Danson, 1995), account for more than 75% of the carbon stored in vegetation and soils (Schlesinger and Lichter, 2001; Walser and Nodvin, 2007).

The term "Earth System" refers to land-atmosphere interactions which comprise both the physical climate system and the biogeochemical processes (Flato, 2011), along with the human systems (i.e. social and economic systems), such as the carbon cycle and its concentration in the terrestrial and oceanic ecosystems (Schimel et al., 2015). Understanding the Earth's system dynamics and quantifying spatial and temporal

variation in factors that influence environmental change will provide decision makers with the best information to manage and protect vital ecosystem services. This will improve our ability to mitigate the effects of environmental change. In this regard, one of the primary challenges is accurate metrics of key environmental variables. In spite of great advances in *in situ* instrumentation, measuring environmental variables at appropriate temporal and spatial scales remains as a significant challenge in ecosystem studies. Most environmental data are still derived from point location-based observations. This might be acceptable if the point observations were sufficiently numerous, but they are sparse or even non-existent in many regions of the world (Barrett and Curtis, 1999).

Remote sensing (RS), often referred to as Earth Observation (EO), has the potential to provide useful quantitative data covering large areas, which traditional *in situ* measurements cannot achieve. Remote sensing was defined by the American Society for Photogrammetry and Remote Sensing (ASPRS) as:

"*Remote Sensing is art, science, and technology of obtaining reliable information about physical objects and the environment, through the process of recording, measuring and interpreting imagery and digital representations of energy patterns derived from non-contact sensor systems*" (Lillesand et al., 2008).

Earth Observation data, from airborne and satellite platforms, can provide systematic measurements of the land surface which can be used to parameterize biophysical and physiological models and monitor ecological processes across large spatial extents at variable temporal and spatial resolutions, tasks that are not easily achieved by field surveying methods or traditional *in situ* measurements. The state-of-the-art in this research area is needed to monitor environmental changes for ecological applications. However, effective use of advanced Earth Observation data and products is challenging, and has become an important research topic.

Satellite sensor data are used widely for environmental studies; however, airborne remote sensing systems provide an important complementary source of Earth Observation data. As environmental processes occur over a period of time and across

geographic regions, the suitability of a given platform/sensor combination will vary with the temporal, spatial and spectral scales of the variable being measured. For example, changes in certain key physiological processes involving photosynthetic regulation at the leaf scale can be detected over seconds to minutes and require data in narrow spectral bands, whereas, changes in green vegetation cover at regional scale can be detected over seasons with broad spectral bands. Therefore, airborne multi- and hyper-spectral imagery from dozens to hundreds of discrete bands, as a bridge between *in situ* measurements and satellite sensor observations, has a critical role to play in improving and validating satellite sensor data and products, as well as in scaling-up environmental variables. An example of an airborne RS system is the Airborne Thematic Mapper (ATM) operated by the UK Natural Environment Research Council (NERC) Airborne Research and Survey Facility (ARSF) throughout the 1980s. The sensor has eleven spectral bands in the visible near infrared (VNIR), shortwave infrared (SWIR) and thermal infrared, some of which match closely those of Landsat TM/ETM+ and UK-DMC (Table 1.1). In general, this table indicates the suitability and the importance of various platform/sensors in terms of the temporal, spatial and spectral resolutions for the variable of interest.

Table 1-1 Spectral band position of the ATM and UK-DMC compared to ETM+

Spectral Region	ATM		ETM+		UK-DMC	
	Band	Wavelength (μm)	Band	Wavelength (μm)	Band	Wavelength (μm)
Visible-Blue	1	0.42 - 0.45	----	----------	----	----------
Visible-Blue	2	0.45 - 0.52	1	0.45 - 0.52	----	----------
Visible-Green	3	0.52 - 0.60	2	0.52 - 0.60	1	0.52 - 0.60
Visible-Red	4	0.60 - 0.62	----	----------	----	----------
Visible-Red	5	0.63 - 0.69	3	0.63 - 0.69	2	0.63 - 0.69
Near-IR	6	0.69 - 0.75	----	----------	----	----------
Near-IR	7	0.76 - 0.90	4	0.77 - 0.90	3	0.77 - 0.90
Near-IR	8	0.91 - 1.05	----	----------	----	----------
Shortwave-IR	9	1.55 - 1.75	5	1.55 - 1.75	----	----------
Shortwave-IR	10	2.08 - 2.35	7	2.08 - 2.35	----	----------
Thermal-IR	11	8.5 - 13.0	6	10.40 - 12.50	----	----------
Panchromatic	----	----------	8	0.52 - 0.90	----	----------

Furthermore, since 1990 the NERC-ARSF has also deployed two airborne imaging spectrometers, an ITRES Instruments Compact Airborne Spectrographic Imager (CASI) and an AISA Eagle/Hawk system. The data from these systems provide much more detailed spectral information of the land surface when compared with typical multispectral sensors, which collect data in just a few broad spectral bands. Such detailed spectral information may be used to identify specific materials within a pixel, based on their reflectance characteristics.

The contribution of remote sensing to global environmental change has been highlighted in recent major international programmes, such as the National Aeronautics and Space Administration's (NASA), Earth Observation System (EOS) and the NASA's Terrestrial Ecology Program Research (TEPR) (NASA, 2012; Ramachandran et al., 2011).

In general, the primary goal of environmental remote sensing is to estimate/retrieve the land surface properties through various quantitative models, such as statistical, physical and hybrid models (Liang, 2004). This process refers to a systematic scheme of Earth Observation involving the acquisition of data, analysis procedures, information extraction and product validation regarding environment variables. Figure 1.1 is a schematic diagram showing the steps involved in retrieving environmental information from Earth Observation data.

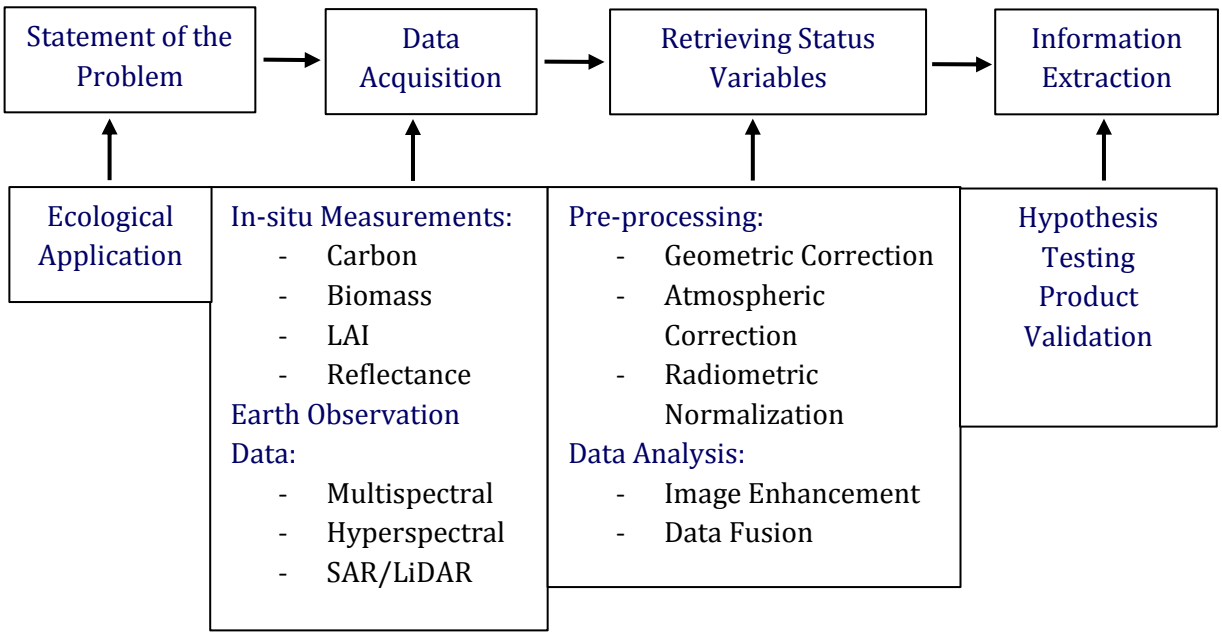

Figure 1-1 Key components of environmental remote sensing (Lillesand et al., 2008)

As Figure 1.1 illustrates, the process of retrieving environmental information from EO data consists of pre-processing and information extraction. While, the latter depends upon the specific application, the former is more general, as its aim is to discriminate the true signal of the variable of interest from noise introduced by the sensor, the measurement configuration and a host of extraneous environmental variables, for example, the atmosphere. In most remote sensing systems, data are acquired in the form of digital numbers (DN), the scaled integers from quantization, which need to be converted into physical units such as radiance, for example $mWm^{-2}sr^{-1}\mu m^{-1}$ where ***sr*** is the unit for measuring solid angles[1] and μm measures wavelength, before they can be considered as reliable scientific data (Liang, 2004). In general, digital numbers are linearly related to radiance, and most remote sensing data providers produce the conversion coefficients which users may apply to convert their data to physically meaningful units.

1. Solid angle (Ω) is an extension of two-dimensional angle measurement.

Due to the nature of remotely sensed techniques, the relation between the data collected and the information desired is indirect (Curran and Atkinson, 1998). Therefore, the successful application of environmental remote sensing depends on understanding the relevant surface properties with respect to the temporal, spatial and spectral attributes of the variables of interest (Lillesand et al., 2008). The process of extracting information from Earth observation data requires taking consideration of uncertainty and identifying its sources (Atkinson and Foody, 2002a). Many factors, for example solar position, sensor view angle, sensor response and atmospheric effects influence Earth observation data from each spectral band differently, which may contribute uncertainties in environmental variables. Among these, the atmosphere introduces a large amount of uncertainty as it affects both the amount of irradiance reaching the target from the Sun and the amount of radiance reaching the sensor from the target (Baret, 1995; Danson, 1995).

In the context of environmental remote sensing, particularly ecological applications, variables observed may be categorized into two groups: state and inference variables. The state variables, also known as biophysical variables (Danson, 1995), are those variables that are correlated directly with the remotely sensed data. For example, absorbed photo-synthetically active radiation (APAR), leaf area index (LAI) and canopy height are all related to biophysical variables such as vegetation biomass. In this aspect, the importance of APAR and LAI in understanding the biogeochemical cycles and modelling the climate-vegetation- carbon cycle feedback has made their accurate estimation a priority research topic. In ecosystem models, moreover, the APAR term is often estimated as a function of LAI and therefore the accuracy of the LAI products determines how accurately APAR is represented in these models. The second group of variables is the inference variables; also referred to as hybrid variables. These variables are created by systematically analysing more than one biophysical variable. For instance, vegetation modelling that is influenced by more than one state variable is based on hybrid variables, such as plant chlorophyll absorption characteristics, cell structure, and water content (Danson, 1995).

Earth System Models (ESMs)[1] have been developed and are widely used to understand the land-atmosphere interaction and the planet's natural cycles (Flato, 2011). The ESMs can be evaluated by direct continuous ecosystem observations of sensible heat, latent heat, water vapour, and CO_2 exchange (Xiao et al., 2012; Williams et al., 2009). However, uncertainty in the Earth's surface energy budget and terrestrial CO_2 fluxes can lead to variations in atmospheric carbon concentration and a dominant constraint for robust climate projections. The appropriate algorithm to extract environmental information from the inference variables necessarily involves interdisciplinary methods because of the multivariate nature of the problem. Accordingly, the need to better understand land surface characteristics and the factors that affect the Earth's system dynamics has been the main driving force for identifying the sources of uncertainty and increasing the accuracy of RS-based estimates of environmental variables.

1. Earth System Models (ESMs) are global climate models with the added capability to explicitly represent biogeochemical processes that interact with the physical climate and so alter its response to forcing such as that associated with human-caused emissions of greenhouse gases.

1.2 Terrestrial Ecosystem Productivity

Terrestrial ecosystem productivity usually refers to ecosystem products that contribute to the production of both commercial and ecological goods and services (Foody, 2010). This section contains some theoretical background relating to plant production, here referred to as ecosystem productivity, followed by a more technical description of the quantitative methods, as well as their advantages and limitations.

The vast majority of life on Earth depends on energy and materials for survival. Although several sources of energy are available on the Earth, the most significant is solar radiation. Solar radiation can be converted into biochemical energy by plants as it flows through ecosystems, a process that is referred to as photosynthesis. The basis of life in ecosystems is plant photosynthesis, which converts atmospheric carbon dioxide (CO_2) into organic compounds, also known as biomass, using sunlight energy and the green pigment chlorophyll. The photosynthesis process may be summarized by:

$$nCO_2 + nH_2O + light\ energy + chlorophyll \rightarrow (CH_2O)n + nO_2$$

There are two fundamental phases in the photosynthesis process, the light-dependent and the light-independent reactions. In the first phase of photosynthesis, sunlight is absorbed by proteins containing chlorophylls, resulting in the generation of Adenosine Triphosphate (ATP) and Nicotinamide Adenine Dinucleotide Phosphate Hydrate (NADPH). In the light-independent reactions, also referred to as dark reactions, the products of the light-dependent reaction are used to convert CO_2 into carbohydrate (Hall et al. 1993). In contrast, the related process, autotrophic respiration, releases CO_2 into the atmosphere and also converts some of the energy captured by photosynthesis into heat energy as:

$$(CH_2O)n + nO_2 \rightarrow nCO_2 + nH_2O + heat\ energy$$

The balance between photosynthesis and respiration, also known as carbon fixation, determines primary production in the form of above and below ground biomass[1]. An

1. Plant biomass is the weight of living plant material contained above and below a unit of ground surface area at a given point in time.

ecosystem is usually referred to as a net carbon sink if the CO_2 influx from photosynthesis exceeds the outflow from respiration. It is referred to as a net carbon source if more carbon is lost than is gained.

The primary production by plants, as Figure 1.2 illustrates, is expressed by Gross Primary Production (GPP) that represents photosynthesis capacity, and Net Primary Production (NPP) that represents the total amount organic component assimilated after the total respiration "R_E", autotrophic $respiration$ "R_A" and heterotrophic "R_H" respiration (Hall et al. 1993; Lambers et al. 2008).

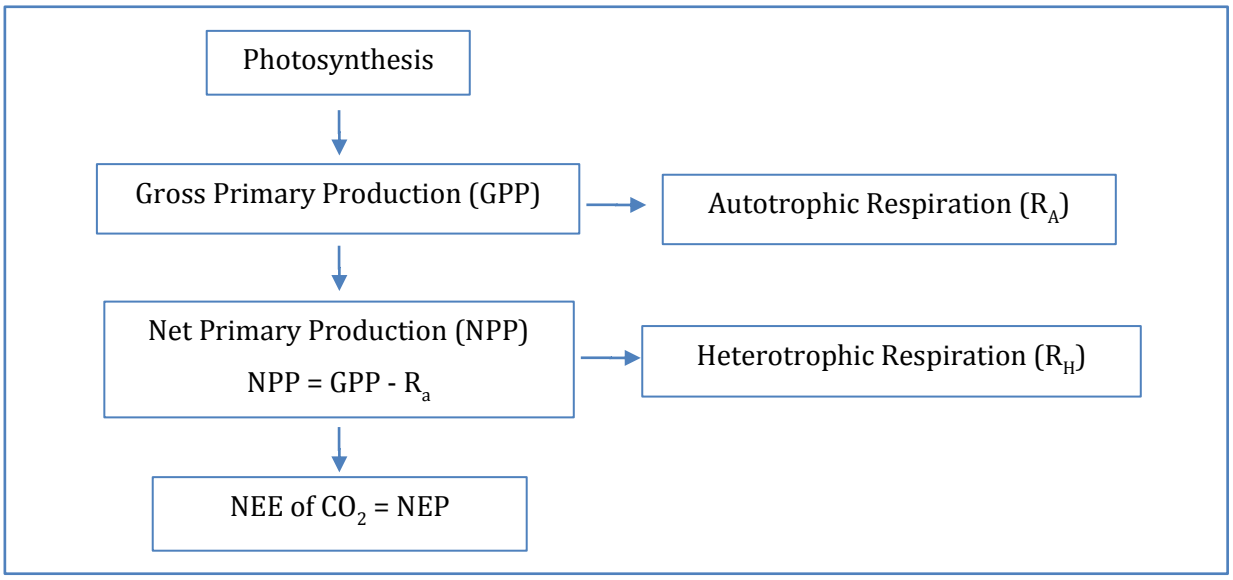

Figure 1-2 Key Component of Net Ecosystem Exchange

In terrestrial ecosystems, in general, the exchange rate of CO_2 is controlled mainly by the photosynthesis-respiration process. Thus, ecosystem productivity and its dynamics can be studied by measuring net CO_2 exchange rate, a process that is referred to as Net Ecosystem Exchange (NEE) (Lambers et al., 2008; Monteith, 1972). To quantify ecosystem productivity it is convenient to track CO_2 uptake from the atmosphere over various spatial and temporal scales (Prentice et al., 2000; Xiao et al., 2012).

1.3 Quantitative Methods of Ecosystem Productivity

Since the main focus of the thesis is on above-ground terrestrial ecosystem productivity, only methods of estimating this component of ecosystem productivity is discussed. The methods of quantifying ecosystem productivity can be broadly categorised into direct and indirect methods.

The two most commonly used direct methods are *field harvest* and *allometry* methods (Gower et al., 1999; Olofsson et al., 2013). The field harvest method entails periodic destructive sampling during the growing season of all live tissue in randomly located plots. Although, this method is suitable for estimation of grassland and cropland biomass, it is unsuitable for most forest ecosystems. Alternatively, allometry is a widely used method for estimating carbon stock and biomass variation in forest areas. The allometry technique is based on the relation between sizes of organs or parts of organisms such as wood-biomass versus diameter at breast height (DBH).

The general allometric model for forest ecology is given by following equation.

$$M_D = \beta D^{\alpha}$$

In this equation, "M_D" refers to the standing mass of an individual tree (kg), "D" is the diameter at breast height, "β" is a proportionality coefficient, and "α" is the scaling exponent which is equal to the slope of the line when plotted on logarithmic coordinates. While "α" is often quite similar between diverse organisms, "β" differs from species to species.

The implementation of the direct methods for quantification of ecosystem productivity can be problematic due to being labour intensive; species- and local-specific; and unfeasible at regional and global scales.

On the other hand, two commonly used indirect methods for terrestrial ecosystems productivity are process-based models (Baldocchi et al., 2001; Ruimy et al., 1994; Running et al., 2000) and measuring CO_2 uptake from the atmosphere at specific sites (Baldocchi, 2008; Baldocchi et al., 2001; Burba and Anderson, 2010a). A process-based model takes into account both the structure and function of ecosystems simultaneously (i.e.

photosynthesis capacity and efficiency) and is the most sophisticated approach, but requires multiple parameters that are not generally available at the ecosystem level (Baldocchi et al., 2001; Ruimy et al., 1994). The tower-based eddy covariance (EC) method provides a direct measurement of the CO_2 exchange rate between the terrestrial ecosystem and the atmosphere of a particular spatial scale and over a particular time interval (Burba and Anderson, 2010a). The first approach involves the use of models to predict ecosystem productivity of biomes/plant functional types (e.g. Leith, 1975; Potter et al., 1993; Running and Hunt, 1993; Field et al., 1995; Sitch et al., 2003; Rahman, 2004; Xiao, 2004; Sims et al., 2005; Yuan et al., 2007; King et al., 2011; Sannigrahi, 2017). The second approach involves measuring gaseous exchange at specific sites through the use of eddy covariance techniques (e.g. Baldocchi et al., 2001, 2003). Despite the state-of-the-art in quantification of terrestrial ecosystem productivity, it remains a challenging issue to extend these measurements to other temporal and spatial scales.

1.3.1 Modelling Ecosystem Productivity

At regional and global scales, Gross Primary Production (GPP), Net Primary Production (NPP) and Heterotrophic Respiration (H_R) as well as their spatiotemporal variation cannot be measured directly. Therefore, the values of these variables are usually derived using modelling techniques. A number of models have been developed over the past three decades to aid with the quantification of terrestrial ecosystems productivity across various spatial levels from landscape to regional and global scales. The models generally aim to investigate many different aspects of terrestrial carbon cycle, including changing vegetation distributions and land carbon sinks. These models have approved to be useful tools for estimating terrestrial productivity for large areas which cannot be quantified using *in situ* measurements. Detailed description of the most widely used models is provided in Appendix I. Even though numerous models for estimating terrestrial ecosystem productivity have been developed, analysis of the output from these models has often been found to vary significantly. For example, the global NPP estimates from several models ranged from approximately 40–80 $PgCyr^{-1}$. In general, these variances result from uncertainty due to differences in the initial model conditions, model parameters, model structures, and quality of data inputs.

1.3.2 Tower-based Eddy Covariance Approach

Since the late 1980s the eddy covariance (EC) technique has been used by micrometeorologists and environmental scientists (Burba and Anderson, 2010a). This technique is the most widely used, accurate and direct method to measure the exchanges of various gases (for example, carbon dioxide; water vapour; and methane) and energy between the land surface and atmosphere for a variety of applications, including: ecosystem gas exchange, carbon sequestration, climate change and agricultural research, as well as landfill emissions and urban flux (Burba and Anderson, 2010a). The measurements of CO_2 exchanges, also known as CO_2 flux[1], can be used to determine carbon budgets across a variety of natural and agrarian ecosystems, as well as industrial and urban areas. An ecosystem may be called a source of carbon, when net CO_2 flux is away from the land surface. In reverse, a green canopy may be a sink of carbon during the growing season due to uptake of CO_2 from the atmosphere through the photosynthesis process.

The eddy covariance technique is based on turbulent flow theory in the atmospheric boundary layer and is used to measure scalar fluxes from the covariance between the vertical wind speed and the gas concentration averaged across a particular spatial scale in the upwind direction, referred to as the flux tower footprint, and over a particular time interval typically a period of 30 minutes (Baldocchi et al., 2001; Burba and Anderson, 2010a). A typical eddy covariance system, as illustrated in Figure 1.3, includes a gas analyser (for example, open path and enclosed gas analyser), 3D sonic anemometer, analyser interface unit, and power supply mounted on the stationary platform, referred to as a flux tower.

1. In more scientific terms, flux can be defined as an amount of a physical property that flows through a unit of surface per unit time.

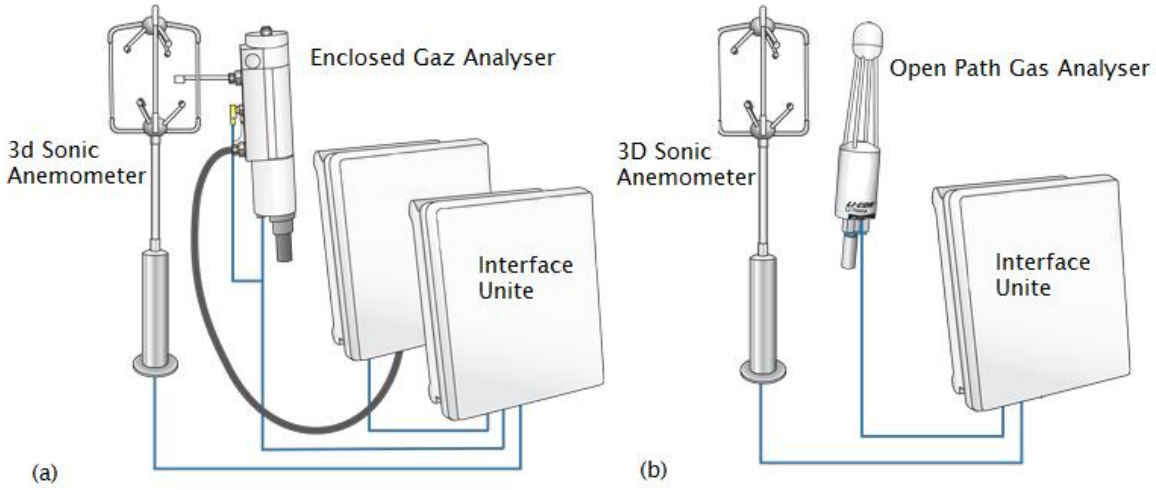

Figure 1-3 Typical Eddy Covariance System: (a) indicates an enclosed gas analyser system designed to provide measurements in harsh weather conditions and environments; (b) shows an open path gas analyser with low power consumption (Burba and Anderson, 2010a).

The flux tower footprint area represents an upwind surface where measured fluxes are registered by the instruments. In other words, the measured flux is the integral of the contributions from all upwind surface emissions fluxes (Baldocchi et al. 2001; Burba and Anderson 2010a). Figure 1.4 depicts the general concept of flux tower footprint. In this figure, the darker red colour shows the contributions that are coming from the surface areas at certain distances away from the eddy covariance system. The size and shape of the footprint coverage is a dynamic area depending on three main factors including: measurement height; surface roughness; and meteorological conditions such as atmospheric thermal stability condition, wind speed and direction (Baldocchi et al. 2001).

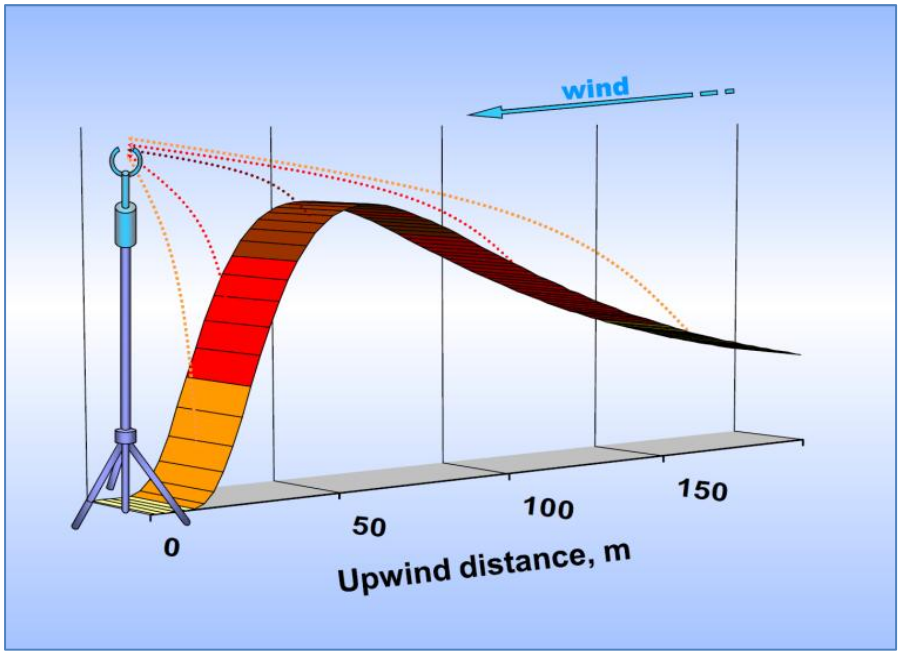

Figure 1-4 General concept of flux tower footprint (Burba and Anderson, 2010a)

In general, an increase in measurement height, decrease in surface roughness, and change in atmospheric thermal stability from unstable to stable would lead to an increase in the size of footprint coverage and would move the peak contribution away from the eddy covariance system. Since at a specific flux tower site measurement height is usually constant, surface roughness; atmospheric thermal stability; and wind speed and direction play a significant role in determining the size and shape of the time-varying flux tower footprint.

Many studies have shown close agreement between allometric sampling and the EC method concerning land-atmosphere CO_2 fluxes and GPP estimates in forest ecosystems (Curtis et al., 2002; Fenn et al., 2010; Thomas et al., 2010). Fenn et al. (2010) and Thomas et al. (2010) established confidence in the robustness of both biometrical and EC methods for the temperate deciduous forests in southern England. Although, the latter study has a finer temporal scale (i.e. annually versus half-hourly) and much coarser spatial scales (approximately 1 km^2) than the former, EC methods are not possible to apply at the landscape or regional scale (Chen et al., 2009a; Chen et al., 2012; Chen et al., 2009b; Kim et al., 2006; Melaas et al., 2013; Rahman et al., 2001).

Consequently, parameterising components of a process-based model for quantification of ecosystem productivity across a wide range of spatial and temporal scales requires that tower-specific EC flux measurements be extended using EO data and remote sensing techniques. In other words, the EC measurements of the CO_2 flux may provide valuable information (i.e. NEE of the CO_2) for calibration and validation of process-based remotely sensed models. Despite the success of the EC technique, confidence in these data with regard to extending to the ecosystem level remains uncertain, particularly in heterogeneous landscapes. The most important errors and issues associated with the EC technique are dependent on its intrinsic assumptions as follows:

- Flux measurements are made at only a few points;
- Flux measurements are restricted to periods when the atmosphere conditions are steady;
- Flux towers are installed across relatively homogeneous locations, while landscape heterogeneity is considerable;
- The location of flux tower sites has to be relatively flat;
- Flux measurements are associated with a uniform footprint of vegetation upwind;
- The sensors and the data-logging system are able to sense and record the fastest and smallest eddies (Baldocchi, 2008; Baldocchi et al., 2001; Burba and Anderson, 2010a; Schwartz et al., 2013).

Unfortunately, very few natural ecosystems meet these strict criteria. In reality, many natural and semi-natural ecosystems are situated in and among complex landscapes with varying atmospheric conditions (Forman, 1995; Forman and Godron, 1986; Frohn, 1998; Turner et al., 2002).

1.3.3 Remote Sensing of CO_2 Flux

Most applications of remote sensing in ecological studies derive from the ability to detect spectral features associated with the photosynthetic process, which can then be used for spatially explicit models of photosynthesis capacity and efficiency. As mentioned previously, Net Primary Production (NPP) takes into account the uptake of CO_2 by vegetation during photosynthesis and its release during autotrophic respiration. In this aspect, the MOD17 GPP/NPP model is the first continuous satellite-driven dataset monitoring global vegetation productivity at 1 km spatial resolution (Running et al., 2000; Running et al., 2004). However, these data require appropriate algorithms for scaling and interfacing eddy covariance flux measurements (Chen et al., 2009a).

There is a robust theory for the relationship between surface reflectance of incident radiation and the process model for modelling vegetation productivity based on the concept of Light Use Efficiency (LUE) (Monteith, 1972). This expresses GPP as a function of the absorbed photosynthetically active radiation (APAR) between the wavelengths of 400-700 nm and the efficiency of the photosynthesis process (Sellers et al., 1992). Monteith (1972) defined the photosynthesis efficiency term as the ratio of energy stored in formation of carbohydrates to APAR, which generates the LUE logic for estimating GPP from EO data. The LUE model, rather than describing complex biochemical, meteorological and canopy structure information, attempts to describe the overall ability of canopies or ecosystems to convert incident energy into biomass. The ƒAPAR concept implies the fraction of the incoming solar radiation in the photosynthetically active radiation (PAR) spectral region, which is converted into biomass by a photosynthesising organism (Sellers et al., 1992). Therefore, the basic LUE model describes GPP in terms of APAR, here referred to as photosynthesis capacity, and photosynthetic efficiency as:

$$GPP = \downarrow PAR \times fAPAR \times \varepsilon$$

where "$fAPAR$" represents the fraction of "PAR" absorbed by vegetation, and "ε" refers to realised LUE or the efficiency of converting $fAPAR$ into fixed carbon, (Hilker et al., 2008; Monteith, 1972; Running et al., 2000; Running et al., 2004; Sellers et al., 1992). The photosynthesis efficiency may be influenced by environmental constraints, the

scalars that attenuate maximum efficiency of the photosynthesis process, including air temperature and water availability as:

$$\varepsilon = \varepsilon_{max} \times T \times VPD$$

where "ε_{max}" is the biome-specific maximum efficiency of the photosynthesis process,"T" refers to the daily temperature, and "VPD" is the daylight average vapour pressure deficit. For example, high VPD has been shown to induce stomata closure in many species, while low temperatures inhibit the photosynthesis process. These scalars, as illustrated in Figure 1-5, vary linearly between 0 and 1 as a consequence of sub-optimal temperature and water availability for the photosynthesis process.

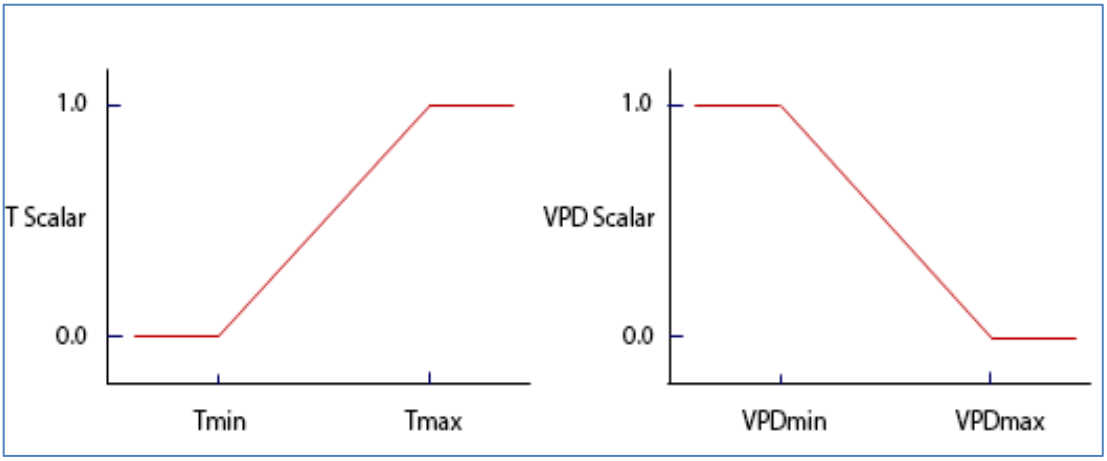

Figure 1-5 The T and VPD attenuation scalars are simple ramp functions of daily temperature and water availability

The LUE model parameters can be determined remotely using both empirical models relying on curve fitting of canopy reflectance measurements and physical models based on a canopy reflectance models. The empirical approaches are based on spectral vegetation indices (VI), which employ discrete spectral wavelengths. Various relationships between ƒAPAR and spectral VIs have been investigated for different vegetation types across a range of spatial and temporal scales (Gamon et al., 1990; Gamon et al., 1995; Glenn et al., 2008; Hilker et al., 2008; Nakaji et al., 2007; Sellers et al., 1992; Wylie et al., 2003; Gamon et al., 2016; Wang et al., 2016). The spectral vegetation indices have also been used to monitor the seasonal trend of vegetation using temporal profile analysis (Tucker, 1979).

The next section discusses the LUE logic and the spectral signature of vegetation and canopy reflectance modelling, followed by more details on spectral vegetation indices proposed for the estimation of process model components, which can be used to assess the spatial and temporal patterns of CO_2 flux and ecosystem productivity.

Table 1-2 Comparing quantitative methods of ecosystem productivity

Quantification of CO_2 Flux	Advantages	Limitations
Process-based model, for example, photosynthesis-respiration	Sophisticated Model NEE of CO_2 = GPP – (R_A + R_H)	Need to measure multiple parameters that are not easily available at various scales; as well as lack of temporally continuous data.
Eddy Covariance Methods Tower-Specific Measurements	Direct Measurements	Strict standards of EC method; and limited to flux tower footprint coverage.
Remotely Sensed Models; spectral indices of CO_2 flux	Parameterising process-based models at various spatial and temporal scales.	Uncertainty in spectral indices of CO_2 flux in terms of spectral, spatial and temporal variations.

1.3.4 Spectral Vegetation Indices of CO_2 Flux

The incident radiation reaching a plant leaf is reflected, absorbed and/or transmitted depending upon the characteristics of the vegetation (Lillesand et al. 2008). The spectral reflectance of green vegetation is variable with wavelength (Hoffer 1978) and depends on solar position, sensor view angle, sensor response, and atmospheric effects, as well as soil background and canopy structure (Danson and Rowland 2003). Curran and Milton (1983) showed that the optical properties of individual leaves are only one factor in determining canopy reflectance, and other factors such as leaf physiology, canopy density and geometry must be considered (Sellers et al. 1992). Furthermore, the nature of the interaction between incident radiation and green vegetation may change as a function of time, (i.e. during the growing season), and space (i.e. geographic location). Figure 1-6 depicts a typical spectral reflectance curve for green vegetation, and identifies the major physical controls on reflectance. Leaf pigments are significant determinants of reflectance in visible wavelengths, ranging from 400–700 nm (Danson 1995; Gamon and Surfus 1999).

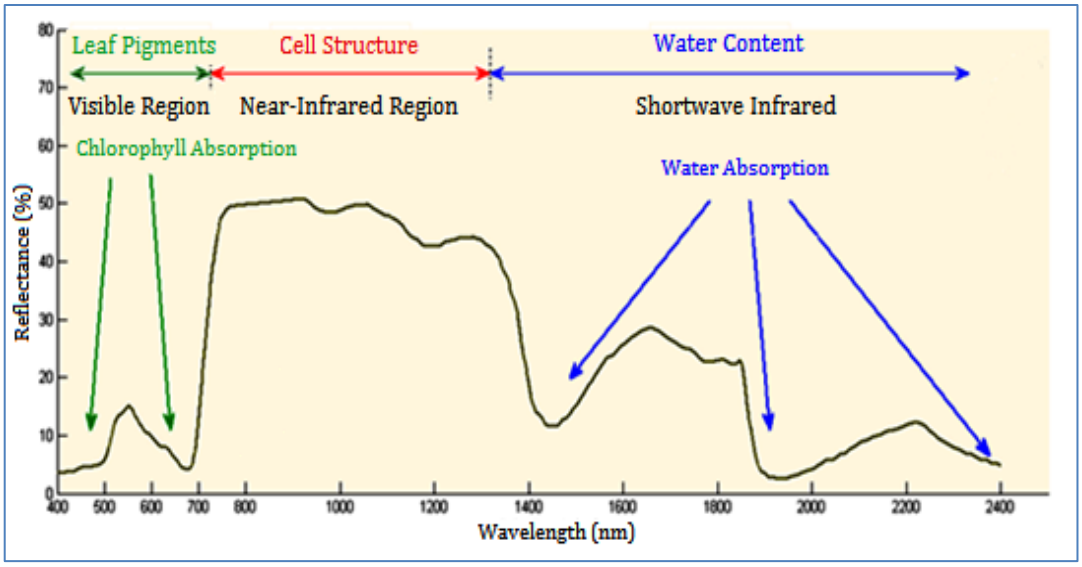

Figure 1-6 Significant spectral signature of green vegetation, adapted from Lillesand et al. (2008)

Several types of plant pigments harvest the energy of light for the photosynthesis process, so measurement of leaf pigment amount and concentration provides significant physiological information (Gamon and Surfus 1999; Richardson and Berlyn 2002). The most commonly used biochemical property of vegetation is chlorophyll content. The existence of chlorophyll in the vegetation, that is chlorophyll-a as a primary pigment and chlorophyll-b as an auxiliary pigment, is a key factor of the photosynthesis process. Chlorophyll changes can be detected by remote sensing, using specific spectral indices.

In the NIR region, 700-1300 nm, the reflectance is much higher than that in the visible region due to internal leaf structures. Therefore, again as is well known, vegetation can be identified by having a high NIR reflectance, but generally low visible reflectance. In the short-wave infrared region, 1300-2600 nm, water content absorbs incident radiation in particular wavelengths, centred on 1400, 1900 and 2600 nm.

Vegetation characteristics can be studied based on their contrasting reflectance patterns in the VNIR and SWIR spectral regions. Vegetation indices (VI) have been developed to facilitate the remote sensing of vegetation at various spatial and temporal scales, as well as to be able to retrieve biophysical and physiological properties of vegetation. In this regard, numerous studies have shown that spectral VIs can be developed with sensitivity of indices to ecological significant canopy characteristics, such as biomass (Cho et al. 2007; Du et al. 2010; Edirisinghe et al. 2012; le Maire et al. 2011; Soenen et al. 2010; Tan et al. 2007; Tucker 1979), chlorophyll content (Curran and Milton 1983; Harris and Dash 2010), leaf area index (Baret and Guyot 1991; Carlson and Ripley 1997; Chen et al. 1999; Curran and Milton 1983; Fensholt et al. 2004; Gupta et al. 2000; Wang et al. 2005) and ƒAPAR (Baret and Guyot 1991; Fensholt et al. 2004; Myneni and Williams 1994b). Ratio-based indices, in particular, have the advantage that they minimize the sensitivity to unknown and confounding variables, such as atmospheric effect, Sun angle variation (Gamon et al. 1992) and soil background (Danson 1995; Danson et al. 2003; Huete 1988; Qi et al. 1994).

The most commonly-used VIs are either ratios of two bands or a linear combination of several spectral bands. The input data may be sensor DN, radiance (i.e., at-sensor or ground-leaving) or surface reflectance (Jackson and Huete 1991). In most vegetation

studies, these indices are calculated using data in the Red and NIR wavelengths as these are directly connected to the absorption and scattering processes within plant canopies, as explained above, and therefore relate to the amount (or state) of photosynthetically active green biomass (Tucker 1979).

The most widely used VI is the normalized difference vegetation index (NDVI), which can be used to assess the magnitude and direction of vegetation changes and monitor seasonal trends in vegetation abundance and distribution (Bartlett et al. 1990; Tucker 1979). This index is defined as the reflection difference between the visible Red and NIR reflectance's divided by their sum.

$$NDVI = (R_{NIR} - R_{Red})/(R_{NIR} + R_{Red}) \quad (1)$$

The robust relationship between NDVI and ƒAPAR can be used to generate the LUE-based logic for estimating CO_2 flux and GPP from EO data. Multiple studies have shown that NDVI can be used to estimate ƒAPAR (Carlson and Ripley 1997; Gamon et al. 1997; Huemmrich and Goward 1997; Myneni and Williams 1994a; Sellers et al. 1992), LAI (Baret 1995; Baret and Guyot 1991; Carlson and Ripley 1997; Curran and Milton 1983; Danson 1995; Danson and Rowland 2003; Fensholt et al. 2004; Gupta et al. 2000; Wang et al. 2005) and CO_2 fluxes and ecosystem productivity (Bartlett et al. 1990; Burgheimer et al. 2006; Hill et al. 2006; Kim et al. 2006; La Puma et al. 2007; Ricotta et al. 1999; Wohlfahrt et al. 2010; Wylie et al. 2003; Yan et al. 2009). Tucker (1979) assessed combinations of various spectral bands to predict biomass, chlorophyll and water content of grassland and showed that the NDVI was correlated with chlorophyll content. Sellers et al. (1992) showed that the area-averaged NDVI may provide an accurate estimate of the area-integrals of the canopy assimilation rate even for spatially heterogeneous vegetation covers. Myneni and Williams (1994b) and also Danson and Rowland (2003) have used a canopy reflectance model to show that NDVI and ƒAPAR are sensitive to LAI. In addition, Bonan (1993) used two ecological variables, LAI and canopy type, to assess their effects on net canopy assimilation. His results show that uncertainty in LAI and species composition can cause error in the estimation of net canopy assimilation. In general, LAI and canopy type can influence CO_2 uptake by determining ƒAPAR. Gamon et al. (1997) demonstrated that NDVI was a useful indicator of canopy

structure, APAR and photosynthesis activity across a wide range of vegetation types, even in heterogeneous landscapes. Their results also show that, despite a large correlation between NDVI and ƒAPAR, this spectral index was not a reliable indicator of instantaneous photosynthetic rates. Therefore, to provide accurate estimates of canopy-atmosphere CO_2 fluxes, NDVI needs to be coupled with an estimate of canopy photosynthesis LUE (Gamon et al. 1997). The NDVI is a very sensitive spectral indicator of biophysical variables in sparse canopies, where the soil background is visible (LAI values between 0.0 and 2.0) (Baret and Guyot 1991; Danson 1995; Danson and Rowland 2003; Huete 1988). This sensitivity decreases when the amount of LAI exceeds a threshold value, typically around 3.0 (Carlson and Ripley 1997; Danson and Rowland 2003; Gamon et al. 1997). To address this issue, Baret and Guyot (1991) presented a generic relationship between VIs and LAI.

$$LAI = -\frac{1}{k}\ln(VI - VI^{\infty}/VI_{soil} - VI^{\infty})$$

where "VI_{soil}" is the vegetation index value for bare soil, "VI^{∞}" is the vegetation index value when "LAI" tends towards infinity[1] and "k" is the extinction coefficient. They initially found that the "VI_{soil}" based on a measure of an angle in spectral feature space (e.g. NDVI) performed more accurately than those indices based on a measure of Euclidean distance (e.g. perpendicular vegetation index, PVI); and also compared their predictive performances for LAI estimation (Baret and Guyot 1991). Accordingly, the results showed that the best index was the modified soil-adjusted vegetation index (MSAVI), due to it minimizing the soil background effects and increasing the sensitivity for large LAI values compared to the NDVI.

Most ecological remote sensing uses relatively broadband sensors to compute vegetation indices and, thereby, estimate land surface biophysical variables. Perhaps the most widely used vegetation index is NDVI. Although NDVI has been often shown to have a large correlation with some canopy biophysical variables such as canopy structure, biomass, LAI, APAR and canopy photosynthesis capacity (Sellers et al. 1992),

1. Optically dense canopy without transmission

it is often unable to represent the physiological process of photosynthesis at fine temporal and spatial scales (Gamon et al. 1992). For example, CO_2 uptake rate, also referred to as photosynthesis efficiency, can undergo seasonal trends in photosynthesis efficiency without the corresponding changes in photosynthesis capacity or canopy structure (Gamon et al. 1992; Sellers et al. 1992). Since photosynthesis is an optical process, the reflectance of leaves or canopy may contain a signal for photosynthetic efficiency, and therefore provide an algorithm to detect changes in photosynthesis performance using a particular spectral vegetation index.

Relatively new indices using narrow-band reflectance can provide direct assessment of physiological processes linked to photosynthetic performance and efficiency (Soenen et al. 2010). Gamon et al. (1990) showed that reflectance changes indicative of the xanthophyll cycle pigment (i.e. roughly at 531 nm), provided an indicator of photosynthetic performance and could be useful to increase the accuracy of remotely sensed techniques in monitoring photosynthesis efficiency at canopy or landscape scales. In reality, when the capacity of photosynthesis is saturated by excess APAR, the xanthophyll cycle pigments de-epoxy, which is also reversed under limiting APAR (Gamon et al. 1990). The common expression of this signature is the photochemical reflectance index (PRI), an index of the "*epoxidation*" state of xanthophyll cycle pigments that expresses the short-term variation in the efficiency of the photosynthesis process given by the following equation.

$$PRI = (R_{531} - R_{Ref})/R_{531} - R_{Ref})$$

where "R_{531}" referred to as carboxylation reflectance, represents reflectance at 531 nm and "R_{Ref}" indicates reflectance at an insensitive reference band (Coops et al. 2008; Fensholt et al. 2004; Gamon et al. 1997; Tan et al. 2007). Several studies have illustrated the possibility that the PRI derived from narrow waveband reflectance at 531nm and the reference reflectance at either 550 nm or 570 nm, can be used as a useful indicator of photosynthetic function at leaf and canopy or landscape level, respectively (Coops et al. 2008; Fensholt et al. 2004; Gamon et al. 1992; Gamon et al. 1997; Gamon and Surfus 1999). Some recent studies have also shown that PRI has considerable promise as a means of estimating vegetation photosynthesis performance and efficiency, commonly

known as CO_2 uptake (Nichol et al. 2000; Rahman et al. 2001). Gamon et al. (1997) have indicated that the PRI derived at 531 nm and a reference wavelength is insensitive to short-term changes in light energy conversion efficiency, usually at 570 nm, and is significantly correlated with both CO_2 uptakes. Their investigations support the use of this index as an indicator of photosynthesis efficiency for leaves and canopies in full Sun, but not across wide ranges in illumination. This means that the PRI is influenced by viewing and illumination geometry (Coops et al. 2008; Tan et al. 2007). Nichol et al. (2000) and Rahman et al. (2001) have also shown that PRI can be effectively used as an indicator of photosynthetic efficiency at the stand and landscape level. However, a single formulation of this index is not applicable across all canopy types or canopies of diurnally changing structure (Gamon et al. 2005; Gamon and Surfus 1999).

Accurate radiometric calibration, as well as proper correction for atmospheric scattering in the derivation of surface reflectance, appears to be a critical challenge in deriving a valid PRI from high-altitude platforms (Gamon et al., 1998). Currently, there is a lack of satellite sensors with appropriate bands for this index, and there are no direct ways for validating optical estimates of gross photosynthesis at a scale (i.e. area) larger than the single stand or canopy. Consequently, this optical index of light use efficiency will continue to be most readily applicable at the stand scale and scaling-up this index from canopy to landscape or regional level, will remain a challenging issue (Hilker et al. 2008).

To sum up, the potential of spectral VIs in addition to the LUE logic, for estimating canopy GPP or gross CO_2 uptake rate from airborne and satellite sensing data might be expressed as the following equation.

$$GPP \propto f(PRI \times NDVI)$$

1.4 Concluding on Scaling CO_2 Flux and Productivity Models

As mentioned previously, the global carbon fluxes from the atmosphere to the biosphere are the major contributor for ecosystem productivity as compared to any other fluxes (Hazarika et al., 2005). The model estimation of global net productivity varies within 40–80 PgC $year^{-1}$ has clearly shown the uncertainty in the estimate of spatiotemporal net productivity. Thus, the focal points are as (1) spatial resolution (2) land cover, and (3) light use efficiency (LUE) for accurate quantification of terrestrial ecosystem productivity using remote sensing LUE approach, RS-based LUE Model (Running et al., 1999a,b; Ahl et al., 2005).

In this aspect, a fundamental challenge is the scale mismatch between a small-scale, spatially non-uniform EC flux footprint and the typically larger-scale gridded, continuous predictions made in simulations. The flux measurement footprint typically represents a small fraction of the RS-based LUE model grid cell, and the location of this fraction changes with time. Any error bias that occurs from changes in sampled characteristics with time can alter model-data comparison (Rahman et al, 2001, Chen at al., 2009, Xu at al., 2017).

Direct measurement of CO_2 fluxes from atmosphere to biosphere is challenging, and as such, a number of remote sensing approaches have developed in the last few decades with the primary aim to accurately estimate and predict regional and global net productivity (Canadell et al., 2000; Ogutu et al., 2013; Zhang et al., 2015). Recent analysis has shown that consideration of footprint for scaling chamber emissions can significantly improve comparison of tower-based EC measurements to chamber-scaled fluxes (Budishchev et al., 2014). Therefore, accurate quantification of terrestrial ecosystem productivity using different LUE models are essential for (1) analysing spatial and temporal changes of carbon stock density; (2) evaluating the spatiotemporal variability of forest dynamics and its relationship with global and regional net productivity;(3) data for model based global and regional carbon and biomass change assessment (Tang et al., 2010; Yan et al., 2011; Yuanet al., 2014a,b).

Several LUE models have been developed to deal with the uncertainty of accounting global and regional net productivity over varied ecoregion across the world (Lieth and Whittaker, 1975; Potter et al., 1993; Field et al., 1995; Ruimy et al., 1996, 1994; Running et al., 2004; Xiao et al., 2004, 2007; Yuan et al., 2014a,b). However, the structural differences between the estimated magnitude and spatiotemporal distribution of net productivity have substantially persisted in different LUE models (Yuan et al., 2014a,b).

Parametric models estimate net productivity from the incident radiation use and absorption efficiency by plant canopies namely Carnegie-Ames-Stanford-Approach (CASA) model (Potter et al., 1993); Eddy Covariance – Light Use Efficiency (EC-LUE) model (Yuan et al., 2007); Vegetation Photosynthesis Model (VPM) (Xiao et al., 2004); CENTURY model (Partonet al., 1996); C-Fix model (Veroustraete et al., 2002); Global Production Efficiency Model (GLO-PEM) (Prince and Goward et al.,1995). The process-based models works on the LUE approach and are widely used for calculating terrestrial net productivity across the biomes (Amthor et al., 2001; Rui et al., 2002; Ogutu et al., 2013), for instance, BIOME-BGC model (Running and Coughlan, 1988), MODerate resolution Imaging Spectroradiometer (MOD17) model (Running et al., 2004;Liu et al., 1997). During the last few decades, several approaches were introduced for biome specific modelling of terrestrial ecosystem productivity at any ecosystem scale (Monteith, 1977). In direct comparison approach, mathematical formulation of each model treated as control variables which significantly alter the amplitude of model performances in various experimental setups (Adamset al., 2004). However, this approach found to be inappropriate in a more complex ecosystem (i.e. terrestrial ecosystem) (Wang et al., 2011; Ogutu et al., 2013). In production efficiency approach, a constant light use conversion has been observed over the various environmental condition to assimilate dry carbon (Running et al., 2004), which seems to have decreased as of increasing biomass and temperature (Ruimy et al., 1996). A radiative transfer approach has been developed and followed out to estimate satellite derived LAI (Hazarika et al., 2005). In multi-model ensembles approach, numerical formulations of process-based models are taken into consideration to run a group of models with the same input approximation and boundary/layer condition within the robust experimental setup. The mean output of the ensembles models are then analysed, and

the simulated variance between each model treated as the model's structural uncertainty (Tebaldiand Knutti, 2007; Wang et al., 2011; Ogutu et al., 2013). Remote sensing LUE models could accurately estimate the spatiotemporal net productivity over diverse ecosystems (Higuchi et al., 2005; Ichiiet al., 2005).

1.5 Aims and Objectives

The key to understanding carbon flux and managing ecosystem services is to track vegetation productivity and dynamics. In this context, knowledge of the amount of carbon fixed by the photosynthesis process and its sequestration by vegetation is important for the quantification of ecosystem productivity. Remote sensing in its various forms clearly has a role to play in better characterization of the photosynthetically active canopy various scales over a growing season. However, the application of remote sensing to this task is not straightforward, and the main aim of this research is to address this, using a combination of tower-based EC flux data, airborne and satellite remote sensing from sites in the UK and the eastern United States. The specific aims of the present research are listed in Table 1-3.

Table 1-3 The Specific Aims of the Research

Specific Aim	Objectives to Fulfil the Aim
1. Investigate how the three-dimensional structure of a heterogeneous forest canopy affects the remotely sensed signal, in particular how different representations of the flux footprint affect the most commonly used broadband vegetation index (e.g. NDVI).	1.1. Create an accurate three-dimensional model of a heterogeneous forest based on airborne LiDAR data in order to characterise the spatial patterns of vegetation and the vertical structure of the canopy around an EC tower. 1.2. Implement an established flux footprint model in order to simulate the area of the canopy contributing to the EC measurements under different conditions 1.3. Investigate whether differences in the size and shape of the flux footprint significantly affect spectral indices of CO_2 fluxes over a growing season. 1.4. Assess the effect of the mismatch between the spatial support of various remote sensing systems and the actual flux footprint, using spatial statistical techniques, taking account of their spatial co-variability.

2. Investigate the potential of airborne imaging spectrometry to provide information on ecosystem processes in a heterogeneous forest through the use of a narrowband vegetation indices (e.g. NDVI and PRI).	2.1. Acquire and calibrate one or more hyperspectral remotely sensed data sets from the same forest studied in Aim 1. 2.2. Classify spectral based of canopy cover 2.3. Investigate the sensitivity of several narrowband vegetation indices to various extraneous variables (AOT, view/illumination geometry, etc.)
3. Investigate the potential of a constellation of satellite sensors to provide useful ecological information from a heterogeneous forest throughout the growing season.	3.1. Obtain and calibrate as many satellite images (high spatial and temporal resolutions) of the chosen forest site during a growing season. 3.2. Determine the repeatability of many satellite images over a period of few days to investigate temporal variability. 3.3. Test geostatistical techniques of predicting vegetation indices across the flux tower domain based on image data from satellite remote sensing systems
4. Reduce the uncertainty in parameterizing a spectral index based EC-LUE model which will enable the direct estimation of the efficiency of carbon uptake (i.e. LUE) using on satellite observations across heterogeneous landscapes	4.1. Estimate ecosystem function (i.e. photosynthetic LUE) using a satellite-derived spectral index. 4.2. Estimate LUE model parameters by combining regional flux network observations from tower-based instruments with data from satellite observations. 4.3. Investigate whether a satellite-based model of LUE could be applied across a range of plant functional types (PFT).

1.6 Experimental Design

The concept of "**scaling**[1]" was central to the research project and it was therefore necessary to devise an experiment design that involved a range of remote sensing systems. Although multi-scale remote sensing would provide the tool to study the problem, the main focus of the research was "**uncertainty**" within the relationship between ground-based estimates of carbon flux and those made using remote sensing systems. In order to study this, it was necessary to conduct the research at one or more sites where EC towers were already established and, at least in the initial stages, where high quality data from an airborne imaging spectrometer already existed. Chapter 2 provides a description of the sites selected for study, and the rationale behind their choice. Inevitably, there had to be a compromise between what was possible and what would have been desirable and this is discussed further in the concluding chapter of this thesis.

Although spatial scaling was at the heart of the research, the time dimension was also vital as flows of carbon are a process operating over time. This meant that any remote sensing system chosen had to be capable of delivering a time series of data throughout a growing season (or longer), not just a single image. Consideration of all the requirements above led to selection of two potential remote sensing approaches: (i) airborne imaging spectrometry (AIS) applied to a small area test site, and, (ii) satellite sensor data drawn from a global archive. The initial experiment design envisaged use of multi-date AIS data from an instrumented test site in southern England, complemented with coarser resolution multispectral data from a range of established test sites in the eastern United States. However, at an early stage in the research the opportunity arose to acquire a time series of images of the test site in southern England from a constellation of satellite-based sensors, and this was invaluable in providing a bridge between the two primary approaches. Good weather conditions during 2010 allowed

1. The up-scaling process (i.e. in terms of space and time) is the expansion of information from a smaller scale to derive processes at larger scale, for example, field spectrometric data into airborne or satellite pixel size. In contrast, down-scaling involves the decomposition of data collected at larger scales into information at smaller scales.

the acquisition of an excellent time series of data from the DMC constellation of satellites, the analysis of which is described in Chapter 5. This chapter is to some extent a link between the fine spatial resolution AIS analysis presented in Chapter 3 and 4, and the coarse spatial resolution multispectral analysis presented in later chapters.

2. Preliminary Research

The previous chapter opened the general area of research, high-lighting the importance of uncertainty associated with estimating carbon fluxes and ecosystem productivity at various spatial and temporal scales using modelling- and/or RS-based approaches. Although multi-scale remote sensing would provide the tool to study the problem, the main focus of the research was "uncertainty" within the relationship between field-based estimates of CO_2 flux and those made using remote sensing systems. In order to study this, it was necessary to conduct the research at one or more sites where EC towers were already established and, at least in the initial stages, where high quality data from an airborne imaging spectrometer already existed. This chapter describes the sites selected for study, existing data, preparing EO data, and estimation of flux tower footprint.

2.1 Study Sites

2.1.1 The UK's Flux Tower Network

At present, over 500 active flux tower sites are operated on a long-term and continuous basis throughout the world and about 17 sites are reported to be operating across the UK (FluxNet 2013). These monitor the net exchange of CO_2, water vapour and energy flux in a variety of ecosystems, including deciduous broadleaf forest, coniferous forest, grassland and cultivated cropland. Among the UK's flux tower network (Table 2-1), Wytham Woods, one of the UK Environmental Change Network's (ECN) terrestrial sites was selected for study due to the availability of high quality ecological data, eddy covariance flux measurements, and Earth observation data. Figure 2-1 illustrates the distribution of flux tower sites across the UK, highlighting Wytham Woods as a main study site in southern England.

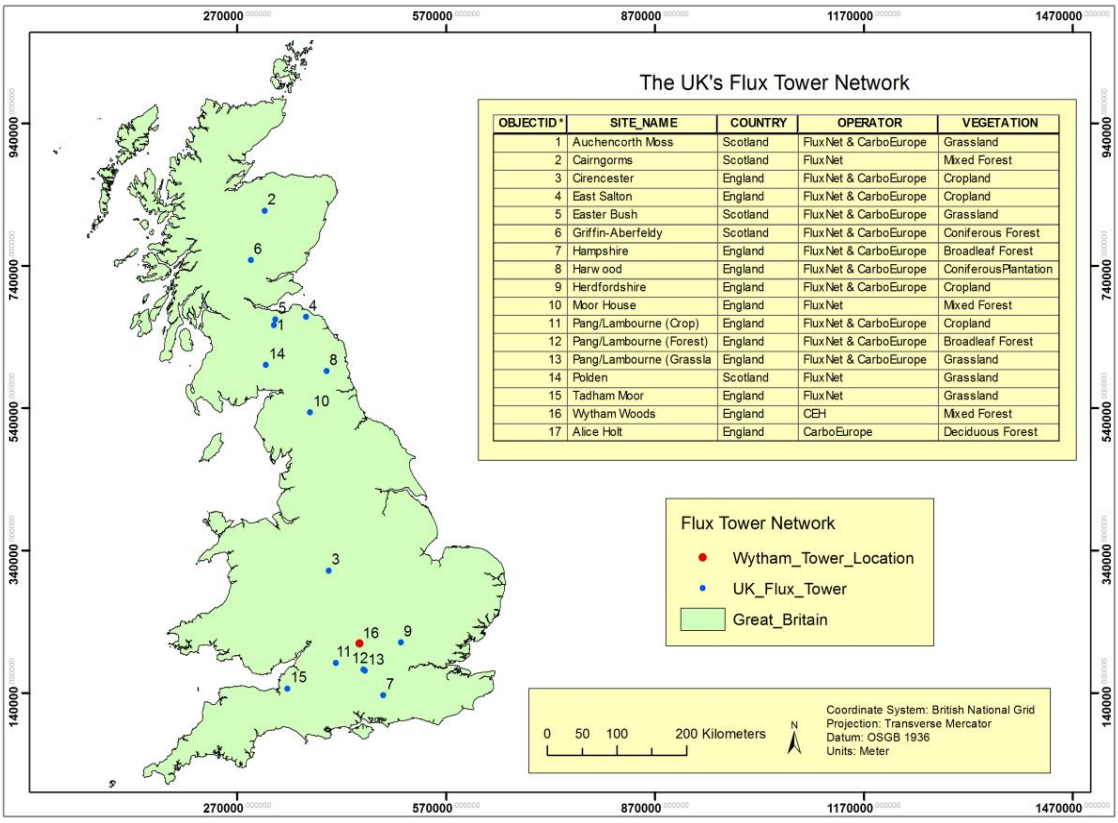

Figure 2-1 Distribution of the UK flux tower network (FluxNet 2013)

Table 2-1 Characteristics of the UK's flux tower network (FluxNet 2013)

Site Name	Lat (N)	Long (W)	Land Cover / PFT	Elevation (m)
Alice Holt	51.15	0.86	Deciduous Forest	82
Auchencorth Moss	55.79	3.24	Grassland/Cropland	265
Cairngorms	57.23	3.50	Evergreen Coniferous Forest	461
Cirencester	52.70	1.98	Cropland	176
Easter Bush	55.87	3.21	Grassland	208
East Salton	55.90	2.86	Cropland	307
Griffin	56.61	3.79	Evergreen Coniferous Forest	343
Hampshire	51.12	0.86	Deciduous Broadleaf Forest	76
Harwood	55.22	2.04	Evergreen Coniferous Forest	282
Hertfordshire	51.78	0.47	Cropland	142
Moor House	54.69	2.39	Evergreen Coniferous Forest	600
Pang/Lambourne	51.53	1.48	Cropland	159
Pang/Lambourne	51.45	1.27	Deciduous Broadleaf Forest	104
Pang/Lambourne	51.43	1.23	Grassland	78
Polden	55.29	3.40	Grassland	180
Tadham Moor	51.21	2.83	Grassland	28
Wytham Woods	51.78	1.33	Deciduous Broadleaf Forest	119

2.1.2 Site Description – Wytham Woods

Wytham Woods is a temperate broadleaf forest located in the upper Thames basin, 5 km north-west of Oxford in southern England (Lat: 51.77 N; Lon: -1.33 E). The site contains a 25 m high micrometeorological flux tower where eddy covariance measurements of turbulent fluxes have been recorded continuously since May 2007 (Thomas et al. 2010). Wytham's EC instruments include a 3D sonic anemometer measuring wind vector components and an open-path gas analyser (LI-COR 7500) measuring atmospheric CO_2/H_2O fluxes. Wytham Woods is comprised of ancient, secondary and plantation woodlands (i.e. mixed forest of 400 ha) with four main elements forming a landscape mosaic including deciduous forest; patches of semi-natural grassland and scrub; cultivated cropland; and some small wetland areas. The whole site covers 770 ha (UK-ECN 2012). The flux tower system, as illustrated in Figure 2-2 and 2-3, is located on the north slope of a hill surrounded by mixed forest, also depicted by Figure 2-4 that includes scrub, non-coniferous and coniferous trees for approximately 450 m to the north and approximately 1000 m to the east and the south-west. The altitude ranges from 60 m above sea level on the river floodplain to 165 m at the top of Wytham Hill. Meteorology data from the UK Environmental Change Network (ECN) Wytham site have been recorded by an Automatic Weather Station since 1992 (Savill et al. 2010). The climate is typical of central England, with a mean annual temperature and precipitation of approximately 10.0°C and 720 mm, respectively.

According to the National Vegetation Classification (Rodwell 1991), both ancient and secondary woodlands are part of community W8, *Fraxinus excelsior - Acer campestre - Mercurialis perennis* woodland, the most prominent species being ash (*Fraxinus excelsior*), field maple (*Acer campestre*), and hazel (*Corylus avellana*), as well as sub-dominant species oak (*Quercus robur*) and sycamore (*Acer pseudoplatanus*).

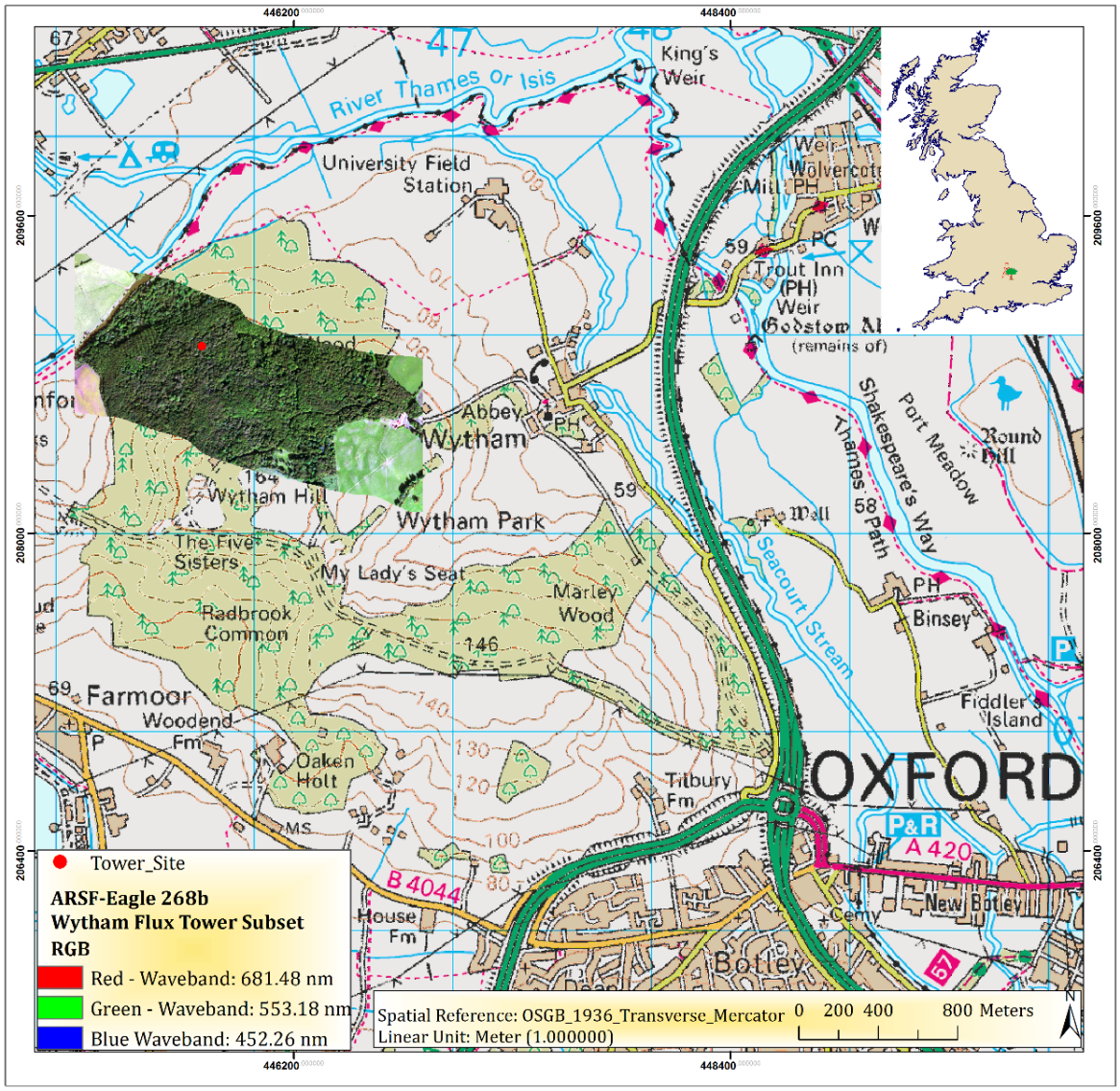

Figure 2-2 Location of the Study Site, Wytham Woods, Oxfordshire-UK; overlaid on a true colour composite of airborne hyperspectral imagery (NERC-ARSF Eagle data), and OS 1:50,000 Colour Raster SP40 (Adapted from Ordnance Survey DigiMap, 2010 and NERC-ARSF, 2009)

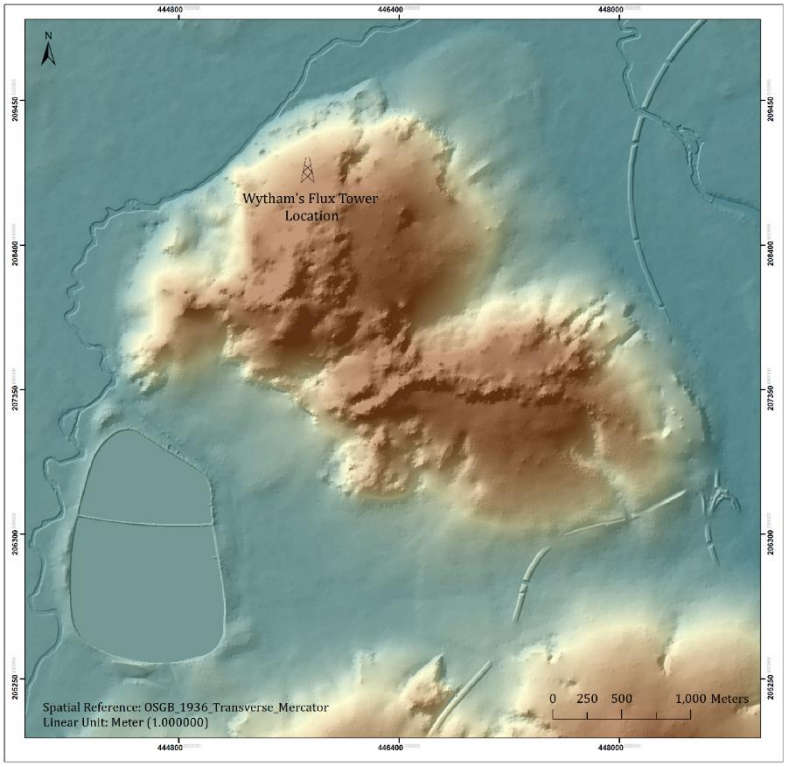

Figure 2-3 Wytham Woods digital elevation model (DEM) (Adapted from Ordnance Survey DigiMap, 2010)

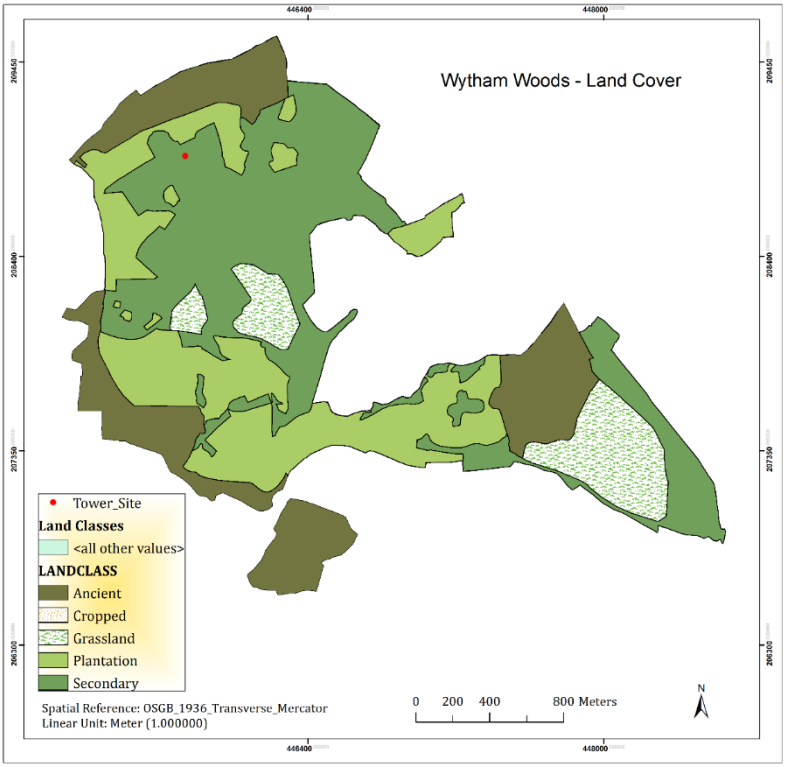

Figure 2-4 Wytham Woods Land Cover/Plant Function Type (Adapted from Ordnance Survey DigiMap, 2010)

2.1.2.1 Site Background: CO_2 Flux Measurements

Fenn et al. (2010) compared biometrics and chamber estimates of ecosystem productivity (i.e. GPP) and respiration at Wytham Woods with tower-based measurements. Their results showed that there was close agreement between the monthly and annual estimates of ecosystem productivity and respiration. This investigation also gives confidence in the robustness and suitability of both bottom-up biometrics and flux chamber measurements, as well as top-down eddy covariance measurements (Schimd 2002). Thus, not only tower-based CO_2 flux, but also biometrical estimates may be used to validate remotely sensed indices of CO_2 flux and ecosystem productivity, particularly at sites with lack of data (tower-based CO_2 flux and/or remotely sensed imagery) as per the main aim of the current research. Furthermore, Thomas et al. (2010) quantified the absolute magnitude and temporal variability in flux data for a period of two-years from 1 May 2007 to 30 April 2009. They showed that eddy covariance data were close to a biometric assessment of net ecosystem productivity generated using allometric equations relating trunk circumference at breast-height to biomass within a 1 ha plot close to the flux tower (Thomas et al. 2010).

2.1.3 Site Description - The Chequamegon Ecosystem-Atmosphere Study (ChEAS) Region - USA

In addition to data from the UK test site, this research presents and analyses a five-year record of eddy covariance data from four flux towers selected across various plant functional types (PFT) in the Upper Midwest region of northern Wisconsin and Michigan, United States, which are part of both the AmeriFlux network and the Chequamegon Ecosystem-Atmosphere Study (ChEAS)[1]. The region is an area of temperate/sub-boreal forest with many small former glacial lakes and wetlands. The location of the flux tower sites is illustrated in Figure 2-5. The main characteristics of these sites, such as PFT/vegetation and geographic attributes are also detailed in Table 2-2 (Desai et al. 2005; Desai et al. 2008).

Table 2-2 Location and characteristics of selected sites for CO2 flux measurement made in the ChEAS region

Site Name	Lat (N)	Lon (W)	Land Cover/PFT*
Lost Creek (LC)	46.08	89.98	Woody Wetland
Wisconsin South Fork (SF)	45.92	90.13	Woody Wetland
Willow Creek (WC)	45.81	90.08	Deciduous Forest
Wisconsin Young Jack Pine (YJP)	46.62	91.08	Evergreen Forest
Wisconsin Mature Red Pine (MRP)	46.74	91.16	Evergreen Forest
Sylvania Wilderness (SW)	46.24	89.35	Mixed Forest
Park Falls / WLEF (WLEF)	45.65	90.27	Mixed Forest
University of Michigan Biological Station (UMBS)	45.56	84.71	Mixed Forest

* Woody Wetland (WW); Deciduous Forest (DF); Evergreen Forest (EF); and Mixed Forest (MF)

The Chequamegon Ecosystem-Atmosphere Study (ChEAS) is a focused area for ecosystem-atmosphere interaction research, aiming to understand the processes controlling forest-atmosphere exchange of CO_2 and the response of these processes to environmental change within a mixed forest within or near the Chequamegon Nicolet National Forest in northern Wisconsin, in the upper peninsula of Michigan. The land cover in this region is a highly heterogeneous mixture of dense upland and wetland forests with relatively flat terrain (Xiao et al. 2011b).

1. http://cheas.psu.edu/

Figure 2-5 Location of the ChEAS flux tower sites across the Upper Midwest, USA

The majority of upland forest consists of mature hardwood forest of maple (*Acer spp.*), birch (*Betula allghaniesis*), basswood (*Tilia americana*), ash (*Fraxinus spp.*), and younger fast growing aspen (*Populus termulouides*) forests. Coniferous species, in this region, cover a smaller area similar to Wytham Woods in southern England, including red pine (*Pinus resinosa*), jack pine (*Pinus banksiana*), eastern hemlock (*Tsuga canadensis*), and white pine (*Pinus strobus*) forests. Approximately 30% of the region is covered with forested wetlands that contain primarily black spruce (*Picea mariana*), white cedar (*Thuja occidentalis*), tamarack (*Larix laricina*), and shrub weltlands typically containing alder (Alnus spp.) and willow (Salix spp.) species and open meadows (Desai et al. 2008; Xiao et al. 2011b).

2.2 Data Acquisition

2.2.1 Micrometeorological Flux Tower Measurements

Wytham tower-based CO_2 flux tower measurements were recorded from May 2007 to December 2010 and filtered corresponding to the secondary remotely sensed data overpass to identify and assess the main sources of uncertainty for scaling between tower-specific flux tower footprint coverage and regional scales using coarse satellite sensor observations.

In addition, long-term EC-based CO_2 flux data across four selected sites in the Upper Midwest region of northern Wisconsin and Michigan, drawn from the ChEAS programme at the Pennsylvania State University, were used to compute CO_2 uptake rate (i.e. based on LUE model, Equation 1-4 and 1-5) and used to assess satellite-derived PRI for estimation of photosynthesis efficiency at the regional scale.

2.2.2 DigiMap Ordnance Survey Data

Ordnance Survey (OS) Master Map Topography Layer including OS Vector Map District SP40 and OS 1:50,000 scale Colour Raster SP40, as well as a Great Britain outline map were collected to visualize the Wytham Woods Study site and associated geospatial and Earth observation datasets. All datasets were re-projected into the British National Grid (BNG), Datum OSGB36.

2.2.3 Satellite Remote Sensing Data

2.2.3.1 DMC Imagery

The UK Disaster Monitoring Constellation (UK-DMC) is a constellation of satellites capable of acquiring multispectral images with two imagers, SLIM-6 and SLIM-6-22, that provide three spectral bands between 520 nm and 900 nm. The UK-DMC characteristics and the provided data are presented in Tables 2-3 and 2-4 (Crowley 2010).

Table 2-3 Comparing characteristics of the UK-DMC and UK-DMC2

DMC Characteristics	UK-DMC	DEIMOS	UK-DMC2
Imager	SLIM-6	SLIM-6-22	SLIM-6-22
Imager Type	Optical	Optical	Optical
GSD at Nadir	31.822 m	22.001 m	22.001 m
FOV	26.62 °	25.97 °	25.97 °
Swath	324.58 km	340 km	340 km
Altitude	686 km	659 km	659 km
Spectral Bands	Green, Red and NIR	Green, Red and NIR	Green, Red and NIR

Table 2-4 Comparing spectral bands of DMC and Landsat5 Thematic Mapper

Spectral Band	Spectral Bandwidth	Central Wavelength	Equivalent Landsat 5
Green	0.52 – 0.60 µm	0.56 µm	TM 2
Red	0.63 – 0.69 µm	0.66 µm	TM 3
NIR	0.77 – 0.90 µm	0.835 µm	TM 4

DMC satellite sensor imagery (i.e. UK-DMC, UK-DMC2 and DEIMOS datasets) were acquired from 2007 to 2010 throughout the growing season by DMC International Imaging Ltd. over southern England (Table 2-5) and made available for this project (Mackin, personal communication, 2011).

Table 2-5 DMC datasets acquired across southern England

Data File	Imaging Date	Imaging Time	Mission	Image Clarity	Sun Elevation (Deg.)
DU000a43T_L1T.tif	01/03/2007	09:13:42	UK-DMC	Shaded	20.0597293961
DU000aa5T_L1T.tif	28/04/2007	09:16:40	UK-DMC	Hazy	39.8806456059
DN000597T_L1T.tif	16/02/2008	09:23:02	UK-DMC	Clear	14.6849645669
DU000cd7T_L1T.tif	06/05/2008	09:07:32	UK-DMC	Hazy	40.6132513816
DU000e7eT_L1T.tif	02/03/2009	08:35:57	UK-DMC	Clear	15.4465961633
DN0007ceT_L1T.tif	11/05/2009	08:39:13	UK-DMC	Cloudy	38.2181310960
DU000e7eT_L1T.tif	02/06/2009	08:19:43	UK-DMC	Clear	41.0905297922
DU00103bT_L1T.tif	01/03/2010	08:13:04	UK-DMC	Cloudy	10.4912568286
U200001bb_L1T.tif	02/03/2010	09:43:21	UK-DMC2	Clear	22.6538620894
U200001c5_L1T.tif	05/03/2010	09:46:39	UK-DMC2	Clear	23.6911926930
DE000173a_L1T.tif	07/03/2010	09:54:31	DEIMOS	Clear	25.2433764386
DE0001867_L1T.tif	01/04/2010	09:43:16	DEIMOS	Cloudy	34.3848218805
DU001066T_L1T.tif	20/04/2010	08:03:51	UK-DMC	Clear	27.2746531232
U20000272_L1T.tif	27/04/2010	10:08:21	UK-DMC2	Clear	45.5615917954
U200002f9_L1T.tif	23/05/2010	09:52:10	UK-DMC2	Clear	49.8549780362
U20000335_L1T.tif	04/06/2010	09:56:34	UK-DMC2	Clear	51.9558988937
U2000036f_L1T.tif	16/06/2010	09:52:02	UK-DMC2	Clear	51.6702394975

2.2.3.2 MODIS Vegetation Indices

MODIS vegetation indices were designed to provide insight into the spatial and temporal variability of the vegetation conditions from atmospherically corrected bidirectional surface reflectance in the Blue, Red and NIR wavelengths at regional and global scales. The MODIS NDVI and EVI (i.e. minimizes canopy background variation and maintains sensitivity over dense vegetation conditions) products are provided every 16 days at 250 m spatial resolution (Huete et al. 2002).

MODIS VI products including MOD13Q1 and MOD13A2 from the Terra satellite platform were obtained from the USGS EarthExplorer (EE)[1] data online for

1. http://earthexplorer.usgs.gov/

Wytham Woods and the ChEAS region, respectively. The quality of each product was determined using the quality assurance (QA) flags (Xiao et al. 2008). The UK's flux tower network, whose footprints correspond roughly to one or more pixels in the MOD13Q1 (i.e. MODIS VI) and MOD17 (i.e. MODIS GPP/NPP) products, can be used for either model validation or parameterization (Rahman et al. 2001). The MOD13Q1 product, which was provided every 16 days at 250 m spatial resolution as a gridded level-3 product, was acquired through the growing season between March and October 2010 to monitor spatial and temporal vegetation conditions and compare their variability with other fine spatial resolution broadband VIs.

The MOD13A2 product is provided every 16 days at 1 km spatial resolution as a gridded level-3 product. For the entire ChEAS region this VI was also collected over the period 2000-2006 to parameterise the LUE model, Equation 1.4.

2.2.3.3 MODIS Reflectance

Three MODIS products from both the Terra (MOD) and Aqua (MYD) satellite platforms were acquired as:

- MOD/MYD021KM contained the calibrated and geo-located radiances for 36 MODIS spectral bands at a spatial resolution of 1 km, and included coefficients for calculation of the top-of-atmosphere (TOA) reflectance values;
- MOD/MYD03 products with the same spatial extent and resolution contained the geo-location and sensor/solar geometry for every pixel in the granule; and
- MOD/MYD04 contained the aerosol optical thicknesses (AOT) at 550 nm over land at a spatial resolution of 10 km, which can be used for correcting the TOA reflectance values to surface reflectance with the MOTRAN model.

2.2.4 Airborne Remote Sensing

Airborne remotely sensed data provide fine spatial and spectral resolution with reduced atmospheric interference with respect to satellite sensor imagery, which can be used as a key tool in validating satellite-based information, as well as providing a bridge between tower-based CO_2 flux measurements and satellite sensor imagery. Two types of airborne RS data, hyperspectral and Light Detection and Ranging (LiDAR) data, were provided by the Natural Environment Research Council (NERC) Airborne Research and Survey Facility (ARSF). Airborne hyperspectral and LiDAR data were acquired to characterise the spatial variability of canopy structure and function at Wytham Woods.

2.2.4.1 Airborne Hyperspectral Data

The NERC ARSF acquired hyperspectral data using an Airborne Imaging Spectrometer for Applications (AISA) Eagle imaging spectrometer which sensed in 252 narrow spectral wavebands, ranging from 392 nm to 987 nm, and an AISA Hawk which sensed in 233 narrow spectral wavebands, ranging from 1003 nm to 2467 nm. These data were provided as system corrected (Level 1b) datasets in modified hierarchical data format (HDF). The HDF data contain information from various ancillary devices for recording the attitude (i.e. roll, pitch and yaw) and position of the sensors and basic meteorological parameters during the mission, as well as a radiometrically corrected Band Sequential (BSQ) image file. The level 1b data contained geodetic information and radiometric calibration values, but the data were not yet mapped to an appropriate geographic coordinate system. Therefore, Level 1b data were corrected into Level 3a using *AZGCORR*, an airborne remote sensing geo-correction package provided by the NERC ARSF, based on the on-board attitude, positional information and platform altitude, as well as a fine resolution digital surface model (DSM) for relief correction.

2.2.4.2 Airborne LiDAR Data

The NERC ARSF also provided aerial LiDAR data collected using a fine resolution airborne laser scanner, Optech ALTM 3033. This system emits high energy pulses and records the time of pulse return. Pulse ranging is used to convert the elapsed time between transmission and reception of the pulse to the distance between the sensor and feature on the ground. These first and last energy responses above a specified threshold for each laser pulse are converted to first and last return coordinates. The high pulse emission rate results in a three-dimensional point cloud of first and last return coordinates. Therefore, to identify canopy structure, the NERC ARSF LiDAR data were acquired over Wytham Woods in both leaf-off and leaf-on seasons, on 9th March 2009 and 29th June 2009, respectively.

2.3 Preparing the EO Data - RS Data Analysis

Analysis focused on the 2010 growing season due to the quality of existing datasets. The multiple satellite sensor datasets were pre-processed in terms of image registration and radiometric correction of atmospheric and illumination effects. Subsequently, VIs and canopy structure information were extracted using fine and coarse spatial resolution satellite sensor imagery and airborne LiDAR data, respectively. The following sections explain the remotely sensed data analysis methods used in this study. All image processing was performed within the ENVI/IDL remote sensing package version 4.7. Point cloud airborne LiDAR data analysis was carried out within ArcGIS version 10.1 and Fusion/LDV Analysis and Visualization System, Version 3.30 (McCaughey, 2013).

2.3.1 Radiometric and Atmospheric Correction

It would be very convenient if the radiance recorded by the sensor, also known as at-sensor radiance, equalled the radiance reflected from the target feature of interest (i.e. ground-leaving radiance). Unfortunately, both the amount of irradiance and radiance are influenced by the atmosphere before reaching the target and the sensor, respectively. These effects are often called atmospheric effects and are due to scattering and absorption by molecules, aerosols and water vapour (Liang 2004).

As illustrated in Figure 2-6, at-sensor radiance (L) in the solar region 0.35 – 2.5 μm for flat terrain contains three main components as follows:

a. Path Radiance (L_1), radiation scattered into the sensor's IFOV without having ground contact;
b. Surface reflectance from a certain pixel (L_2), reflected solar radiation incident from the surface, and
c. Radiation reflected by the neighbourhood (L_3), referred to as adjacency effect.

Only surface reflectance from a certain pixel contains information from the currently viewed pixel. The total radiance signals that reach the sensor can be expressed by Equation 2.1.

$$L = L_1 + L_2 + L_3 \qquad 2\text{-}1$$

For each spectral band of a specific sensor a linear equation describes the relationship between the digital number (DN) and the at-sensor radiance as in Equation 2.2.

$$L = C_0 + C_1 DN \qquad 2\text{-}2$$

where the *"C_0"* and *"C_1"* are radiometric calibration coefficients.

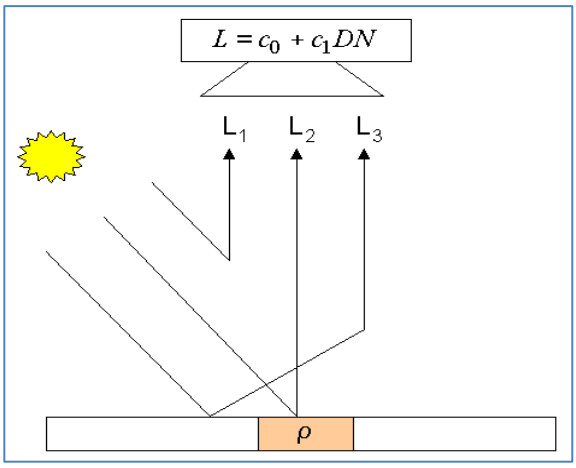

Figure 2-6 Schematic sketches of solar radiation components in flat terrain

Quantitative retrieval of physical parameters of the environmental variables requires taking into account the influence of the atmosphere and illumination effects. Therefore, radiometric and atmospheric correction is an essential part of pre-processing and a prerequisite for the derivation of certain surface variables, particularly when dealing with time-series data (Liang 2004; Lillesand et al. 2008). The most common procedure to retrieve surface reflectance from at-sensor radiance is radiometric correction relying on physical models (Liang, 2004). However, there are two major approaches to compensate the atmosphere and illumination effects. These approaches consist of absolute radiometric correction resulting in a significant number of atmospheric models based on radiative transfer codes and relative radiometric correction or normalization.

2.3.2 Absolute Radiometric and Atmospheric Correction

The main objective of absolute radiometric correction is to convert the at-sensor radiance values into accurate and reliable surface reflectance values; this requires both knowledge of atmospheric properties and sensor calibration parameters at the time of sensor overpass. This approach may be performed based on either physical models such as radiative transfer models, or empirical models, for example, the empirical line calibration (ELC) method.

Derivation on an empirical model using the ELC method relies upon a linear relationship between remote sensing derived spectra and *in situ* spectral reflectance measurements obtained at approximately the same time as the sensor overpass (Smith and Milton 1999). The gain and bias values estimated, that is radiometric calibration coefficients, are applied to the remote sensor data on a band-by-band basis to remove the path radiance and illumination effects.

Physical-based radiometric correction requires sensor calibration coefficients and radiative transfer code and also requires knowledge of both the sensor spectral response and the atmospheric properties at the same time of data acquisition, to provide realistic estimates of the influence of atmospheric scattering and absorption and convert the imagery to scaled surface reflectance. The radiative transfer model has been developed in ready-to-use software, for example "Fast Line-of-sight Atmospheric Analysis of Spectral Hypercubes" (FLAASH) and 'Atmospheric and Topographic Correction' (ATCOR), which is used later in the present study and is described here since it supports multi/hyper-spectral imagery of both wide field-of-view (FOV) airborne optical scanner data and narrow FOV satellite sensor images.

FLAASH is a physical-based atmospheric correction package developed by the Air Force Phillips Laboratory, Hanscom Air Force Base and Spectral Sciences, Inc. to support the analysis of VIR and SWIR hyperspectral and multispectral imagery (Berk et al. 1989). The main objective of this package is to provide an accurate physical based derivation of surface and atmospheric properties, such as surface

albedo; water vapour column; aerosol and cloud optical depths; and surface and atmosphere temperature (Berk et al. 2002).

ATCOR is also a physical-based atmospheric correction package which was developed by the German Aerospace Centre - ReSe Applications Schlapfer (Richter 2013). This package consists of two separate codes optimized for narrow/medium FOV satellite sensors, that is, ATCOR-2 for flat terrain and ATCOR-3 for rugged terrain, and for wide FOV airborne sensors, that is, ATCOR-4, as well as thermal scanner data sensors. ATCOR extracts surface reflectance accurately relying upon absolute radiometric correction of atmospheric and topographic effects using the MODerate resolution atmospheric TRANsmission (MODTRAN) radiative transfer codes. The ATCOR algorithm uses the MODTRAN4 code to calculate the look-up table (LUT) of the atmospheric correction functions that depend on atmospheric parameters, solar geometry, and terrain elevation (Richter 2013).

As mentioned previously, physical-based radiometric correction requires an accurate radiometric calibration coefficient in each spectral band, an accurate estimate of the main atmospheric parameters, such as aerosol type, visibility or optical thickness, and water vapour. These parameters for a scene, which influence the values of path radiance transmittance (Richter 2013) can be estimated using the ATCOR algorithm. The various standard atmospheres consist of a profile of air temperature, water vapour content, and ozone concentration. The standard atmosphere types offered by ATCOR are:

- Mid-latitude summer;
- US standard atmosphere;
- Tropical atmosphere; and
- Mid-latitude winter.

ATCOR supports four pre-defined aerosol types in the atmospheric correction functions that can be selected based on the geographic location as: Rural; Urban; Maritime; and Desert. Table 2-6 gives an overview of the common specific features of the ATCOR package as distributed through ATCOR-IDL in comparison to the FLAASH model.

Table 2-6 Overview of the features of ACTOR-IDL versus FLAASH, adopted from Richter (2013)

Feature	ATCOR-IDL	FLAASH
Airborne Sensors	YES (ATCOR 4)	YES
Satellite Sensors	YES (ATCOR 2/3)	YES
Multi/Hyper-spectral	YES	YES
Variable Visibility	YES	YES
Aerosol Type Detection	YES	NO
Adjacency Effect	YES	YES
Water Vapour Retrieval	YES	YES
Haze Removal	YES	NO
Cirrus Cloud Removal	YES	NO
Cloud Shadow Removal	YES	NO
Normalizing to Nadir View	YES	NO
Spectral Polishing	YES	YES
Empirical Line Correction	NO	YES
Spectral Calibration	YES	YES
Terrain Height (DEM)	YES	NO
DEM Illumination Effects	YES	NO
Empirical BRDF Correction	YES	NO

2.3.3 Relative Radiometric Correction/Normalization

Statistically-based atmospheric correction models can be used to remove atmospheric effects and estimate surface reflectance, assuming that the spectral reflectance characteristics of a reference image are known accurately (Canty and Nielsen 2007). This approach relies upon the assumptions that there are some pixels in a scene with stable reflectance through time, referred to as invariant-objects (Schott et al. 1988). The linear relationship between the at-sensor radiance of the invariant-objects and surface reflectance can be used to normalize imagery acquired at different times. This statistical technique is useful whenever absolute surface reflectance is not required. Therefore, if *N* invariant pixels are identified from *M* images acquired at different times, with the selection of a clear image as a reference, other images can be normalized to the reference image using a linear regression based on these *N* pixels. This, so-called relative radiometric normalization, is expressed by Equation 2.3.

$$L_j^k = a_i^k + b_i^k L_i^k \qquad 2\text{-}3$$

where "L_j^k" refers to the radiance of the reference image for band "k" and "L_i^k" refers to the radiance of any other images for the same band. This linear regression analysis for each band will produce two coefficients "a_i^k" and "b_i^k" that can be used to create images that match the illumination and atmospheric conditions of the reference image. The critical aspect of this approach is the determination of suitable time-invariant objects upon which to base the normalization (Schroeder et al. 2006).

The iteratively reweighted multivariate alteration detection (IR-MAD) transformation (Nielsen 2007), a new extension of multivariate alteration detection (MAD) (Nielsen et al. 1998) is based on the multivariate statistical technique of canonical correlation analysis. The IR-MAD scheme provides a fast, reliable and robust method for automatic radiometric normalization of a multispectral image time-series (Canty and Nielsen 2008). Canty and Nielsen (2008) showed the ability of the IR-MAD transformation to identify suitable time-

invariant pixels for performing radiometric normalization. Therefore, in the present study, the IR-MAD method was used to locate time-invariant pixels (i.e. invariant pixels with a high no-change probability, typically ≥ 0.95) between each image in the growing season and an ATCOR-IDL corrected reference image. The selected time-invariant pixels were subsequently used to normalize each image, band-by-band, to the reference image by means of orthogonal linear regression (Canty 2010).

2.3.4 Vegetation Indices

Vegetation indices have been developed to facilitate the investigation of vegetation in terms of its abundance at various spatial and temporal scales, as well as to be able to retrieve vegetation biophysical and physiological variables. As mentioned in chapter one, numerous studies have shown that spectral VIs can be developed with sensitivity of indices to ecologically significant canopy characteristics. The most commonly used VIs are combinations of surface reflectance at two or more wavelengths designed to enhance a particular property of vegetation.

In this research, VIs as spectral indicators of CO_2 flux and the photosynthesis process were computed to assess the spatial and temporal patterns of ecosystem productivity and identify sources of uncertainty in up-scaling tower-specific EC CO_2 flux measurements. Accordingly, VIs were grouped into three categories (i.e. broadband greenness, narrowband greenness and light use efficiency) on the basis of existing multispectral satellite and hyperspectral airborne imagery. These indices can be used to indicate different properties in vegetation and ecosystem productivity, such as ecosystem greenness (Tucker 1979), photosynthesis capacity (Sellers et al. 1992), CO_2 uptake rate and photosynthesis efficiency (Gamon et al. 1990; Gamon et al. 1992).

2.3.4.1 Normalized Difference Vegetation Index (NDVI)

NDVI, as a broadband greenness vegetation index, was used for the main purpose of the current study. This was computed from a combination of the UK-DMC Red and NIR band as Equation 2.4.

$$NDVI_{DMC} = R_{NIR} - R_{Red}/R_{NIR} + R_{Red} \quad 2\text{-}4$$

where "R_{Red}"and "R_{NIR}" indicate the reflectance in the Red and NIR wavelengths of UK-DMC2 imagery, respectively.

NDVI is based on the contrast between the maximum absorption in the Red because of chlorophyll pigments and the maximum reflection in the NIR due to leaf structure (Sellers et al. 1992; Tucker 1979). Simultaneously increasing the LAI and chlorophyll content (i.e. increasing Red absorption and NIR reflectance) the contrast between these two spectral bands increases. Therefore, NDVI was used to quantify vegetation amount and photosynthesis capacity.

2.3.4.2 Red Edge Position (REP)

Red Edge Position (REP) index is a narrowband greenness vegetation index that indicates changes in chlorophyll concentration. Increased chlorophyll concentration increases the absorption features and shifts the red edge to longer wavelengths. The spatial and temporal variability of this index can be used to monitor ecosystem function and model photosynthesis process (Curran et al. 1995).

2.3.4.3 Photochemical Reflectance Index (PRI)

The light use efficiency vegetation index is designed to provide a quantitative value of the efficiency with which vegetation is able to use incident radiation for photosynthesis. The ASIA Eagle based PRI across the Wytham flux tower domain was computed (Equation 2.5) to assess the spatial variability of CO_2 uptake efficiency in terms of flux tower footprint variation (Gamon et al. 1992; Gamon et

al. 1997). This can be used to identify the effect of spatial variability on photosynthesis efficiency.

$$PRI_{ASIA\ Eagle} = R_{531} - R_{570}/R_{531} + R_{570} \quad 2\text{-}5$$

where "R_{531}" refers to carboxylation reflectance at 531 nm and "R_{570}" indicates reflectance at an insensitive reference band (Gamon et al. 1997).

2.3.5 LiDAR Data Analysis

Interaction between landscape heterogeneity and ecological processes requires an algorithm to quantify spatial variation in spectral indices of CO_2 flux and to identify the sources of uncertainty in their scaling across various levels. Ecological processes are governed by vegetation function (i.e. CO_2 uptake and biomass production) and structure (Forman 1995). The properties of canopy structure such as canopy height and density must be quantified to understand their role in ecosystem function, in particular, for characterising the spatial variability in spectral indices of CO_2 flux. Furthermore, leaf area index (LAI); defined as one half of the total green leaf area per unit ground surface area, is also a significant canopy structure characteristic used to estimate biomass and productivity due to its influence as a state variable for a variety of ecological processes. On the other hand, canopy structure influences surface roughness length, which is a critical input to flux tower footprint models (Schmid 2002; Schmid and Lloyd 1999).

Estimating canopy structure characteristics from both direct and indirect methods at an appropriate spatial and temporal scale remains a significant issue in ecological studies. The direct methods of estimating LAI (e.g. destructive sampling of the forest canopy or leaf litter fall collection) and canopy height and density are time-consuming. Moreover, such *in situ* measurements are suitable for only small areas. However, although direct methods are limited, they provide useful information to validate results obtained from indirect methods.

Optical remote sensing is used widely to predict or map LAI by correlating spectral indices and ground based measured LAI values. The relationship between

hyperspectral VIs and LAI has been examined for various scales. For example, Walthall et al. (2007) showed the potential of data from the AISA imaging spectrometer to create an LAI variogram map using the residual maximum likelihood method, and the result derived was cross-validated with LAI estimated using a kriging interpolation method. Although passive optical remote sensing can indirectly estimate LAI at landscape or regional scales, it encounters problems at the local level. The problem with these sensors is saturation at high levels of leaf area and understory vegetation effects on reflectance that introduce significant noise to the estimation of LAI.

The other issue regarding remotely sensed optical-based estimation of LAI is landscape heterogeneity (Forman 1995). The accuracy of estimating vegetated-ground depends on the size of vegetation patches in relation to the pixel size. If the pixel size is too large compared to the vegetation patch, each pixel is not identified individually as vegetation. In those cases, the estimation relies on this mixed spectral response of the canopy. Landscape and canopy heterogeneity is a critical concept and the main source of uncertainty in scaling biophysical and physiological variables from *in situ* measurement to coarser scales.

Another significant aspect of LAI estimation is seasonality. Sometimes, due to non-availability of fine spatial resolution imagery for a certain time range, the monthly LAI images cannot be obtained. To address this issue, algorithms have been developed to fill the gaps. The MODIS LAI product, which is an 8-day interval time series of images with 1 km spatial resolution may be applied to fine spatial resolution imagery to generate time-series LAI datasets, which requires an appropriate algorithm to retrieve LAI at the local level.

Airborne LiDAR remote sensing, also known as airborne laser scanning (ALS), is a relatively new active remote sensing technique that overcomes some of the limitations of passive remote sensing. For instance, LiDAR data are not saturated by high leaf area (Lefsky et al. 2002) and they accurately discriminate properties of understory from top of canopy (Hill and Broughton 2009). Airborne LiDAR data have been used to retrieve more details and accurate information about canopy

structure at the stand level. Therefore, it may complement or partly replace other spatial data acquisition technologies for LAI estimation in both dense and sparse canopy forests.

The main focus of this section is the assessment of the capacity of LiDAR data to extract canopy height and density information, addressing two specific topics: (a) to model variation in the flux tower footprint definition due to different meteorological status (e.g. atmospheric stability and wind speed and direction) and its effect on the temporal variability of VIs; and (b) to assess the influence of canopy height on the VIs and productivity.

The discrete LiDAR system provides multiple returns for each laser pulse and records two different kinds of information: the three dimensional spatial position coordinates and an intensity value. LiDAR remote sensing has the capability to capture reflectance data from the returning pulses and directly record data characterizing the physical structure of phenomena; they provide an opportunity to directly assess the 3D structure of features on the surface, such as canopy structure.

One of the main applications of LiDAR remote sensing is the generation of a Digital Terrain Model (DTM) and a Digital Surface Model (DSM) from the same data source. In the process of generating the DTM, only reflections from the ground level are used, and backscatter from vegetation or other above ground features are considered first return (Lillesand et al. 2007). Therefore, LiDAR techniques allow a 3D analysis of canopy structure.

A canopy height model (CHM) can be generated by deducting the last return from the first return. The normalized canopy model (nCM) can be expressed as Equation 2.6, which estimates canopy height.

$$nCM = DSM - DTM \qquad 2\text{-}6$$

In this study, the canopy structure was generated by means of FUSION/LDV (Version 3.30) and ArcGIS (Version 10.1) software packages from airborne LiDAR

datasets across the Wytham flux tower domain. LiDAR datasets are usually stored in American Standard Code for Information Interchange (ASCII) text format. Raw LiDAR data were initially converted into SHP or airborne laser scanning ALS, which may be readable easily in common software packages. Prior to analysing the LiDAR point data and extracting the canopy structure model, LiDAR point spacing (i.e. a more in-depth view of the point cloud distribution) was assessed.

Although the leaf-on first return is the most likely to retrieve the most accurate representation of the over-storey canopy (Hill and Broughton 2009), using leaf-on last return LiDAR points reduces the accuracy of the DTM and may result in under-estimation of canopy height, particularly in a dense canopy (Kraus and Pfeifer 1998; Razak et al. 2011). The best nCM is the one obtained by subtracting the leaf-off DTM from the leaf-on DSM (Wagner *et al.*, 2005). Therefore, DSM and DTM were generated using leaf-on first return and leaf-off last return LiDAR data, respectively. This approach increases the accuracy of estimating the canopy height.

2.4 Flux Tower Footprint Estimation

Spatial heterogeneity is inherent in terrestrial ecosystems (Forman 1995; Forman and Godron 1986). In natural ecosystems, heterogeneity occurs in the form of both horizontal and vertical structure (Forman 1995; Frohn 1998). Spatial heterogeneity greatly influences the land-atmosphere CO_2 exchange, and subsequent ecological processes over a wide range of scales (Kim et al. 2006; Rahman et al. 2003). In addition, the microclimate surrounding vegetation influences directly eco-physiological processes, which control land-atmosphere CO_2 exchange (Avissar and Pielke 1989).

It is often necessary to compare remotely sensed products (e.g. spectral indices of CO_2 flux) with *in situ* measurements (e.g. tower-based CO_2 flux measurements) at the time of the sensor overpass. This approach, relating point-based measurements to remotely sensed products with a certain pixel size, facilitates comparison with the image referred to as up-scaling (Atkinson 2006). Up-scaling the CO_2 exchange rate (i.e., taking spatial, temporal and process information at a flux tower site and using it to derive information at another scale, for example, landscape and regional scales) must take into account the spectral, temporal and spatial variability to estimate uncertainty (Kim et al. 2006; Lillesand et al. 2007).

In this effort, there is a major challenge in the research community. Remote sensing typically provides continuous spectral data in the spatial domain but represents a snapshot in time. On the other hand, flux towers typically provide the continuous CO_2 flux data in the temporal domain (i.e. at half-hourly to daily intervals) but are spatially limited to their footprint ($< 10^4$ to 10^6 m^2). Specifically, they can be considered as spatially weighted integrals over the flux tower footprint. In general, flux towers can provide suitable CO_2 flux data for comparison with a small portion of remotely sensed images (Huemmrich and Goward 1997; Kim et al. 2006; Wohlfahrt et al. 2010). This means that, remotely sensed data are spatially continuous at their specific pixel resolution, whereas tower-based CO_2 fluxes are temporally continuous at their recording intervals. They only interact at a point in time and across the small area of a footprint coverage.

On the basis of the objectives of this study, bridging the gap between these scales requires to examine the temporal and spatial variability of a flux tower footprint and the associated influence of canopy-patches on tower-based flux measurements. Since patchy canopies are the norm in natural vegetation, the effect of landscape heterogeneity on CO_2 flux measurements is of great importance to remote sensing up-scaling. It is possible to determine an area of influence of CO_2 flux measurements by physically-based criteria. Therefore, flux tower footprint analysis has become a significant tool to quantitatively assess the influence of landscape heterogeneity on up-scaling processes.

In recent years, several flux tower footprint models have been applied to quantitatively estimate the source area of turbulent scalar fluxes (Desai et al. 2008; Kormann and Meixner 2001; Schimd 1994; Schmid 1997; Schmid 2002; Schmid et al. 2000; Schmid and Lloyd 1999). Despite many current studies on detailed footprint modelling, the temporal and spatial variability of footprints and the associated influence of varying landscape heterogeneities (i.e. canopy patches) on tower-based measurements have not yet been accurately investigated.

One of the practical problems in using a footprint model is that the source area of turbulent scalar fluxes is not explicitly known, particularly in heterogeneous landscapes (Kim et al. 2006). Recently, it has been demonstrated that seasonal and annual patterns of a flux tower footprint provide essential information about the vegetation sampled when measuring long-term fluxes over heterogeneous landscapes (Schmid 2002; Schmid and Lloyd 1999).

The flux tower footprint is the weighted average of the upwind surface flux, which contributes each element of this upwind surface area to a measured vertical flux turbulence (Schimd 1994; Schmid 1997; Schmid 2002).

Equation (2-7) can be used to express the flux tower footprint for an observation point at "X, Y, Z_m".

$$fm\,(X,Y,Zm) \;=\; \int_{-\infty}^{\infty}\int_{-\infty}^{X} f_0\left(X',Y',Z=0\right) f\left(X-X',Y-Y',Z_m\right) d_{X'} d_{Y'} \qquad 2\text{-}7$$

where "X," and "Y" refer to upwind and crosswind distance, respectively and "Z_m" indicates EC flux measurement height. The size of a flux tower footprint and the position of the peak of its probability distribution are influenced by horizontal wind velocity, standard deviation of vertical and horizontal velocity fluctuations and surface roughness, which are affected by canopy structure (Schmid 1997).

The possible upwind distribution of source area that contributes to measuring vertical turbulent CO_2 fluxes at Wytham Woods was estimated using the EdiRe Footprint Tool (School of Geo-Sciences, University of Edinburgh) based on the Korman and Meixner analytical model, which requires information on the environmental conditions of the site.

In general, an increase in measurement height, decrease in surface roughness, and change in atmospheric thermal stability from unstable to stable would lead to an increase in the size of the footprint and would move the peak contribution away from the instrument. Since at the specific flux tower site, measurement height is usually constant, surface roughness; atmospheric thermal stability; and wind speed and direction play a significant role in determining the size and shape of flux tower footprints (FluxNet 2013). The data under stable and un-stable conditions associated with certain wind speed and direction are used separately to estimate the flux tower footprint.

Turner (1964) and Bowen et al. (1983) presented a method to determine the atmospheric stability categories. Table 2-7 and Table 2-8 give the stability class as a function of wind speed. Roughness classification, provided in Table 2-10, represents terrain classification in terms of effective Surface Roughness Length (Z_0).

Table 2-7 Meteorological conditions that define the atmospheric stability classes

Wind Speed (ms^{-1})	Strong	Moderate	Slight	Weak
0.0 – 0.7	A	A	B	C
0.8 – 1.8	A	B	B	C
1.9 – 2.8	A	B	C	D
2.9 – 3.3	B	B	C	D
3.4 – 3.8	B	B	C	D
3.9 – 4.8	B	C	C	D
4.9 – 5.4	C	C	D	D
5.5 – 5.9	C	C	D	D
≥ 6.0	C	C	D	D

Table 2-8 The atmospheric stability classes (Pasquill 1961)

Stability Class	Definition
A	Extremely unstable
B	Moderate unstable
C	Slightly unstable
D	Neural
E	Slightly stable
F	Moderate stable
G	Extremely stable

Table 2-9 Insolation class as a function of solar altitude (Bowen et al. 1983)

Solar Altitude (degrees)	Insolation
$60 < \phi$	Strong
$35 < \phi \leq 60$	Moderate
$15 < \phi \leq 35$	Slightly
$\phi \leq 15$	Weak

Table 2-10 Terrain classification in terms of effective Surface Roughness Length

Terrain Description	*Surface Roughness Length* (m)
Open sea, fetch at least 5km	0.0002
Open flat terrain, grass, few isolated obstacles	0.03
Low crops, occasional large obstacles	0.10
High crops, scattered obstacles	0.25
Parkland, bushes, numerous obstacles	0.50
Regular large obstacle coverage (e.g. suburb and forest)	0.50 – 1.00

3. Quantifying CO_2 Flux: Tower-based EC Measurements and Potential of EO Data

This chapter aimed to familiarise the author with the study area and datasets available, and to add to the evidence base concerning the relationships between photosynthetically active canopy and the spectral indices reviewed in Chapter 1. It focused on data from the UK test site, Wytham Woods, and used remotely sensed data from aircraft and satellite sensors. Some of these data were acquired from a global archive (MODIS); other data were acquired from previous research flights over the site conducted by the UK Airborne Research and Survey Facility (ARSF). The ARSF data were expected to be particularly suitable for use in the current chapter because they had fine spatial resolution, many spectral bands and were obtained at different dates during the year. Such high dimensionality data are likely to be too difficult to work with operationally, but they would be invaluable in helping identify the optimum sensor parameters for the main study. A further advantage of the ARSF data was that they included measurements from an airborne LiDAR, which provided information on canopy spatial structure (horizontal and vertical). Despite the numerous advantages and limitations of using EO data for the above purpose, there are also several potential uncertainties that need elimination through the application of accepted corrective algorithms. By comparing tower-based EC flux measurements and spectral vegetation indices, the current study attempted to gain an appreciation of the impacts of temporal and spatial variability in spectral separately VIs on photosynthesis capacity and efficiency, and how this could be applied to gain greater understanding of coarse spatial resolution EO data.

In summary, this chapter was divided into two main sections, (1) tower-based CO_2 flux Measurements: sink or source of carbon, and (2) potential of RS to provide information on the photosynthesis process (i.e. CO_2 flux). Accordingly, the objectives of the current chapter were:

- To implement an established flux tower footprint model to simulate the area of the canopy contributing to the EC measurements under different conditions;
- To determine NEE of CO_2 at this temperate mixed forest and assess whether Wytham Woods was a sink or source of carbon over the period 2007-2009, on the basis of the existing EC observations;
- To compare trends in GPP and NEE measured using the EC method with trends in VIs shown in coarse spatial resolution satellite sensor products;
- To investigate the potential of imaging spectrometry to provide additional information on the photosynthesis process; and
- To generate an accurate three-dimensional model of Wytham Woods based on airborne LiDAR data, in order to characterise the spatial patterns of vegetation and the vertical structure of the canopy around the EC tower.

3.1 Tower-based CO_2 Flux: Sink or Source of Carbon

3.1.1 Estimating Flux Tower Footprint Coverage

The EC technique is based on the turbulent fluctuations of vertical velocity in the atmospheric boundary layer to measure scalar fluxes of gas concentration averaged across a particular spatial coverage in an upwind direction (Baldocchi et al., 2001; Burba and Anderson, 2010a). Estimation of the spatial coverage of the accumulated flux tower observations is important in the interpretation and up-scaling of measured fluxes (Chen et al., 2009a; Chen et al., 2012; Kim et al., 2006; Zhao et al., 2014; Zhang et al., 2016).

Spatial variability, as mentioned previously, is inherent in terrestrial ecosystems. This variability occurs in the form of both horizontal and vertical structure (Forman and Godron 1986). Spatial variability of canopy cover strongly influences land-atmosphere exchange of CO_2 over a wide range of scales (Kim et al. 2006; Rahman et al. 2003; Peltola et al., 2015, Zhang et al., 2016). Assessing the variability of the flux tower footprint in terms of the spatial and temporal variation in canopy properties is challenging and this is needed for up-scaling EC-based flux observations.

Several flux tower footprint models have been used to estimate the spatial coverage of source contributions for a particular time interval, typically a short period of 30 minutes (Kljun et al., 2003; Kormann and Meixner 2001; Schimd 2002; Schmid 1997; Schmid and Lloyd, 1999). Despite many current studies on flux tower footprint modelling (Chen et al., 2009a; Sogachev et al., 2004; Vesala et al., 2008), one of the practical problems in using a footprint model is that the source area of turbulent scalar fluxes is not known explicitly, particularly in heterogeneous landscapes (Kim et al., 2006; Matthes et al., 2014). In recent years, it has been shown that long-term patterns of flux tower footprint provide significant information regarding the spatial and temporal variability of canopy cover especially across heterogeneous landscapes (Chen et al., 2009a; Chen et al.,

2012; Peltola et al., 2015; Schmid and Lloyd 1999; Zhang et al., 2016; Zhao et al., 2014).

The size and shape of the footprint coverage is a dynamic area depending on the observation height (Z_m); surface roughness length (Z_0); atmospheric stability (Z_m/L)[1]; and wind speed and direction (Baldocchi et al., 2001). The possible upwind distribution of source coverage that contributes measurements of vertical turbulence of CO_2 fluxes was estimated for a particular time interval (i.e. RS sensor overpass) using a simple analytical model, the *EdiRe Footprint Tool*[2] based on the Kormann and Meixner model which requires knowledge of the environmental conditions of the site, as mentioned above. In addition, the long-term (i.e., average) pattern of flux tower footprint coverage was applied for assessing spatial variability during the study period in 2010.

Wytham's flux tower footprint coverage was estimated relying upon the EC-based tower measurements over 2010 and LiDAR-derived information, i.e. observation height (Z_m) and canopy height. In this study, surface roughness length (Z_0) was assumed to be constant based on the regular large obstacle coverage, i.e. suburb and forest (Table 2-10). Table 3-1 gives details of influencing criteria of the flux tower footprint modelling associated with the overpass dates of the DMC satellite images. To assess the size and shape of the source coverage, the flux tower footprint was estimated for two prevailing wind directions[3] of 225° (South-West) and 315° (North-West) from moderate to unstable conditions, i.e. $-0.1 < Z_m/L < -0.001$ at flux tower site with Z_m/Z_0 of 19.23, i.e. $Z_m = 25m$ and $Z_0 = 1.30m$.

1. L is a parameter with dimension length that is used to describe the effect of buoyancy on turbulent flows. Atmospheric stability (Z_m/L): $Z_m/L = -0.5m\ very\ unstable$; $Z_m/L = -0.1m\ moderate$; $Z_m/L = -0.001m\ very\ stable$; and $Z_m/L \leq 0\ during\ night\ time$. Stable conditions are found to require a much greater fetch than do unstable conditions.

2. Developed by School of Geo-Sciences, University of Edinburgh

3. According to the Radcliffe Meteorological Station (Lat: 51°46' N; Lon: 1°46' W; Alt: 63.4m).

Table 3-1 Wytham Woods's flux tower footprint modelling criteria in 2010

Imaging Date	Measurement Height (m), Z_m	Canopy Height (m)	Wind Direction/ Speed	Atmospheric Stability	Surface Roughness *Length*	Sun Elevation (Deg.)
02/03/10	25	17	268°/ <2ms^{-1}	Slightly	0.75	22.65
05/03/10	25	18	30°/ 2.8ms^{-1}	Slightly	0.75	23.69
07/03/10	25	17	202°/ 2.3ms^{-1}	Slightly	0.75	25.24
20/04/20	25	16	310°/ 3.9ms^{-1}	Slightly	0.75	27.27
27/04/20	25	18	74°/ <2ms^{-1}	Moderate	0.75	45.56
23/05/20	25	16	314°/ <2ms^{-1}	Moderate	0.75	49.85
04/06/10	25	18	165°/ <2ms^{-1}	Moderate	0.75	51.95
16/06/10	25	18	217°/ 3.9ms^{-1}	Moderate	0.75	51.67

Figure 3-1 illustrates the estimation of the horizontal (i.e., spatial) position of 90% cumulative footprints for two prevailing wind directions under different atmospheric stability conditions. The coloured points signify a greater source weight and distance for 90% cumulative footprints. That is, the spatial coverage of the red and yellow points indicates the flux tower footprint under unstable and moderate atmospheric thermal stability conditions, respectively.

Appendix II shows both the EC-based wind rose and flux tower footprint estimated taking into account the overpass date of the satellite sensor images. Using the *EdiRe Footprint Tool* concerning the particular environmental conditions, the area between the sonic anemometer mounted on the tower and 90% distance that provides 90% of the total flux was estimated as the flux tower footprint, and then plotted on an aerial image, as shown by Figure 3-2, using the *Openair R Package 0.7-0* and *ArcGIS 10.1* software.

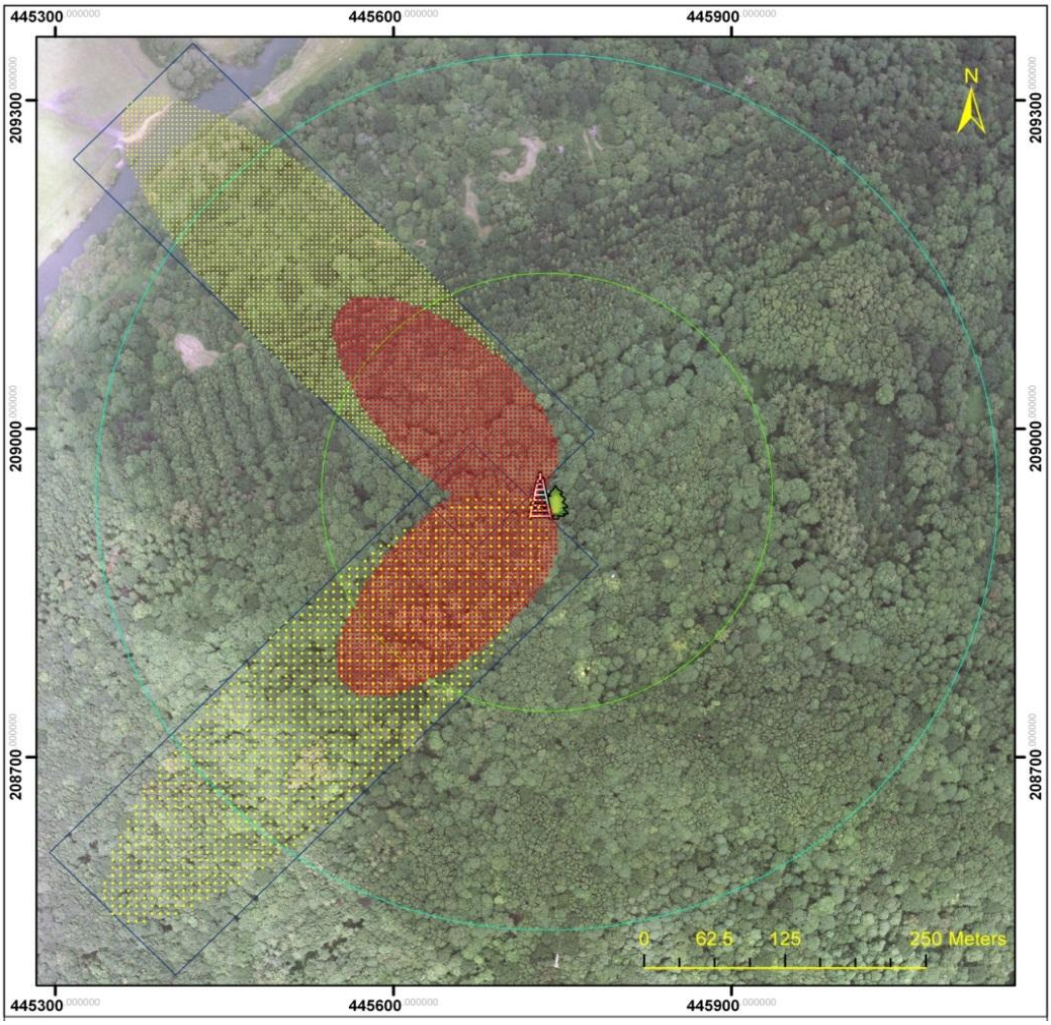

Figure 3-1 Flux tower footprint estimated, overlaid with Wytham Woods's aerial image, based on two prevailing upwind directions (i.e. 225° and 315°) on the crosswind integrated surface coverage under moderate (i.e. yellow points) and unstable (i.e. red points) atmospheric stability conditions. Green and Cyan lines show the buffer distance off by 200m and 400m around flux tower site, respectively.

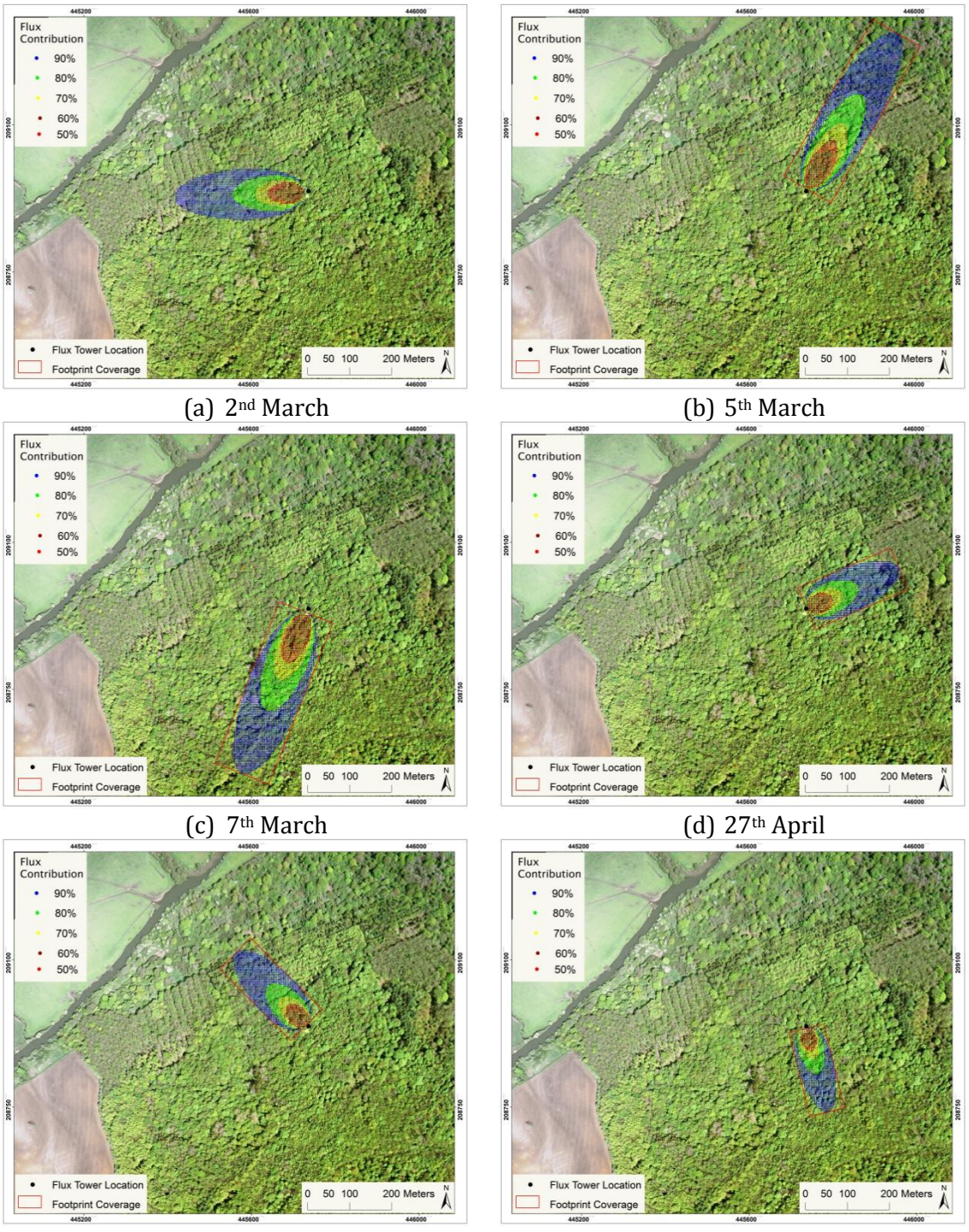

(a) 2nd March (b) 5th March

(c) 7th March (d) 27th April

(e) 23rd May (f) 4th June

Figure 3-2 Realistic estimated flux tower footprints overlaid on Wytham's aerial image for six particular dates involving a platform-sensor overpass; the gradient colours signify the source weight and distance for the probability cumulative footprints (50%, 60%, 70%, 80% and 90%).

Figure 3-3 also depicts the annual percentile of wind speed and frequency of counts by wind direction separated by daylight and night-time. These plots provide more insight regarding the prevailing wind speed and direction that influence flux tower footprint. On the basis of Figure 3-3, the largest percentile of wind speed and frequency of counts by wind direction during both daylight and night-time was from the North-East and the South-West during 2010.

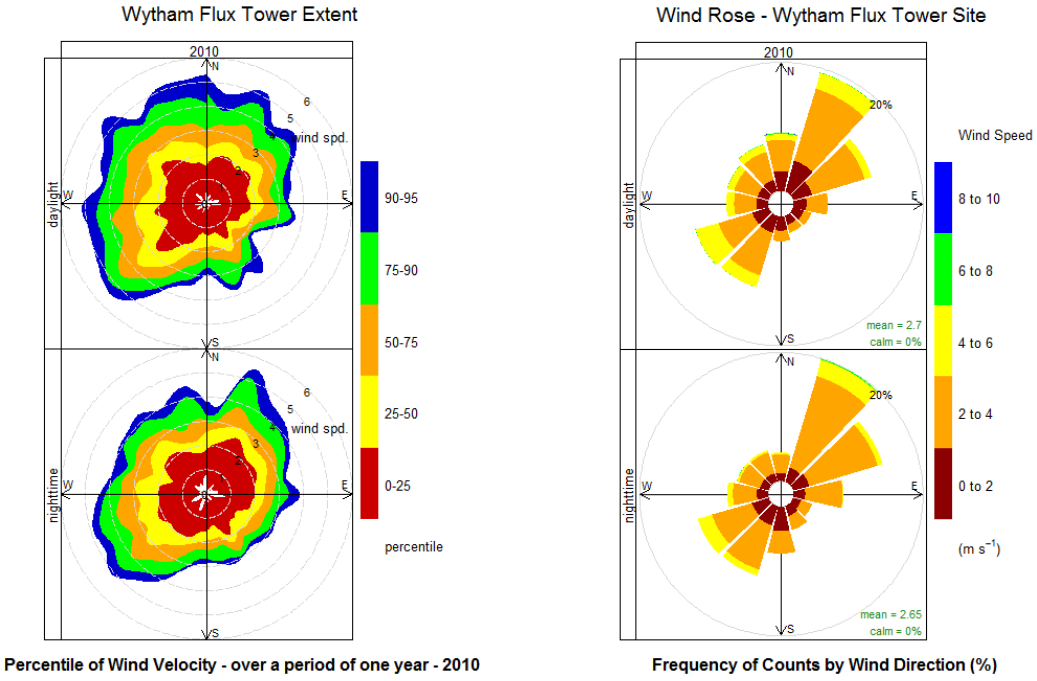

Figure 3-3 Annual wind analysis across Wytham Woods's flux tower site

Finally, the long-term pattern of flux tower footprint coverage was plotted based on the peak distance from which the largest relative individual contribution to the flux came (Table 3-2). Accordingly, the long-term pattern of peak distance was estimated as a circle of radius 200 m centred on the Wytham's flux tower site.

In summary, the long-term pattern of flux tower footprint was estimated for the contribution of each element of the long-term pattern of upwind surface area to the measured vertical CO2 fluxes. This area is illustrated in Figure 3-4 for a period of tower-based flux measurements in 2010, which represents the annual day-time peak footprint coverage of about 200 m from tower location.

Table 3-2 Descriptive statistics of flux footprint estimated by the *EdiRe Footprint Tool*

Statistics	Wind Speed (m/s)	Wind Direction (degree)	X_Peak (m)	X_10% (m)	X_30% (m)	X_50% (m)	X_70% (m)	X_90% (m)
Mean	2.68	156	178	64	158	246	360	657
Median	2.61	164	185	63	158	242	340	511
SD	1.08	109	48	37	77	149	258	956
Range	8.18	360	3351	3115	6465	12245	12670	19080
Minimum	0.02	0	0	5	5	10	15	30
Maximum	8.19	360	3351	3120	6470	12255	12685	19110
50%	2.61	164	185	63	158	242	340	511
70%	4.11	311	197	68	169	259	365	550
90%	4.65	333	201	70	173	266	380	694

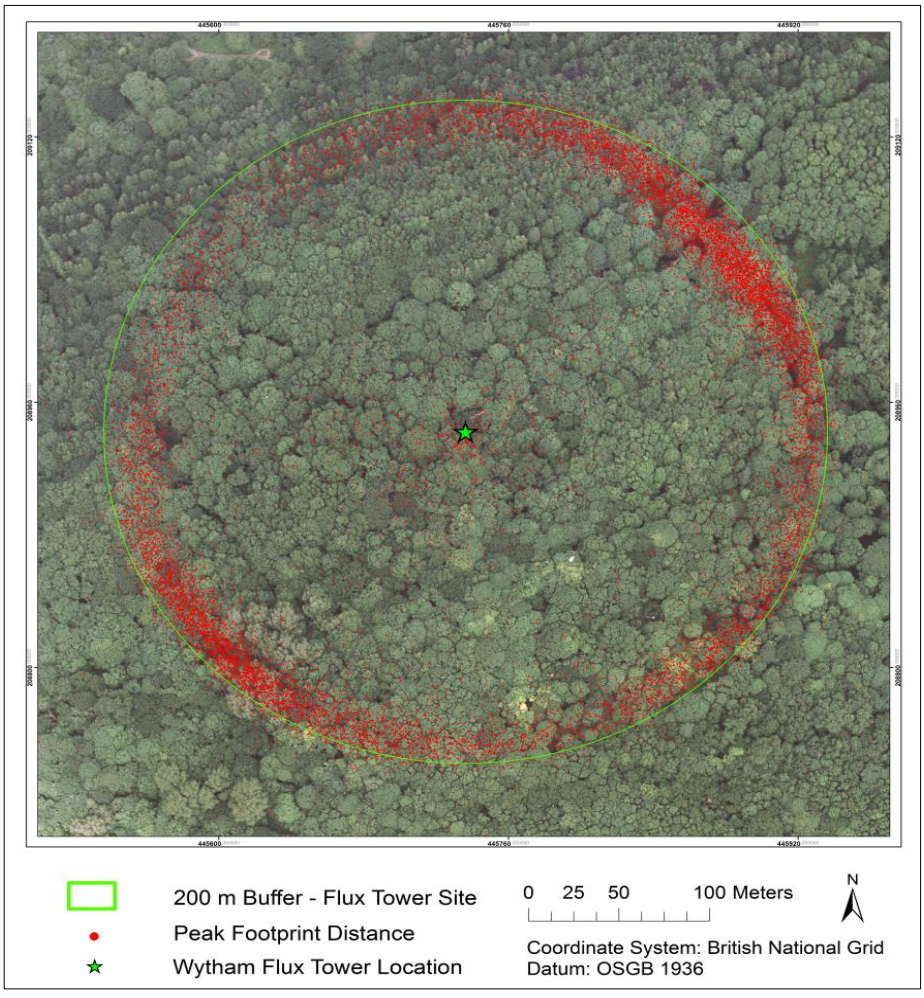

Figure 3-4 Long-term pattern of peak distance across Wytham's flux tower site over 2010.

3.1.2 Wytham Woods: Sink or Source of Carbon?

3.1.2.1 Tower-based EC Flux Data Analysis

Having established the likely area of canopy contributing to the EC measurements under different weather conditions, attention shifted to the actual data from the tower to determine the carbon status of Wytham Woods over the period 2007-2009. Thus, the intention here is to use the detailed knowledge of the flux tower footprint established above to answer a substantive question about the carbon flux status of the site.

Binary files from May 2007 to April 2009 recorded by the data logger were initially processed based on the standard averaging interval of 30 minutes using the *EddyPro* software version 3.0 from LI-COR Biosciences. The main outputs are described in Table 3-3.

Table 3-3 Key outputs of EC flux data processing

Output	Unit	Description
Solar Radiation	W/m^2	The power of electromagnetic radiation per unite area incident on the Earth surface.
LE	W/m^2	Latent heat of evaporation flux
H	W/m^2	Sensible heat flux that added or removed from the air without an associated change in water vapor content.
CO_2 Flux	g CO_2/m^2s	The corrected NEE of CO_2 between forest canopy and the atmosphere.
Air Temperature	°c	The average of air temperature
U*	m/s	Frictional velocity, a measure of turbulence used to identify thermal stratification on calm nights.
GPP	µmol	Gross Primary Production calculated based on CO_2 flux excluded night time (i.e. solar radiation <20 W/m^2)
z-d/L	unit less	Indicates roughness length and atmospheric thermal stability
X-Peak	m	Indicates the peak flux tower footprint, also known as fetch

The night-time CO_2 fluxes were determined, i.e. by selecting only the period when solar radiation was less than 20 W/m^2, to partition the NEE of CO_2 into GPP and net respiration and determine the growing season at Wytham Woods. This threshold was also used to compare fluctuation in GPP with MODIS products. Finally, the NEE of CO_2 and GPP were converted into "µmol" carbon per area and summed for each 30 minute period.

Figure 3-14 shows the half-hourly average CO2 flux values for GPP, respiration (i.e. red lines) and NEE of CO2 from May 2007 to April 2009. The green lines represent daytime fluxes that are predominantly negative, representing net assimilation of carbon into forest biomass. Average 30-minute GPP peaked at about 40 µmol Carbon/m^{2}s between mid-June and the end of July and falls to a minimum of less than 1 µmol Carbon/m^{2}s during the winter months.

Increasing GPP occurred in three distinct phases during 2008. Firstly, GPP rose slowly until early May, perhaps as a result of a flourishing understorey. This was followed by a rapid rise during May as the forest canopy came into leaf. The final rise depicted in Figure 3-5 could have resulted from late developing trees such as oak reaching full photosynthetic capacity by mid-June. Of particular interest is the fluctuation in GPP following leaf emergence during the spring and summer months due to micro-climate conditions. Accordingly, the growing season is defined as the number of days from the first to the last day with net uptake, and was approximately 130 days in 2008.

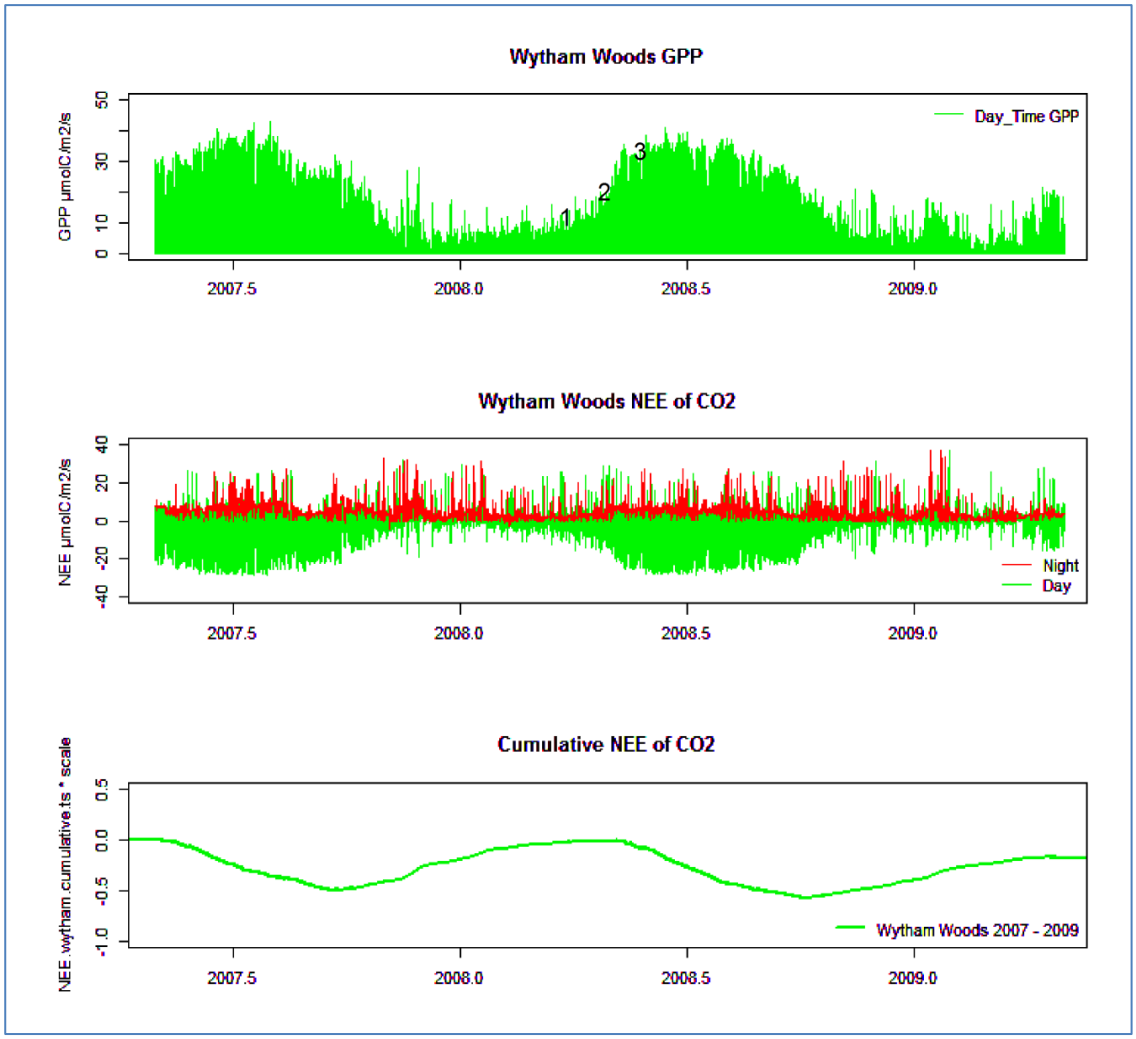

Figure 3-5 Half-hourly GPP, respiration and NEE of CO_2 flux values period May 2007 to April 2009, Adapted from binary files recorded by the data logger initially processed using EddyPro-3.0.

3.1.2.2 Tower-based GPP vs. MODIS Vegetation Indices

The MODIS vegetation indices, MOD13Q1, of a central pixel and a subset of 3×3 pixels centred on the EC flux tower site were calculated to enable the assessment of spatial and temporal variability of MODIS products. Figure 3-6 shows the central tendency and variation in MOD13Q1 over the period of study. As descriptive statistics show in Table 3-4, the MOD13Q1 domain is relatively homogeneous (i.e. mean value of single central pixel on flux tower site is similar to a subset of 3×3 pixels centred on the tower site) (Figure 3-7).

Table 3-4 MODIS products across Wytham's flux tower extent over the period 2007-2009

	MOD13Q1-NDVI			MOD13Q1-EVI		
	Central Pixel	Average 3×3 Pixel	SD 3×3 Pixel	Central Pixel	Average 3×3 Pixel	SD 3×3 Pixel
Mean	0.7297	0.7284	0.02216	0.4030	0.4015	0.03291
Median	0.7488	0.7453	0.01800	0.3715	0.3701	0.01980

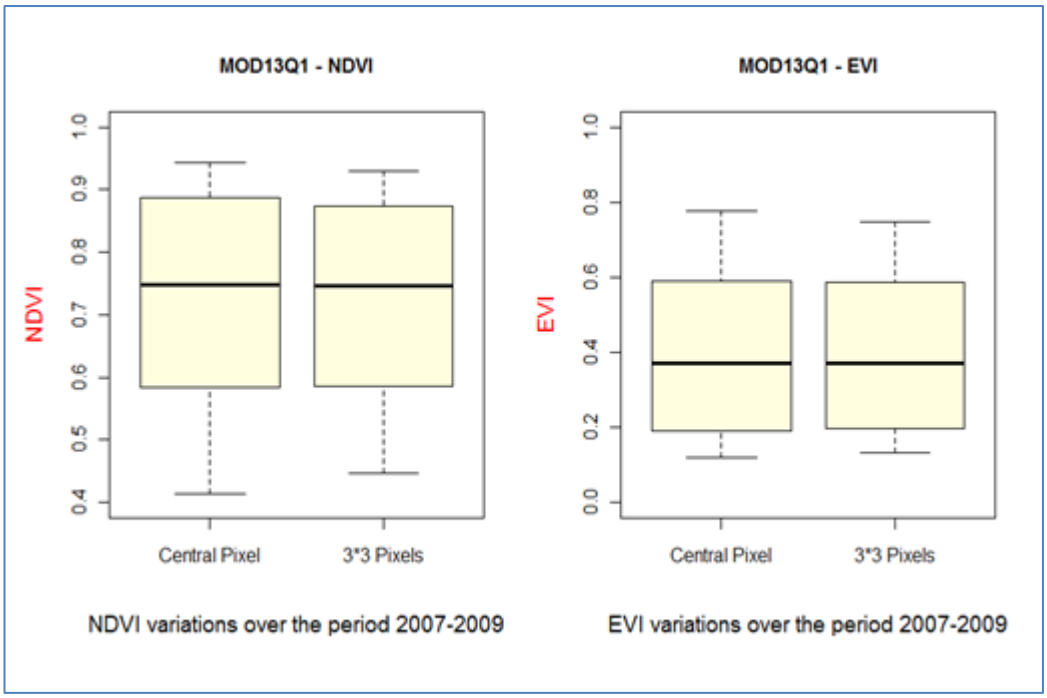

Figure 3-6 MOD13Q1 variations in Wytham's flux tower site over the period 2007-2009

Figure 3-7, in addition, shows a comparison between single pixel values of MOD13Q1 containing the tower site and the 3×3 pixels centred at the site. The coefficient of determination for this comparison for NDVI and EVI are approximately 0.94 and 0.93, respectively.

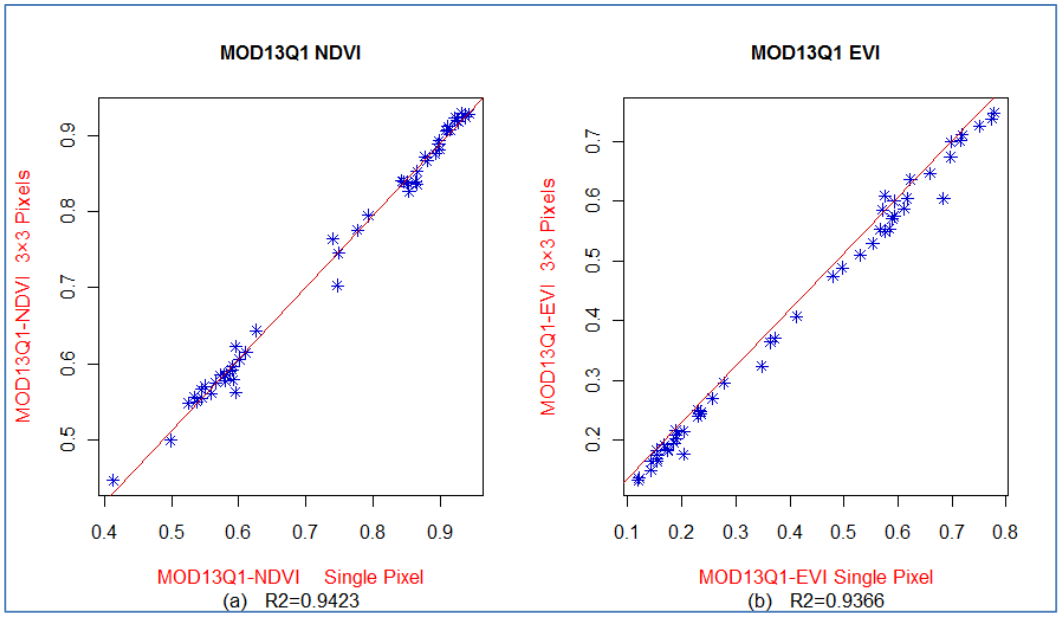

Figure 3-7 Central pixel versus the 3×3 pixels of MOD13Q1 centred on Wytham tower site; (a) MODIS NDVI; and (b) MODIS EVI.

Figure 3-8 illustrates the MODIS VIs from January 2007 to April 2009. Average VI values for both subsets (single pixel containing the flux tower site and the 3×3 pixels centred on the tower site) peaked at around 0.9 for NDVI and 0.7 for EVI between mid-May to early-June and decreased to a minimum of around 0.5 for NDVI and 0.15 for EVI in the winter months. In early-April VIs began to rise to more than 0.7 for NDVI and 0.4 for EVI as the trees grew. As Figure 3-8 shows, both NDVI and EVI rose rapidly during April and May, as the forest canopy came into leaf. The final rise, in comparision with EC-based GPP on Figure 3-10, could have resulted from late developing trees reaching full photosynthetic capacity by May and early-June.

Seasonal changes in photosynthesis capacity were evident from EC-based GPP and spectral vegetation indices across the Wytham Woods flux tower site. In mid-spring photosynthesis increased due to rapid growth of leaf area and relatively low rates of respiration, since soil temperatures were relatively low (Baldocchi et al. 2001; Desai et al. 2008). Although in the winter seasons both GPP and its spectral indices were low (i.e. due to leaf-off conditions of forest canopy and low levels of solar radiation), CO_2 flux and MODIS NDVI and EVI values were greater than zero suggesting photosynthesis by understory and adjacent evergreen coniferous trees (Figure 3-9).

Figure 3-10 shows the seasonal dynamics of MODIS GPP (i.e. MOD17A2) of the central pixel over the Wytham Woods flux tower site. Although, greater MOD17A2 values were identified for the summer months, there is temporal variation in the GPP in comparison with EC-based GPP measurements (Figure 3-10). This could result from both spatial variability of photosynthesis, as well as spatial and temporal variability in the EC-based CO_2 flux measurements (i.e. flux tower footprint variability).

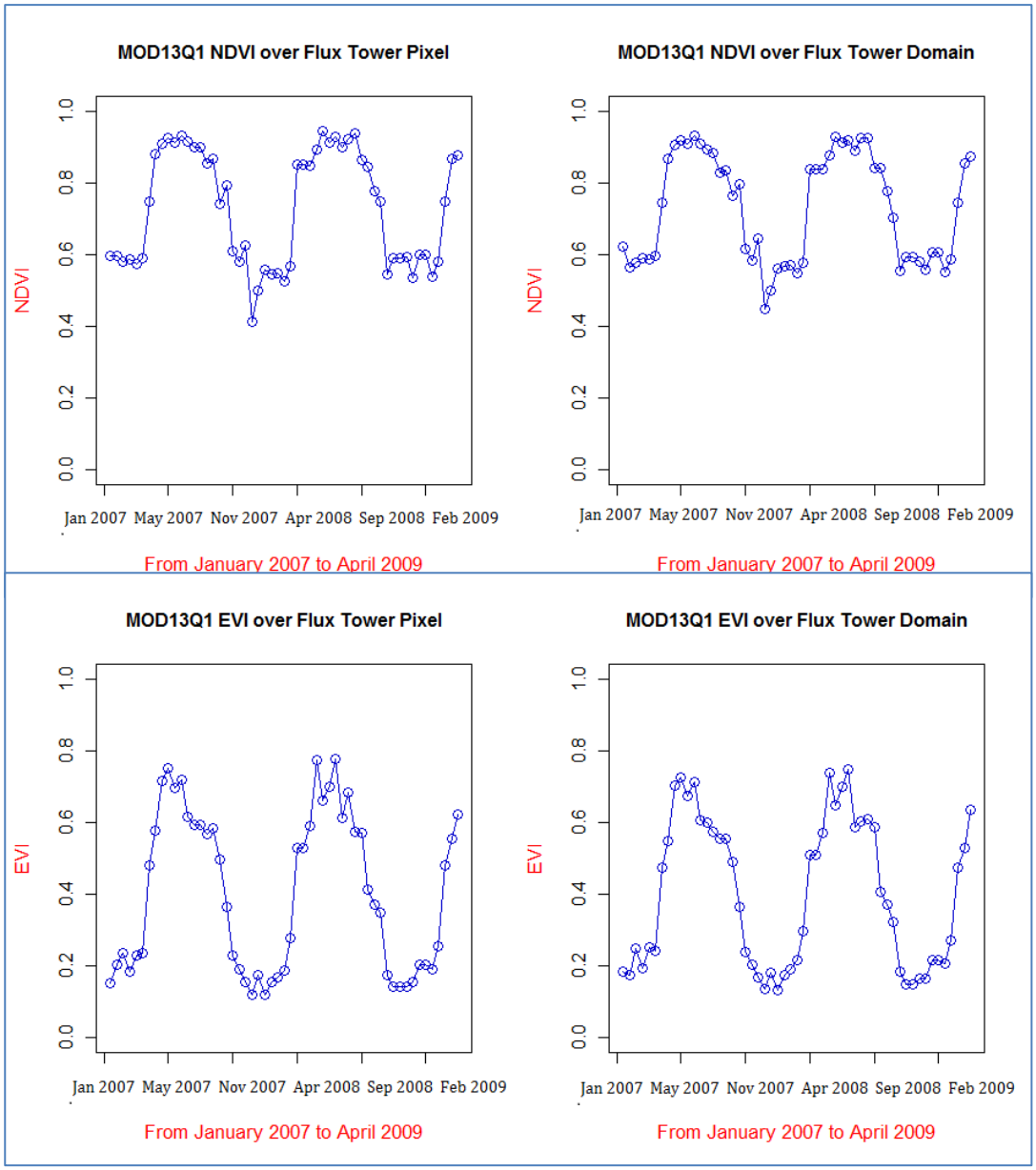

Figure 3-8 MOD13Q1 in Wytham's flux tower site through period Jan. 2007 to Apr. 2009

Figure 3-9 Wytham Woods mixed forest, Top of the flux tower - Feb. 2013

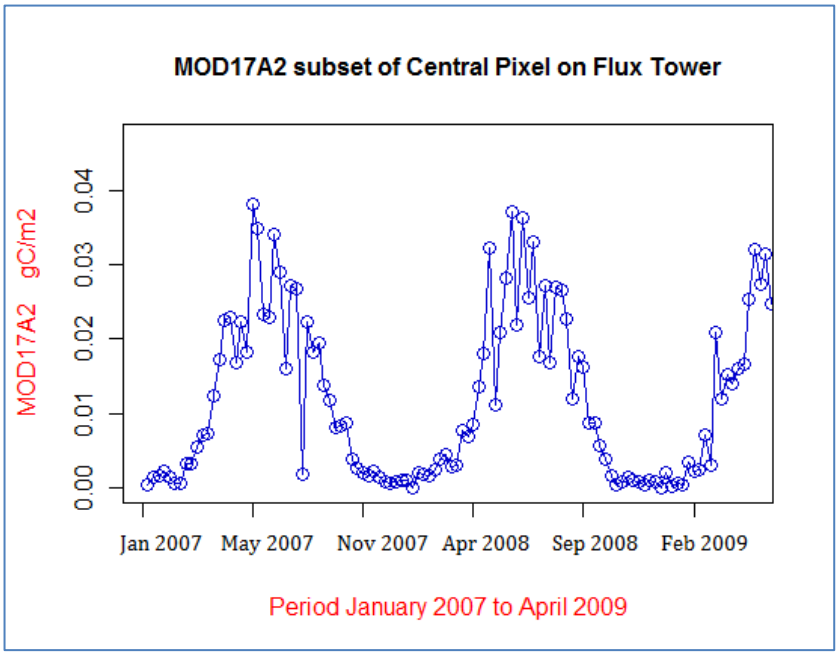

Figure 3-10 Seasonal MODIS GPP, MOD17A2, trend at Wytham Woods, 2007- 2009

Additionally, Figure 3-11 shows the relationship between MOD13Q1 ((a) NDVI and (b) EVI) and GPP derived from EC flux measurements through the period May 2007 to April 2009. Accordingly, MODIC EVI reveals a greater correlation than MODIS EVI, which indicates the effect of canopy background on the spectral index of photosynthesis capacity.

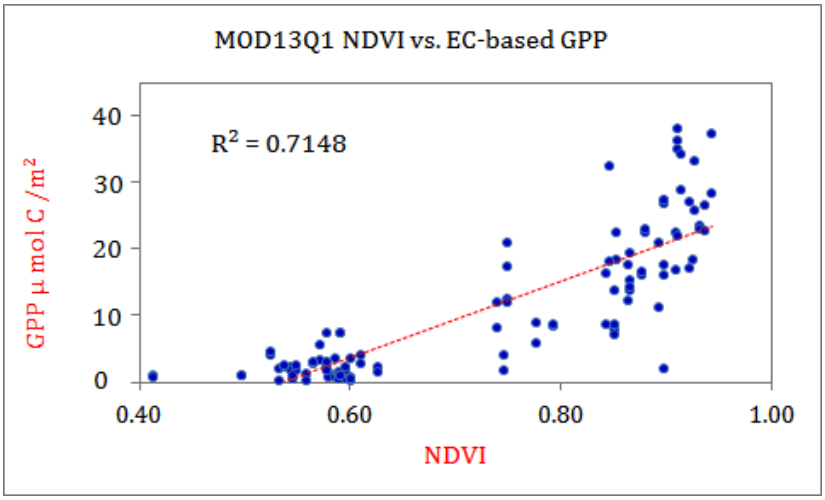

(a) MOD13Q1 NDVI versus GPP derived from EC flux measurements

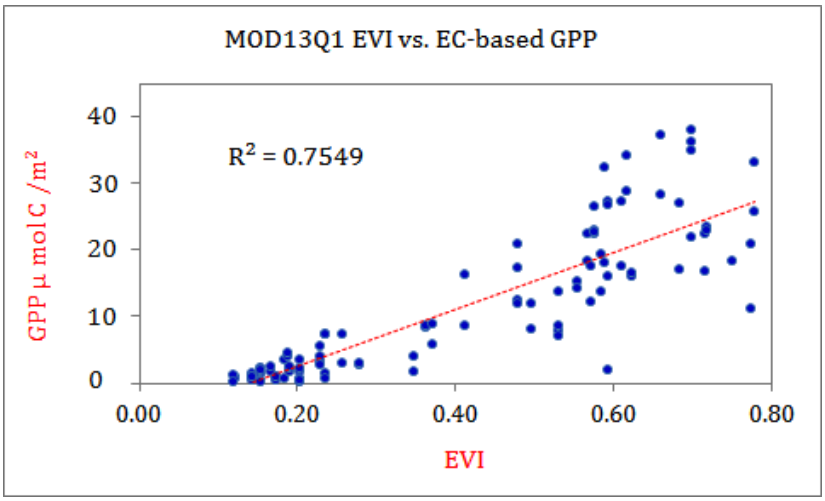

(b) MOD13Q1 EVI versus GPP derived from EC flux measurements

Figure 3-11 Scatterplot representing the relationship between MOD13Q1 (a 3*3 window of MODIS NDVI and EVI) and EC-based GPP across Wytham Woods flux tower over the period May 2007 to April 2009

3.1.3 Discussion on Tower-based EC CO_2 Flux Measurements

The NEE of CO_2 was measured between the land surface and the atmosphere in Wytham Woods, covering various canopy types. The measurements were conducted using the EC technique that provided a continuous time series of data at landscape/stand level.

The seasonal cycle of the CO_2 exchange in this mixed forest is distinctly divisible into the growing season and the non-growing season. This division is determined by the ability of the ecosystem to utilize the solar energy. Both abiotic and biotic factors determine the length of the growing and non-growing seasons, following the seasonal changes in the incident radiation (i.e. PAR), as well as air and soil temperature which has impact on the photosynthesis process (i.e. CO_2 flux).

As seen from Figure 3-5 (i.e. cumulative NEE of CO_2 and day of year), two characteristic shoulder-seasons mark the transition to the season of net uptake of carbon. The seasonal variation in abiotic forcing can be used to divide the year into five characteristic parts including winter, spring thaw, pre-green, green, and post green. During winter incident radiation and soil temperatures are low and canopy cover is in leaf-off condition, which results in small losses of CO_2 from the ecosystem. The flux at this time of year is seen to be relatively stable. In the spring thaw period, soil micro-organisms are protected from the extreme variations in air temperature, and are able to produce more CO_2. During this period a maximum release of CO_2 is seen. The release at the spring thaw is probably related to the build-up of CO_2 produced prior to the thawing event and consequently released upon thawing as a combination of release of the enhanced heterotrophic decomposition. During the pre-green period the net ecosystem exchange increases, and the CO_2 flux start to show a diurnal pattern. At this early stage of the summer season the amount of solar radiation is at its peak which is important for the development of the plants and the photosynthetic process. In the growing season (i.e. leaf-on condition), the trees start developing leaves. In this period the ecosystem switches from a source to a sink in response to the increased photosynthesis, and the ecosystem constitutes a sink with a net daily uptake of

carbon. During this period uptake of carbon is observed almost 12 hours of the day, due to incoming radiation. When LAI starts to decrease, the net uptake diminishes, and the plant senescence becomes more and more significant. Eventually the ecosystem turns into a source of CO_2, and the post-green period begins, which characterizes the autumn. This period is characterized by large releases of CO_2 to the atmosphere. The length of the leaf-off and leaf-on conditions consequently exerts strong control on the annual budget.

The results have documented that the landscape is sink of CO_2 during the growing season. The cumulative NEE of CO_2 as depicted on Figure 3.5 has also showed that this temperate woodland was a large carbon sink over the period of study (2007-2009). However, the inter-annual variation in cumulated NEE of CO_2 uptake rates was found to range from 0 to -0.5 (Figure 3-5), mostly caused by the seasonal changes in the incident radiation and the climate conditions.

In conclusion, results showed that the tower-based EC CO_2 measurements could track seasonal fluctuations of ecosystem carbon exchange at a mixed forest site level. Good agreement between the MODIS GPP and those determined from two years of eddy flux measurements further supports the values of integrating at monthly time steps. This work also denoted that flux measurements taken from a single stationary tower may not represent CO_2 exchange from a large forest, in particular mixed forest (e.g. Wytham Woods). For example, when deciduous and conifers are clumped in their distribution (Figure 3-9), the wind direction may have a major influence on their contribution to area-wide fluxes (i.e. flux footprint). It seems this problem can be solved in part by measuring fluxes and airborne remotely sensing canopy properties (i.e. following section).

Finally, the EC technique has been demonstrated to be a useful tool for the estimation of CO_2 flux and assessment of ecosystem dynamics (Burba and Anderson, 2010a; Desai et al., 2008; Desai, 2014; Peltola et al., 2015; Xiao et al., 2012; Xiao et al., 2008; Zhang et al., 2016). Despite the wide applicability of the EC technique, confidence in these data with regard to extending into the ecosystem/regional level remains low, particularly in a heterogeneous landscape.

There are several sources of uncertainty associated with expanding CO_2 flux measurements at various spatial and temporal scales (Chen et al., 2009a; Chen et al., 2012; Coops et al., 2008; Curtis et al., 2002; Desai et al., 2008; Fenn et al., 2010; Gamon et al., 2016; Horst and Weil, 1992; Huemmrich et al., 2010; La Puma et al., 2007; Peltola et al., 2015; Schmid, 2002; Xiao et al., 2012; Xiao et al., 2008; Zhang et al., 2016). Since natural and semi-natural ecosystems are spatially heterogeneous (Forman, 1995; Forman and Godron, 1986; Frohn, 1998; Hutchings et al., 2000), extending CO_2 flux from tower-specific coverage to a landscape and regional scale must take into account the variation of spectral indices of CO_2 fluxes with respect to space (i.e. canopy patches and realistic flux tower footprint) and time (i.e. seasonal variation and trends). The influence of these extraneous variables on the spectral indices of CO_2 fluxes is described in following chapters.

Scaling of the EC-based CO_2 exchange to larger areas may be accomplished through the LUE model using satellite/airborne estimates of relevant parameters. As mentioned previously, despite the numerous advantages and limitations of using EO data and LUE model for the above purpose, there are also several potential uncertainties that need elimination through the application of accepted corrective algorithms (Chen et al., 2012; Coops et al., 2008; Desai et al., 2008; Desai, 2014; Gamon et al., 2016; Xiao et al., 2012; Zhang et al., 2016).

3.2 Potential of EO Data to Provide Information on CO_2 Flux

3.2.1 Use of Airborne LiDAR to Create a Three-dimensional Model of the Canopy in Wytham Woods

Accurate estimates of woodland biomass and carbon storage over large areas are required to characterise both the structure and function of these ecosystems (Desai et al. 2005; Hardiman et al. 2013; Lal 2005; Lefsky et al. 2002). The vertical structure of woodlands (i.e. single and multi-storey canopies) strongly influences land-atmosphere exchange of CO_2, photosynthesis capacity, and habitat dynamics, that is, habitat availability and quality (Kim et al. 2006; MacArthur and MacArthur 1961; Rahman et al. 2001). Information on the vertical structure of woodlands can be essential for accurate estimation of carbon flux and photosynthesis capacity (Patenaude et al. 2004).

Airborne LiDAR has been a key technology involved in existing efforts to estimate above ground biomass and carbon storage (Lefsky et al. 1999a; Lefsky et al. 2002), and has also been identified as a promising technique for modelling vegetation structure and habitat dynamics (Hill and Broughton 2009; Hill and Thomson 2005) using measurements of forest inventory such as tree height, timber volume, crown height, canopy closure and LAI. Elton and Miller (1954) described a habitat classification system with four levels: (a) terrestrial and aquatic; (b) woodland and open ground; (c) shrub and high canopy; (d) conifer and deciduous. This system requires appropriate methods to identify both horizontal and vertical land-cover distribution. Recent work by Næsset and Bjerknes (2001) clearly revealed that tree height can be measured from LiDAR data as accurately as ground measurements. Geerling et al. (2007) examined the ability of LiDAR data to employ the spectral response of plants to map vertical vegetation structures for floodplain management. They showed that the similar vegetation types, for example, grass and low shrubs are difficult to distinguish, but discrimination between bushes and trees was readily achieved. Multiple studies have demonstrated the application of LiDAR data in forestry, particularly the estimation of aboveground forest biomass

and carbon content (Boudreau et al. 2008; Gonzalez et al. 2010; Hudak et al. 2002; Lefsky et al. 1999a; Lefsky et al. 1999b; Lefsky et al. 2005; Patenaude et al. 2004). Chen et al (2008) produced fine spatial resolution maps of gross ecosystem production using multi-angular canopy level reflectance measurements combined with the canopy structure information derived from airborne LiDAR data to upscale EC flux measurements to the landscape level.

The main goal of this section is to extract the vertical structure of canopy cover using airborne LiDAR data for assessing the spatial variability of photosynthesis capacity over the Wytham Woods flux tower extent. Airborne LiDAR data were acquired with an ALTM-3033 instrument, by the NERC-ARSF on 9th March 2009 (Julian-day: 068) and 29th June 2009 (Julian-day: 180) over the Wytham Woods flux tower. These data are referred to in this research as leaf-on and leaf-off conditions, respectively. The leaf-on first return data were examined in this research, as the amount of laser penetration into the canopy. For the leaf-off data both first and last return data were examined.

Figure 3-12 illustrates line transects (i.e. 20 m×200 m) through the leaf-on point cloud, giving a good visualisation of the fully developed canopy structure over the Wytham Woods flux tower extent.

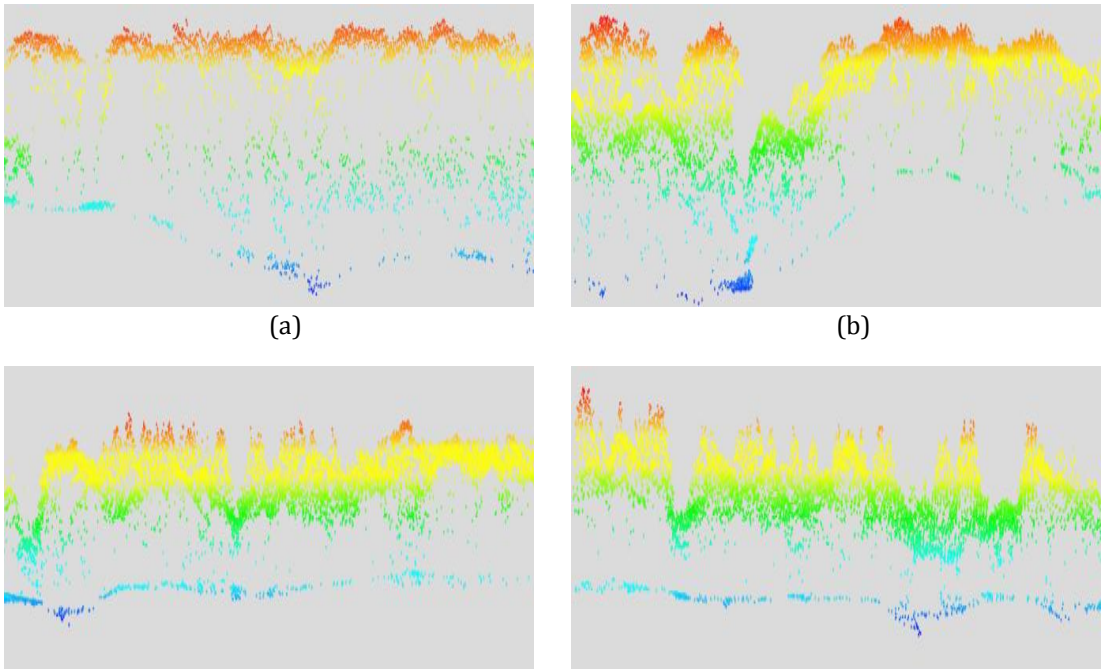

(a) (b)

(c) (d)

Figure 3-12 Measurements of canopy structure extracted using airborne LiDAR point cloud coloured in height intervals. (a) Top-left plot shows data from dense mature deciduous trees with a mean height of ≈18m; (b) Top-right plot depicts patchy deciduous trees with mean height of ≈16.5m over secondary canopy type with generating gap and complex canopy structure; (c) Lower-left plot represents dense coniferous tress and mean height of ≈17m over plantation canopy type; and (d) Lower-right plot shows relatively young coniferous trees and mean height of ≈16.5m over plantation canopy type with high diversity of canopy heights.

The point data were interpolated into raster grids, which were converted into a digital surface model (DSM) and digital terrain model (DTM). The selected spatial resolution was 2 m, the approximate horizontal accuracy of the leaf-on acquisition relying upon point spacing assessment, was roughly 0.55 m. This approach was utilized separately for the first return data from both leaf-on and leaf-off condition and for the leaf-off last return data. Figure 3-13 shows the leaf-on first return DSM.

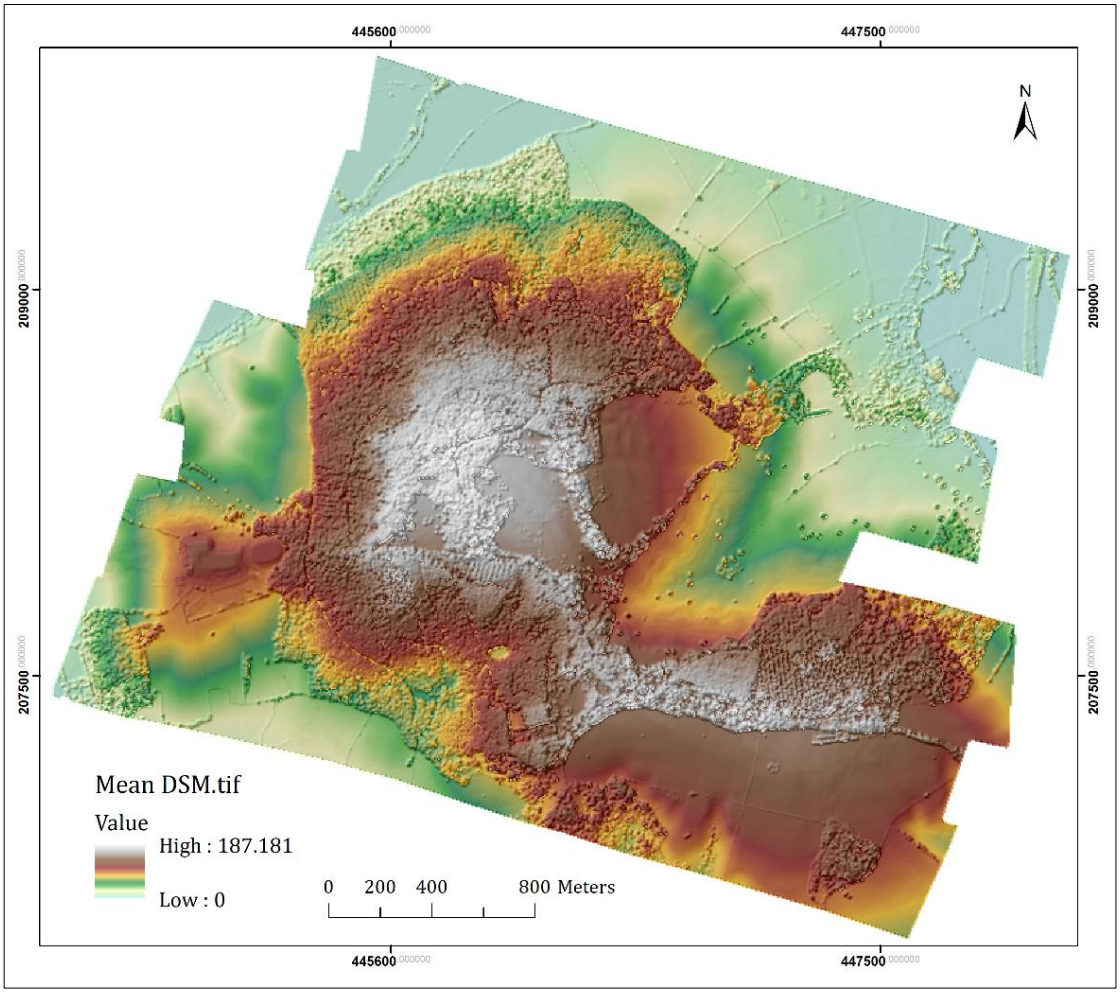

Figure 3-13 Airborne LiDAR derived Leaf-on DSM

Underlying the LiDAR data analysis objectives, flux tower footprint size and shape is dependent on the measurement height, local terrain, surface roughness and meteorological conditions, and canopy structure influences the surface roughness length, alongside flux tower footprint modelling. On the basis of this theory, the directional estimation of canopy height was performed over a distance of 400 m centred on the flux tower site. Figure 3-14 shows a 3D perspective of the LiDAR point cloud, based on the generated canopy surface model over Wytham Woods and signifies flux tower heights, approximately 25 m with highest first return.

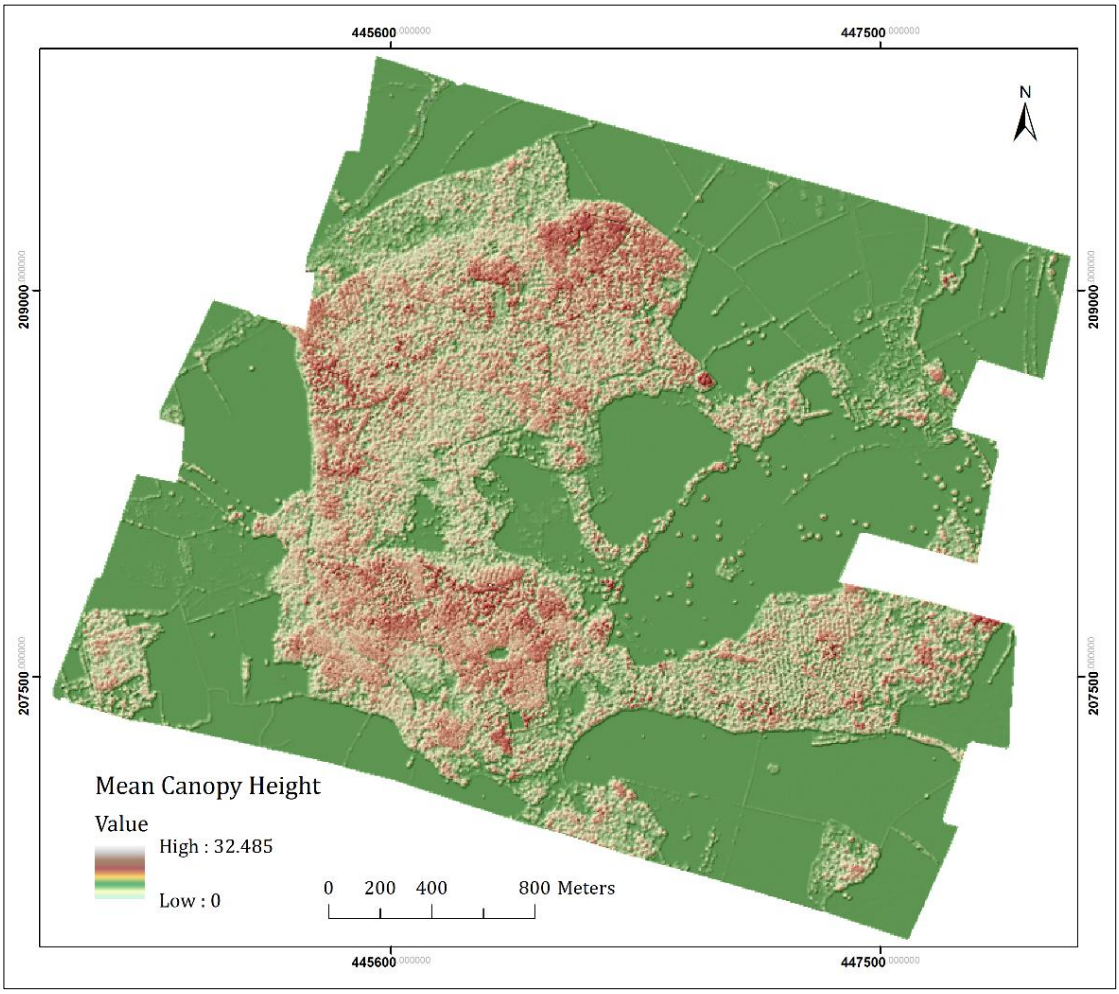

Figure 3-14 Airborne LiDAR derived normalized Canopy Height Model (nCHM)

As Figure 3-14 shows, the subtraction per pixel of the leaf-on first return DSM from the leaf-off DTM generated a normalized canopy height model (nCHM), which expressed canopy height above ground level. Figure 3-15, furthermore, depicts the percentage of vegetation height in three classes to identify the vertical structure of the canopy stand. Finally, the nCHM was reclassified into seven classes in terms of vegetation height. Figure 3-16 depicts these different classes of canopy height. It is clear that the LiDAR derived nCHM represents an approximately 17.5m mean canopy height, which was buffered in the region of Wytham Woods flux tower site (Figure 3-17) to identify the canopy stand height around the flux tower site. In addition, Figure 3-18 displays the percentage frequency distribution of each canopy height class. The most frequent with 39.23% is the fourth class, with a canopy height between 15 m and 20 m.

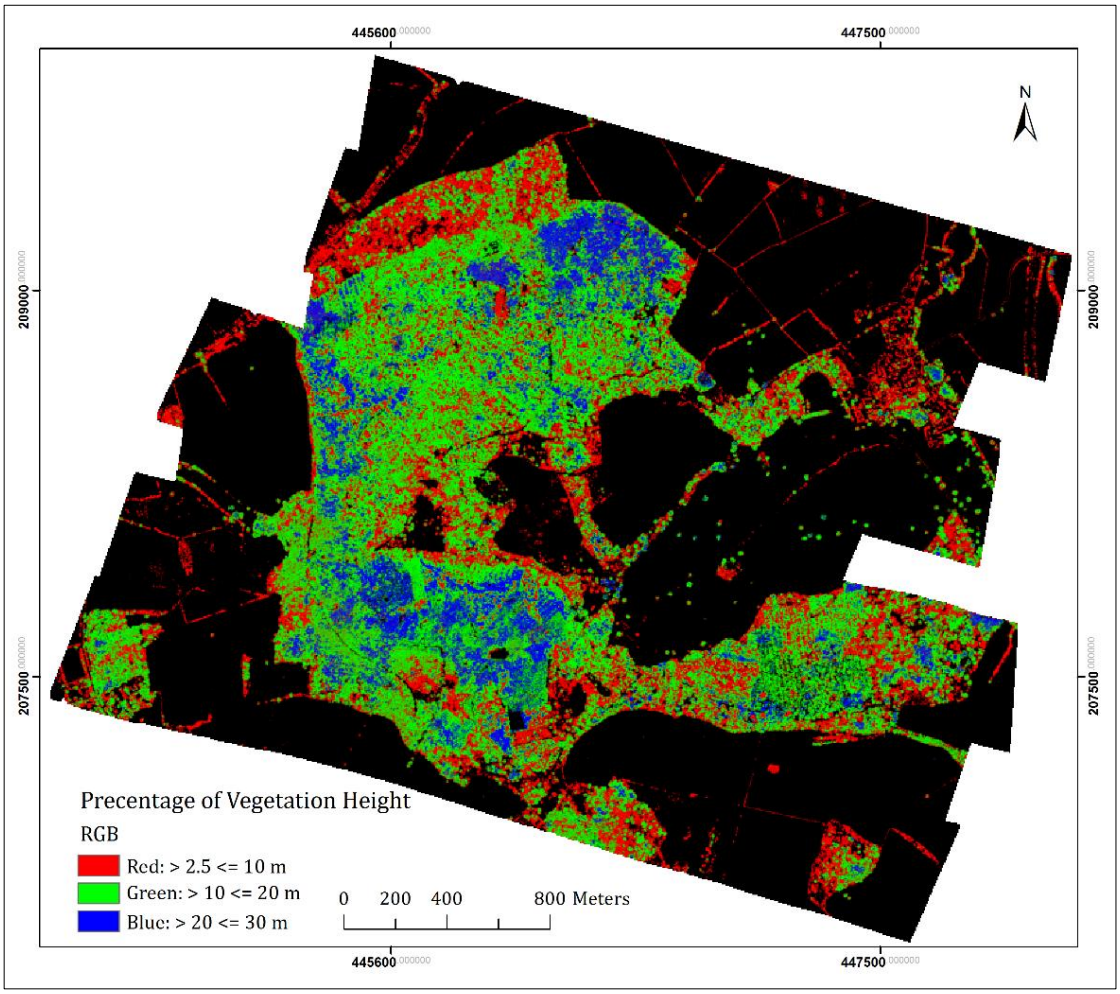

Figure 3-15 Airborne LiDAR derived Canopy Stratification

Having used the LiDAR data to help visualize the site, and also as a source of quantitative information on tree height and spatial pattern, attention is now turned to the second objective, the use of these data to simulate the effective flux tower footprint for the tower-based EC measurements.

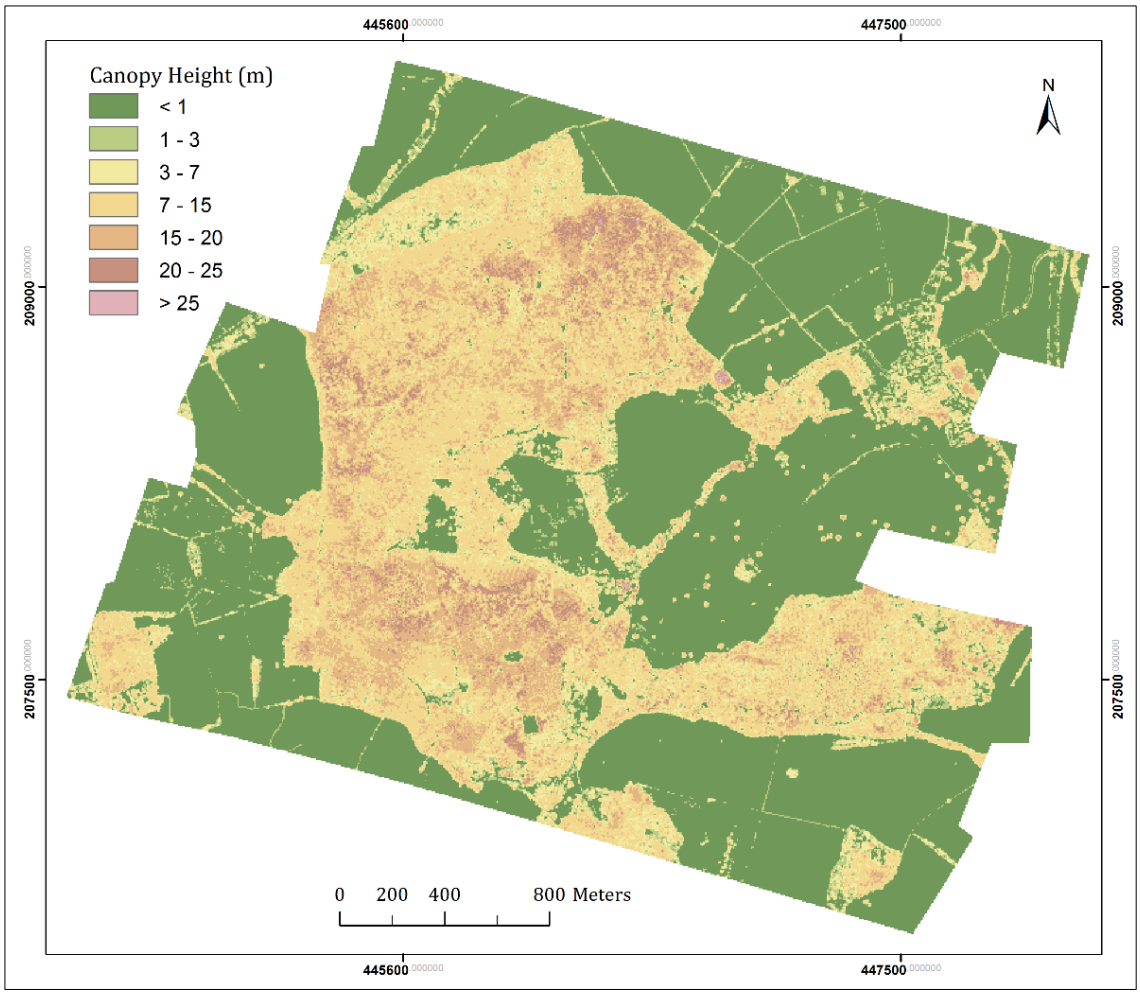

Figure 3-16 Airborne LiDAR derived Canopy Height Map

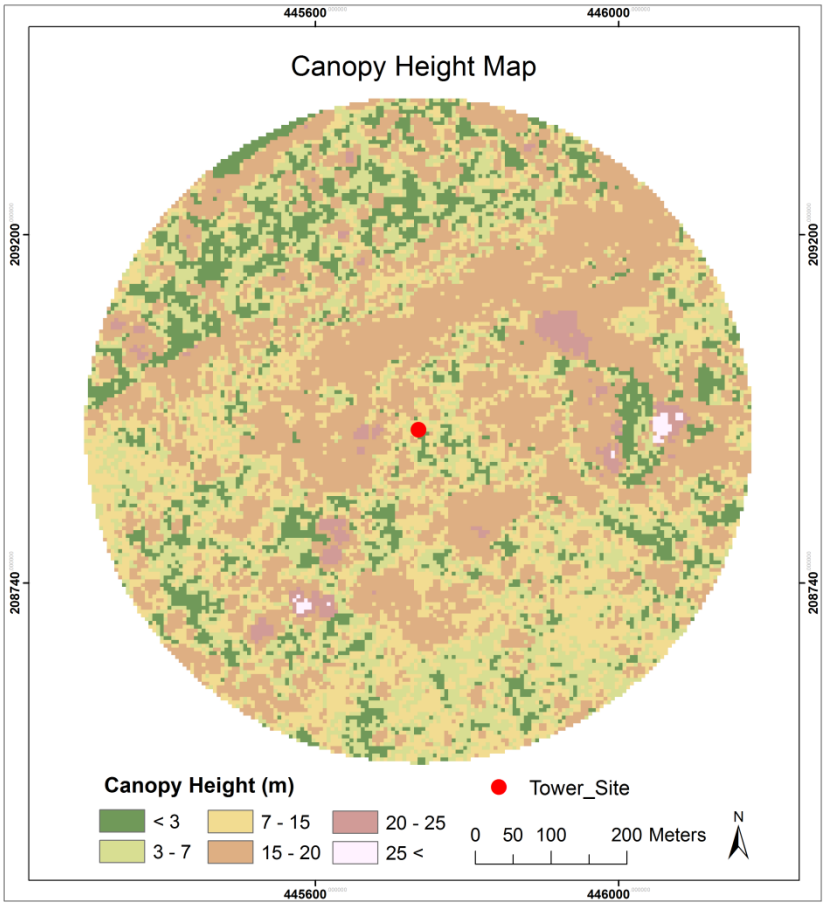

Figure 3-17 Airborne LiDAR derived normalized Canopy Height Model (nCHM), within a circular buffer of 400 m radius centred on the Wytham flux tower site.

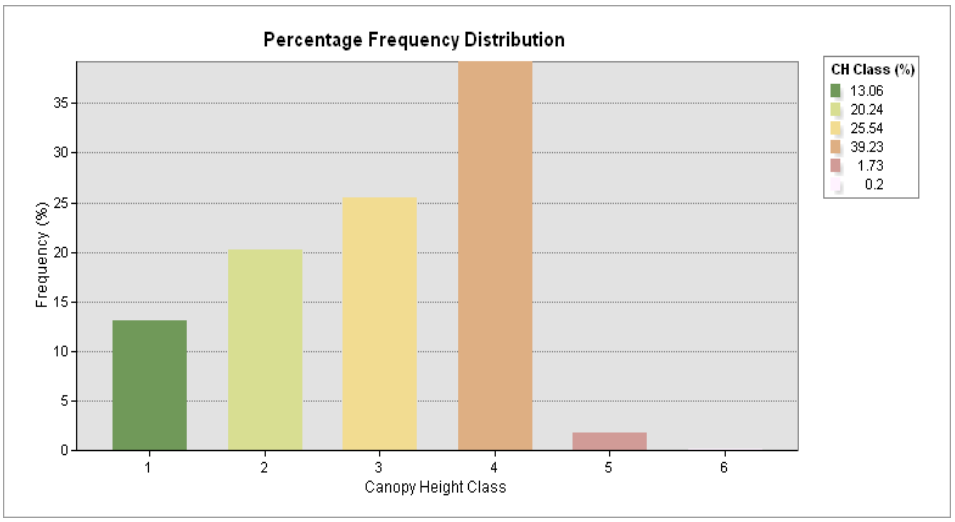

Figure 3-18 Frequency distribution of normalized Canopy Model Model (nCHM), Circular buffer 400m radius centred on the Wytham flux tower site.

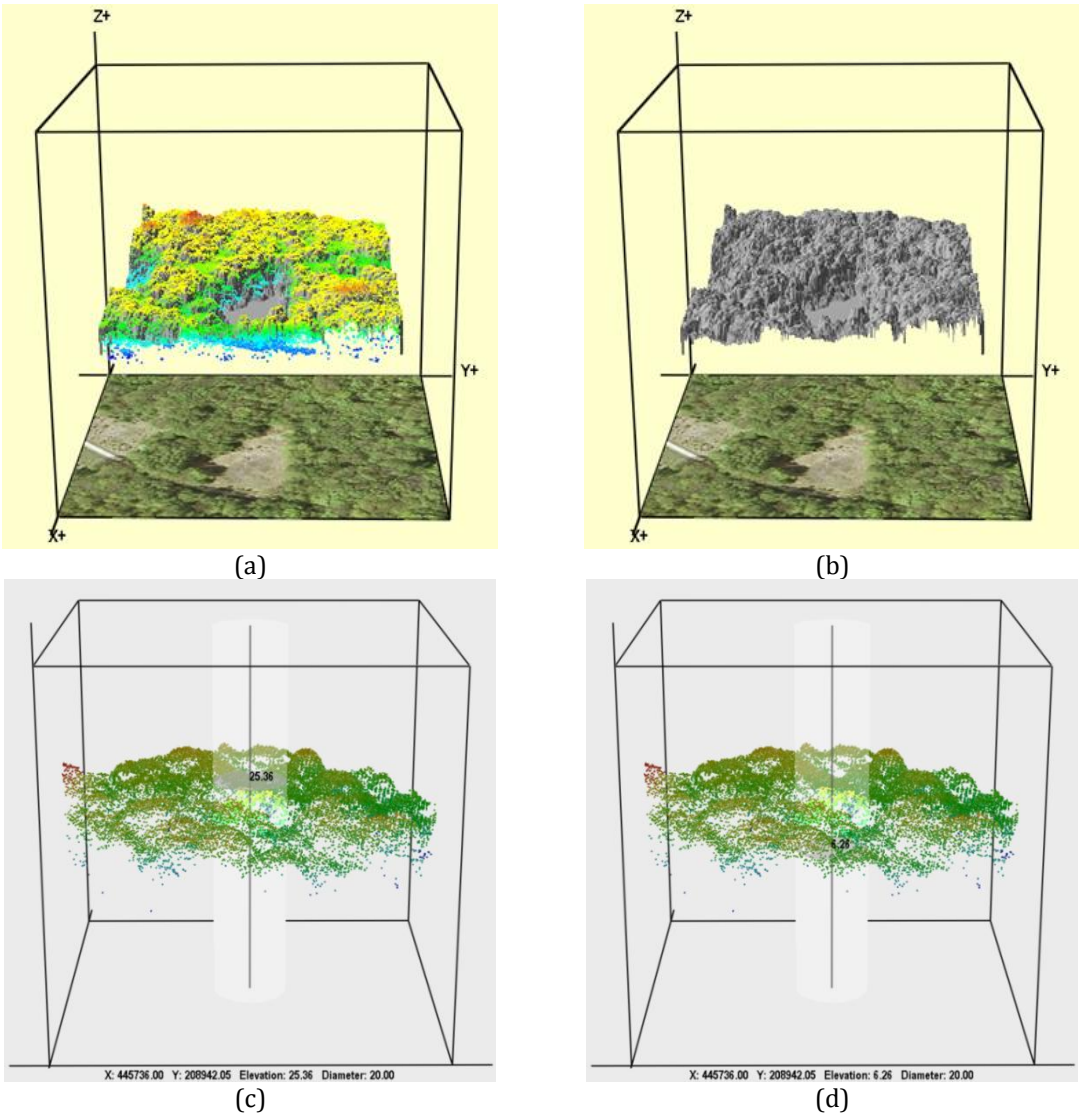

Figure 3-19 Three-dimensional perspective view of LiDAR point cloud over Wytham flux tower site; Top plots, (a) and (b) show LiDAR-based canopy surface model overlaid with aerial image; and lower plots illustrate measurements of flux tower height (i.e. approximately 25.36m highest first return data point and 6.26m lowest first return data point).

3.2.2 The Potential of Airborne Imaging Spectrometry (AIS) to Provide Information on the Photosynthesis Process

Airborne Imaging Spectrometry (AIS) data generally have a fine spectral and spatial resolution, and so have great potential to act as a transfer standard addressing ecosystem function in the up-scaling process from tower-based EC flux measurements to coarse satellite sensor observation (Boschetti et al. 2007; Cochrane 2000; Martin et al. 1998). The combination of data acquired by AIS and LiDAR provides information on both canopy structure and composition (Geerling et al. 2007; Hill and Thomson 2005; Jones et al. 2010) and so is potentially a very powerful tool for ecological survey and mapping.

Because of its national scientific importance as a long-term ecological monitoring site, many remotely sensed datasets have been acquired over Wytham Woods, including several annual campaigns involving AIS (Table 3-5). Preliminary study of all the available AIS data for the site led to one campaign being chosen for detailed study, based on the quality of the data, the absence of cloud and haze, and the season of the year (For example, Figure 3-21). A dataset from the Airborne Imaging Spectrometer for Application (AISA) Eagle[1] acquired under cloudless conditions on 9th September 2009 (Julian day 252) was selected for detailed study (Figure 3-22).

The AISA Eagle hyperspectral imagery comprised 252 narrow spectral wavebands ranging from 392.57 nm to 987.24 nm with a full-width at half maximum (FWHM) ranging from 2.20 nm to 2.44 nm in the VNIR wavelengths.

1. AISA Eagle data, acquired by the UK NERC-ARSF, are actually in radiance unites (i.e. $\mu W/m^2/nm$); so the scaling factor is the relationship between DN and radiance value.

Table 3-5 NERC ARSF airborne remotely sensed data over Wytham Woods (Red tick indicates available dataset, and AISA includes Eagle/Hawk)

Project Code	Year	Day	ATM	CASI	AISA	LiDAR
GB08/08	2009	268b	----	----	✓	✓
GB08/08	2009	252b	----	----	✓	✓
GB08/08	2009	180b	----	----	✓	✓
GB08/08	2009	154a	----	----	✓	✓
GB08/08	2009	75b	----	----	✓	✓
GB08/08	2009	68	----	----	✓	✓
GB08/08	2008	198	----	----	✓	----
GB08/08	2008	176	----	----	✓	----
GB08/08	2008	175	----	----	✓	----
GB08/08	2008	134b	----	----	✓	----
GB08/08	2008	127b	----	----	✓	----
GB07/12	2008	49b	----	----	✓	----
CEH07/05	2007	171a	✓	✓	✓	✓
CEH07/05	2007	73	----	----	✓	----
MC03/15	2005	92	✓	✓	----	----
MC03/13	2005	171	✓	✓	----	----
MC03/11	2004	90	✓	✓	----	----
MC03/15	2004	96	✓	✓	----	----
MC03/11	2003	209	✓	----	----	----

Figure 3-20 A mosaic of ATM imagery (true colour composite) over Wytham Woods on 28th July 2003 (Julian day of flight: 209)

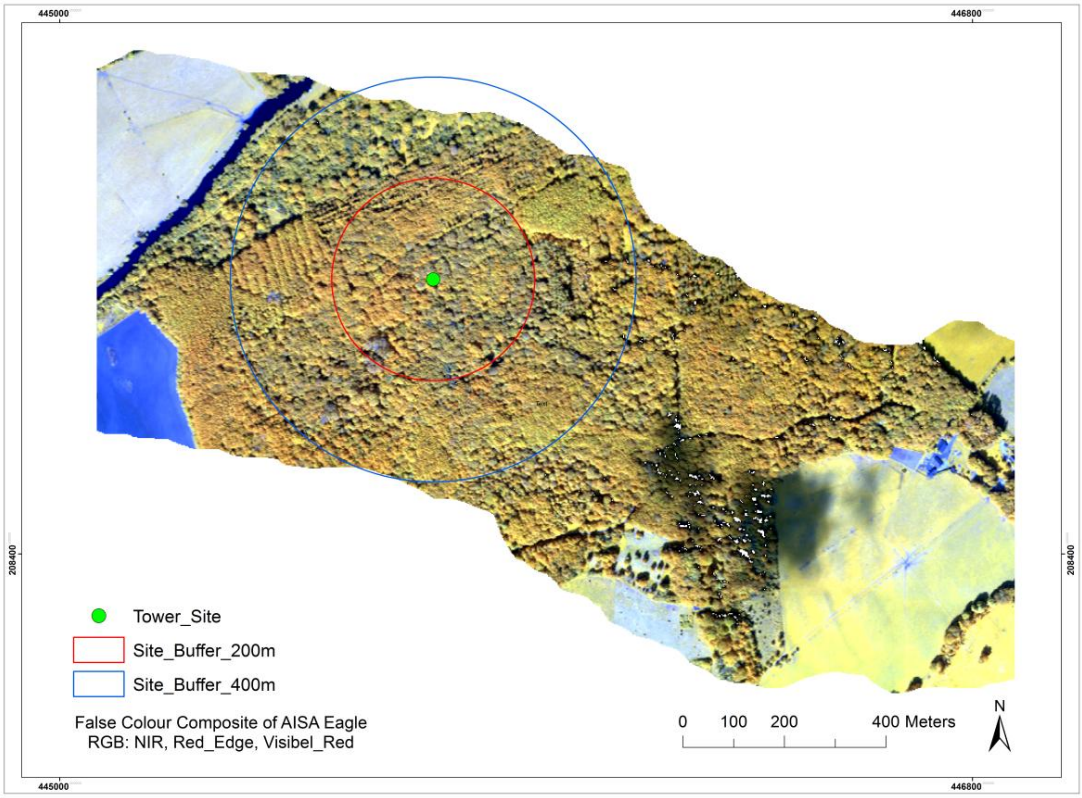

Figure 3-21 False colour composite of the AISA Eagle data (RGB: NIR, Red Edge, Visible Red). Although canopy structure heterogeneity is evident, the differences between tree species in spectral response is unclear in this composite.

The AIS data have the general appearance of the solar spectrum with radiance decreasing at longer wavelengths (Figure 3-22), and exhibit several absorption bands due to absorption by gasses in the atmosphere (Thenkabail et al. 2011; van der Meer 2006). The major absorption bands present in the AISA Eagle data were the water vapour (H_2O) bands centred at approximately 816 nm and 936 nm, and the oxygen (O_2) band at 762 nm. The NERC ARSF provided the AISA hyperspectral data as system-corrected Level 1b and in modified hierarchical data format (HDF). The HDF data contain information from various ancillary devices for recording the attitude (i.e. roll, pitch and yaw) and position of the sensors and basic meteorological parameters during the mission, as well as radiometrically corrected Band Sequential (BSQ) image files. Despite the level 1b data containing geodetic information and radiometric calibration values, the data were not projected to an appropriate geographic coordinate system. Therefore, Level 1b data were corrected into Level 3a using *AZGCORR*, an airborne remote sensing geo-correction

package provided by the NERC ARSF, based on the on-board attitude, positional information and platform altitude, as well as a fine spatial resolution DSM for relief correction. In other words, the level 3a data were produced by considering three aspects including optimising platform variation, topography and reference to a given projection and datum.

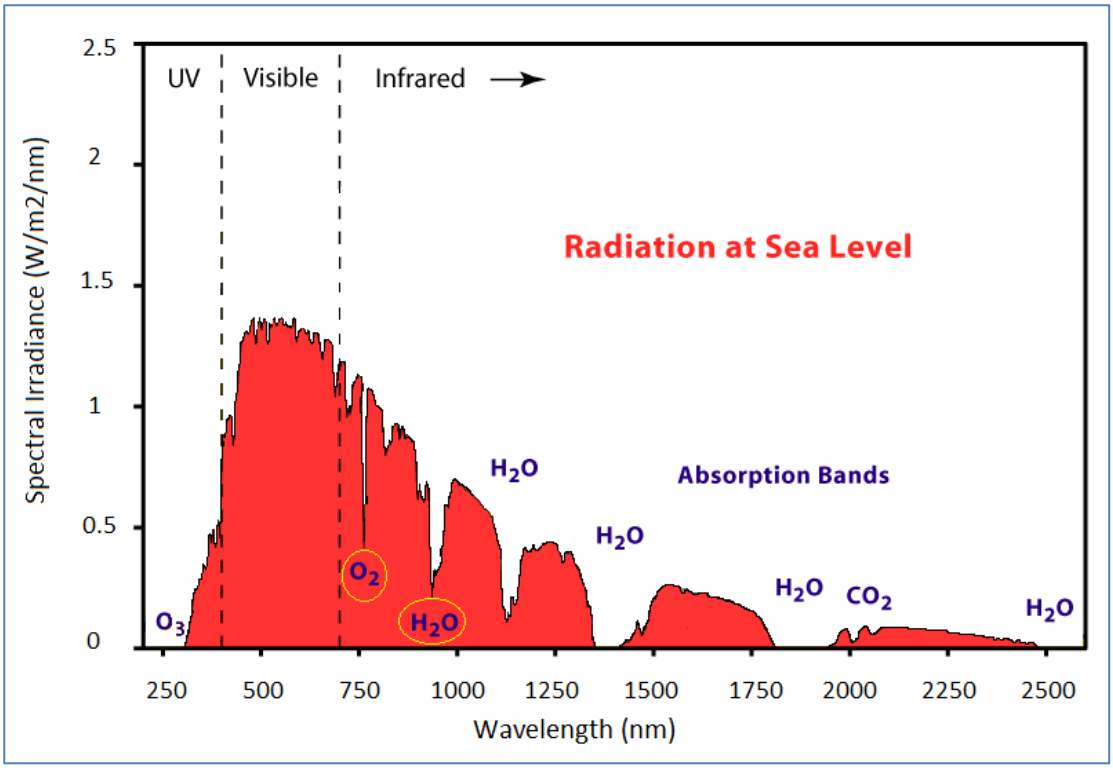

Figure 3-22 Solar Irradiance Spectrum, adopted from Lillesand et al. (2008)

3.2.2.1 Cross Track Illumination Correction

Cross-track illumination variation is common in airborne scanner data as a result of bidirectional reflectance effects (i.e. sun-sensor geometry) (Kennedy et al. 1997). In such data, the spectral signature of an individual feature varies with respect to view angle. Cross-track illumination correction followed by relative calibration can be used to normalize the AISA Eagle observations to the nadir view angle. Consequently, a multiplicative correction based on a second-order polynomial was applied to each individual flight line to reduce variation in the cross-track illumination of the AISA Eagle hyperspectral imagery.

3.2.2.2 Relative Calibration of the AISA Eagle Data

An imaging spectrometer is often calibrated to absolute measurements in System International (SI) units such as spectral radiance (e.g. $\mu W/m^2/n$). However, calibration of the AIS data into surface reflectance is vital for quantitative investigation of land surface characteristics. The atmospheric correction of the AISA-Eagle data re-scaled radiance to reflectance by correcting for atmospheric influences, yielding a dataset in reflectance units (van der Meer et al. 2006). In general, calibration to reflectance can be conducted to result in absolute or relative reflectance data. Absolute reflectance calibration is not always necessary and may not be possible without ground data acquired at the time of the sensor overpass. In relative reflectance data, in contrast, reflectivity is measured relative to a certain standard reference in the scene. Although the image created does not depict true reflectance, the spectra are meaningful in a relative sense with certain assumptions. Accurate interpretation of the AIS data required information on the shape of the spectra and on the position of absorption features, such as leaf pigments and water content, both of which, could in principle be obtained from relative calibration.

In general, an important aspect of the relative metrics of reflectance calibration is how much contemporary *in situ* data are needed to perform the calibration. Since the current research involved secondary EO data, and aimed to assess spatial variability in spectral indices of ecosystem productivity in terms of up-scaling tower-based EC CO_2 flux, further analysis of the AIS data was conducted with relative reflectance data based on a confident standard reference in the original scene such as roof and roads.

There are several methods for calibrating the AIS data to apparent relative surface reflectance including: (a) normalization of the scene to an area of known flat reflectance, also called Flat Field Correction; (b) the scene-averaged method, also referred to as Internal Average Relative Reflectance; and (c) calibration using field reflectance measurements (Roberts et al. 1986; Zhang et al. 1998). Roberts et al. (1986) investigated these methods as a means for addressing two main features

with respect to the AIS data that is, decreasing solar irradiance towards infrared wavelengths and atmospheric absorption. Their results shown that the field reflectance calibration method was demonstrated to be superior in terms of noise and normalization, and that the flat field correction was the noisiest.

The most common method for reducing the atmospheric influence in the raw AIS data and eliminating the solar irradiance drop-off at longer wavelengths, as well as any residual sensor effects not requiring the radiometric calibration coefficient is the flat field correction (FFC). This technique involves the formation of the ratio of the radiance from an unknown target to the mean value of a flat area whose spectral reflectance is known (Roberts et al. 1986). The flat field reference area should meet the following criteria:

- Topographically flat;
- Spectrally homogeneous (i.e. uniform spectral reflectance at all wavelengths without significant absorption features); and
- High albedo area to avoid decreasing the signal-to-noise ratio (SNR).

In that case, the raw AIS data can be calibrated to relative reflectance by eliminating atmospheric effects and solar irradiance drop-off. The flat field calibration technique is often used when no information on the reflectance of a field target or atmospheric conditions is available.

Despite the weakness of the FFC technique in compensating path radiance in the shorter wavelengths (Roberts et al. 1986) this method should be appropriate for retrieving relative reflectance to obtain information on the position of absorption features, such as leaf pigments and water content, from the AISA Eagle observations.

To implement the FFC method, an area of concrete and a roof with high albedo were chosen as the most suitable spectrally homogeneous flat areas available in the scene. Figure 3-23 illustrates the spectral profile of the FFC-based calibrated AISA Eagle observations over three main canopy types including mixed forest (deciduous and coniferous tress) and grassland.

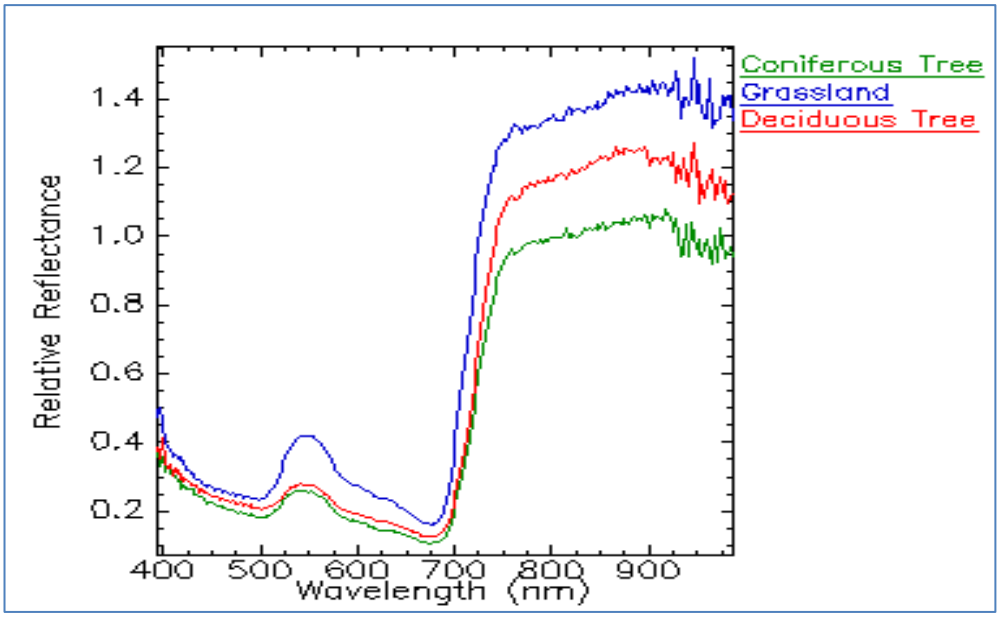

Figure 3-23 Spectral Profiles from the calibrated AISA Eagle hyperspectral image

3.2.2.3 Dimensionality Reduction

While AIS data offer great potential for addressing complexities associated with the spatial variability of photosynthetically active radiation in forest ecosystems (Atkinson et al. 2007; Hill and Thomson 2005; Jones et al. 2010; Peerbhay et al. 2013), due to its high dimensionality (i.e. hundreds of wavebands) and inherent redundancy (i.e. extensive correlation between adjacent wavebands) the utilization of full hyperspectral imagery is inefficient and may influence analytical methods (Jones et al. 2010; Lillesand et al. 2008; Riedman 2003; Tsai et al. 2007). Accordingly, dimension reduction through spectral subsets which maintain the most useful information in the dataset and maximize the discrimination of land surface features is typically considered a practical necessity in AIS data processing and analysis (Webb, 2002).

Dimension reduction of the AIS data, in this context, refers to feature selection and extraction. The term 'feature' refers to equally to hyperspectral bands. Feature selection is the process of selecting a subset of spectral bands from the original image bands by optimizing a certain criterion, which quantifies the amount of information contributed by each band subset under investigation. The new spectral subset contains the highest possible amount of information (Riedman

2003). In contrast, feature extraction algorithms aim to transform the original data into more informative new features for the purpose of dimensionality reduction. Among various feature extraction methods, principal component transformation is a commonly adopted technique to reduce the dimensionality of remotely sensed data (Liang 2004).

3.2.2.4 Feature Selection

On the basis of the typical spectral signature of green vegetation (Figure 1-6), measurement of the biochemical properties of a plant canopy provides significant insight into factors influencing photosynthesis capacity and performance (Danson 1995; Danson and Rowland 2003; Gamon and Surfus 1999; Richardson and Berlyn 2002). The existence of leaf pigments in the vegetation, such as chlorophyll content (Danson and Rowland 2003; Sellers et al. 1992) and xanthophyll (Gamon et al. 1990), is key to the photosynthesis process and a significant determinant of the spectral reflectance in the visible wavelengths ranging from 400 nm to 700 nm, which can be detected using specific spectral indices.

The maximum absorption of "chlorophyll-a" is at 430 nm and 662 nm and "chlorophyll-b" is at 453 nm and 642 nm for the Blue and Red spectral region, respectively. In the NIR region between 700 nm and 1300 nm the reflectance is much higher than that in the visible region due to internal vegetation leaf structure. Chlorophyll spectral indices are divided into two categories: (a) indices based on chlorophyll absorption in the Blue and Red spectral regions; and (b) indices based on the red edge inflection point, between 650 nm and 800 nm. The narrowband greenness index makes use of the wavelengths of maximum slope in the Red-NIR region (Liang 2004), termed the Red Edge Position (REP), which correlates with chlorophyll status at the leaf level. The advantage of this index over the NDVI is that it is less sensitive to varying soil and atmospheric conditions, as well as sensor view angle (Curran et al. 1995). Moreover, reflectance changes of the xanthophyll pigment at 531 nm provide an indicator of photosynthesis performance and can be useful to improve spectral indices (e.g. PRI) for monitoring photosynthesis efficiency at the canopy and landscape levels.

Spectra from the Wytham flux tower extent, averaged over areas contained within circular areas of radius 200 m, 300 m, and 400m centred on the flux tower location were calculated using ENVI 4.8 and the Spectral Analysis and Management System (SAMS)[1]. Figure 3-24 illustrates the mean value of the green vegetation spectrum covering visible and near-infrared wavelengths (VNIR) and computed mean red edge position, at 727±0.08 nm, using the first derivative (i.e. inflection point) of this spectrum.

The data shown in Figure 3-24, and theoretical considerations based on the known spectral properties of vegetation, provided the basis for selecting 20 of the existing 252 Eagle wavebands (Table 3-6). This process of feature selection greatly reduced the data volume (approximately from 1.5 GB to 550 MB) for the single flight line shown), without significant loss of information.

Feature selection was also used to obtain spectral reflectance values for selected narrowband VIs. Although most remote sensing has been based on broadband indices such as NDVI, there is some evidence that data acquired in selected narrow bands may provide a more direct link to the processes of photosynthesis (Rahman et al., 2001; Cho et al., 2007; Thenkabail et al., 2011). The Red Edge NDVI (also known as $NDVI_{705}$) and PRI (as given in section 1.5), two narrowband spectral indices of photosynthesis capacity and efficiency, respectively, were computed to test this.

1. The Spectral Analysis and Management System (SAMS), http://sams.projects.atlas.ca.gov/, as a Java application to manage field spectral data sets and analysis, which it can be also used for the AIS analysis.

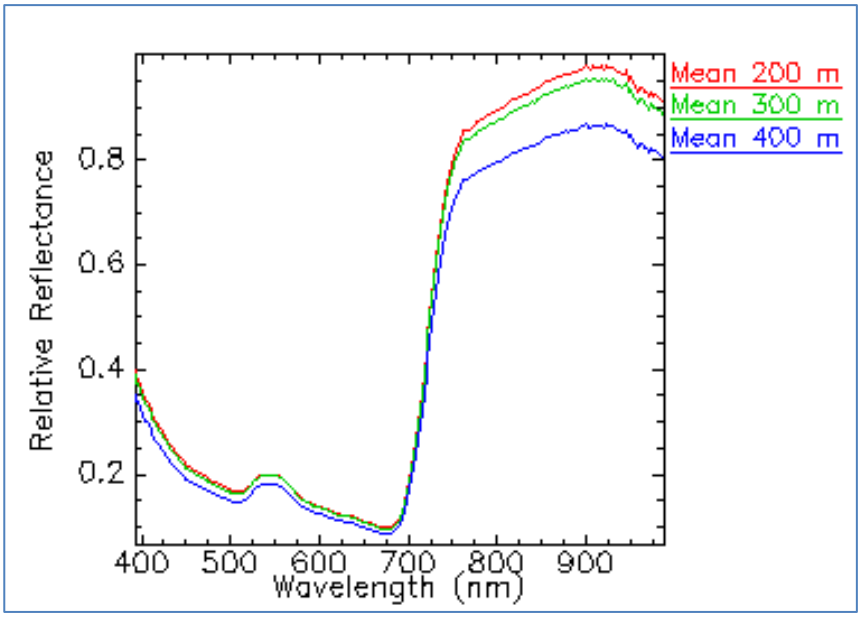

(a) Mean value of the vegetation spectrum

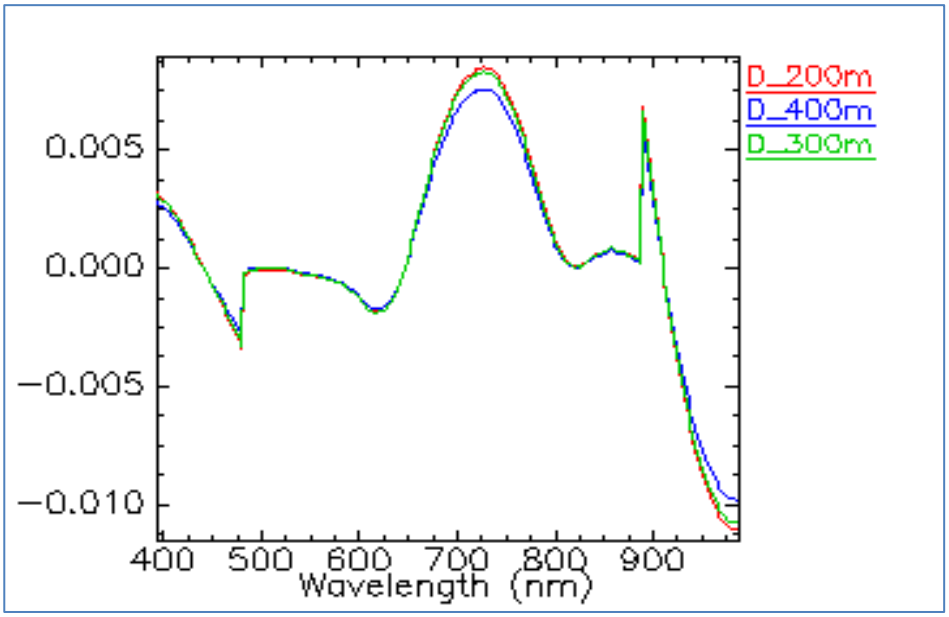

(b) First derivative of the vegetation spectrum, REP

Figure 3-24 Average of sampled spectra from the Wytham flux tower extent

Table 3-6 The 20-waveband selected from the AISA Eagle hyperspectral data of Wytham Woods flux tower extent based on woodland spectral signature

Band	Wavelength Centre (nm)	FWHM[1] (nm)	Comments
1	452.53	2.29	Theoretical Chlorophyll absorption
2	473.11	2.29	Blue center wavelength for calculating EVI
3	507.42	2.29	Minimum Blue-Green response due to chlorophyll absorption
4	530.29	2.29	Xanthophyll response of Green an indicator of photosynthesis
5	551.06	2.37	Maximum Green response, expected reference band for PRI
6	570.05	2.37	Expected reference band for PRI at canopy level
7	641.26	2.38	Theoretical Chlorophyll absorption
8	655.54	2.38	Red center wavelength for various vegetation index, e.g. NDVI
9	662.69	2.38	Theoretical Chlorophyll absorption
10	681.73	2.38	Maximum Red response due to chlorophyll absorption
11	710.35	2.39	Low-point of red edge
12	727.08	2.39	Mean-point computed REP for woodland coverage
13	739.02	2.39	High-point of red edge
14	750.98	2.42	Start-point of NIR plateau
15	775.35	2.42	Maximum response of early NIR Plateau
16	802.15	2.43	Maximum response of early NIR Plateau
17	828.95	2.43	NIR plateau wavelength for various vegetation index
18	865.42	2.43	Mid-point of NIR plateau
19	906.76	2.43	NIR plateau wavelength for various vegetation index
20	923.82	2.44	Maximum response of NIR plateau

[1]. Full Width at Half Maximum (FWHM)

The Red Edge NDVI is the modified normalized difference of brightness values from the spectral position between the Red and NIR wavelengths where the maximum slope is found (Gitelson and Merzlyak 1994; Sims and Gamon 2002). This index can be used to identify spatial variability of canopy foliage content, and monitor vegetation status. The equations for the calculation of Red Edge NDVI and PRI are the same (structurally) as the equation for the traditional NDVI given by following equations. 3

$$NDVI_{705} = R_{750} - R_{705}/R_{750} + R_{705}$$

$$PRI = R_{531} - R_{570}/R_{531} + R_{570}$$

Although, the value range of both indices varies between ± 1, the common range for green vegetation is 0.2-0.9 for $NDVI_{705}$ and ± 0.2 for PRI. As Figure 3-25 shows, the distribution of these indices is relatively normal with a mean value of 0.5402 for $NDVI_{705}$ and 0.0639 for PRI.

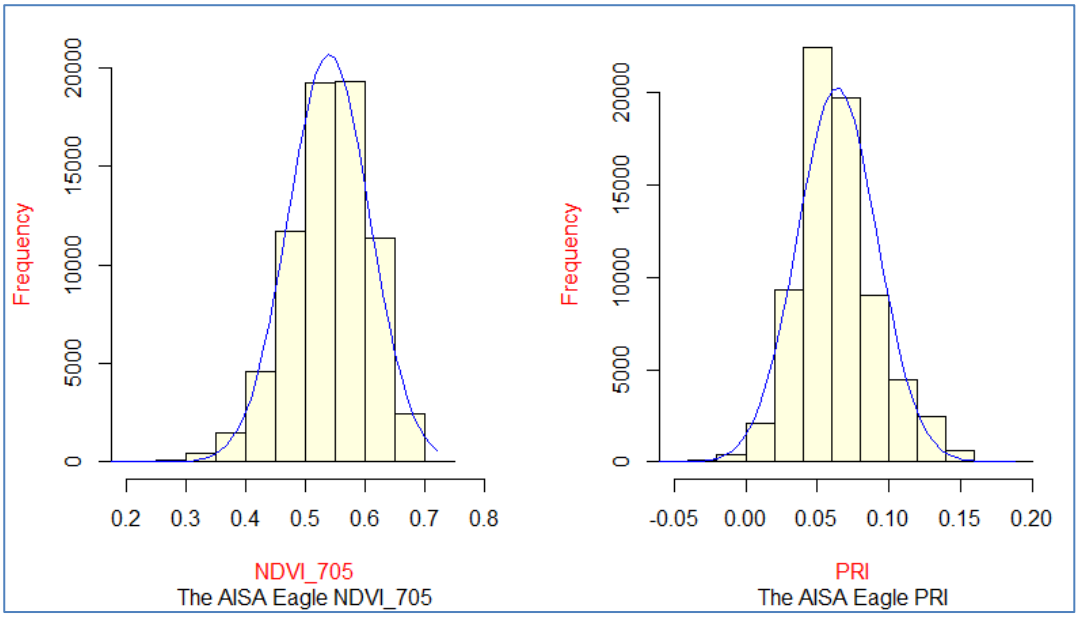

Figure 3-25 Frequency distribution of spectral indices Red Edge NDVI and PRI

An alternative, statistically-based method of feature selection involved inspection of the correlation matrix between all 252 wavebands (Figure 3-26). This showed that the AISA data fell into two main groups: (a) visible region approximately from 400 nm to 690 nm; and (b) near-infrared region around 750 nm upwards. The spectral region of visible wavebands (i.e. top-left of correlation matrix) was also divided into two groups: the Blue region nearby 400 – 500 nm was separated from Green-Red wavebands roughly between 500 nm and 690 nm. This may be as a result of the errors in the flat field calibration in the shorter Blue wavelengths, less than 450 nm (Figure 3-22). In addition, two transitional wavebands can be recognized as the wavelength position of the red edge approximately from 690 nm to 750 nm, and the wavelength position of the "*epoxidation*" state of xanthophyll pigments (i.e. 500 -550nm) that expresses the short-term variation in the photosynthesis performance.

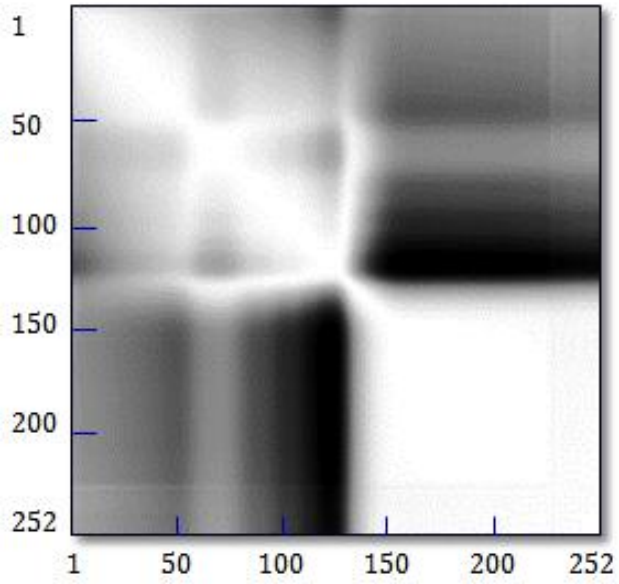

Figure 3-26 Correlation Matrix of the AISA Eagle's original bands
(X *and* Y *axis indicate band number*; *White*: ± 1 *and Black*: 0)

Accordingly, the AISA Eagle wavebands were partitioned into three spectral subsets, as given in Table 3-7, based on theoretical considerations and the computed correlation matrix. In some ways this "data-based" method was more objective than the first "knowledge-driven" method, which relied on visual inspection and prior knowledge.

Table 3-7 Three subsets of selected AISA Eagle Data for Feature Extraction

Spectral Subset	Wavelength (nm)	Number of Band
Visible	452.53 – 681.73	10
Red Edge	710.35 – 750.98	4
Near-Infrared	775.35 – 923.82	6

3.2.2.5 Feature Extraction

Feature extraction was applied to the AISA Eagle dataset to transform the original hyperspectral data into more informative new features for the purpose of assessing the spectral response of the plant canopy and its spatial structure.

3.2.2.6 Principal Component Analysis (PCA)

Principal Component Analysis (PCA), also known as PC rotation, is a useful statistical technique for finding patterns in data of high dimension, which may better capture the essential information. In the remote sensing context, PCA is a linear transformation of a multivariable dataset (i.e. typically, the different wavebands of a multi- or hyperspectral image) into a new coordinate system, which results in fewer orthogonal or uncorrelated features, called principal components (PCs). PC rotation uses the mathematical concepts of eigenvalues and eigenvectors, and is achieved by projecting the original image data onto a transformation matrix based on the eigenvalues and eigenvectors of the covariance matrix of the dataset (Tso and Mather 2001). A detailed description of the mathematical procedures used to derive principal components is outside the scope of this research, see Mather (2004) and Lillesand et al. (2008) for an explanation of the PC transformation procedure.

A standard form of the PC rotation may be computed by using the correlation matrix. The correlation matrix is equivalent to a covariance matrix for an image where each waveband has been standardized to zero mean and unit variance. Many investigations have reported on the robustness of standardization in this approach due to improved interpretability (Byrne et al., 1980), more precise classification (Conese et al., 1988) and the isolation of seasonal effects and variability caused by noise (Eastman and Fulk, 1993).

Despite the effectiveness of the PC rotation approach for dimensionality reduction, this technique is an inappropriate method for feature extraction of the AISA data, particularly for supervised classification applications (Jia and Richards, 1999; Tsai et al., 2007). The primary reason is that the technique is based on global statistics, which may neglect local variance that may be useful for detecting plant canopy variation. If conventional PC rotation is applied to the entire dataset, variances among both vegetated and non-vegetated pixels influence the transformation matrix. Consequently, the PC rotation will possibly extract features for separating major types of land cover instead of discriminating the subtle differences within the forest canopy that are the subject of this research. Subtle features that are useful for discriminating a specific canopy type will be pushed back to lower order PCs (Tsai et al., 2007). Finally, despite all the efforts to eliminate the impacts of undesirable variation in the AISA Eagle data (i.e. calibration effects due to solar spectrum curve and atmospheric attenuation which impose spectral weighting), conventional PC rotation is often dominated by a specific spectral region (Jia and Richards, 1999). In this aspect, Jia and Richards (1999) investigation on classification techniques for hyperspectral remote sensing data showed that selecting highly correlated spectral bands can increase the efficiency of this method. As illustrated in Figure 3.26, correlations between neighbouring spectral bands in either the visible or near-infrared region of the AISA Eagle data are larger than for bands further apart. The efficiency of PC rotation will be increased by separating the small correlations from the highly correlated groups, which leads to the notion of 'spectrally segmented PCA' as a means of extracting variation among different plant canopy types.

The procedure of spectrally-segmented PCA (SS-PCA), for detecting plant canopy variation within a temperate mixed forest is depicted in Figure 3-27. To prevent subsequent PC rotation due to variances between vegetated and non-vegetated areas, a vegetation index (e.g. NDVI) with a certain threshold was computed to filter out non-vegetated areas from the image. To determine the most suitable threshold, masking results of different values of NDVI were compared with an aerial image acquired by the NERC ARSF at the time of the AISA Eagle imagery (i.e. 9th September 2009). The value of 0.4 was found to be the most suitable cut off for separating forested coverage in the study area. Secondly, the selected hyperspectral data were segmented into three highly correlated subsets. Finally, the standardized PC rotation was conducted independently on each spectral subset.

The primary goal of this procedure was to compress all the spectral information contained in the original dataset into fewer components that provide significant features of the plant canopy structure and composition (Blackburn and Milton, 1997; Kauth and Thomas, 1976).

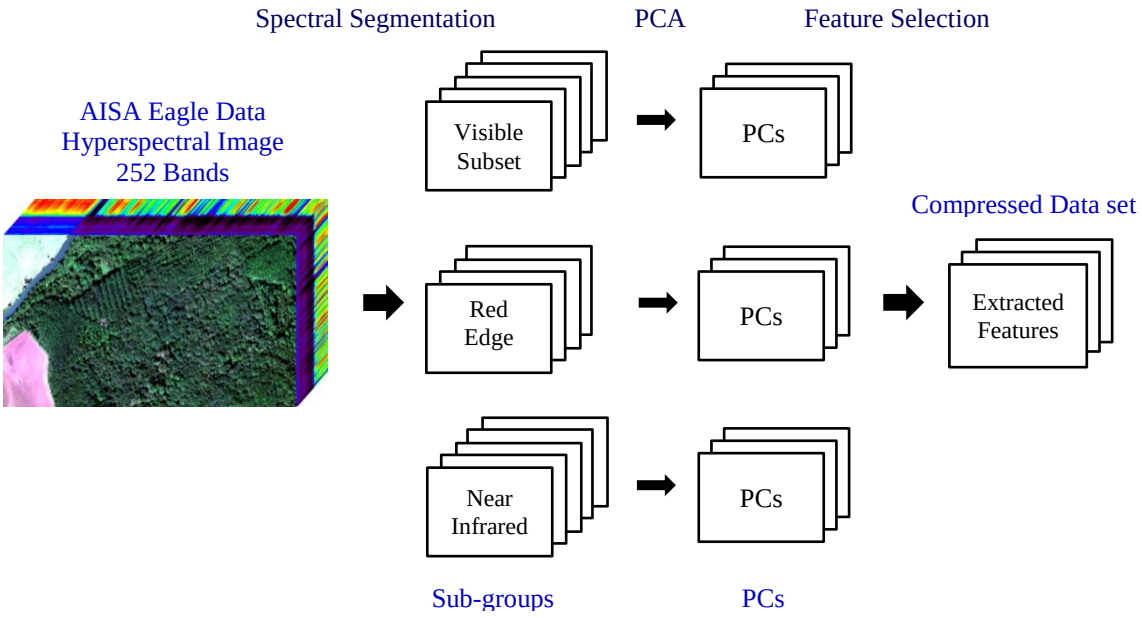

Figure 3-27 Schematic follow-diagram of multistage spectrally segmented PCA

The first three principal components of both visible and red-edge spectral subsets were adequate to delineate the differences in the characteristics of the AISA Eagle imagery, whilst visual interpretation and the eigenvalues suggested that only the first component was important for the near infrared subset (Figure 3-28). Therefore, these spectrally multivariate features that represent more than 99% of the variance in the original image data were used to investigate the spectral-spatial variability in the photosynthetically active plant canopy. Figure 3-29 shows the principal component values for this dataset. As illustrated in Figure 3-30, PC1 expresses the majority of the variance in the original subset, 95.09% for Visible-PC1, 94.81% for RE_PC1, and 99.77% for NIR-PC1. In addition, PC1 and PC2 explain statistically almost all of the variance in the spatial subset (i.e. more than 99%). This compression of image information in the first components of the AISA Eagle dataset is typical and as expected. The PC4 images for both visible and red-edge subsets contain no useful information, and neither does PC3 for the NIR.

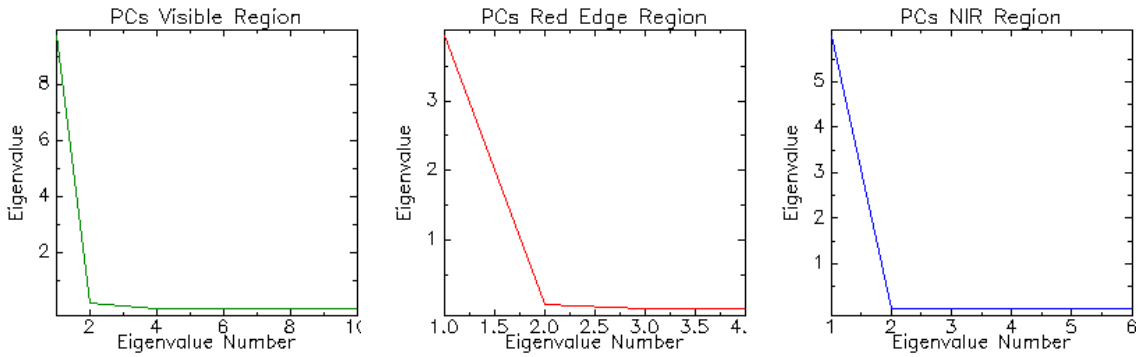

Figure 3-28 Principal Component Eigenvalues for Spectrally Segmented PCA of the AISA Eagle Data, (a) Visible PCA, (b) Red-Edge PCA, and NIR PCA

Table 3-8 shows the eigenvectors resulting from PC rotation of the original bands in the visible wavelengths. The eigenvectors for the first principal component (PC1) reveal moderately negative contributions from all selected spectral bands in the visible region. Thus, PC1 was interpreted as the overall 'darkness' of the image. This means, an increase in DN values in all bands will cause a reduction in PC1, observed as a darker grey tone in the image (Figure 3-29). The second principal component (PC2) is positively weighted on green wavelengths (i.e. 530.29 nm as a spectral index responding to change in the xanthophyll cycle through fluctuation in

this wavelength, 551.06 nm maximum green responses to chlorophyll, and 570.05 nm). On the other hand, PC2 is negatively weighted on blue (i.e. 452.53, 473.11, and 507.42 nm) and red (i.e. 641.26, 655.54, and 681.73 nm) wavebands. The eigenvectors show that PC2 is dependent upon the contrast between reflectance in blue, green and red wavelengths due to chlorophyll absorption in the visible region, analogous to the 'greenness' described by Kauth and Thomas (1976). Higher chlorophyll means greater green reflectance and less blue and red, causing an increase in PC2. The boundary wavelengths, 507.42 and 641.26 nm are quite weakly weighted, which suggests PC2 is caused by a spectrally selective effect[1]. The eigenvectors for the third principal component (PC3) reveal a large negative weighting on 453.53 nm, then progressively smaller on 473.11 nm, and then moderately positive through green and especially in red wavebands. This suggests that PC3 is responding to the amount of red light reflected, relative to that in the blue. The PC3 corresponds to the balance of red-blue.

Table 3-8 Eigenvector matrix of visible PCA

Wavelength (nm)	452.53	473.11	507.42	530.29	551.06	570.05	641.26	655.54	662.69	681.73
PCs[2]	Blue Region			Green Region			Red Region			
PC1 (97.01%)	-0.32	-0.32	-0.32	-0.31	-0.31	-0.31	-0.32	-0.32	-0.32	-0.31
PC2 (99.03%)	-0.13	-0.14	-0.03	0.45	0.54	0.40	-0.12	-0.25	-0.31	-0.37
PC3 (99.09%)	-0.60	-0.49	-0.26	0.04	0.11	0.14	0.28	0.27	0.27	0.27

Table 3-9 shows the eigenvectors resulting from PC rotation of the original wavebands from the red-edge region. The first feature of PC rotation for red-edge region (RE-PC1) is positively weighted on all the wavebands. It is responsive to change in physical processes that influence total reflectance, analogous to the 'brightness' described by (Kauth and Thomas, 1976). The eigenvectors show that the RE-PC2 is positively and then negatively weighted on the selected low-point (i.e. 710.35 nm) and high-point (i.e. 739.98 and 750.98 nm) of the red-edge wavelength, respectively, while there is no effect on the mean-point (i.e. 727.08

[1]. An eigenvalue close to zero means no effect.

[2]. Percentages indicate the eigenvalue associated with each principal component

nm) computed red edge position for woodland coverage. The RE-PC2 is dependent upon the contrast between boundary reflectance between Visible-RE and RE-NIR wavelengths due to chlorophyll absorption. The eigenvectors of the third red-edge principal component (RE-PC3) reveals an interesting pattern of loading on wavelength 727.08 nm (i.e. large negative weighting), which is located on mean value of the Red Edge Position (REP) computed for woodland coverage of the study area (as illustrated in Figure 3-25-b). RE-PC3 represents certain features that were obscured by the more dominant pattern shown in RE-PC2. For example, different trees composition is clearly defined in the woodland portion of the RE-PC3 image, (i.e. appearing as bright canopy crowns in Figure 3-30). In fact, the tonal reversal in the RE-PC2 and -PC3 illustrates the lack of correlation between these components.

Table 3-9 Eigenvector matrix of Red-Edge PCA

Wavelength (nm)	710.35	727.08	739.98	750.98
PCs	Red-Edge Region			
PC1 (98.31%)	0.48	0.51	0.51	0.50
PC2 (99.97%)	0.79	0.08	-0.31	-0.53
PC3 (100.00%)	0.38	-0.74	-0.14	0.54

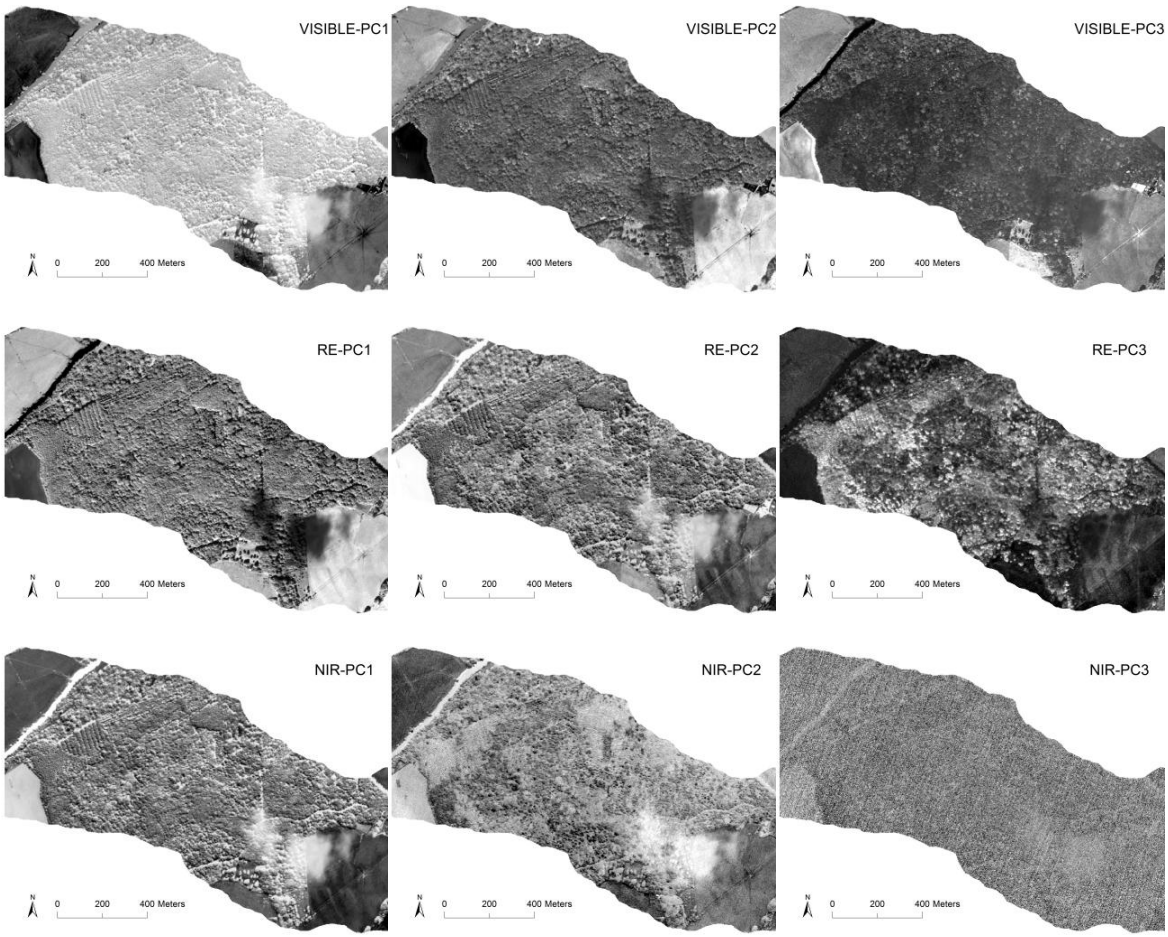

Figure 3-29 Transformed data resulting from PCA of the AISA Eagle imagery

In summary, the spectrally segmented PCA resulted in a reduced set of spectral features, each with plausible physical explanations:

- Feature 1: PC2 from the visible subset, an index of canopy greenness due to plant pigments.
- Feature 2: PC3 from the red edge region, an index related to the shape of the red edge and, therefore, indicative of processes involved in the transition from absorption by plant pigments and enhanced scattering within plant leaves.
- Feature 3: PC1 from the NIR region, an index of reflectance in this region which is known to be strongly controlled by multiple scattering within leaves and, therefore, responsive to canopy structure.

Figure 3.30 shows an RGB composite of these features which may be used for visual interpretation of vegetation patterns within the forest.

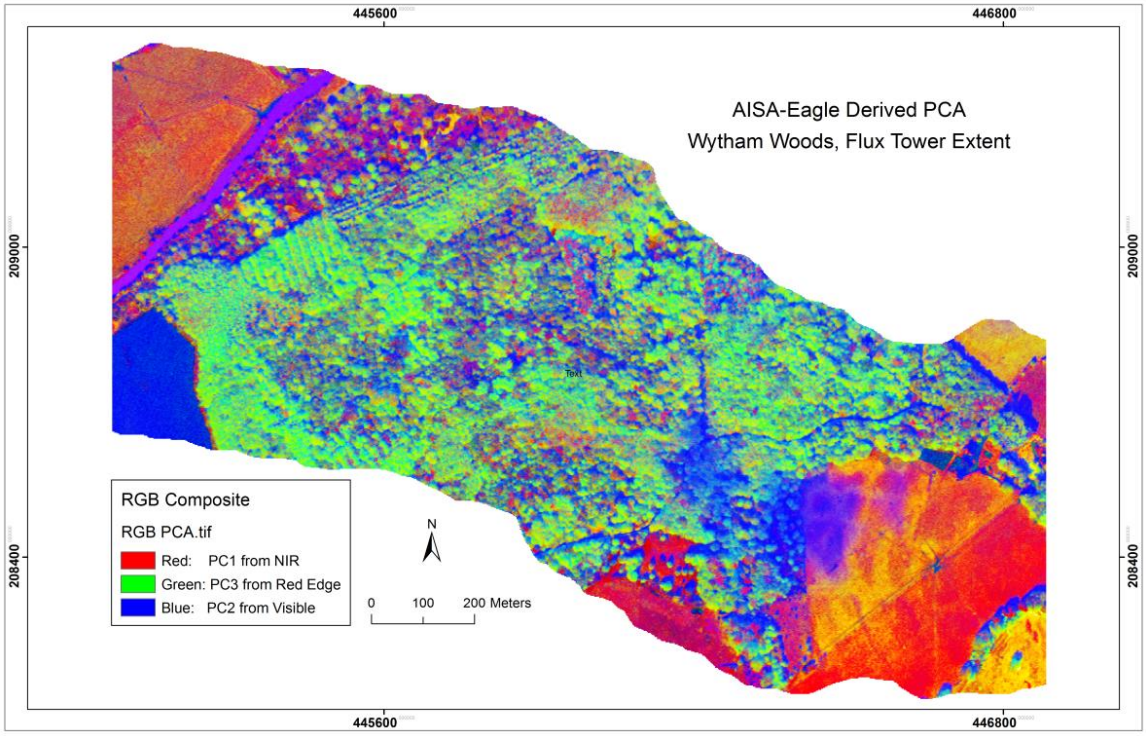

Figure 3-30 Extracted Features based on the SS-PCA for the Wytham flux tower site.

3.3 Discussion

This chapter aimed to familiarise the author with the UK study area and data sets available, and to add to the evidence base concerning the relationships between photosynthetically active canopy and the spectral indices reviewed in Chapter 1. The LiDAR data was used to characterise the spatial patterns of vegetation and the vertical structure of the canopy around the EC tower on various dates during the growing season. This enabled an investigation of the effect of weather conditions on the modelled flux footprint and the relationship between this and vegetation indices measured by MODIS. It was concluded that, despite the small size and spatial variability of the Wytham Woods site, the data from both the EC tower and the MODIS satellite sensor were reliable and representative of the overall condition of the forest on the dates for which remotely sensed data were available in 2010. Over the whole season, Wytham Woods was found to be acting as a net carbon sink. The MODIS EVI was found to estimate GPP slightly more accurately than NDVI.

The second part of Chapter 3 considered the role of airborne imaging spectrometry in providing more information from a heterogeneous forest canopy. In addition to having fine spatial resolution, imaging spectrometry provides many spectral bands and thus allows simulation of many different remotely sensed indices, including those thought to be related to ecological processes, not just canopy state. The AIS data required considerable pre-processing, and the data volume would have become unmanageable for any site larger than Wytham Woods. As part of the investigation of the AIS data, feature selection and feature extraction were used to reduce the dimensionality of the data set and this was useful in enabling informative images of the forest canopy to be produced. Although these were helpful later on in the study as a means of classifying the various areas within Wytham Woods, they were largely subjective and not transferrable to other areas, and for this reason AIS was ruled out as the primary remote sensing system for the main study. Instead, attention was directed towards satellite sensors that had spectral bands comparable to MODIS, but provide data more frequently and with

finer spatial resolution. One system stood out as a strong contender in this respect: the DMC satellite constellation operated by DMC International Imaging [http://www.dmcii.com/].

Although AIS was felt to be unsuitable for operational use over large areas, it was clear that it was uniquely suited to simulation studies and to investigating up-scaling from very small areas (a few square metres) to an area the size of a MODIS or DMC pixel. With this in mind, a study was conducted using an established, highly-regarded forest canopy radiation model (FLIGHT) and the AIS data from Wytham Woods and this is described in the next chapter.

4. Sensitivity Analysis of Vegetation Indices derived from a Mixed Forest Canopy

4.1 Introduction

Satellite-based sensors are a vital source of data on the productivity of vegetation at global scales, and in recent years much effort has gone into the validation of such data to provide confidence in the information provided. Remotely sensed data in the optical region (400-2400nm) can potentially provide information on plant processes such as the rate of photosynthesis (Flanagan et al. 2012; Gamon et al. 2005; Gamon et al. 1992; Sellers et al. 1992) , the amount of vegetation (Ahl et al. 2006; Berry et al. 2007; Carlson and Ripley 1997; Cochrane 2000; Sellers 1987; Tucker 1979) and the type of vegetation (Desai et al. 2008; Gamon et al. 1995; Xie et al. 2008) present. The combination of remotely sensed data with meteorological and other data provides a method to estimate vegetation productivity (and hence CO_2 flux) in the areas not measured by the sensors in the global flux tower network known as FLUXNET (Desai et al. 2005; Desai et al. 2008; Drolet et al. 2008; Heinsch et al. 2006; Hill et al. 2006; Melaas et al. 2013; Ruimy et al. 1996; Xiao et al. 2012; Yan et al. 2009; Yuan et al. 2007). The combination of tower-based sensors providing highly accurate data at fine temporal resolution with satellite sensors providing data over very large areas is the basis for several global scale remote sensing products such as the NASA MODerate-resolution Imaging Spectrometer (MODIS) Gross Primary Productivity (GPP) and Net Primary Productivity (NPP) products, MOD17 (Running et al. 2000; Running et al. 2004) and the European Space Agency (ESA) Earth Observation programme[1]. The effectiveness of this methodology depends, in large part, on the relationship between the measurements made from the towers and those made from space, and this is not straightforward to characterise. The FLUXNET estimates of CO_2 flux are derived

1. http://www.esa.int/Our_Activities?/observating_the_earth/

from measurements of gas exchange between the plant canopy and the atmosphere made using the Eddy Covariance (EC) method (Baldocchi 2008; Baldocchi et al. 2001; Burba and Anderson 2010a). This is a well-established and accepted method, but it is not without problems and limitations, notably missing data when the weather conditions are unsuitable and due to the variability in the area of canopy sensed (Chen et al. 2009a; Kim et al. 2006; Roujean et al. 1992; Schmid 2002). Remotely sensed data also contain errors and uncertainty due to sensor calibration drift (Brook and Dor 2011; Danson and Curran 1993; Milton et al. 2011; Smith and Milton 1999; Teillet 1986; Woodcock 2002), atmospheric conditions at the time of measurement (Gao et al. 2009; Richter 1996; Richter 2011; Schroeder et al. 2006; Song et al. 2001; Thome et al. 1998) and the geometry of illumination and viewing (Kennedy et al. 1997; Penuelas et al. 1995; Ranson et al. 1985; Roujean et al. 1992; San and Süzen 2011; Xiaowen and Strahler 1992). Furthermore, they are generally presented as vegetation indices (VI), rather than a physical quantity such as the photon flux and, therefore, the link with plant productivity is via a model rather than direct.

The uncertainty at the heart of global scale estimates of plant productivity becomes apparent if we consider the use of data from a single flux tower to validate an estimate of plant productivity from a single MODIS pixel (Figure 4-1). First, the three-dimensional (3D) canopy volume sampled by the two sensors is different. The area sampled by the instruments on the flux tower depends on the height of the tower, the canopy architecture and the weather conditions at the time of measurement. The projection of this volume onto a two-dimensional (2D) plane above the canopy is known as the flux tower footprint. In contrast, the 3D volume sampled by a MODIS pixel depends on the relationship between the canopy architecture and the sensor view geometry (i.e. azimuth and zenith angle) at the time of measurement. Second, the physical phenomena measured by the two sensors are different. The instruments on the tower measure gas fluxes using the EC method (Burba and Anderson 2010b), whereas the MODIS sensor measures the spectral radiance integrated over an instantaneous field-of-view, which is nominally 250 m by 250 m ignoring the adjacency effect (Running et al. 2000). The

spectral radiance depends on the composition of the pixel, which is determined both by the materials present (e.g. leaves, bark, understorey) and the geometry of illumination (e.g. shadow, scattering from surroundings). Vegetation indices (VI) are often used because they reduce the effect of many of these extraneous variables, but the fact remains that tower-based EC and satellite-based VIs measure different phenomena from different parts of the vegetation canopy.

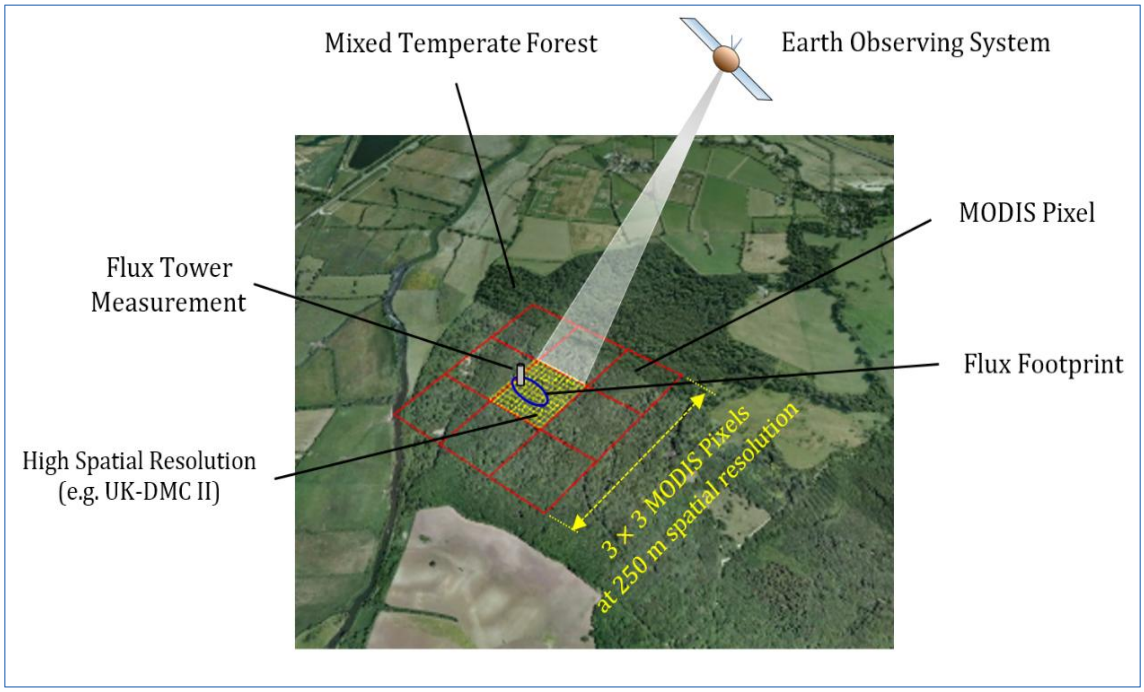

Figure 4-1 Uncertainty in global scale estimates of plant productivity obtained using flux tower measurements to validate MODIS products, showing the difference between the surface sampled from a tower and that seen by MODIS.

As mentioned previously, the main aim of the thesis is to explore spatial aspects of sampling from the tower-based CO_2 flux measurements and the satellite sensor observations. It is necessary to understand the source of measurement uncertainty in VIs, and how these extraneous variables might affect the VIs averaged over a flux tower footprint. In other words, the robustness of the VIs in the presence of uncertainty especially over a complex forest depends both on the reflectance of individual canopy elements and the spatial arrangement of the elements with respect to each other and to the sun-sensor geometry. The need to understand these effects has led some to investigate uncertainty in VIs over a heterogeneous

forest canopy at fine spatial resolution, and at different stages during the growing season. In this chapter, a light interaction model (a 3D model of light interaction in a forest, FLIGHT) is used to investigate the uncertainty in VIs from different canopy types drawn from an actual area of woodland in the UK, and determine how sensitive the VI signal measured above the canopy is to perturbing effects such as atmospheric, canopy structural and angular effects. This will provide a baseline for comparison with the uncertainty inherent in measurements made from flux towers (Chapter 5).

4.2 Methods

4.2.1 Preparation Data

As the aim of this chapter was to investigate the uncertainty in a range of spectral VIs at fine spatial scale, it was necessary to acquire detailed spectral reflectance data from the site. The most efficient way to acquire high quality hyperspectral data over the whole site was to use airborne imaging spectrometry, so data were obtained on several dates during 2009 using an Airborne Imaging Spectrometer for Applications (AISA) Eagle imaging spectrometer sensing in 252 narrow spectral wavebands, ranging from 392 nm to 987 nm (Table 4-1).

Table 4-1 The AISA Eagle data used in the research
(The data from each date comprised seven flight-lines flown in alternate directions)

Date (dd/mm/yyyy)	Day of Year	Time of Survey (UTC)	Solar Zenith Angle (°)	Flying Height (m)
16/03/2009	75	13:55	60.7	1,280
09/09/2009	252	13:10	49.3	1,353
25/09/2009	268	11:15	53.2	1,300

The AISA Eagle data were geometrically corrected using attitude data (i.e. roll, pitch and yaw) collected on-board the aircraft, transformed to the Ordnance Survey National Grid map projection using nearest neighbour resampling, and mosaicked to create a multi-date hyperspectral dataset with 2 m pixels covering the extent of Wytham Woods. The data were corrected for the effect of the atmosphere using FLAASH in ENVI Version 5.1, resulting in a multi-date fine resolution reflectance map of Wytham Woods (Figure 4-2).

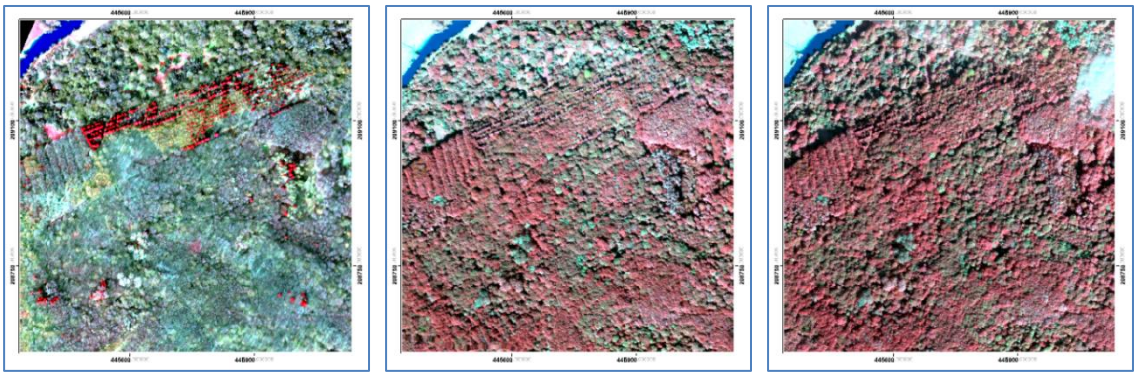

16th Mar. 2009 (Julian day: 075) 9th Sep. 2009 (Julian day: 252) 25th Sep. 2009 (Julian day: 268)

Figure 4-2 The NERC-ARSF Eagle Images
RGB (NIR: 744 nm, Red: 696 nm, and Green: 570 nm) (Adapted from NERC-ARSF, 2009)

Three VIs were computed from the AISA Eagle data acquired on each date, including the Normalised Difference Vegetation Index (NDVI) (Tucker 1979), the Atmospherically Resistant Vegetation Index (ARVI)[1](Kaufman and Tanre 1992), and the Photochemical Reflectance Index (PRI) (Gamon et al. 1997). The first two of these are commonly used to measure vegetation amount, for example Leaf Area Index (LAI), while the third has been proposed as an index of the rate of photosynthetic processes taking place within green leaves (Gamon et al. 1990; Gamon et al. 1992). The vegetation indices were computed as follows:

$$NDVI = R_{\mathrm{NIR}} - R_{\mathrm{Red}} / R_{\mathrm{NIR}} + R_{\mathrm{Red}} \qquad \text{Equation 4-1}$$

$$\begin{cases} ARVI = R_{\mathrm{NIR}} - R_{\mathrm{RB}} / R_{\mathrm{NIR}} + R_{\mathrm{RB}} \\ R_{RB} = R_{Red} - \gamma (R_{Blue} - R_{Red}) \end{cases} \qquad \text{Equation 4-2}$$

$$PRI = R_{531} - R_{570} / R_{531} + R_{570} \qquad \text{Equation 4-3}$$

where "R_{Blue}", "R_{Red}"and "R_{NIR}" indicate the reflectances in the blue, red and near-infrared wavelengths, respectively; while "R_{531}" refers to carboxylation reflectance at 531 nm and "R_{570}" indicates reflectance at an insensitive reference band (Gamon et al. 1997). At high light intensity when there is excess light, the energy must be dissipated to avoid damage to the photosynthetic organism, which results in dissipation of excess energy in the pigment bed associated with photosynthesis.

1. The"γ"constant is a weighting function that depends on the aerosol type. In the absence of the aerosol model, a good value is "$\gamma = 1$".

This change in pigment composition leads to a decrease in reflectance at 531 nm, but has little effect at 570 nm. In other words, at low intensity of light, when most light is used for photosynthesis the PRI has a high value. Figure 4-3 shows each image of these VIs on each of three dates: 16th March (leaf-off), 9th September (leaf-on) and 25th September (early autumn).

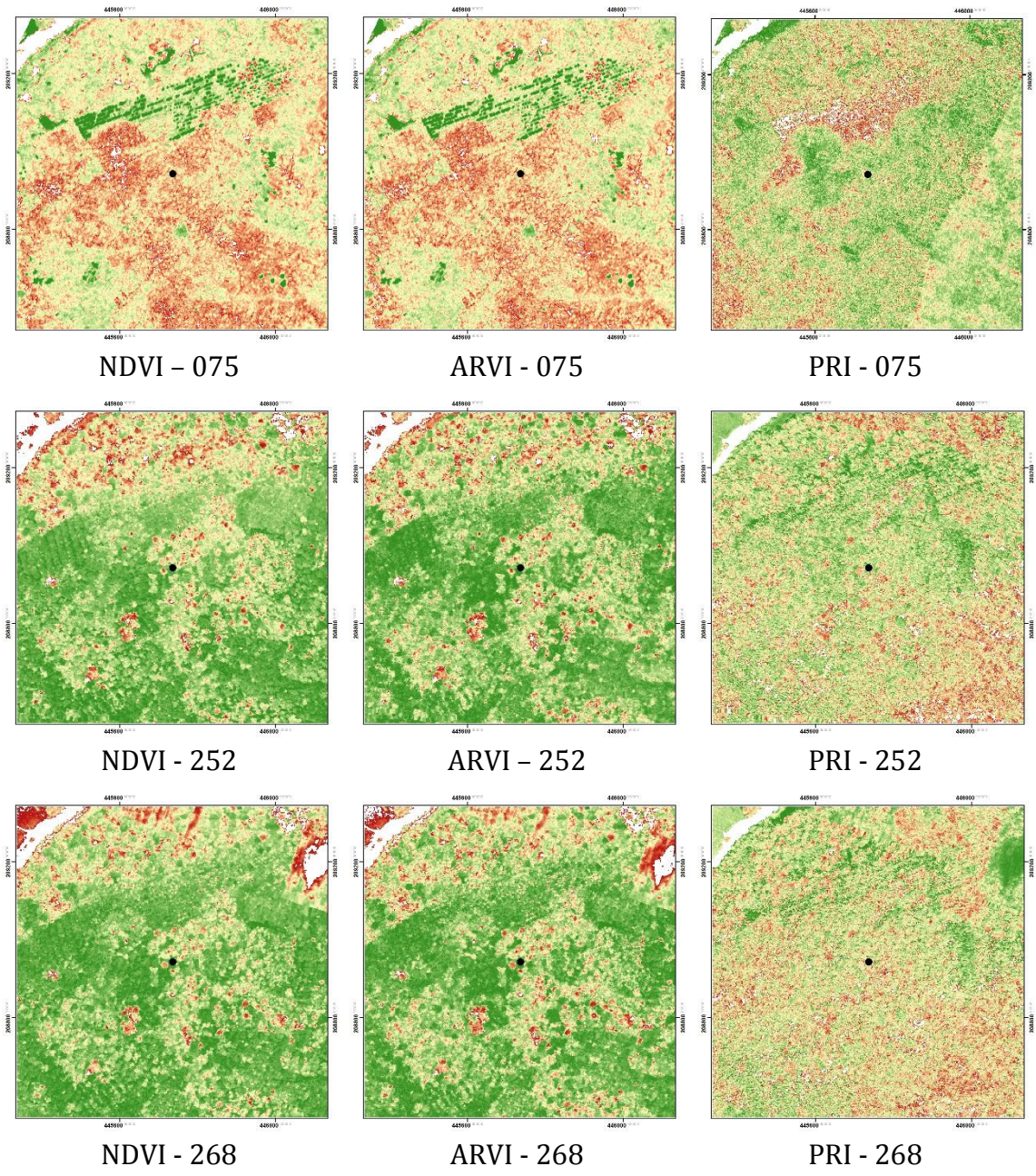

Figure 4-3 The AISA Eagle-based VIs on each of three dates: 16th March (top) (leaf-off), 9th September (middle) (leaf-on) and 25th September (bottom) (early autumn)

Airborne Light Detection and Ranging (LiDAR) data were also acquired during most of the flights using a fine-resolution airborne laser scanner, Optech ALTM 3033. The point data were used to produce maps of various ecological properties, primarily, the leaf-on first return DSM and the leaf-off last return DTM, normalized Canopy Height (nCH) and canopy roughness. These data were used to quantitatively describe the vertical distribution and configuration of the forest components in support of the canopy classification.

Aggregated data of hyperspectral and LiDAR data were to be used to create a realistic 3D model of the woodland which could then be used to study how variation in the conditions of measurement affected each of three mentioned VIs. Both the spectral and the spatial data were acquired with fine spatial resolution (2m pixels) to provide many observations within a pixel of a typical satellite-based sensor which would be used for operational forest monitoring (e.g. the DMC system, 22 m pixels). Although such fine spatial resolution was necessary to resolve the intra-canopy variability, it meant that simulating the whole of Wytham Woods within the FLIGHT model became impossible, so it was necessary to base the analysis on smaller rectangular areas of pixels, referred to as *'Blocks'* in the further analysis. Each block was chosen as representative of a particular plant functional type (PFT), based on a spectral-spatial classification of the whole extent of Wytham Woods.

Figure 4-4, in general, depicts the steps involved in this chapter, including multi-date AISA Eagle and LiDAR used as the primary data, pre-processing of the AISA Eagle and LiDAR, generation of 3D reflectance map, classification and extraction of PFT blocks for running the FLIGHT model in terms of varying those parameters that affect canopy reflectance.

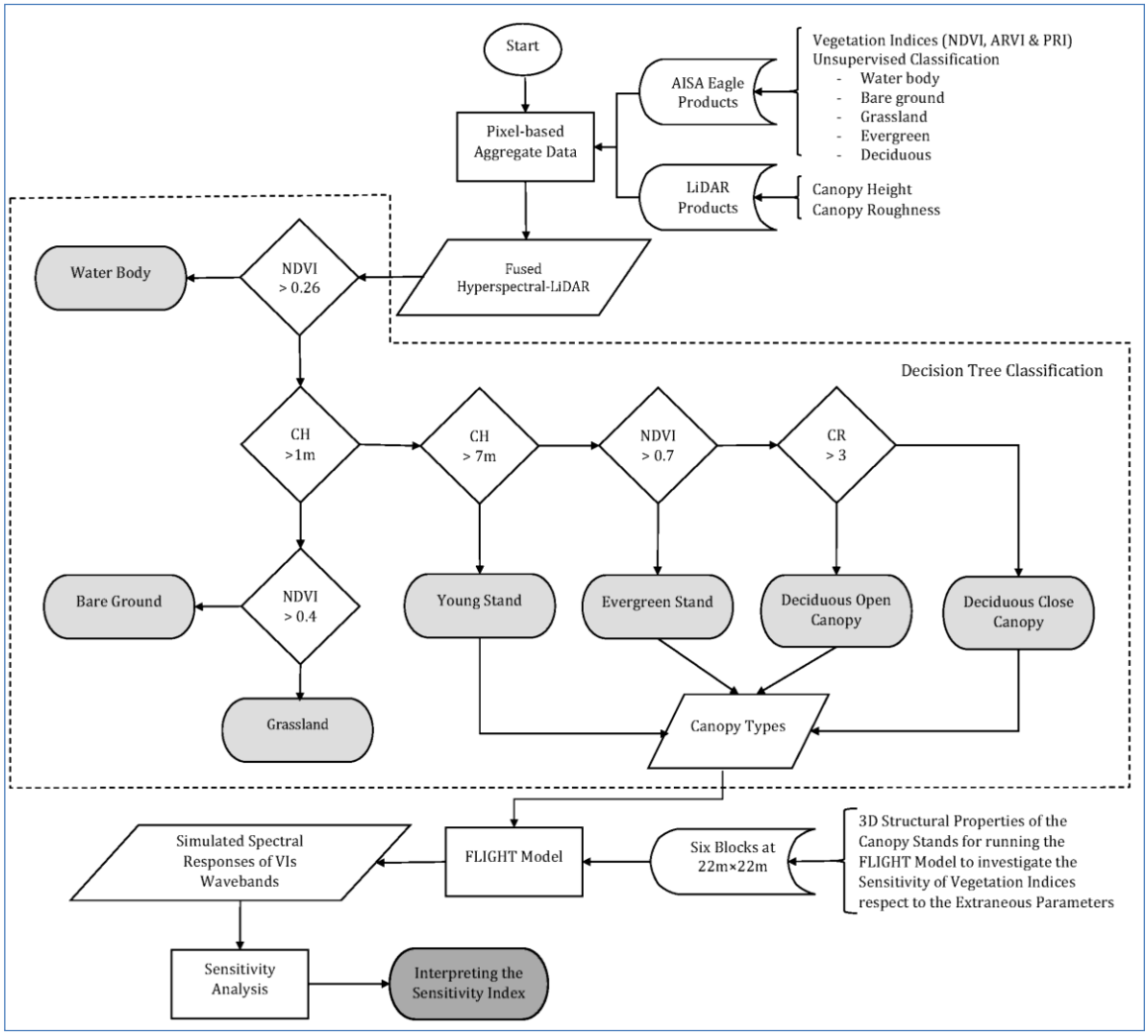

Figure 4-4 Flow diagram showing the process used to define PFT blocks, and to investigate the sensitivity of vegetation indices in terms of the extraneous parameter using FLIGHT Model

4.2.2 LiDAR-based Canopy Structure

The mean canopy height was computed as the mean of all individual normalized height values of LiDAR points ($\boldsymbol{h_i}$) within the cell ($\boldsymbol{n}$ is number of LiDAR points in each cell). Canopy roughness calculated as the standard deviation[1] of the vegetation heights, was found to best capture the variability of the canopy structure and accurately distinguished open and close canopies (Antonarakis et al. 2008). To map the canopy structure, the selected spatial resolution was 2 m, the approximate horizontal accuracy of leaf-on acquisition relying upon point spacing assessment, roughly 0.55. This was done by dividing all of the point data into 2 m grid cells and analysing the data statistically within each cell. Furthermore, LiDAR data obtained during leaf-off conditions (16th March) were used to classify deciduous versus evergreen stands.

$$\bar{h} = \frac{\sum_{i=1}^{n} h_i}{n} \qquad \text{Equation 4-4}$$

$$sd = \sqrt{\frac{\sum_{i=1}^{n} (h_i - \bar{h})^2}{n-1}} \qquad \text{Equation 4-5}$$

The vertical accuracy was estimated using flat areas of bare ground. Within the study area, numerous separate bare ground locations were distributed among multiple flight lines. Initial field investigation of the study site found that the canopy cover was variable from low to high and open to close throughout the study area, exposing a heterogeneous landscape. In summary, the following metrics were computed to be used for different canopy types and forest stand classes: (a) vegetation height assigned to growing stages (ecological succession); (b) percentage of vegetation cover in terms of top of canopy intensity; and (c) vegetation roughness with respect to variation in vegetation height values and percentage of canopy height (Figure 4-5 and Figure 4-6).

1. Standard deviation measures the height variation of LiDAR points around the mean height within each cell.

It is clear that the LiDAR derived nCM (Figure 4-5, ii) represents an approximately 17 m mean canopy height, buffered (400 m) in the region of Wytham Woods flux tower site. However, the height of all trees within sample blocks was calculated to provide the needed parameters of the FLIGHT model. The calculated surface roughness values ranged from near zero to approximately 15 m. Closed canopy, mature deciduous forested areas have a mean surface roughness value of more than 5 m, while the open canopies have a lower mean surface roughness of less than 2 m.

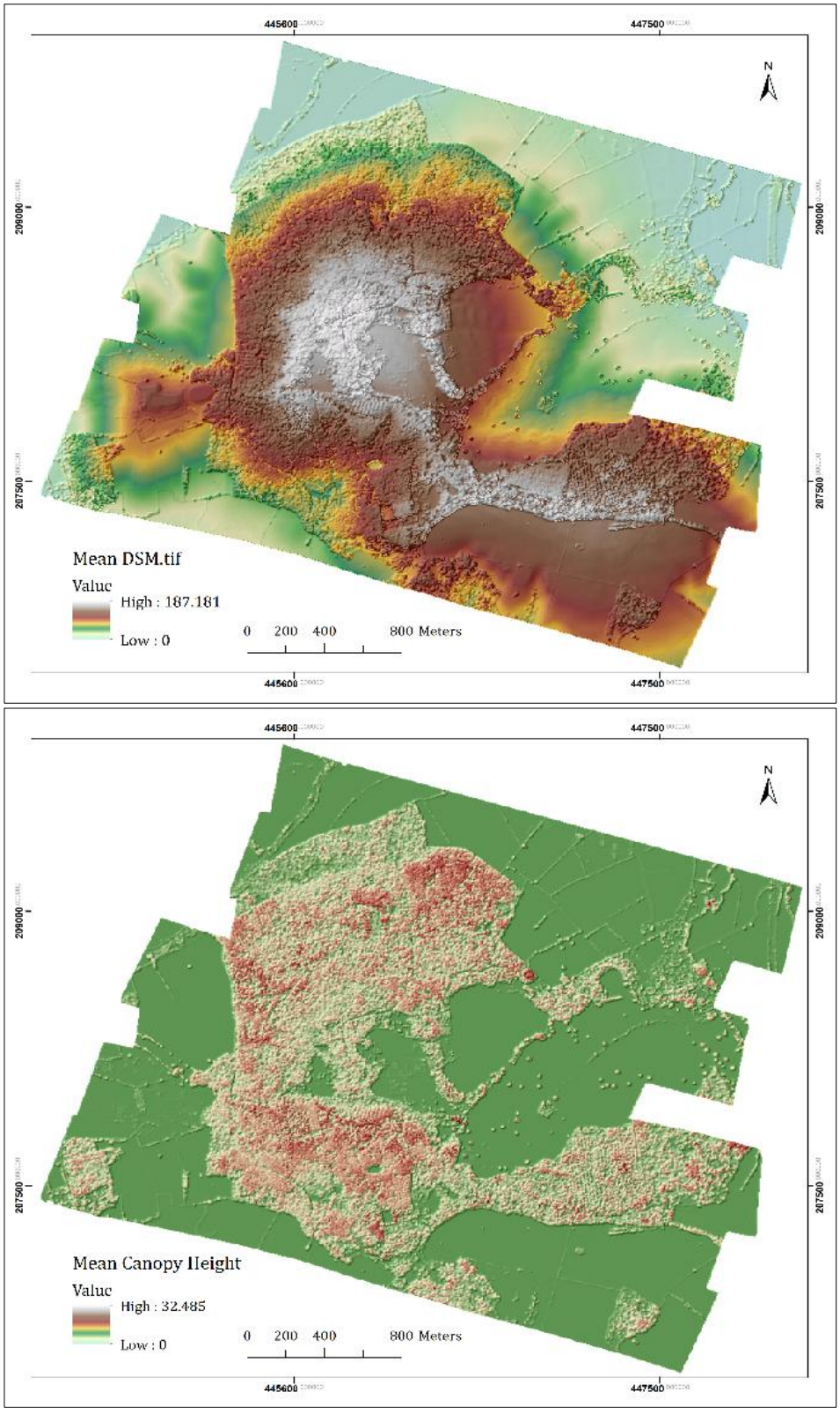

Figure 4-5 The LiDAR-based vertical distribution and configuration of the forest components: (i) top image shows DSM based on the leaf-on condition; (ii) bottom image depicts mean canopy height across Wytham Woods.

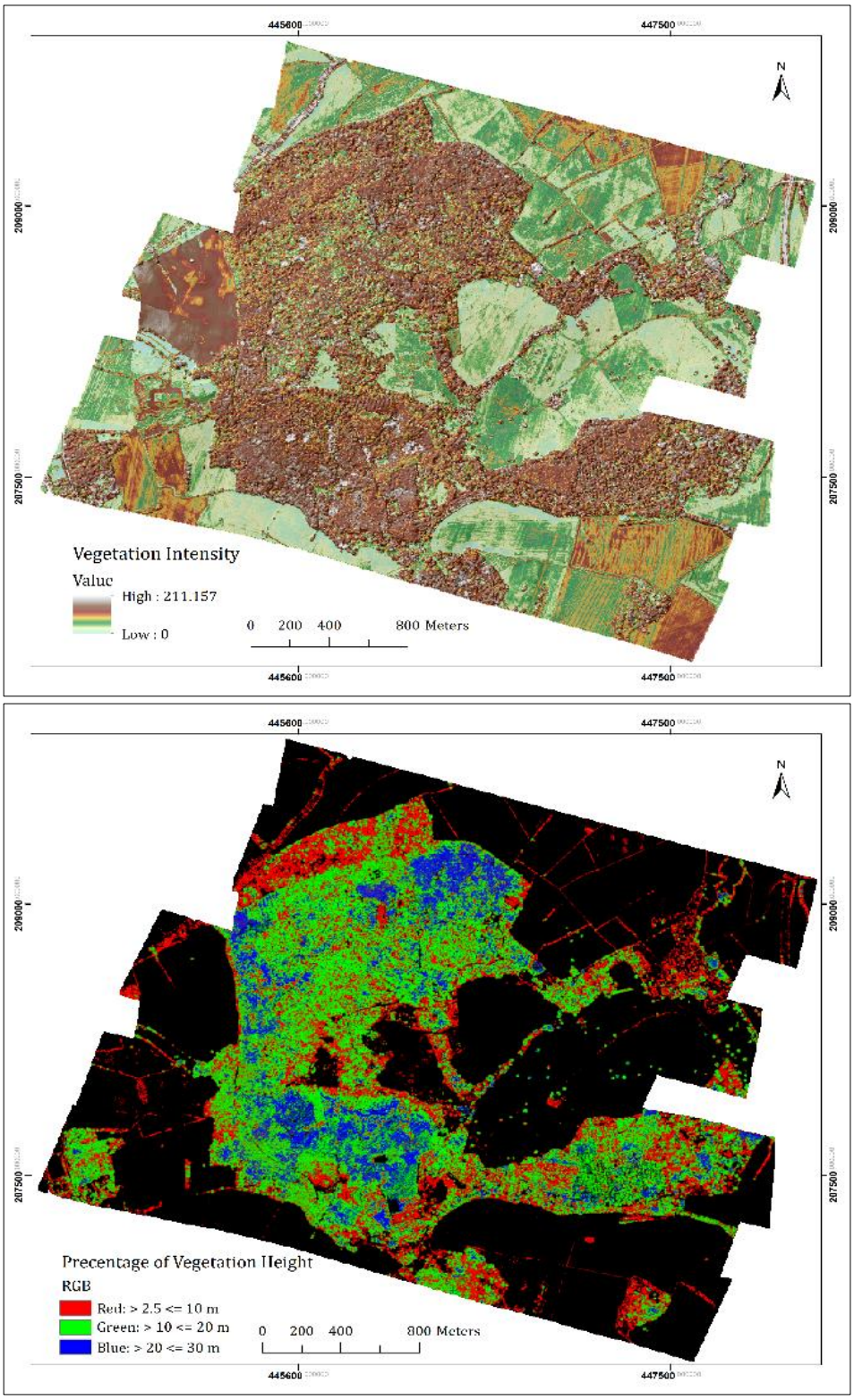

Figure 4-6 The LiDAR-based vertical distribution and configuration of the forest components: (i) top image represents vegetation intensity; and (ii) bottom images demonstrates vegetation stratification across Wytham Woods.

4.2.3 Mapping Plant Functional Types using Fusion of Hyperspectral and LiDAR Data

The combination of hyperspectral (i.e. reflectance and vegetation indices) and LiDAR data enabled a classification of Wytham's canopy which took into account both its spectral properties and the structure of the forest components. The canopy cover for this study was derived from structural attributes from LiDAR (i.e., canopy height and canopy roughness) and the selected wavebands from the AISA Eagle images (see Chapter 3, Table 3-6). The classification shows clearly the distribution of PFTs (trees, shrubs, grass) within the area of woodland which together determine the spectral response of a MODIS pixel. In this respect, initially, the AISA Eagle-based NDVI ("R_{Red}"and "R_{NIR} at 681.73 and 828.95 nm, respectively) was computed from both leaf-off (16th March 2009) and leaf-on (25th September 2009) reflectance values to distinguish coniferous from deciduous stands across the flux tower extent. Water and barren land were identified using both an unsupervised ISODATA classification of the AISA Eagle reflectance values and with NDVI<0.5 and NDVI<0.4, respectively. Open and closed canopies were, then, separated based on canopy roughness at heights corresponding to the top of canopy (1 m<CH<7 m as young stand and CH>7 m as mature forest stand). Finally, evergreen and deciduous forests were separated based the percentage of the AISA Eagle pixels classified as coniferous or deciduous stands (Figure 4-7). A decision tree classifier (i.e. ENVI Version 5.1) was applied using multistage classification, as described above, involving a series of binary decisions to allocate pixels (i.e. fused spectral VI with mean canopy height and canopy roughness) into classes of interest (Figure 4-7). In general, canopy type was classified based on the combination of NDVI and LiDAR products, and the result shows the distribution of PFTs within the area of woodland (Figure 4-7).

Accurate 3D reflectance map of a mixed forest based on the tree key dates during the growing season in 2009 were acquired to address the main question of the current chapter, namely, uncertainty in VIs in terms of measurement conditions. In the first part of this chapter, the results of applying decision-tree techniques to

mapping PFT across a mixed forest are presented to further analyse uncertainty in VIs. Specially, the preliminary results of mapping forest canopy types at 2 m spatial resolution were presented. Input data into the decision-tree model included VIs (e.g. NDVI over leaf-off and leaf-on periods in the growing season), and LiDAR-derived structural characteristics of the forest canopy. Using the decision-tree classifier, four canopy types were identified in training cases and mapped for further analysis. The overall accuracy of the canopy classification was 86.69% and the kappa coefficient was 0.81. Accuracy was higher in homogeneous stands across southern Wytham Woods and lower in areas with open canopy across ancient stands in northern woodland.

Overall, six canopy stands representing the dominated mixed forest were selected randomly for analysis across Wytham's flux tower extent using a 22 m × 22 m block to extract tree location and the structural properties of the stands, such as crown size and shape (e.g. cones for coniferous trees and ellipsoids for deciduous broadleaf trees), the number of tree locations in each block, and canopy height. To evaluate the predictive accuracy of the classifier, the DMC aerial photo was used as complementary metadata to the field survey using GPS points (IPCC, 2014).

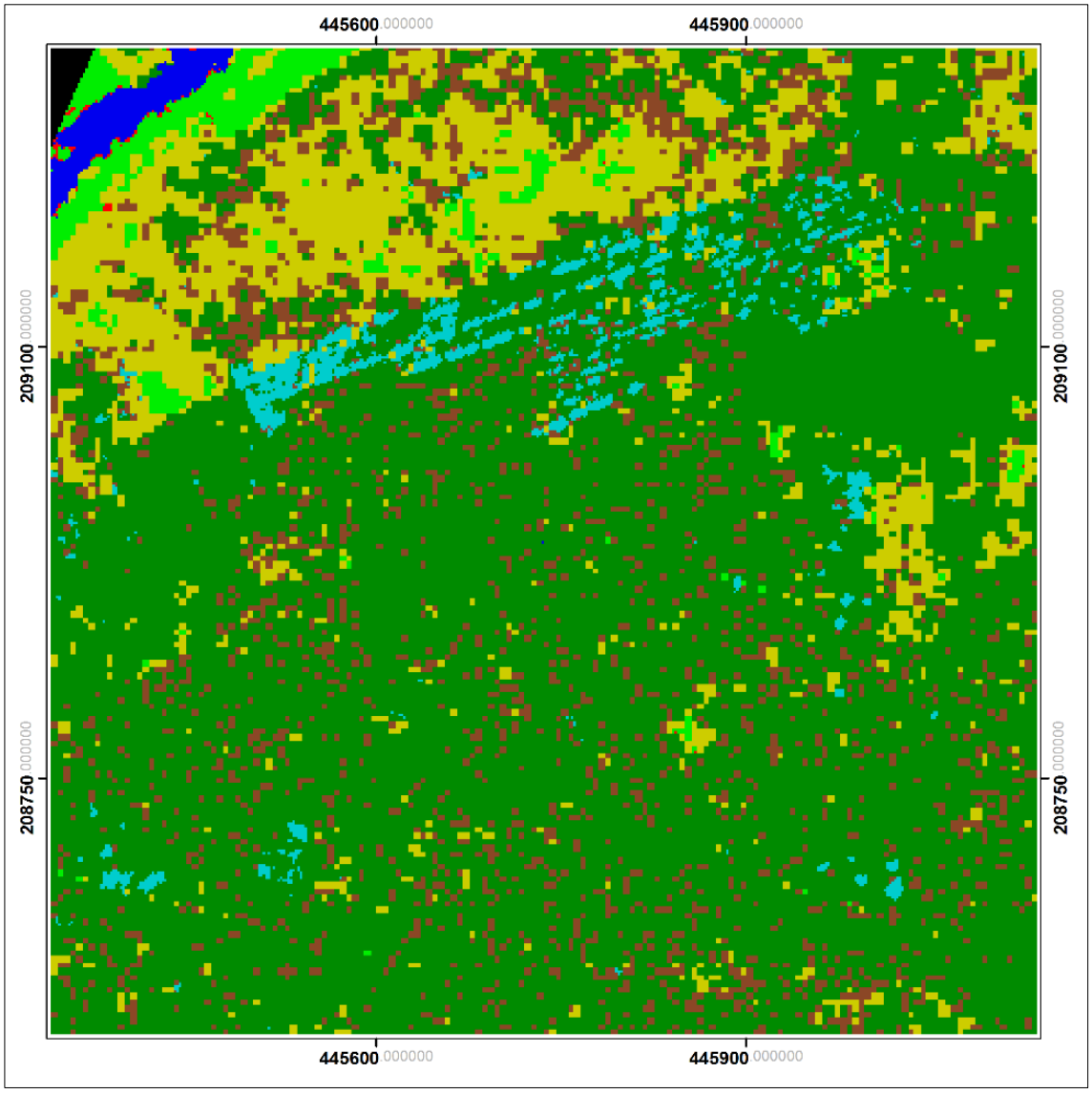

Figure 4-7 Classified canopy types using narrowband-based VI and LiDAR products; black colour as No Data; dark blue as water body; red as Bare Ground; light green as Grass; dark yellow as Young Trees and Shrub; light blue as Evergreen Canopy; brown as Deciduous Open canopy; and dark green as Deciduous Closed Canopy.

4.2.4 Uncertainty in Vegetation Indices caused by Conditions of Measurement

4.2.4.1 Forest Light (FLIGHT) Model

The intensity and direction of radiation in a RS data would be uniform. One could then assume the difference in reflected radiance signals are solely due to different spectral characteristics of ground targets. In reality, the direction and magnitude of

incident radiance is not always uniform due to atmospheric condition and optical geometry, the spectral signature of ground target are therefore altered.

The Forest Light (FLIGHT) model (North, 1996) is a 3D model of light interaction that represents the physical light trajectories in the forest, rather than using only statistical relationships. The temporal and spatial resolution of this model are dependent on the input data (i.e. an instantaneous output at a specific location), while most of the models have a maximum resolution of 1 km and 1 hour. This model has an advantage when studying the pattern and trend of the canopy/stand productivity. It is clear that the FLIGHT model is the most appropriate model in terms of the resolution and the solar irradiance variables to assess the sensitivity of VIs in terms of optical geometry, as well as other canopy/stand parameters. However, in calculation of the canopy/stand productivity (i.e. primary productivity), this model does not include wind direction and velocity component. Therefore, the FLUGHT's output is the canopy/stand productivity at a given point, disregarding horizontal fluxes similar to the flux footprint.

In this chapter, the FLIGHT model was used to investigate how the conditions of measurement might affect the determination of VIs and, therefore, the estimation of plant productivity. This is a Monte Carlo based ray-tracing model which simulates the directional reflectance of 3D forest canopies and has been shown to be applicable to a range of forest types (Alton and North 2007; Barton and North 2001; Disney et al. 2000; Suárez et al. 2009; Verrelst et al. 2008).

It was not possible to produce a model of the whole of Wytham Woods, so a number of image patches were used, selected as representative of each of the main forest canopy types mapped earlier (Table 4-2). The location of every tree trunk in each image patch was digitised and LiDAR data were used to assign an average height to the vegetation in each forest canopy class. The other parameters needed to run the FLIGHT model were validated by comparison against field survey and the literature or were left set at the default values (Table 4-3). However, the values of these parameters are subject to change and error. Thus, sensitivity analysis

investigates these potential changes and errors and their impacts on conclusions to be drawn from the FLIGHT Model.

Reflectance at canopy level is given by the mean value of contributions of all elements visible from a particular direction. Leaf reflectance and transmittance used in the analysis are given in Table 4-4.

Table 4-2 List of forest canopy types simulated using the FLIGHT model

Canopy Type	Forest Canopy class
Block 1	Evergreen Closed Canopy
Block 2	Deciduous Mixed Canopy*
Block 3	Deciduous Closed Canopy
Block 4	Deciduous Closed Canopy
Block 5	Deciduous Mixed Canopy*
Block 6	Deciduous Mixed Canopy*

* Mixed canopy denotes open and closed canopy

Table 4-3 Key variables and actual values used in the FLIGHT Model

Key Variables used in FLIGHT Model	Actual Used Value
Solar Zenith and Solar Azimuth (degree)	Calculated using sun-earth geometry equation, depending on position and time
Total LAI	Ranging from 0.5 to 7.5
Foliage Composition: - Fraction of green leaves in foliage by area - Fraction of senescent/shoot material in foliage - Fraction of bark in foliage	1.0, 0.0, 0.0
Soil Roughness Index (0-1) - Lamertian soil has soil roughness = 0 - The 60˚ slope has soil roughness = 1	0
Aerosol Optical Thickness at 555 nm	Varied from 0.2 to 1.2
Leaf size (radius, approximating leaf as circular disc)	0.1 m
Fraction of ground canopy cover by vegetation	0.5
Crown shape	“e” for ellipsoid
Crown radius	Ranging from 4 to 10 m depend on different blocks
Min and Max height to first branch (m)	1.0 , 9.0

Table 4-4 Leaf reflectance and transmittance at four wavelengths

Wavelength (nm)	Reflectance	Transmittance
470	0.059	0.008
531	0.211	0.016
570	0.133	0.072
660	0.064	0.019
830	0.520	0.430

Table 4-5 Soil Reflectance of wet and dry clay, adopted from Bowker et al., (1985)

Wavelength (nm)	Wet Soil	Dry Soil
470	0.045	0.073
531	0.074	0.150
570	0.111	0.221
660	0.149	0.303
830	0.145	0.325

4.2.4.2 Simulation of Canopy Vegetation Indices

Simulations using the FLIGHT model were run for six blocks, each similar in size to a single pixel from the Disaster Monitoring Constellation (DMC) (22 m x 22 m). Canopy crowns, height and number of trees were taken into consideration for this simulation (Figure 4-8). The simulations were run initially using values of LAI, AOT and Sun-view geometry as appropriate to the sensor overpass.

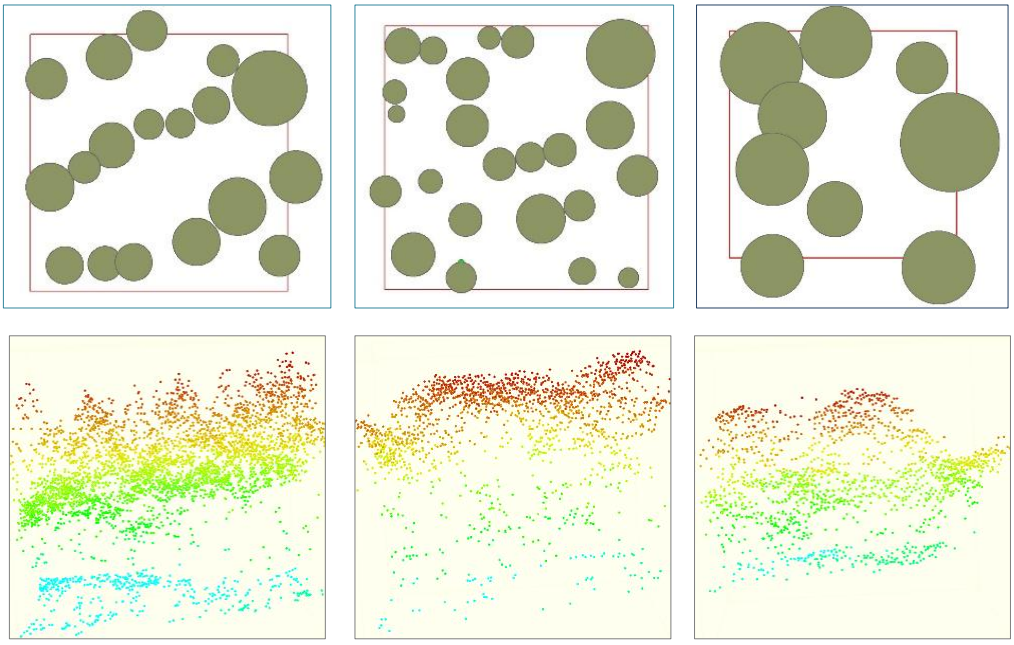

Evergreen Canopy Block 1 | Deciduous Mixed Canopy Block 7 | Deciduous Open Canopy Block 2

Figure 4-8 Differences of each block in terms of canopy crowns, height and number of trees.

4.2.4.3 Sensitivity Analysis

The sensitivity of the VIs was examined by means of the "local" method, also known as "one at a time" approach. This "local" method determines the influence of the variation of one parameter on the output, while all other parameters remain constant. The simplest method of determining the sensitivity of VIs is to calculate the output percentage difference when varying one input parameter from its minimum value to its maximum value (Hoffman and Gardner 1983), referred to as "sensitivity index"(SI) (Equation 4-6).

$$Sensitivity\ Index = \frac{D_{max} - D_{min}}{D_{max}} \qquad \text{Equation 4-6}$$

where, D_{min} and D_{max} repress the minimum and maximum output values, respectively, resulting from varying the input over its possible range (Hoffman and Gardner 1983).

4.3 Results and Discussion

The spectral composition of light reflected from a canopy scene is different from that incident on the scene as a result of differential absorption amongst wavebands by compounds within the components that make up the canopy scene (i.e. leaves, bark, and soil). The strength of the reflected signal depends both on the reflectance of individual canopy elements and also on the orientation and spatial arrangement of the elements with respect to each other and to the illumination and view direction (optical geometry). Different optical geometer within canopy means that there will be a range of light saturation and so a range VIs values present within the canopy. Thus, one of the main goal of this chapter is to determine how sensitive the VIS signal measured above canopy is to perturbing effects such as atmospheric effects, soil background and optical geometry.

4.3.1 Influence of Aerosol Optical Thickness (AOT) on the Vegetation Indices

The quantity of the AOT was varied (from 0.2 to 1.2) while other parameters were held constant (i.e. solar zenith angle: 36.9°, view zenith angle: 0.0°, and LAI: 1.355). For this range of the AOT, initially, reflectance for each of the five wavebands (Blue at 470 nm, Green at 531 nm and 570 nm, Red at 660 nm, and NIR at 830 nm) was simulated using the FLIGHT model, and then interesting VIs (e.g. NDVI, ARVI and PRI). Figure 4-9 shows the variation in the VIs for each simulation in terms of the AOT changes across different canopy types. Accordingly, the values of the VIs across all canopy types increase linearly as the magnitude of the AOT increases, but less in value over the evergreen closed canopy type. This means that variation in these VIs depends upon the canopy types in terms of the balance between evergreen and deciduous stands. For all VIs increase in aerosol optical thickness (from 0.2 to 1.2°), results approximately 3% increase in both NDVI and PRI, and about 7% increase in PRI that shows the sensitivity of canopy PRI regarding to the atmospheric effects.

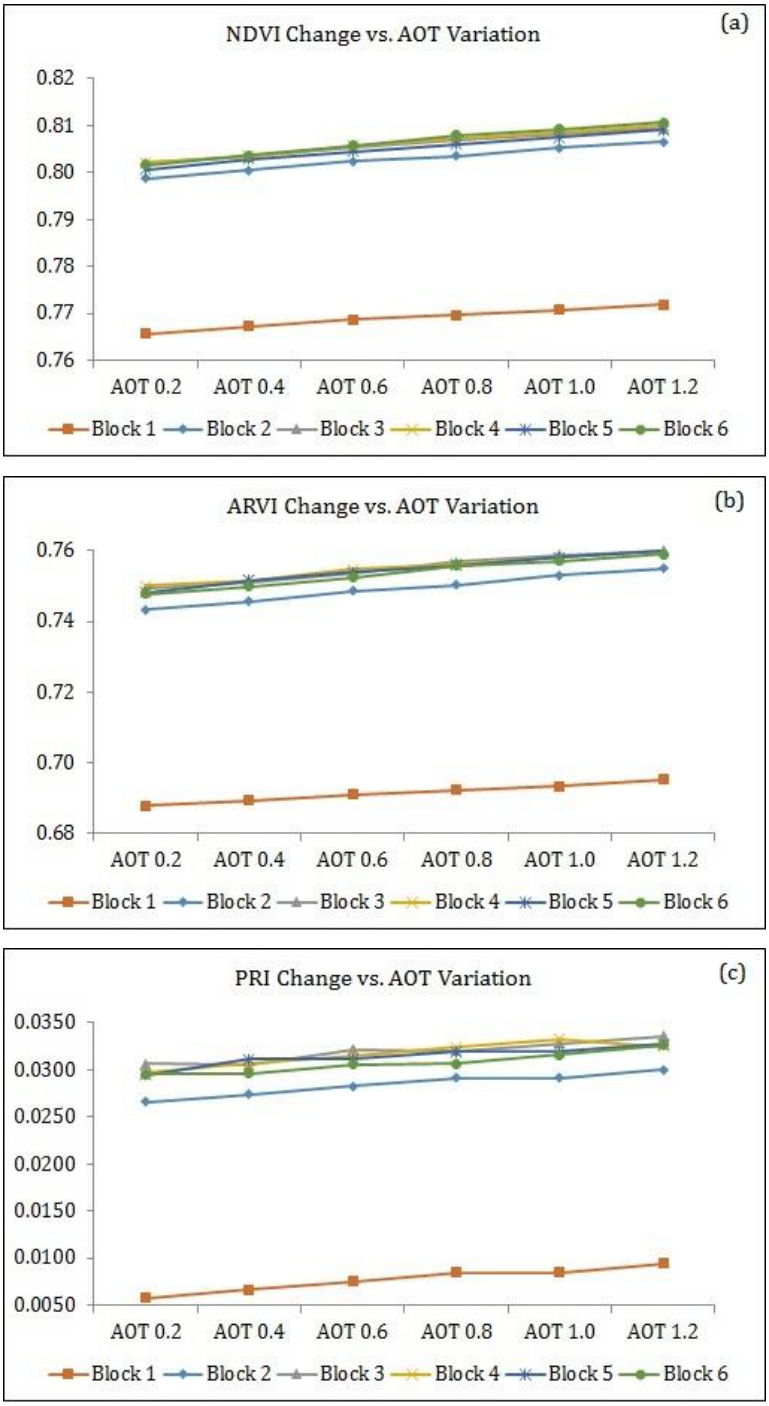

Figure 4-9 Variation in the VIs: (a) NDVI; (b) ARVI; and (c) PRI in terms of the AOT changes across different canopy types.

4.3.2 Influence of Leaf Area Index (LAI) on the Vegetation Indices

To determine the influence of background reflectance on the VIs (e.g. NDVI and PRI), one soil type was considered, while LAI was varied from 0.5 to 7.5 in 1.5 steps, and reflectance computed. As expected, the value of all the VIs increases as the canopy develops during stages in its phenology (i.e. LAI increases). Both VIs behaved similarly as LAI varied (Figure 4-10). The canopy spectral indices of CO_2 flux (NDVI and PRI) increase as a result of LAI increases from 0.5 to 6. At LAI above 6, the canopy VIs become insensitive to the background effect of soil and the canopy NDVI and PRI approach approximately 0.80 and 0.04, respectively. However, below an LAI of 3.0 and 4.5, the background reflectance has a significant influence on the measured NDVI and PRI, respectively. Results show the PRI value is most sensitive to changes in LAI

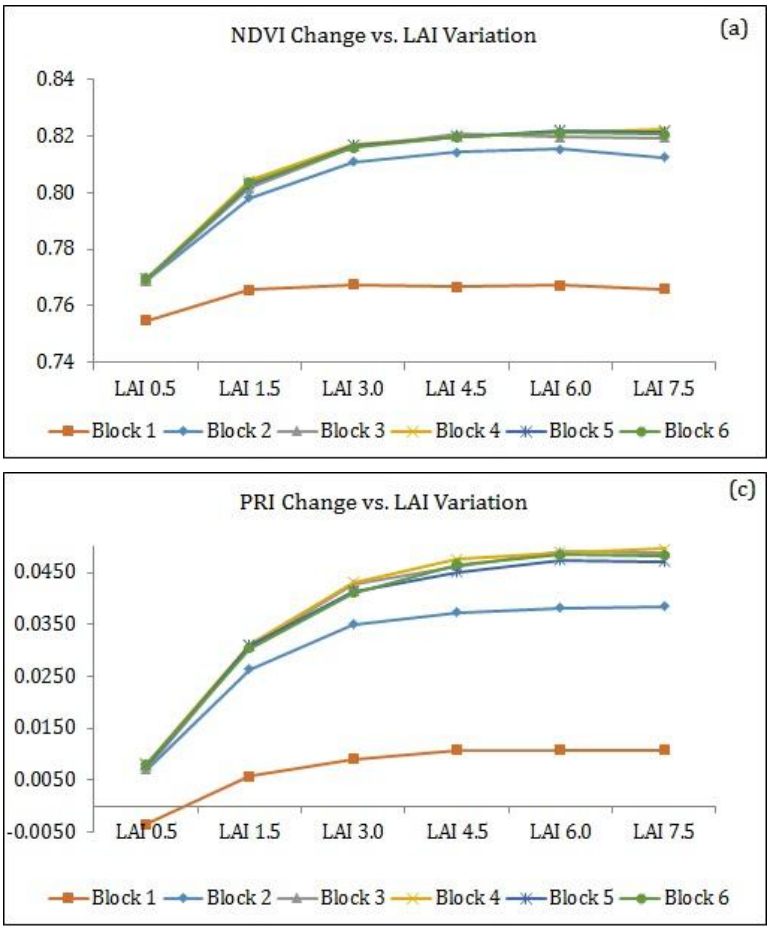

Figure 4-10 Variation in the VIs: (a) NDVI; (b) ARVI; and (c) PRI in terms of the LAI changes across different canopy types.

4.3.3 Influence of Solar/View Geometry on the Vegetation Indices

The solar zenith angle (SZA) was varied from 10˚ to 60˚ in 10˚ steps (Barton and North, 2001) while other parameters were held constant (AOT: 0.2, view zenith angle: 0.0˚, and LAI: 1.355). Furthermore, the view zenith angle (VZA) was varied from 5˚ to 30˚ in 5˚ steps (Barton and North, 2001) while other parameters were held constant (AOT: 0.2, solar zenith angle: 36.9˚, and LAI: 1.355). Figures 4-11 and 4-12 show the behaviour of NDVI and PRI in terms of SZA and VZA.

In Wytham Woods, images collected by those sensors such as UK_DMC, spectral indices of CO_2 flux's channels (e.g. NDVI) are highly sensitive to sun-sensor geometry due to sub-pixel extraneous parameters such as shadow fractions. At Red wavelength in which canopy efficiently absorbs light, increase in solar zenith angle (from 10˚ to 60 ˚), results 10% decrease in VIs channels across Evergreen Closed Canopy in Block 1, while results in about 20% increase across Deciduous Closed Canopy in Blocks 2-6, probably due to less shadow fractions. In addition, the results show that increase in view zenith angle (from 5˚ to 30˚), results in approximately 5% decrease in VIs across deciduous mixed/dense forest reflectance and about 10% decrease across conifers closed canopy. This behaviour is relatively constant across all canopy types, but with a lower value for evergreen stands than deciduous stands.

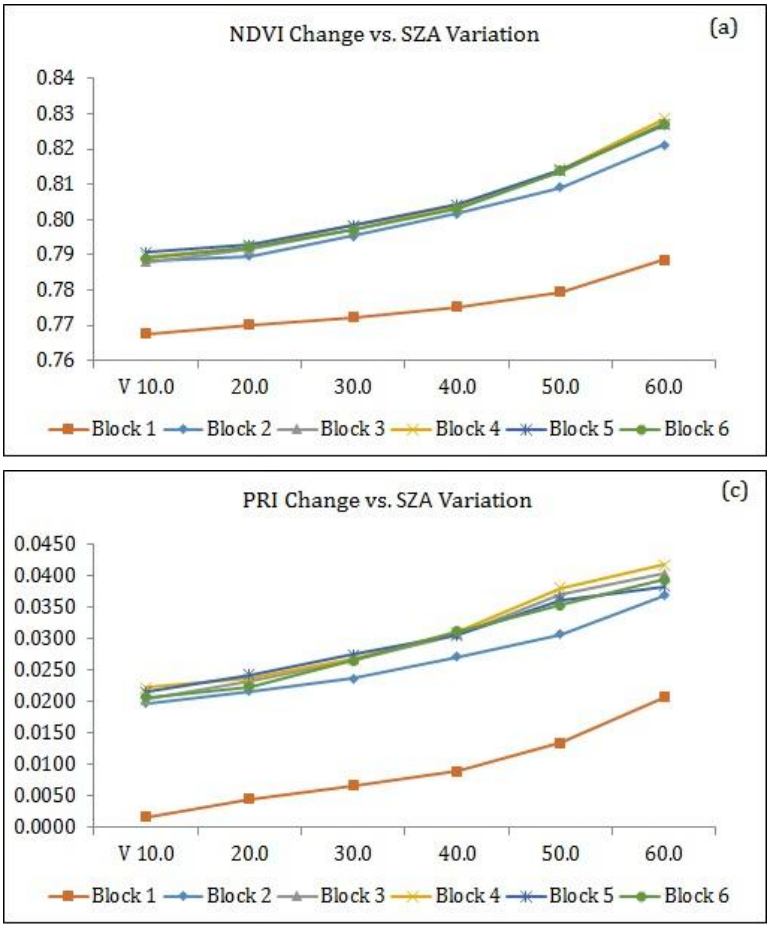

Figure 4-11 Variation in the VIs: (a) NDVI; (b) ARVI; and (c) PRI in terms of the SZA changes across different canopy types.

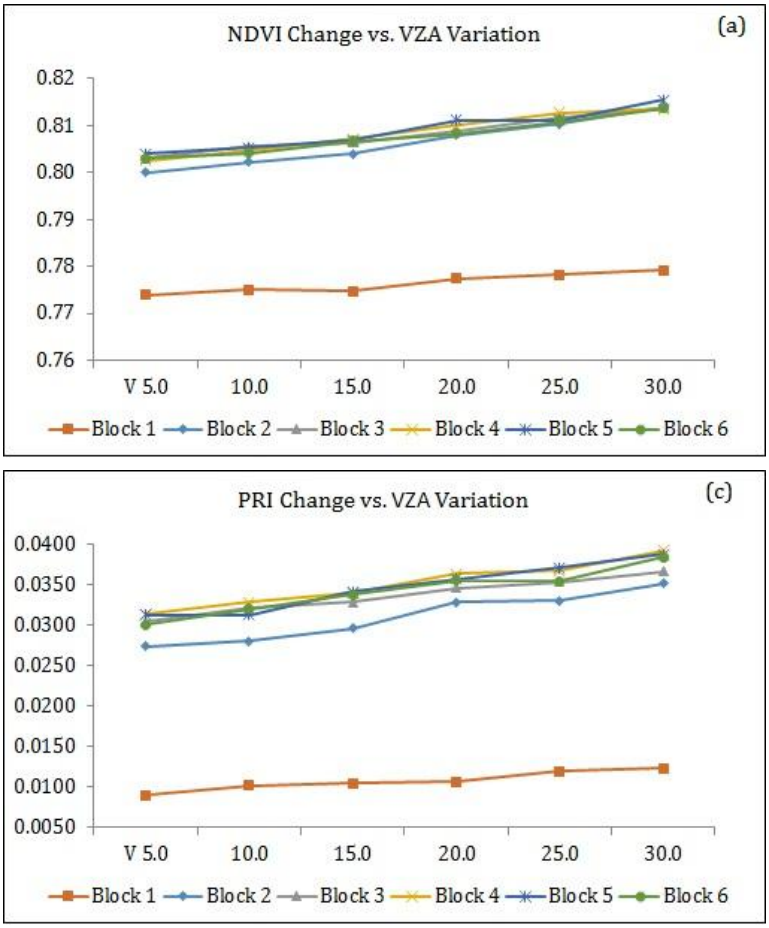

Figure 4-12 Variation in the VIs: (a) NDVI; (b) ARVI; and (c) PRI in terms of the VZA changes across different canopy types.

Table 4-6 represents the sensitivity index of the VIs in terms of the FLIGHT parameter changes separately across each sampling blocks. The SI_{NDVI} and SI_{ARVI} are relatively constant over all canopy types (i.e. ≤ 0.01 and ≤ 0.016 for NDVI and ARVI, respectively), while NDVI is less sensitive than the ARVI in terms of the AOT changes. On the other hand, the SI_{PRI} for all deciduous stands is relatively constant, while PRI simulated over the evergreen stand is more sensitive with respect to the deciduous stands.

As LAI changes over the phonological stages, the SI_{NDVI} and SI_{ARVI} are relatively constant over the deciduous stand even in closed or mixed canopies. However, the sensitivity of these indices across deciduous stands is greater than for the evergreen stand. As the SI_{PRI} is constant across all deciduous sampling blocks, the sensitivity of this index over the evergreen stand is greater than for the deciduous stand with respect to the LAI changes.

The NDVI and ARVI simulated over deciduous stands show high sensitivity over the deciduous stand with respect to the evergreen stand in terms of solar geometry, while this sensitivity is low for PRI. In other words, PRI simulated over the evergreen stand is sensitive to variation in the solar zenith angle. Accordingly, variation in canopy structure (i.e. LAI) and differences in Sun/view geometry affect the VIs, particularly PRI that is more sensitive with respect to the canopy structure and SZA over an evergreen stand. This means that these parameters influence UK-DMC data (i.e. with 22 meter spatial resolution) across a mixed forest and this needs to be addressed by appropriate atmospheric correction.

Overall, the sensitivity of NDVI and PRI respect to the sun zenith angle and soil background (i.e. LAI) is high (Figure 4-13) and this sensitivity will be increase across coniferous stands and spars canopy, probably due to shadow fraction.

Table 4-6 Sensitivity index of vegetation indices in terms of the FLIGHT parameter changes separately across each sampling block.

Sample Block	AOT Variation			LAI Variation			SZA Variation			VZA Variation		
	SI_{NDVI}	SI_{ARVI}	SI_{PRI}	SI_{NDVI}	SI_{ARVI}	SI_{PRI}	SI_{NDVI}	SI_{ARVI}	SI_{PRI}	SI_{NDVI}	SI_{ARVI}	SI_{PRI}
Block 1	0.0079	0.0106	0.3837	0.0148	0.0349	1.3224	0.0267	0.0454	0.9177	0.0067	0.0099	0.2670
Block 2	0.0098	0.0152	0.1141	0.0538	0.1004	0.8163	0.0400	0.0703	0.4638	0.0169	0.0274	0.2218
Block 3	0.0090	0.0142	0.0884	0.0615	0.1174	0.8529	0.0472	0.0817	0.4969	0.0130	0.0164	0.1688
Block 4	0.0097	0.0132	0.0844	0.0643	0.1229	0.8357	0.0470	0.0798	0.4681	0.0135	0.0164	0.2011
Block 5	0.0103	0.0156	0.1011	0.0631	0.1193	0.8305	0.0439	0.0739	0.4379	0.0141	0.0174	0.1937
Block 6	0.0113	0.0148	0.0946	0.0623	0.1189	0.8324	0.0461	0.0784	0.4743	0.0131	0.0159	0.2168

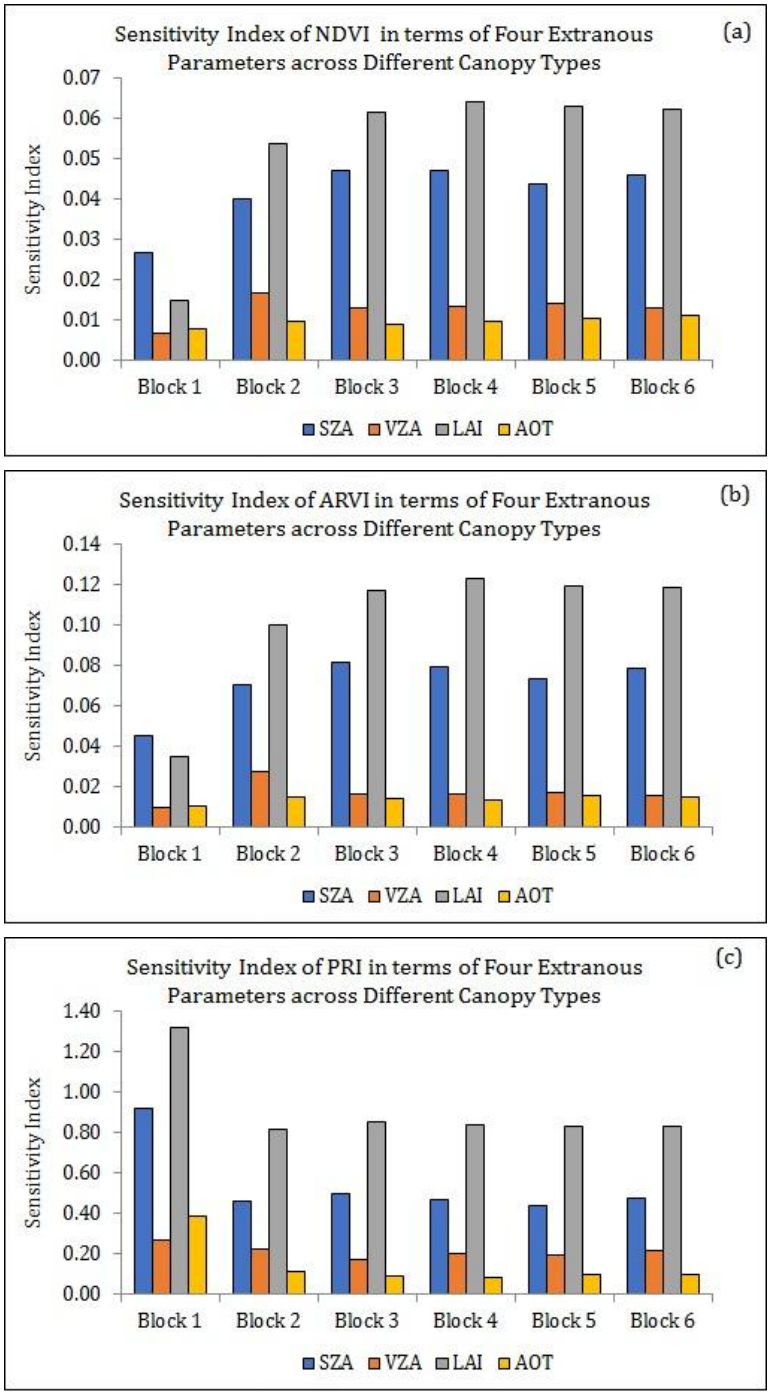

Figure 4-13 Sensitivity index of vegetation indices: (a) NDVI; (b) ARVI; and (c) PRI in terms of the FLIGHT parameters variation across different canopy Types.

4.4 Conclusion

The main aim of the thesis, exploring spatial aspects of sampling from the tower-based CO_2 flux measurements and the satellite sensor observations, lead us to understand the source of measurement uncertainty in spectral vegetation indices, and how the extraneous variables might affect the vegetation indices averaged over a flux tower extent. Therefore, the primary goal of this chapter is to investigate uncertainty in vegetation indices over a heterogeneous forest canopy at fine spatial resolution, and at different stages during the growing season (i.e. varying optical geometry and aerosol content, as well as developing leaf area during phenological trend).

This research examined sensitivity to the canopy structure (approximated by variation in LAI, crown size and dimension, and canopy height) and influence of illumination and view angles on reflectance at five wavebands, and hence on canopy spectral indicators of CO_2 flux (e.g. NDVI and PRI). A 3D forest light simulation model (FLIGHT model) was used, in terms of mentioned extraneous parameters, to demonstrate the sensitivity of vegetation indices over a mixed forest using fine resolution UK-DMC imagery. In this regards, simulations were run for six blocks (canopy types/stands), each similar in size to a single pixel from the UK-DMC (22 m x 22 m).

Generally, this study demonstrates the magnitude and variability of extraneous parameters (e.g. optical geometry, shadow fraction, soil background and aerosol) in remotely sensed observations of a mixed forest[1] in southern England, Wytham Woods. The results indicated that the shadow fractions are substantial and increase with canopy density. When the density of canopy rises (e.g. dense mature deciduous trees), variations in shadow fraction are dominated variation in crown size and dimension, leaf area index, leaf spectral properties, and sun-sensor

1. Temperate Mixed Forest (broadleaf trees with conifer): structurally characterized by four layers: a canopy composed of ***mature full-sized dominated species*** and ***slightly lower layer of mature trees***, ***a shrub layer***, and ***understory layer of grasses and other herbaceous plants***.

geometry. The sun-sensor geometry influence have been isolated from the effect of changing atmospheric conditions (e.g. AOT) and real changes in canopy status and soil background (e.g. LAI). The analysis shows that observed vegetation indices from mixed forest is highly sensitive to variation in solar and view zenith angles. This indicates seasonal and spatial variations in vegetation indices of approximately 10-20% in mixed forested images collected by those sensors such as UK_DMC with 22 m pixel size.

The vegetation indices observed above the canopy (across all blocks/canopy types) varies with both solar and view zenith angles (Figure 4.11 and 4.12). There is a large variation in canopy PRI as solar zenith angle changes for any given view zenith angle. For the most view angles (from 5˚ to 30˚ of nadir), canopy PRI increases with increasing solar zenith angle. Theses variations are relatively similar for all deciduous mixed/dense canopy types (Block 2-6 as depicted by Figure 4-11 and 4-12), while there is a low variation across coniferous stand in Block 1, probably due to shadow fraction. Overall, results show strong anisotropy in reflectance, dominated by shadowing effects of the crowns.

The indices are also strongly influenced by varying soil background for LAI of 3. Ay large viewing angles (greater than 30˚), the spectral indices are also sensitive LAI. The results also depicts that the indices are relatively robust to aerosol scattering.

Reflectance of coniferous stand (Block 1) appeared to be primarily the result of canopy shading, which varied with species structural characteristics and overall canopy cover. Soil reflectance also contributed to the observed reflectance, but only at sufficiently sparse canopy cover. However, other parameters, such as LAI can have significant effects on reflectance and should be considered.

In general, we can conclude that the sun-sensor geometry effects accounted for approximately 10-20% of the variance in spectral indicators of CO_2 flux's wavelengths responses in mixed forested images collected by those sensors such as UK_DMC with 22 m pixel size.

Canopy types and uncertainty in the vegetation indices required for (i) RS-based models of CO_2 flux and (ii) estimation of GPP using single flux tower and a single pixel of coarse satellite sensor observation, were mapped and tested across a mixed forest in southern England. The FLIGHT model results can be apportioned to different sources of uncertainty in inputs. The necessary distinction of the important parameters of the FLIGHT model is in the type of analysis being conducted sensitivity analysis (SA). Sensitivity analysis can be used for a range of purposes, including testing the robustness of the vegetation indices in the presence of uncertainty especially over a complex 3D surface such as a mixed forest; increased understanding of the relationships between the extraneous variables that influence the vegetation indices (i.e. between the input and output variables in the FLIGHT model); and identifying extraneous parameters that cause significant uncertainty in the vegetation indices to be the focus of the attention if robustness is to be increased.

The use of the FLIGHT model allowed realistic 3D tree canopies to be simulated and then used to investigate how the conditions of measurement might affect each of the VIs. Variation in solar and view zenith angles (SZA and VZA), atmospheric optical thickness (AOT) and leaf area index (LAI) will all lead to changes in canopy vegetation indices and subsequently canopy LUE. Overall, these results suggest that using spectral indicators of CO_2 flux for scaling in situ carbon flux and ecosystem productivity should be with caution. However, spectral vegetation indices on a large scale may be problematic, as the assessed indices shows a significant variation with extraneous parameters.

5. Hyper-temporal Remote Sensing Using a Constellation Approach

5.1 Introduction

The previous two chapters showed the potential of narrowband spectral data from an aircraft (AISA Eagle) or satellite sensor (MODIS) to provide useful information on the actual LUE of a forest canopy. They also revealed the critical importance of the spatial domain, both in terms of the pixel size and the extent of the image (e.g. the practical difficulties of mosaicking the Eagle data). A further consideration is the temporal domain, not least since the basis of flux measurement involves a change over time, but primarily because significant variation in the reflected signal is expected through a growing season and the effects of this change on LUE estimates needs to be considered fully. Accurate measurement and understanding of processes implies repeated remote sensing measurements, both over a few days (to study short-term changes in photosynthesis, for example) and over a growing season (e.g. carbon source/sink studies).

The analysis in this chapter returns to the Wytham Woods field site and investigates how data with the necessary spatial and temporal sampling interval may be obtained for this site, which is typical of many woodland areas throughout the UK and Europe. The first thing that is apparent is that data from the MODIS sensor are not ideal for this task. First, its spatial resolution is too coarse for most areas of woodland in the UK, which are either smaller than a MODIS pixel in size or spatially variable (or both). Second, the temporal sampling of the MODIS NDVI product is more irregular and less predictable than it first appears. Although this generally results in a smooth NDVI curve for the year as a whole it presents difficulties when trying to compare the MODIS product with a specific event, such as an overpass of another sensing system or a measurement from a flux tower.

Khavarian (2012) circumvented this problem when validating the MODIS albedo product by making a special arrangement with NASA to obtain the individual MODIS images, but this is not normally possible.

The alternative approach investigated in this research was to identify a remote sensing system that offered a relevant spectral capability, but had more frequent and predictable sampling and finer spatial resolution. The requirement for this to be available globally excludes aircraft and other local solutions (e.g. UAV, balloons, and kites). No satellite sensors provided the narrow spectral bands necessary to calculate PRI, but several provided NDVI data, and so that was chosen as the basic plant canopy spectral variable for this chapter. It is important to recall that the evidence presented in Chapter 4 shows that both NDVI and PRI would be necessary in any future operational system, something which will be returned to in the final chapter of this thesis.

Figure 5-1 shows the main NDVI-capable satellite sensing systems available at the start of this research, in relation to the key parameters of spatial resolution and sampling interval. It is clear from this figure that satellites in the Disaster Monitoring Constellation (DMC) are uniquely suited to this task and arrangements were made to acquire a time-series of DMC images of Wytham Woods during 2010.

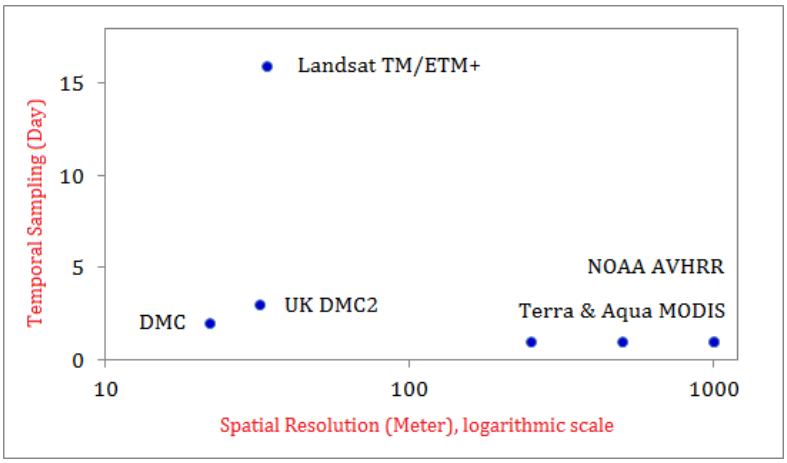

Figure 5-1 possible satellite systems (NDVI capable): spatial resolution vs. temporal sampling.

The objectives of the research described in this chapter were:

- To obtain as many DMC and MODIS images of Wytham Woods as practically possible during one growing period (early Spring to mid-Summer), and to inter-calibrate them rigorously so that they would be suitable for measuring change in NDVI during the year;
- To determine the repeatability of DMC NDVI measurements over a period of a few days;
- To investigate whether differences in the size and shape of the flux tower footprint (e.g. whether it is generalised or realistic) would significantly affect DMC NDVI values, and whether this result varied during the growing season; and
- To assess the pros and cons of DMC data as a means of mapping and monitoring ecological changes in woodlands in southern England.

Precise definition of the flux tower footprint was not an issue in the previous chapter when working with MODIS data as the pixel size was so large, but, as Figure 5-2 shows, DMC data have much finer spatial resolution, so internal spatial variation within the woodland has to be considered.

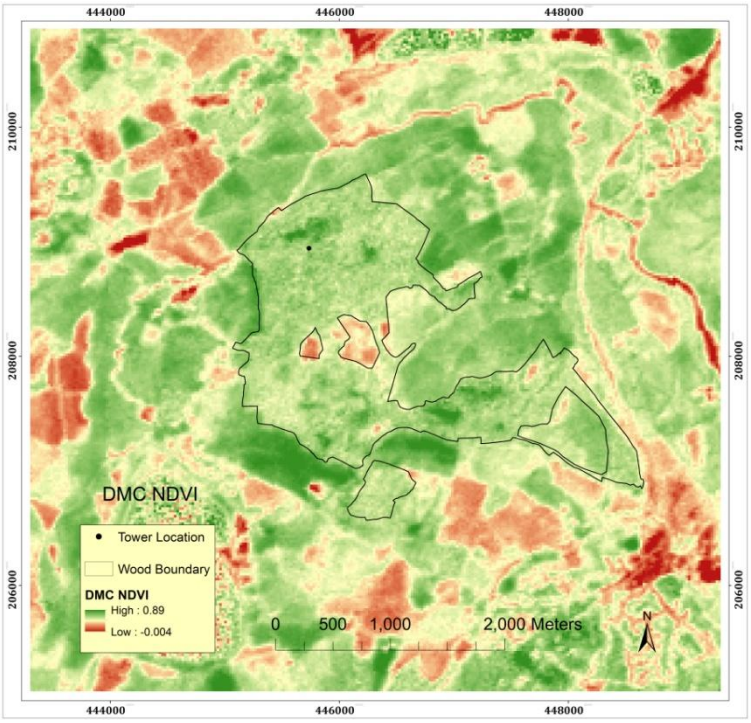

(a) DMC NDVI on 2nd March 2010 (Julian Day: 62)

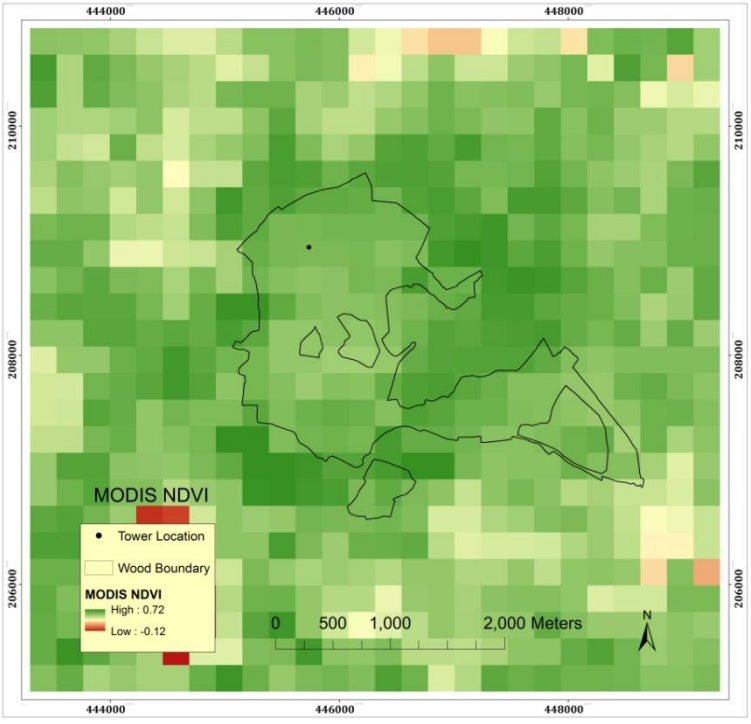

(b) MODIS NDVI over 18th Feb. – 5th March 2010 (Julian Day: 49 - 65)

Figure 5-2 Comparing the spatial resolutions of satellite sensor systems: (a) DMC NDVI with 22 m spatial resolution ; and (b) MODIS NDVI with 250 m spatial resolution

5.2 Data Acquisition and Methodology

5.2.1 Pre-processing the Satellite Sensor Data

A total of eight DMC images were acquired between March and the end of June 2010 (Table 5-1), confirming the power of the constellation approach to obtaining frequent observations, even when faced with intermittent cloud cover. During this same period NASA acquired seven MODIS images of the same area, although of course, with much coarser spatial resolution (250 m compared with 22 m or 32 m).

Table 5-1 DMC datasets acquired during 2010

Imaging Date (dd/mm/yyyy)	Imaging Time (UT)	Mission	Pixel Size (m)	Image Clarity	Viewing Angle[1]
02/03/2010	09:43:21	UK-DMC2	22	Clear	28.74
05/03/2010	09:46:39	UK-DMC2	22	Clear	22.06
07/03/2010	09:54:31	DEIMOS	22	Clear	5.47
20/04/2010	08:03:51	UK-DMC	32	Clear	0.82
27/04/2010	10:08:21	UK-DMC2	22	Clear	20.48
23/05/2010	09:52:10	UK-DMC2	22	Clear	17.85
04/06/2010	09:56:34	UK-DMC2	22	Clear	25.82
16/06/2010	09:52:02	UK-DMC2	22	Cloudy	27.46

The DMC datasets were supplied projected to UTM/WGS84 (Level 1T), so they were re-projected into the British National Grid (BNG), Datum OSGB36 and subsets produced over the extent of Wytham Woods (600×600 pixels). Image registration was performed by using 20 ground control points identified on Ordnance Survey MasterMap and using polynomial, nearest-neighbour resampling. The RMS errors were less than 0.75 pixels. Furthermore, time-series images from MOD13Q1 were geometrically registered to the same coordinate system as the DMC datasets.

[1]. Approximately viewing angle on Wytham Woods

All the satellite sensor data were corrected for the effect of the atmosphere. The MODIS data had already been converted to reflectance and adjusted to nadir angle as part of the MODIS processing chain prior to the calculation of the NDVI (Masuoka et al. 2011).

The DMC data were first converted to radiance at the top of atmosphere (TOA) using the bias and gain values specified by the data provider, Crowley (2010). They divided naturally into three phases based on the date of acquisition. The first three images were acquired within the first week of March, when many of the trees were still bare. The next two images came from a week in late April when the tree canopy was rapidly developing, and the final three images were acquired between 23rd May and 16th June, when the tree canopy was almost fully developed. The DMC data were atmospherically corrected using the ATCOR-2 program (Richter, 2011), using a standard mid-latitude atmosphere and typical values of water vapour and aerosol type. The results showed an apparent change in reflectance during the period 2nd to 7th March (Table 5-2), when none would have been expected, which pointed to some uncertainty in the parameters of the radiative transfer model.

Table 5-2 Red and Near-Infrared wavebands behaviour over the early growing season after absolute atmospheric correction (surface reflectance) across the Wytham flux tower extent.

Acquisition Date	Red Waveband Derived from ATCOR				NIR Waveband Derived from ATCOR			
	Mean	Median	SD	CV	Mean	Median	SD	CV
2nd March	6.05	6.00	1.34	22.15	27.87	27.50	3.24	11.63
5th March	8.17	8.00	1.15	14.01	31.16	31.00	2.98	9.57
7th March	6.34	6.00	1.15	18.07	27.74	27.00	3.05	10.98
20th April	6.07	6.00	0.97	15.90	38.25	38.00	4.45	11.62
27th April	5.66	5.50	0.98	17.23	48.58	47.50	6.48	13.34
23rd May	4.00	4.00	0.68	16.90	77.05	77.00	5.82	7.55
4th June	3.55	3.50	0.49	13.82	80.37	80.50	6.01	7.48
16th June	4.73	4.50	0.71	15.03	83.66	85.00	7.98	9.53

To overcome this, a method of image normalisation was applied in which the image closest to nadir view angle (and visually the clearest) for each phase (the reference image) was corrected to reflectance using ATCOR-2 and then the other images from the same phase were normalised to the reference image using the method of iteratively reweighted radiometric normalisation (IR-MAD) (Canty and Nielsen, 2008). This technique automatically found spectrally invariant targets within a series of related images and adjusted the target images to match the designated reference image by applying a linear transformation to the data. After applying this hybrid ATCOR/IR-MAD technique, the three DMC images from March showed no significant change in reflectance in either the Red or NIR wavebands (Table 5-3).

The IR-MAD scheme holds back one-third of the time-invariant pixels to evalute the normalization procedure by calculating the means and variances of target images, before and after normalization, for performing statistical hypothesis tests for equality in the means and variances of the time-invariant pixels in the reference and nomalized target images (Canty, 2010). These results are given in Table 5-4 as 345 and 656 test pixels for the 2nd and 5th March images vs. the 7th March reference image, respectively; 112 test pixels for the 27th April vs. the 20th April reference image; and 262 and 173 test pixels for the 4th and 16th June images vs. the 23th May reference image, respectively. The significance values ($p < 0.05$) for the *t*-test for equal means and for the *F*-test for equal variances indicate that the hypothesis of equality cannot be rejected for any of the spectral bands in the datasets, so we conclude that the normalization is acceptable.

Table 5-3 Red and Near-Infrared wavebands behaviour over early growing season associated with hybrid ATCOR/IR-MAD technique (normalized surface reflectance) across Wytham flux tower extent

Acquisition Date	Red Waveband from ATCOR/IR-MAD				NIR Waveband from ATCOR/IR-MAD			
	Mean	Median	SD	CV	Mean	Median	SD	CV
2nd March	5.95	5.90	1.31	22.00	27.47	27.12	3.05	11.10
5th March	6.17	6.00	1.15	18.63	27.64	27.48	3.01	10.90
7th March	Reference Image				Reference Image			
20th April	Reference Image				Reference Image			
27th April	6.07	6.00	0.97	15.98	46.86	45.88	5.85	12.50
23rd May	Reference Image				Reference Image			
4th June	3.38	3.32	0.52	15.38	81.40	81.53	7.21	8.86
16th June	3.62	3.41	0.68	18.78	74.72	75.92	7.21	9.65

Table 5-4 Paired *t*-tests and *F*-tests for equal means and variances between target images and normalized images using the IR-MAD normalization method

Acquisition Date	Mean						Variance					
	t-Statistic			P-value			F-Statistic			P-value		
	B1	B2	B3	B1	B2	B3	B1	B2	B3	B1	B2	B3
2nd March	0.176	0.200	0.126	0.860	0.842	0.899	1.008	1.006	1.007	0.939	0.958	0.952
5th March	-0.09	-NaN	0.580	0.927	NaN	0.562	1.002	1.000	1.000	0.980	1.000	0.998
27th April	-0.39	-0.73	-0.22	0.692	0.466	0.827	1.006	1.012	1.002	0.973	0.952	0.990
4th June	0.322	0.287	-0.10	0.748	0.775	0.919	1.006	1.005	1.002	0.960	0.971	0.991
16th June	-0.19	-0.25	0.099	0.844	0.802	0.922	1.049	1.026	1.000	0.754	0.868	0.996

5.2.1.1 Early in Season Normalization, Leaf-off Conditions

Three images were available from 2nd March (UK-DMC2), 5th March (UK-DMC2), and 7th March (DEIMOS), acquired using the same sensor (SLIM-6-22) and spatial resolution (22 m at nadir). The image from 7th March was selected as the reference image for the leaf-off period, based on visual assessment of quality and the fact that it was acquired close to nadir for the study area. The other March images were normalized to the 7th March data as the reference image.

5.2.1.2 Early Spring Normalization, Middle Leaf-on Conditions

The reference image to perform relative illumination and normalization of leaf-on conditions during mid-spring was considered based on near-nadir situation for the study area. The 27th April was normalized to the 20th April absolute corrected reflectance as the reference image.

5.2.1.3 Early Summer Normalization, Leaf-on Conditions

The reference image to perform relative illumination and nadir normalization of leaf-on conditions during early summer was considered based on their high solar elevation and cloud free conditions. Therefore, the 4th and 16th June images were normalized to the 23rd May absolute corrected reflectance as a reference image.

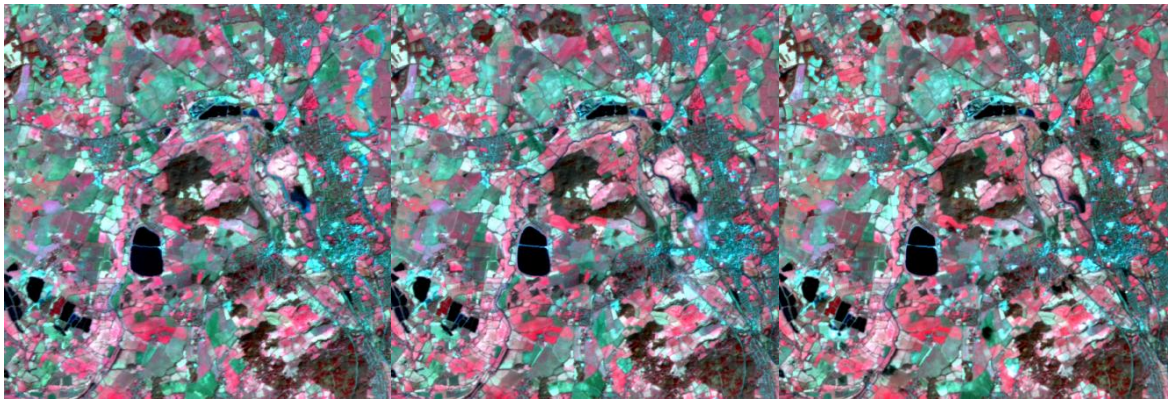

2nd March, NASR 5th March, NASR 7th March, NASR

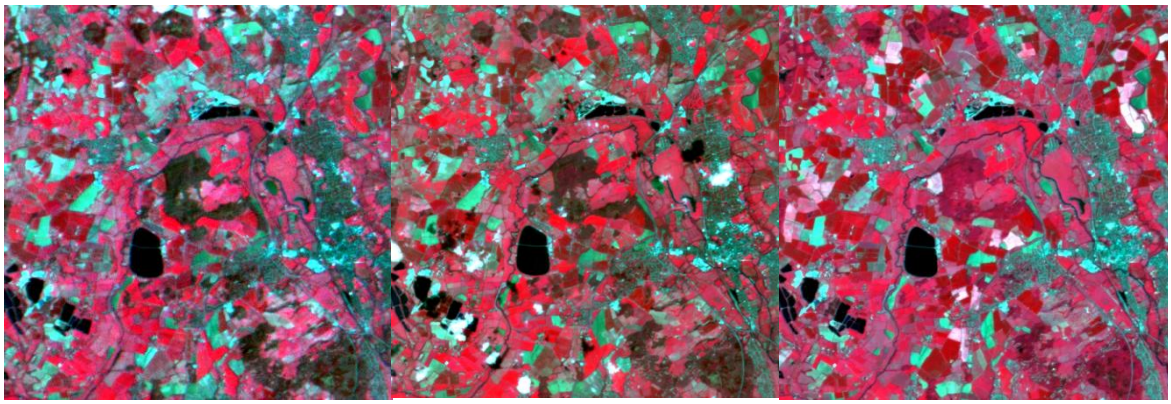

20th April, NASR 27th April, NASR 23rd May, NASR

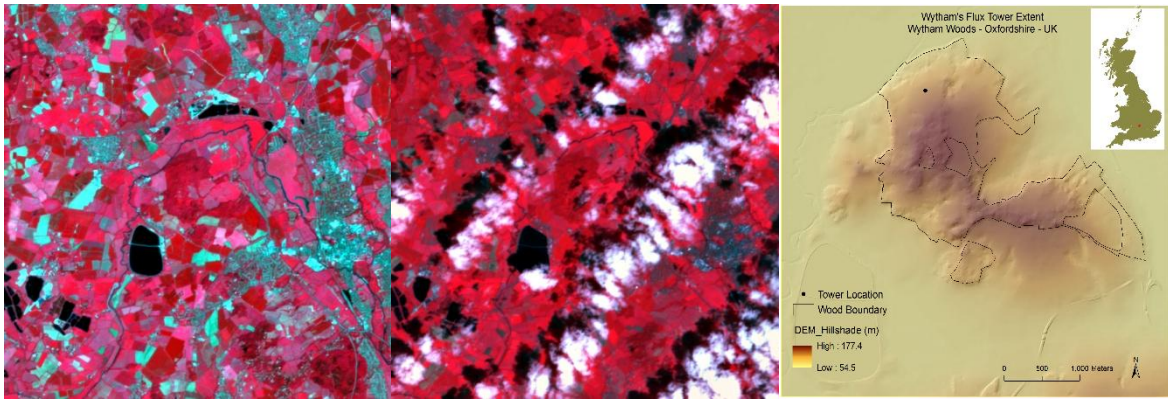

4th June, NASR 16th June, NASR Wytham Woods

Figure 5-3 Time-series of normalized absolute calibrated reflectance DMC images over Wytham Woods for the 2010 growing season.

5.2.2 Defining the flux tower footprint

Several methods of defining the flux tower footprint have been considered in previous chapters, and a buffer distance of 400 m centred on the flux tower location was considered as representative of the long-term pattern of daytime flux tower footprint, referred to here as the circular flux tower footprint (CFF), which corresponds to an array of 37×36 DMC pixels (with 22 m pixel size) and 3×3 MODIS pixels (with 250m pixel size) centred on the tower.

The area-weighted flux tower footprint was estimated using site properties. Canopy height was determined using an airborne Light Detection and Ranging (LiDAR) survey of the site in 2009. Meteorological data from the nearest MetOffice weather station (Lat: 51°46' N; Lon: 1°46' W; Alt: 63.4m) revealed two prevailing wind directions during 2010: 225° (south-west) and 315° (north-west). Therefore, the weighted flux tower footprint was also modelled with wind from each of these directions, under both moderate and unstable conditions, that is, $-0.1 < Z_m/L < -0.001$ at flux tower site with Z_m/Z_0 of 19.23, i.e. $Z_m = 25$ m and $Z_0 = 1.30$ m. The weighted flux tower footprint was, hereafter, termed the realistic flux tower footprint (RFF). Figure 5-4 illustrates the estimated horizontal position of 90% cumulative footprints for two prevailing wind directions under different atmospheric stability conditions. The spatial coverage of red and yellow points indicates the RFF under unstable and moderately stable conditions, respectively. In addition to the RFF, Figure 5-4 also shows circular buffers of 200 m (the peak contribution) and 400 m (as 90% contribution), centred on the flux tower.

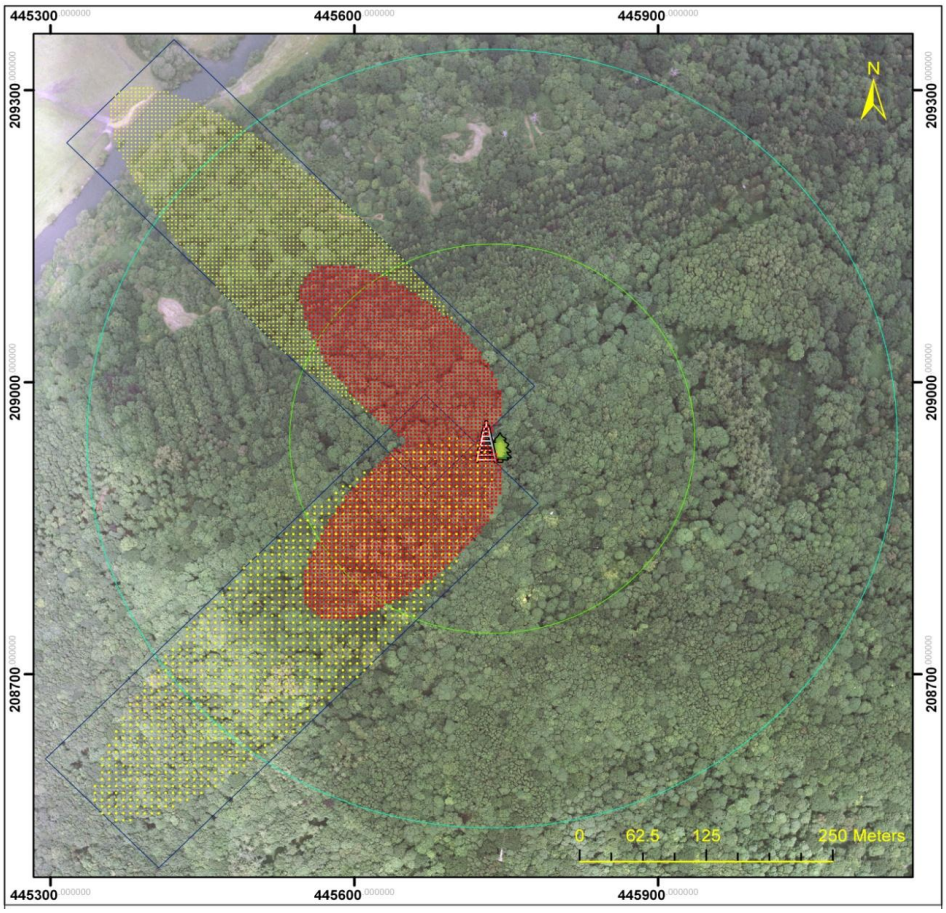

Figure 5-4 Weighted flux tower footprint, overlaid on an aerial image of Wytham Woods, based on two prevailing upwind directions (i.e. 225° and 315°) on the crosswind integrated surface coverage under moderate (i.e. yellow points) and unstable (i.e. red points) atmospheric stability conditions. Green and Cyan lines show the buffer distance of 200 m and 400 m around the flux tower site, respectively.

5.2.3 Statistical Analysis

A non-parametric statistical test was applied to determine whether the flux tower footprint variability in terms of micrometeorological conditions would cause a significant difference in the NDVI over a growing season. Mood's Median test (a robust test with respect to other non-parametric tests) was conducted to test the null hypothesis for equality in NDVI for investigating the uncertainty in terms of imprecise definition of flux tower footprint. In this respect, the null hypotheses are as follows.

- H_0: Under the long-term pattern of daytime flux tower footprint, represented by the circular flux tower footprint coverage, there is no significant difference in median NDVI over short time intervals in leaf-off condition.
- $H_{0:}$ Under different atmospheric stability conditions there is no significant difference in median NDVI between the realistic and long-term circular flux tower footprints depending on the prevailing wind directions.

Moreover, the non-parametric Wilcoxon rank-sum test (Wilcoxon, 1945) was conducted for comparison of differences between two independent NDVI values from DMC and MODIS over short time intervals in the leaf-off period.

5.3 Results and Discussion

5.3.1 Temporal Variability of DMC NDVI across the Circular Flux tower footprint

The descriptive statistics and histogram distribution of the DMC NDVI from within the circular flux tower footprint (CFF) across Wytham flux tower extent are presented by Table 5-5 and Figure 5-5, respectively, which indicate its variability through the growing season as expected.

Table 5-5 Descriptive statistics for the DMC NDVI across Wytham flux tower (circular flux tower footprint) site over a growing season in 2010.

Acquisition Date	Mean	Median	Std. Deviation	Skewness	CV %
2nd March	0.6468	0.6375	0.0492	1.059	7.61
5th March	0.6363	0.6285	0.0442	1.610	6.95
7th March	0.6292	0.6232	0.0440	1.542	6.99
20th April	0.7280	0.7241	0.0354	0.194	4.86
27th April	0.7905	0.7905	0.0402	-0.139	5.09
23rd May	0.9012	0.9054	0.0184	-2.925	2.04
4th June	0.9191	0.9207	0.0111	-1.474	1.21
16th June	0.9080	0.9112	0.0160	-2.114	1.76

The mean value of NDVI was relatively high across the CFF coverage during the early Spring in March-April, perhaps a result of flourishing understory canopy and many sparse evergreen coniferous trees. This was followed by a rise during April-May as the forest canopy came into leaf. High values of NDVI in mid-June could have resulted from late developing trees such as oak reaching full photosynthesis capacity.

As Figure 5-5 shows, the distribution of NDVI values during leaf-off conditions early in the season (2nd -7th March) was positively skewed, probably due to the mixture of understory and sparse coniferous trees present (Street et al., 2007), while it is negatively skewed during leaf-on conditions (May – June) when the canopy response is dominated by the intact tree canopy. In general, the

distribution of NDVI was positively skewed and centred on 0.6 in leaf-off conditions and negatively skewed and centred on 0.9 in leaf-on conditions. This suggests that the spatial variability of the canopy changed significantly during transition from leaf-off to leaf-on conditions because of canopy patchiness at fine spatial resolution, that is, scales finer than a MODIS pixel (Williams and Rastetter, 1999; Street et al., 2007; Steltzer and Walker, 2006), for example, at 22 m spatial resolution. This means that using directly MODIS VIs as a proxy of GPP necessitates the addition of uncertainty into the scaling process from the EC flux tower to landscape and regional level without precise definition of area contributing to CO_2 flux measurements in Wytham Woods.

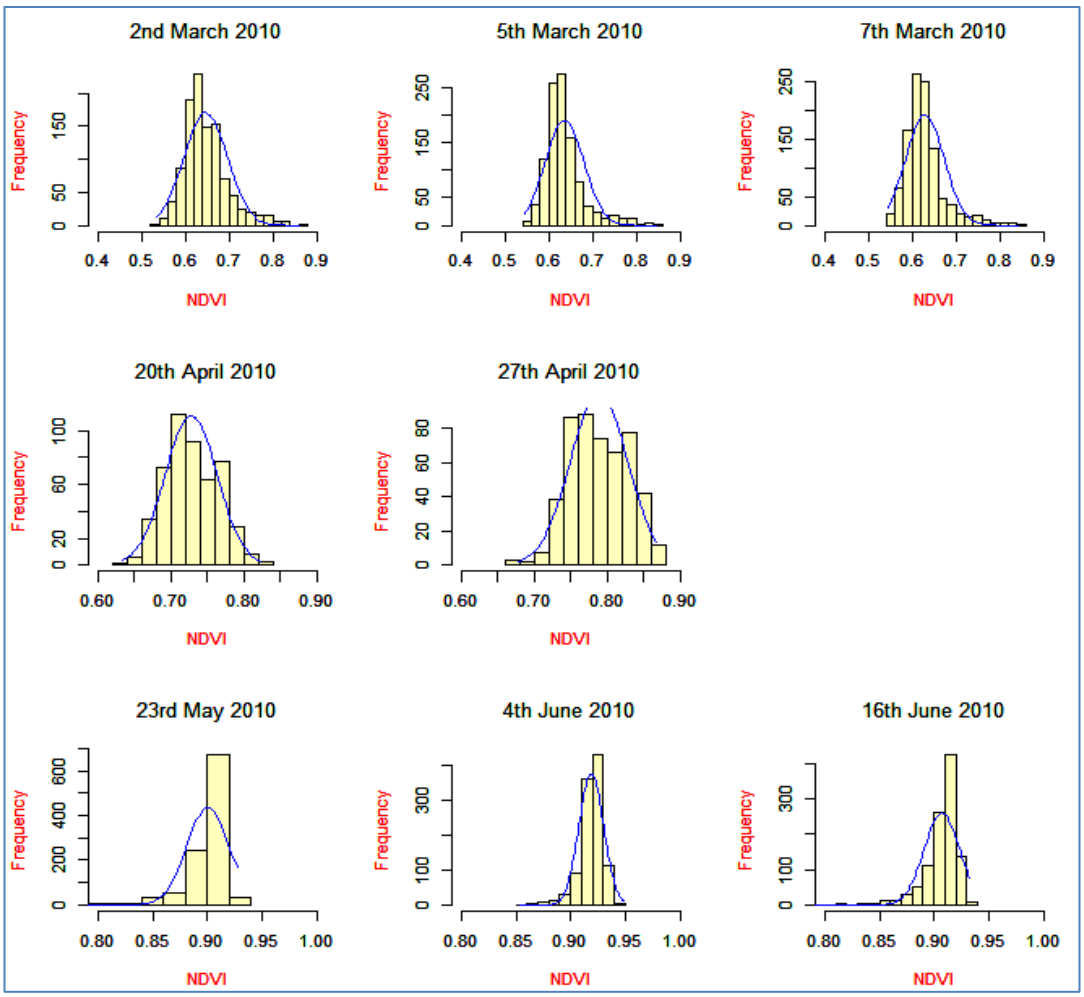

Figure 5-5 Histogram distribution of the DMC NDVI based on the ATCOR/IR-MAD correction.

Figure 5-6 presents the behaviour of canopy reflectance for Red and Near-Infrared spectral bands associated with the hybrid ATCOR/IR-MAD technique from within the CFF during the 2010 growing season, and Table 5-5 shows its central tendency and dispersion indices. Typically, canopy reflectance varies approximately between 0 and 10% in the Red waveband, and 20 and 100% in the Near-Infrared waveband. As is widely known, temperate broadleaf and mixed forests have strong absorption in the Red waveband due to chlorophyll content, and strong reflectance in the Near-Infrared waveband due to internal scattering within vegetation. There was also an unexpected decrease in the NIR band and slight increase in the Red band on 16th June, possibly due to the influence of adjacent cloud shadow as depicted by Figure 5-6.

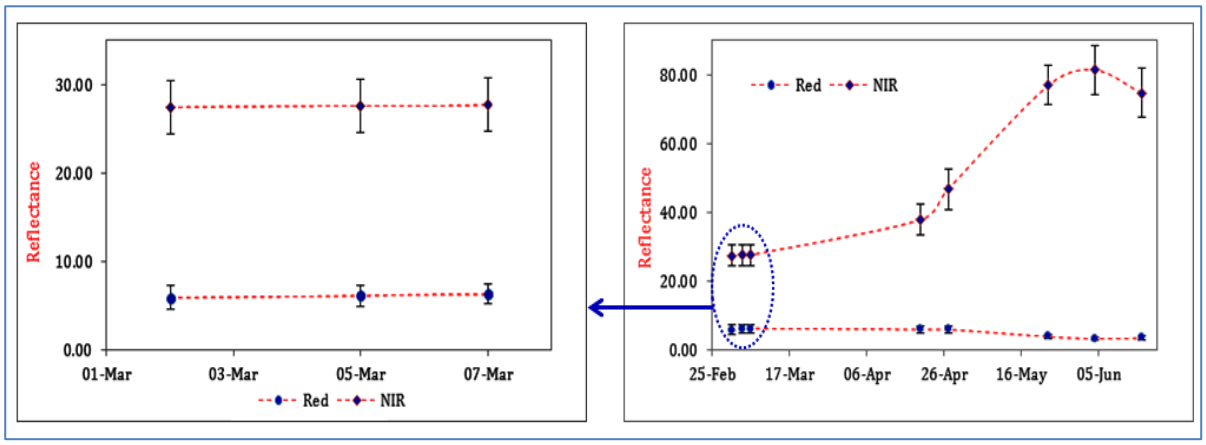

Figure 5-6 DMC Red and Near-Infrared waveband behaviour associated with the hybrid ATCOR/IR-MAD technique across Wytham flux tower extent, i.e. circular flux tower footprint (CFF), over a growing season in 2010

The availability of three acquisitions within five days during early March, when one would expect little change in the biophysical properties of Wytham Woods, provides the opportunity to look at the sensitivity of NDVI to extraneous factors such as changes in viewing conditions, atmospheric variability and sampling error. Table 5-6 and Figure 5-6 show that the reflectance and the NDVI determined from DMC data changed very little during this period (less than 0.018 and 0.015 mean and median NDVI, selectively). This result is important in the context of MODIS, as the MOD13Q1 product is derived from sampling observations within a 16-day

window. MODIS is, therefore, not suitable for identifying the precise moment of change or for following rapidly fluctuating NDVI values. Two MODIS images related to the period 2nd-7th March, the first derived from the 16-day window 18th February – 5th March, and the second from 6th-21st March. Median NDVI from the CFF was slightly higher in the later MODIS image, but the difference was not statistically significant (Wilcoxon-Rank-Sum test, *W=21, p- value = 0.09*).

Figure 5-7 illustrates central tendency and normality plots for samples derived for these short-terms intervals. For each Q-Q plot, the tendency is not linear. Thus, it is reasonable to assume that those samples are from a non-normal population. Furthermore, the slopes in the Q-Q plots from 5th and 7th March are similar, so it appears that the variances are the same, but they vary for 2nd March.

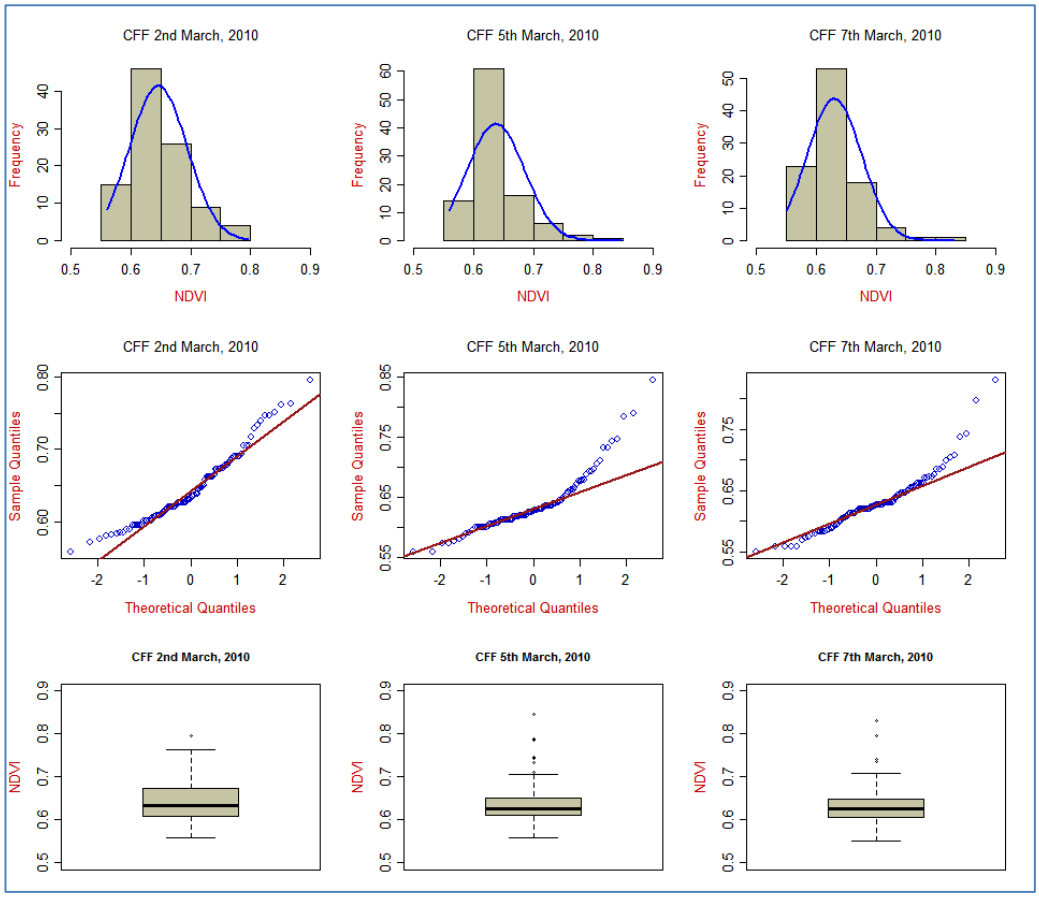

Figure 5-7 Central tendency and normality plots of samples derived for short-terms intervals for DMC imagery in early March 2010.

Table 5-6 Difference below and above the overall Median of the NDVI values across the long-term circular flux tower footprint in Wytham Woods over a-five day interval of leaf-off condition in March 2010.

Difference from Median	DMC NDVI over a-five day interval in early March 2010			Total
	2nd March	5th March	7th March	
≤ Median	46	51	56	153
> Median	54	49	44	147
Total	100	100	100	300

The Mood's median test using the Pearson's Chi-square test (Zar, 2010) was conducted to compare the medians of sample datasets (testing first null hypothesis). Table 5-6 presents the results of the Mood's Median test between three datasets of DMC NDVI during early in the season. The overall median is equal to 0.6271 and the Pearson Chi-square statistic is equal to 2.001 (N= 300; df= 2; and *p*-value= 0.368), which means that there is no significant difference in the NDVI datasets through this short time interval. The percentage of the absolute deviation from the overall median was calculated for these three samples as approximately 3.4% (2nd March: 3.8%; 5th March 3.2%; and 7th March: 3.1 March), which is less than the 5% error in DMC NDVI across southern England predicted by Wilson et al. (20XX) due to aerosol patchiness (i.e. unresolved variation in space and time).

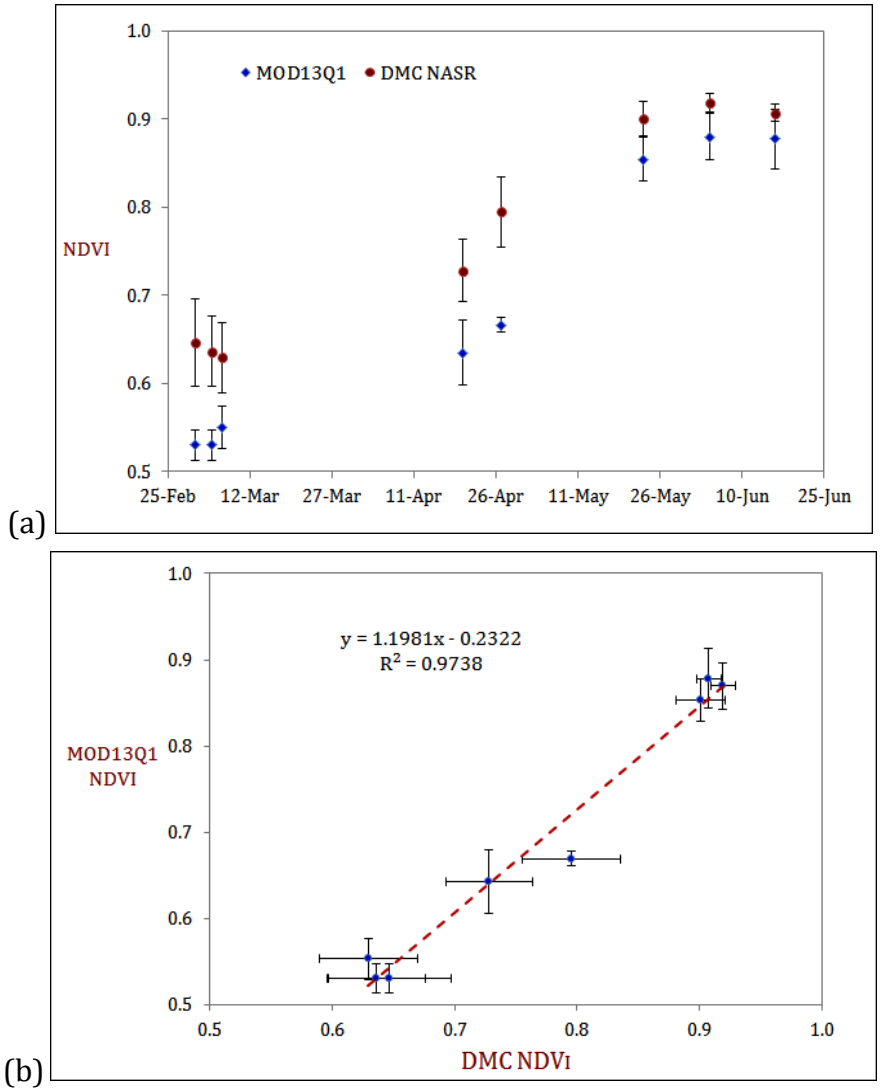

Figure 5-8 Comparison of NDVI derived from DMC constellation and MOD13Q1: NDVI across Wytham's circular flux tower footprint over the early growing season in 2010.

Figure 5-8 compares the NDVI values from an array of 3×3 MODIS pixels centred on the flux tower location (i.e. approx. 400m buffer), with the averaged values of an array of 37×36 DMC pixels within the same area. The error bars on the Y-axis (Figure 5-8a) show ± 1 standard deviation of the DMC NDVI and MOD13Q1 values. The two datasets were highly correlated ($R^2 = 0.974$, $p < 0.05$), showing that data from the DMC SLIM-6-22 sensor closely matched MODIS over this period of time (Figure 5-8b). However, the DMC NDVI values are higher than the MODIS NDVI values for all dates through the growing season, which indicates a significant bias.

The source of this bias is unknown; however, it is most likely due to differences in Sun-sensor geometry between DMC and MODIS. In addition, there was a small unavoidable spatial mismatch between MODIS- and DMC-based subsets across the CFF due to the different pixel sizes. A further factor to consider is the difference in the wavelength of maximum sensitivity for the Red and Near-Infrared bands, which are 660 nm and 835 n for DMC, and 645 nm and 858 nm for MODIS, respectively.

5.3.2 Temporal Variability of DMC NDVI across the Realistic Flux tower footprint

Since the observed data from within the CFF and RFFs were not normally distributed, median absolute deviation (MAD), a robust measure of statistical dispersion that is more resilient to outliers in a dataset than the standard deviation (Huber, 2004), was computed for use as a consistent estimate of the standard deviation, i.e. $\hat{\sigma} = b \times MAD$ where b is a constant scale factor, and equal to the inverse of the third quintile of the underlying distribution (Q_3). The MAD is defined as the median of the absolute deviations from the median of the dataset, i.e. $MAD = Med(|x_i - Med(x_i)|$ where x_i refers to NDVI (Huber, 2004).

The main results presented in Figure 5-9 compare the temporal trend of DMC NDVI from within the CFF with the trend of DMC NDVI from four realistic flux tower footprints, NW Moderate, NW Unstable, SW Moderate, and SW unstable conditions. As expected, the variability in the DMC NDVI across all flux tower footprint coverages decreased during developing canopy greenness, which shows that the forest canopy was more homogeneous in leaf-on than leaf-off condition, an expected trend in temperate deciduous forests. Of particular interest in the NW Moderate RFF is the relatively high variability in the temporal DMC NDVI trend, caused by the footprint fetch reaching beyond the forest canopy and including some of the surrounding landscape. These extraneous patches contributed to the composite surface reflectance and, therefore, the VI.

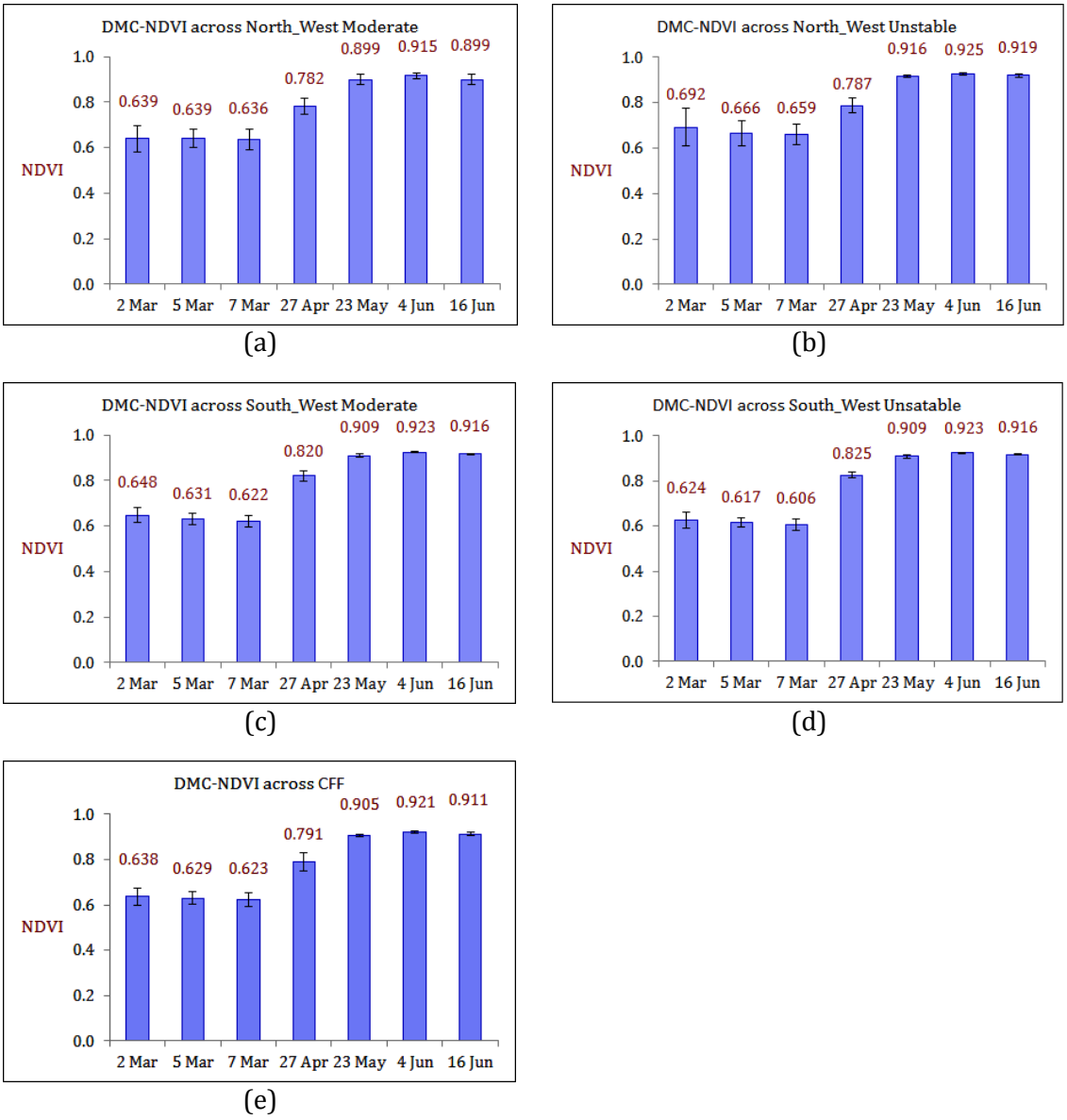

Figure 5-9 Plot of ATCOR/IR-MAD based median of DMC NDVI and MODIS NDVI across various flux tower footprint coverages over the growing season in 2010 as: (a) RFF NW Moderate, (b) RFF NW Unstable, (c) RFF SW Moderate, (d) RFF SW Unstable, and (e) DMC NDVI over CFF; Error bars show the estimated standard deviation based on the median absolute deviation (Huber, 2004).

To address the second hypothesis, the median difference between the CFF and all RFFs was computed to show the spatial variability of the DMC NDVI throughout the growing season. As Figure 5-10 illustrates, there were three distinct phases. The first phase, covering five days in March showed that the median NDVI computed from the RFF differed from that computed from the CFF by up to 5%

depending upon the strength and direction of the wind. The NDVI of the RFF was larger than that from the CFF on most occasions, but the percentage difference varied. The sole exception was a strong wind from the south-west, which caused the NDVI of the RFF to be less than that from the CFF.

The second phase, represented by the data from 27th April showed smaller differences between the NDVI of the RFF and the CFF. A south-westerly wind at this time of the year caused the NDVI from the RFF to be up to 4% higher than the CFF, whereas a north-westerly wind caused a slight reduction in the NDVI from RFF compared to the CFF (around 1%).

The third phase comprised data collected in May and June, when the tree canopy was fully developed. The NDVI values from the RFF differed slightly from the CFF (around 1-2%) during this period, and the direction of the difference was the same on each occasion: a moderate wind from the north-west resulted in the NDVI from the RFF being slightly lower than the CFF, whereas the other conditions all lead to a slight increase for the RFF compared with the CFF.

The relatively high percentage of the median deviation from unstable RFF with respect to moderate RFF, in particular early in the season, shows that the small area of contributing flux measurements are more homogeneous than the larger area, because as fetch distance increases, the similarity of biophysical properties are more similar to the CFF.

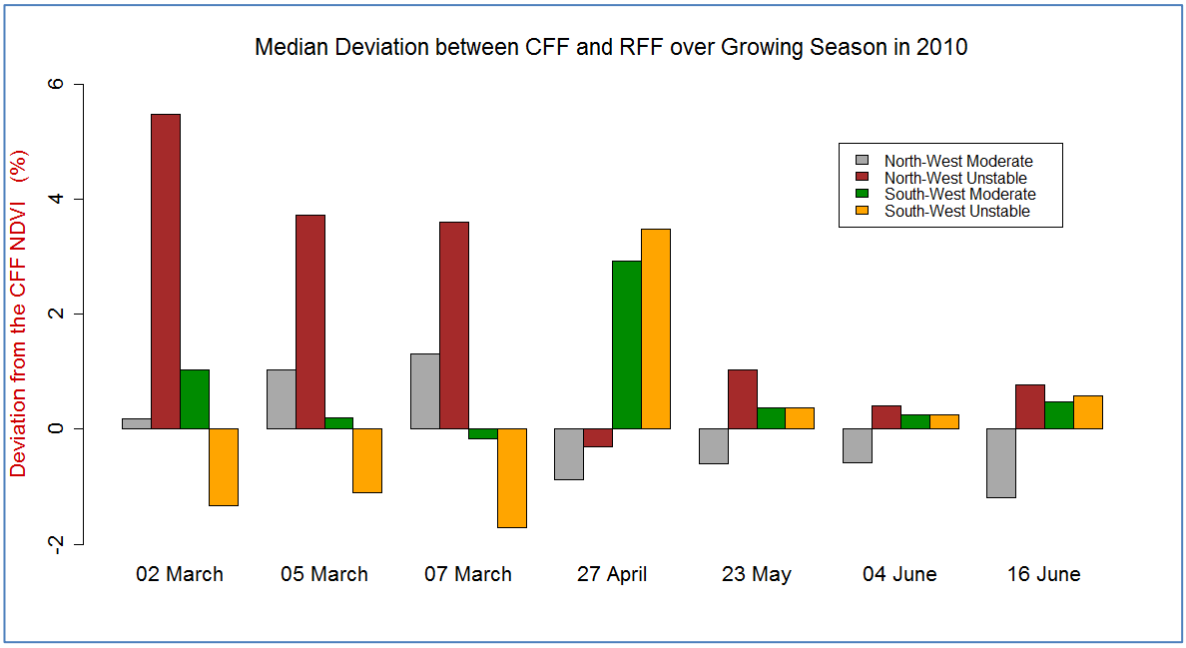

Figure 5-10 The Median DMC NDVI as percentage deviation from the CFF NDVI for each of the weighted flux tower footprint coverage

The Mood's Median test was applied to test the effects of flux tower footprint variability in the NDVI with respect to wind direction and atmospheric stability condition. Table 5-7 shows the results of this investigation under two atmospheric stability conditions: moderate and unstable conditions, respectively, whether the median DMC NDVI differs between the CFF and those derived from the weighted flux tower footprint (i.e. RFF_S), during the study period.

The assumption was that there were no median differences between the CFF and the weighted RFFs. While, there are complex results for all contexts, the north-west unstable RFF shows that there is a significant difference (p-value < 0.05) through the period of the growing season. The CFF, which covers various canopy patches such as secondary, plantation, and ancient canopies, encompasses spatial variation in NDVI. However, the footprint is fixed through time. Since both wind direction and atmospheric stability condition can influence the RFF footprint fetch (i.e. shape and size), the weighted RFF coverage is relatively more homogeneous than the CFF, presumably due to the effects of greater averaging. Therefore, using MODIS NDVI as a proxy for GPP in Wytham woods (pixel size from 250 m to 1 km)

is problematic, because validating MODIS NDVI derived GPP using the tower specific CO_2 flux measurements needs to take into account local spatial variability.

Table 5-7 Mood's test between the CFF and RFF in terms of wind direction and atmospheric stability condition across Wytham flux tower extent over growing season in 2010, degrees of freedom for each case is equal to one.

	2nd March	5th March	7th March	27th April	23rd May	4th June	16th June
(a) NW Moderate RFF vs. CFF							
N	150	150	150	150	150	150	150
Median	0.6348	0.6305	0.6271	0.7924	0.9006	0.9179	0.9085
Chi-square	0.120	6.454	3.414	1.920	9.015	9.720	8.339
P Value	0.729	**0.011**	0.065	0.166	**0.003**	**0.002**	**0.004**
(b) NW Unstable RFF vs. CFF							
N	130	130	130	130	130	130	130
Median	0.6452	0.6336	0.6308	0.7847	0.9048	0.9217	0.9141
Chi-square	8.493	17.333	15.397	11.093	10.922	8.493	8.493
P Value	**0.004**	**0.000**	**0.000**	**0.001**	**0.001**	**0.004**	**0.004**
(c) SW Moderate RFF vs. CFF							
N	150	150	150	150	150	150	150
Median	0.6455	0.6285	0.6271	0.7934	0.9048	0.9212	0.9132
Chi-square	6.454	1.334	0.857	3.000	5.918	2.260	1.614
P Value	**0.011**	0.248	0.355	**0.083**	**0.015**	0.133	0.204
(d) SW Unstable RFF vs. CFF							
N	130	130	130	130	130	130	130
Median	0.6321	0.6246	0.6217	0.7924	0.9048	0.9212	0.9138
Chi-square	0.103	2.172	4.333	2.773	15.532	5.175	6.240
P Value	0.749	0.141	**0.037**	0.096	**0.000**	**0.023**	**0.012**

However, before we can conclude that the observed differences in NDVI are real, and a function of the canopy area sensed, we must set the measured variation in NDVI into context. In particular, Wilson et al. (2012) modelled the spatial variability of aerosol amount over southern England and showed that NDVI could have a relative variation of up to 5% from that source alone. Thus, the observed differences in NDVI between the RFF and the CFF are comparable in magnitude to the uncertainty in the atmospheric correction, and could even be due to real variation in aerosol amount and type, caused by different air masses over the site, rather than actual variations in the area of the canopy sensed. The next chapter

will seek to overcome this uncertainty by replacing empirical observation with geostatistical modelling.

5.4 Conclusion

The available evidence shows that NDVI is a reliable estimator of biophysical variables closely related to photosynthesis capacity at various spatial and temporal scales over a wide range of plant functional types (Tucker 1979, Sellers, Berry et al. 1992, Turner, Ritts et al. 2005, Turner, Ritts et al. 2006).

The research reported in this chapter has shown that NDVI can be accurately measured using data from the DMC constellation, and that this system has several important advantages over the more commonly used systems such as MODIS. First, the data from DMC are of finer spatial resolution, which means that smaller areas of uniform land cover can be sensed, and also that heterogeneous sites can be studied. This is particularly important if the aim is to compare the satellite observation with ground measurements, either for model calibration or for product validation purposes. In the specific example studied, the uncertainty in NDVI as a result of differences in the conditions of measurement did affect the median NDVI. However, the difference was less than that due to uncertainty in the atmospheric correction. Thus, in the case of Wytham Woods, it is more important to improve the representation of aerosols in the atmospheric model used than replace the generalised circular flux tower footprint with a realistic flux tower footprint. However, that does not mean that computing and investigating the RFF is not important, because an accurate estimate of the RFF is crucial in linking plant spectral properties, notably NDVI, to the EC data measured from the flux tower.

The second advantage of DMC over MODIS concerns the temporal precision of the measurements. The 16-day sampling window of MODIS could become a limitation at certain times during the growing season. In the case of Wytham Woods in 2010, the DMC time-series shows an increase in NDVI between 20th and 27th April, whereas the MODIS data show no significant change between these dates.

DMC is not without its limitations for this task, and perhaps the greatest is the large off-nadir view angle of some pixels as a consequence of the very wide swath. The eight DMC images of Wytham Woods acquired in 2010 were imaged at view zenith angles from 0.82 to 28.74.

In summary, a time-series of ten DMC images were acquired and inter-calibrated, and these provided a unique insight into the seasonal changes occurring in one of the most important ecological sites in the UK. The author is not aware of any other analysed time-series of multispectral data of comparable spatial resolution and temporal frequency from southern England.

The accuracy of the calibrated DMC data was assessed by comparing it with MODIS, and although there was evidence of a consistent bias, there was a large linear correlation between the two sensors. The heterogeneity of Wytham Woods had greatest impact on the DMC data early in the season, and this highlighted the importance of understanding how the flux tower footprint varies with weather conditions. As the canopy began to green-up, the precision of temporal sampling became more important. The rapid rise in NDVI in late Spring was captured effectively by DMC images one week apart, whereas in the MODIS data from the same period this was less clear.

The research showed that differences in median NDVI between the CFF and the RFF decreased consistently as the season progressed, so the advantages of DMC over MODIS are likely to be most important when the canopy is greening-up in late-Spring, when NDVI is changing rapidly and the when the woodland canopy is still quite open.

In the next chapter the spatial variability within the Wytham Woods site will be investigated in more detail using geostatistical methods.

6. Assessing the Adequacy of Different Supports for Scaling between Remote Sensing Images and Flux Tower Measurements

6.1 Introduction

The previous chapter demonstrated the potential of the DMC constellation as a source of fine spatial resolution, high temporal frequency NDVI data for mixed woodland in southern England. Figure 5-2 clearly shows the utility of such data for validation of the comparable MODIS product, for example. In this chapter, the final piece of the jigsaw is studied – the relationship between the point-based, time-integrated measurements made from the flux tower in Wytham Woods and the spatially continuous three-dimensional multispectral surface sampled by DMC.

Remote sensing has a crucial role to play in scaling tower-specific flux measurements to larger areas; tasks which are not easily achieved using *in situ* field surveying alone (Atkinson and Foody 2002b; Milton et al. 2011). Despite the consensus that current remotely sensed models provide valuable data on the NEE of CO_2 with spatially and temporally consistent coverage, these data carry large uncertainties (Chen et al. 2012; Kim et al. 2006; Xiao et al. 2011a). A significant challenge, in the context of RS-based modelling, is to identify the sources of uncertainty, and subsequently reduce the expected uncertainties in new products based on proposed platform-sensor and processing algorithms (Woodcock 2002).

There are several sources of uncertainty associated with scaling RS-based models of the NEE of CO_2 at various spatial and temporal scales, including sensor limitations in terms of support size defined by spatial and temporal resolution (Dungan 2002); the spatial heterogeneity of land surface properties (Atkinson and Foody 2002b; Chen et al. 2012; Kim et al. 2006; Sogachev et al. 2004; Xiao et al. 2012); pre-processing calibration (Baret 1995; Danson 1995; Liang 2004; Woodcock 2002); and the structure of the model proposed and estimation of its

parameters (Dungan 2002). Among these, spatial heterogeneity due to differences in species composition (Flanagan et al. 2012; LeCain et al. 2002; Wang et al. 2013) and seasonal variation (Richardson et al. 2013; Schwartz et al. 2013; Wu et al. 2012a; Wu et al. 2012b) introduce a large amount of uncertainty as they affect different functions for the same fraction of photo-synthetically active radiation (fPAR) and subsequently NEE of CO_2.

Lack of understanding of the spatial heterogeneity of land surface properties at various scales limits our ability to integrate *in situ* measurements and remotely sensed data (Atkinson and Curran 1995; Atkinson and Kelly 1997; Curran and Atkinson 1998). Spatial heterogeneity is commonly the result of complex spatial processes occurring simultaneously over a long period of time (Forman 1995). In ecology, such heterogeneity can be decomposed into the two components of spatial variability and spatial structure. Spatial variability refers to the spatial variance distribution over space and time (Forman 1995). Spatial heterogeneity also depends on spatial structure (horizontal and vertical structure) at a certain scale, but refers to objects in a mosaic and may include patches or corridors (Forman 1995).

In the context of the scaling process, the use of remotely sensed data has been limited by the availability of reliable algorithms to convert, for example, tower-based EC measurements to represent the larger area desired. Although satellite sensor data are used widely to investigate photosynthesis function and carbon sequestration, airborne remote sensing systems provide an important complementary source of remotely sensed observations. An example of an airborne RS system is the Airborne Imaging Spectrometer for Application (AISA) Eagle sensor operated by the UK Natural Environment and Research Council (NERC) Airborne Research and Survey Facility (ARSF). As changes in vegetation occur over space and time, the suitability of a given platform-sensor will vary with the spatial, temporal and spectral scales of the variable being measured (Jensen 2005; Lillesand et al. 2008).

In this chapter, NDVI is assumed reasonably to be a reliable spectral index of CO_2 flux and as a proxy of photosynthesis capacity. Accordingly, the potential of a spectral vegetation index (for example, NDVI) for investigating the variability in CO_2 flux from airborne and satellite sensing data might be expressed as:

$$CO_2\ Flux\ = f(NDVI) \quad 6\text{-}1$$

Calibration and validation of a spectral index of CO_2 flux requires a relation between the *in situ* measurements (i.e. EC flux data obtained across a tower-specific footprint coverage) and selected platform-sensor pixels (Atkinson and Kelly 1997): for example, a transfer function between NDVI and CO_2 flux.

Previous studies have demonstrated RS-based models for the up-scaling process for various ecosystems (Chen et al. 2009b; Desai et al. 2008; Kim et al. 2006; Xiao et al. 2012). However, these studies have taken at best an empirical approach to characterising the difference in spatial and temporal scales between the platform-sensor pixels and the realistic flux tower footprint coverage.

Therefore, this chapter aimed to investigate the spatial heterogeneity in NDVI (as a proxy for CO_2 flux) relative to various choices of image support (i.e. the effect of choice of support) as a primary source of uncertainty associated with the process of scaling between tower-based EC measurements and coarse satellite sensor observations, for example, from MODIS. In this investigation, there were two overall goals:

- To test the methods of predicting the NDVI across the flux tower domain based on observed imaged data from satellite remote sensing systems (i.e. DMC and MODIS);
- To test the effect of the mismatch between the various supports of remote sensing systems and the actual flux tower footprint, which itself varies through time, using spatial statistical techniques, taking account of the spatial co-variability.

This led to three hypotheses:

H_0: There is no significant difference in NDVI value between that averaged across the flux tower domain and that area-weighted by the flux tower footprint criteria.

H_0: There is no significant spatial variation in NDVI within a certain support size at a scale smaller than the data observed.

H_0: There is no co-variability in NDVI between that area averaged across the choice of support of remote sensing systems and that weighted by the flux tower footprint criteria as a tower-based true value.

6.2 Methodology

6.2.1 Site Study and Data Acquisition

Tower-based flux measurements form Wytham Woods in 2010 were applied to estimate the true flux tower footprint coverage to support investigation of the effect of choice of support (e.g. various spatial resolutions of remotely sensed datasets) with which to characterise the true flux tower footprint.

A hyperspectral vegetation index, red edge NDVI, was derived from hyperspectral imagery acquired by the Airborne Imaging Spectrometer for Application (AISA) Eagle sensor across the Wytham's flux tower domain to support investigation of the spatial heterogeneity in NDVI, which itself influences the effect of choice of support. The imagery was acquired in cloudless conditions on 9th September 2009 (i.e. Julian day of flight: 252). The AISA Eagle hyperspectral imagery comprises 252 narrow spectral wavebands ranging from 392.57 nm to 987.24 nm with a full-width at half maximum (FWHM) ranging from 2.20 nm to 2.44 nm in the VNIR wavelengths.

In addition, the broadband NDVI was derived from measurements obtained by the UK Disaster Monitoring Constellation (DMC) satellite, the best available multi-temporal dataset at 22 m spatial resolution (Crowley 2010). The UK-DMC2

imagery with SLIM-6-22 imager is a unique satellite constellation that delivers frequent images in three spectral wavelengths: green (0.52-0.60 μm) and red (0.63-0.69 μm) to near-Infrared (0.77-0.90 μm) wavelengths, equivalent to Landsat Thematic Mapper (TM) bands two, three and four (Crowley 2010). The UK-DMC2 data acquired across southern England for a short-period during Spring-2010, as well as the corresponding tower-specific measurements for estimating the flux tower footprint coverage, are presented in Table1.

Table 6-1 UK-DMC2 dataset acquired across southern England through Spring-2010

Imaging Date	Imaging Time	Corresponding Tower-specific Measurements				
		wind speed (m/s)	wind direction (degree)	x-peak (m)	x-offset (m)	x-90% (m)
02/03/2010	09:43:21	0.5834	269	141.78	-21.52	259.23
05/03/2010	09:46:39	2.7794	31	177.49	-26.93	324.51
07/03/2010	09:54:31	2.3303	202	184.15	-27.95	336.67
27/04/2010	10:08:21	1.9535	66	203.70	-30.91	372.43
23/05/2010	09:52:10	1.1281	315	151.11	-22.93	276.28
04/06/2010	09:56:34	1.0245	166	150.68	-22.87	275.49

6.2.2 Image Pre-processing

The pre-processing of the AISA Eagle data and the DMC data to relative reflectance has been described in previous chapters and will not be repeated here.

The UK-DMC2 satellite-derived NDVI, following Tucker (1979) and (Sellers et al. 1992), was calculated as

$$NDVI = R_{\mathrm{NIR}} - R_{\mathrm{Red}} / R_{\mathrm{NIR}} + R_{\mathrm{Red}} \qquad 6\text{-}2$$

where "R_{Red}" and "R_{NIR}" indicates the reflectance in the red wavelengths (centered at 0.660 μm) and near-infrared wavelengths (centred at 0.835 μm), respectively.

Furthermore, red edge NDVI (also known as $NDVI_{705}$), a narrowband spectral index of CO_2 flux, was computed from the AISA Eagle data. The red edge NDVI is the modified normalized difference of brightness values from the spectral position between the red and near-infrared wavelengths where the maximum slope is found (Gitelson and Merzlyak 1994; Sims and Gamon 2002). Calculation of $NDVI_{705}$ is the same as for the conventional NDVI (equation 2), where"R_{Red}" and "R_{NIR}" are 705 nm and 750 nm, respectively.

6.2.3 Estimation of Flux tower footprint Coverage

Several footprint models have been applied to estimate the flux tower footprint coverage across various ecosystems (Kljun et al. 2003; Kormann and Meixner 2001; Schmid 1997; Schmid 2002; Schmid and Lloyd 1999). However, using flux tower footprint models can be problematic in practice because the source area is not explicitly known, particularly in heterogeneous landscapes (Kim et al. 2006). To address this problem, Schmid and Lloyd (1999) and Chen et al. (2009a) demonstrated that long-term patterns of flux tower footprint provide significant information particularly across heterogeneous landscapes.

In this research, the flux tower footprint for a particular time interval (platform-sensor overpass) was computed relying upon Wytham's tower-based EC measurements and the corresponding available high quality UK-DMC2 imagery over 2010 using a simple analytical model, the *EdiRe Footprint Tool* based on the Kormann and Meixner (2001) model which requires parameters that influence the size and shape of the footprint coverage, such as observation height (Z_m); surface roughness length (Z_0); atmospheric stability (Z_m/L); and wind speed and direction (Baldocchi et al. 2001). Additionally, the long-term pattern of daytime weighted flux tower footprint, when solar radiation was more than 20 Wm^{-2}, was computed across the Wytham Woods flux tower extent. As a final point, this area was plotted against the corresponding airborne and satellite sensor imagery to define representative samples for further analysis.

6.2.4 Choice of Image Support

Four different support sizes were examined to test the effect of choice of support to on ability to predict flux tower observation from high temporal resolution of satellite images including:

- Single MODIS pixel at 1km spatial resolution (support size 1);
- Average of a 3×3 window of MODIS pixel at 250 m spatial resolution based on the nearest pixel to the flux tower location (support size 2);
- Average of a 3×3 window of weighted MODIS pixels at 250 m spatial resolution based on the nearest pixel to the flux tower location (Support size 3); and
- Average of MODIS pixels at 250 m spatial resolution across time-specific weighted flux tower footprint (Support size 4).

6.2.5 Spatial Data Analysis

Initially, a paired samples *t*-test was used to compare mean values of NDVI between those averaged across the estimated long-term pattern flux tower footprint and those area weighted by the flux tower footprint criteria, to test the first research hypothesis.

In the context of Earth science, spatial autocorrelation exists in most environmental variables (Isaaks and Srivastava 1989) and the degree of similarity depends on the environment of the observed variables (Curran and Atkinson 1998). Spatial autocorrelation means that a variable is correlated with values of the same variable at nearby locations, the first law of geography (Tobler 1970), usually due to the influence of similar environmental conditions (Curran and Atkinson 1998). In general, if the covariance between attributes of a variable defined at two locations is non-zero, spatial autocorrelation exists between those locations. Remote sensing has the potential to provide useful quantitative data,

normally available as pixels (Stein et al. 1999) with different spatial resolutions. A deeper understanding of the variation in spatial autocorrelation at one spatial resolution compared with another will increase our ability for up-scaling processes (Curran and Atkinson 1998).

Matheron (1971) demonstrated that spatially auto-correlated data can be interpolated on the basis of their spatial structure and known-samples, a branch of statistics that is referred to as geostatistics. Geostatistics is the application of the theory of regionalized variables to address typical questions regarding the Earth-sciences in terms of spatial heterogeneity (Hengle 2009).

A Random Function (RF) is a set of random variables that vary as a function of some set $D \subset \mathcal{R}^d$ containing spatial coordinates $s = [s_1, s_2, \dots s_n]$. For a process in two dimensions, $d = 2$, coordinates are often identified as $s = [x, y]$, the Cartesian coordinates (Schabenberger and Gotway 2005). Accordingly, the value of the variable "Z" at location $s = [x, y]$ is referred to as a realisation of the Random Function or spatial process $Z(s)$ (Plant 2012; Schabenberger and Gotway 2005). A spatial process $\{Z(s): s \in D \subset \mathcal{R}^d\}$ is stationary if the distribution of observations is invariant under translation of the coordinates. Under this assumption, the spatial process $Z(s)$ has a constant mean (μ) and variance (δ^2); and the covariance between attribute values at different locations, $Z(s)$ and $Z(s + h)$, varies only as a function of their spatial separation h, the lag vector (Schabenberger and Gotway 2005). Accordingly, the covariance function $C(s, h)$ of a spatial process $Z(s)$ such as a remotely sensed variable is expressed as in Equation 5.5 and plays an important role in statistical modelling of regionalized variables.

$$C(s, h) = Cov[Z(s), Z(s + h)] \qquad 6\text{-}3$$

In geostatistical applications, a common tool to study the spatial dependence of a process is the variogram (Isaaks and Srivastava 1989; Schabenberger and Gotway 2005). The variogram is a function that relates (semi)variance to spatial separation and provides a brief description of both of the aforementioned components of spatial heterogeneity. The theoretical variogram function is defined as

$$\gamma(h) = \frac{1}{2}E[(Z(s) - Z(s+h))^2] \quad 6\text{-}4$$

where $Z(\mathbf{s})$ refers to a RF associated with location $\mathbf{s} = (x, y)$; "E" refers to the mathematical expectation and **h** is the lag or separating distance. Figure 6-1 illustrates a typical variogram function. The variogram transitions smoothly from the intercept, corresponding to the nugget variance (C_0) and stabilizes at a value that corresponds to the *a priori* variance of the observation process, also known as the sill variance I, which means that there is a distance beyond which $Z(\mathbf{s})$ and $Z(\mathbf{s} + \mathbf{h})$ are uncorrelated. The lag distance at which the sill variance is maximum, is often called the range (A_0), beyond which there is no spatial autocorrelation amongst the observed data. In general, the shape of the variogram provides information regarding the spatial structure in the observed data. The sill variance indicates the absolute amount of spatial variability whereas the range reflects the spatial scale of variability (Isaaks and Srivastava 1989). The nugget variance reflects both any measurement error in the observed values and micro-structure that exists at distances smaller than the minimum distance amongst the observed data (Journel and Huijbregts 1993).

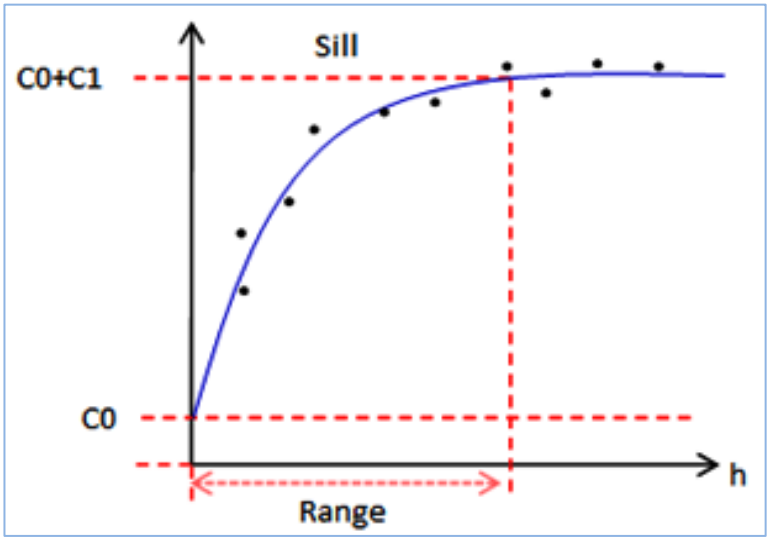

Figure 6-1 Schematic representation of a variogram, adopted from Isaaks and Srivastava (1989).

In geostatistics, an important technique for interpolation is kriging (Leuangthong et al. 2008), whereby the set of unknown values is regarded as a set of spatially dependent random variables (Goovaerts 1997; Matheron 1971) which can be predicted based on the available samples weighted by a certain coefficient determined by the empirically estimated variogram or covariance function (Starck et al. 1998).

The transfer function from spectral index (e.g. NDVI) to EC-based CO_2 flux measurements is assumed to be a process model that is identified over a specific weighted flux tower footprint, and then the value of CO_2 flux is defined as

$$Tower\ Specific\ \ CO_2\ Flux = \frac{1}{n}\sum_{\boldsymbol{s}} CO_2\ flux\ (\boldsymbol{s}) \qquad 6\text{-}5$$

where **s** corresponds to spatial coordinates.

The DMC NDVI was considered as the realisation of a punctual spatial process, $Z(\mathbf{s}) = \text{NDVI}(\mathbf{s})$ which can describe the spatial distribution of CO_2 flux over the image domain. Let "$\text{NDVI}(\mathbf{s}_i)$" denote a regionalized variable defined on a DMC pixel with a point support. Its average over the flux tower footprint coverage "**v**" defines a new spatial process as

$$f\left(\overline{NDVI}_v(\boldsymbol{s})\right) = \frac{1}{n}\sum_s f(NDVI(\boldsymbol{s_i})) \qquad 6\text{-}6$$

Accordingly, the transfer function between NDVI and CO2 flux ($CO_2\ Flux = f(NDVI)$) can be expressed by the following expression.

$$Observed\ Tower\ Specific\ CO_2\ flux = \frac{1}{n}\sum_s f(NDVI(\boldsymbol{s})) \qquad 6\text{-}7$$

The experimental variogram provides an empirical description of the spatial heterogeneity of NDVI, in a valid stationary domain.

To investigate key parameters of spatial heterogeneity in NDVI, testing the second research hypothesis, the experimental variogram was computed across the long-

term pattern of the flux tower footprint coverage over multi-temporal NDVI images during leaf-off and leaf-on conditions, defined as

$$\hat{\gamma}(h) = \frac{1}{2N(h)} \sum_{i=1}^{N(h)} [NDVI(s_i) - NDVI(s_i + h)]^2 \quad 6\text{-}8$$

where "$N(h)$" is the number of paired DMC pixels at specific lag intervals in units of 22 m from the centre DMC pixel.

An experimental variogram contains a signal that results from both the true variogram and sampling error. To test the goodness-of-fit of the variogram model, therefore, a simple Monte Carlo technique based on permutations of the data across the locations was used to simulate the upper and lower envelopes under the null hypothesis of no spatial correlation in the observed values (Diggle and Ribeiro Jr. 2007).

The theoretical variogram was estimated by fitting a permissible mathematical model to the experimental variogram (Atkinson and Jeganathan 2010). Two commonly used mathematical models, the exponential model (equation 9) and spherical model (equation 10), were fitted to the observed values of semi-variance and the best fit determined (Isaaks and Srivastava 1989).

$$\gamma(h) = C_0 + C[1 - exp\left(-\frac{3h}{a}\right)] \quad 6\text{-}9$$

$$\gamma(h) = \begin{cases} C_0 + C(1.5\left(\frac{h}{a}\right) - 0.5\left(\frac{h}{a}\right)^3) & if \quad h \leq a \\ C_0 + C & if \quad h > a \\ 0 & if \quad h = 0 \end{cases} \quad 6\text{-}10$$

The initial observed data, as given by equation 7, is spatially limited to a particular weighted flux tower footprint, while estimates are desired for the same area based on imagery. The study area was sampled on a continuous grid of 22 m × 22 m (using the DMC NDVI), whereas the remotely sensed MODIS image pixels had a pixel size of approximately 231×231 m, represented in the British National Grid coordinate system. Hence, there is a bias between the support sizes of the DMC (22

m) observed data and the MODIS pixels (231 m) used for prediction. Thus, it needs to be established a relation between the observed value and the desired support size.

One possible means of downscaling is to estimate the MODIS NDVI value over the flux tower site through a technique known as block kriging (Burgess and Webster 1980), resulting in small (optimal) prediction variances (Atkinson and Kelly 1997). With this approach of using block-kriging, as illustrated in Figure 6-2, one essentially takes into account the spatial covariance (i.e. co-variability) between the observed points, as well as the point-to-block covariance over the weighted flux tower footprint and the points to be estimated within the desired landscape domain, block-to-block covariance as equation 6-11, were computed by means of the *Package "SpatialTools"*, *Version 0.5.4* in *R Environment*, *Version 3.0.2*.

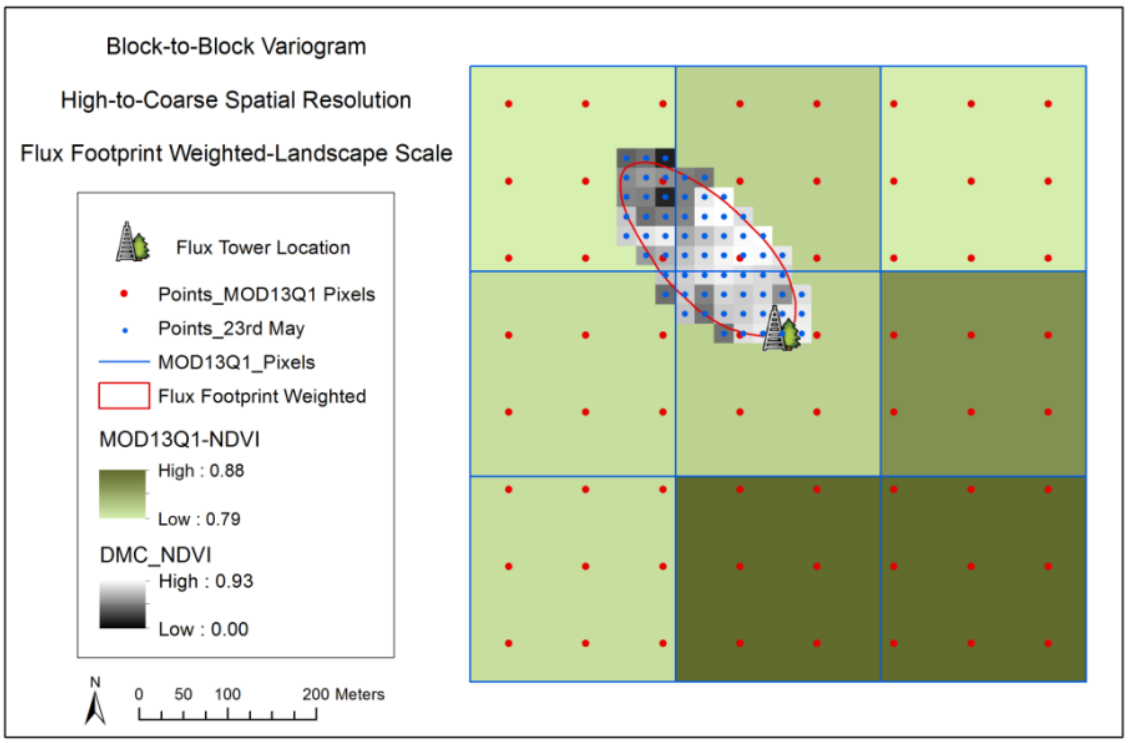

Figure 6-2 Spatial cross-covariance using block kriging technique between the observed responses across tower-specific weighted flux tower footprint and the responses to be estimated within desired support size (i.e. landscape domain cover the Wytham Woods flux tower extent)

The mean value of the block-to-black covariance $\bar{\gamma}(\mathbf{V}, \mathbf{v})$, considering a regular grid of points $(s_i, i = 1, 2 \ \dots \ n)$ as fine spatial resolution over the weighted flux tower footprint and $(s_j, j = 1, 2 \ \dots \ m)$ as coarse spatial resolution over the desired landscape domain are localized over the support size "**v**" and "**V**" respectively, was approximated as

$$\bar{\gamma}(\mathbf{V}, \mathbf{v}) \cong \frac{1}{nm} \sum_{i=1}^{n} \sum_{j=1}^{m} \gamma(s_i - s_j) \qquad 6\text{-}11$$

where *"n"* and *"m"* refer to the observed DMC spatial resolution pixels and the coarse satellite spatial resolution pixels, respectively.

As a final point, cross-validation by block-kriging was performed to quantify the goodness-of-fit for the variogram model and estimation bias as uncertainty in terms of the root square (RMS) error. The lower the RMS error represents the better the performance.

All geostatistical computations were carried out in the packages *"geoR"*, (Ribeiro Jr and Diggle 2001) and *"SpatialTools"*, (French 2013) in the *R Environment* (R Core Team 2013).

6.3 Results and Discussion

6.3.1 Flux tower footprint Coverage

Wytham's flux tower footprint coverage was estimated relying upon the tower-specific EC observations over the early growing season in 2010 (observation height at 25 m and mean canopy height at 17 m). Table 6-2 provides the criteria applied to estimate the true flux tower footprint associated with the corresponding platform-sensor overpasses on the basis of the Kormann and Meixner (2001) model using the *EdiRe Footprint Tool*.

Table 6-2 Wytham's flux tower footprint modelling criteria

Acquisition Date	Time	Sensible Heat Energy (Wm-2)	Air Temperature (°c)	Wind Speed (ms-1)	Wind Direction (degree)	Surface Roughness Length
02/03/2010	10:00	178.70	2.2	< 2	269	0.75
05/03/2010	10:00	58.37	0.6	2.8	31	0.75
07/03/2010	10:00	111.13	-2.2	2	202	0.75
27/04/2010	10:30	316.32	15	2	66	1
23/05/2010	10:00	329.71	19	< 2	315	1
04/06/2010	10:00	209.13	15.7	< 2	166	1

Figure 6-3 illustrates the estimation of the horizontal shape and position of the flux tower footprints for particular dates and times. The gradient colours signify the source weight and distance for the weighted footprints. The time-specific weighted flux tower footprint is hereafter termed the real flux tower footprint (RFF). In addition, the long-term pattern of day time flux tower footprint coverage was calculated based on the annual mean of 90% cumulative footprints (fetch distance was approximately 400 m). Accordingly, a buffer distance from the flux tower location of 400 m was considered as representative of the long-term pattern of day time flux, here referred to as the circular flux tower footprint (CFF), which covers a 3×3 MODIS window at 250 m resolution. Representative samples of the DMC NDVI as a spectral index representative of CO_2 flux were defined over both the real and circular flux tower footprint coverage using ENVI version 4.8 (Exelis Visual

Information Solutions, Boulder, Colorado) to test the primary goal of this investigation.

6.3.2 Statistical Analysis

A paired-samples t-test was conducted to compare the NDVI values averaged across the specific flux tower footprint criteria with the NDVI area weighted by the long-term pattern flux tower footprint at 95% confidence interval (Table 6-3). Figure 6-4 depicts the NDVI variation for the paired samples over the early growing season in 2010. There were statistically significant differences in the NDVI values in all datasets for the realistic and circular flux tower footprint (p-value < 0.05) over the period of study.

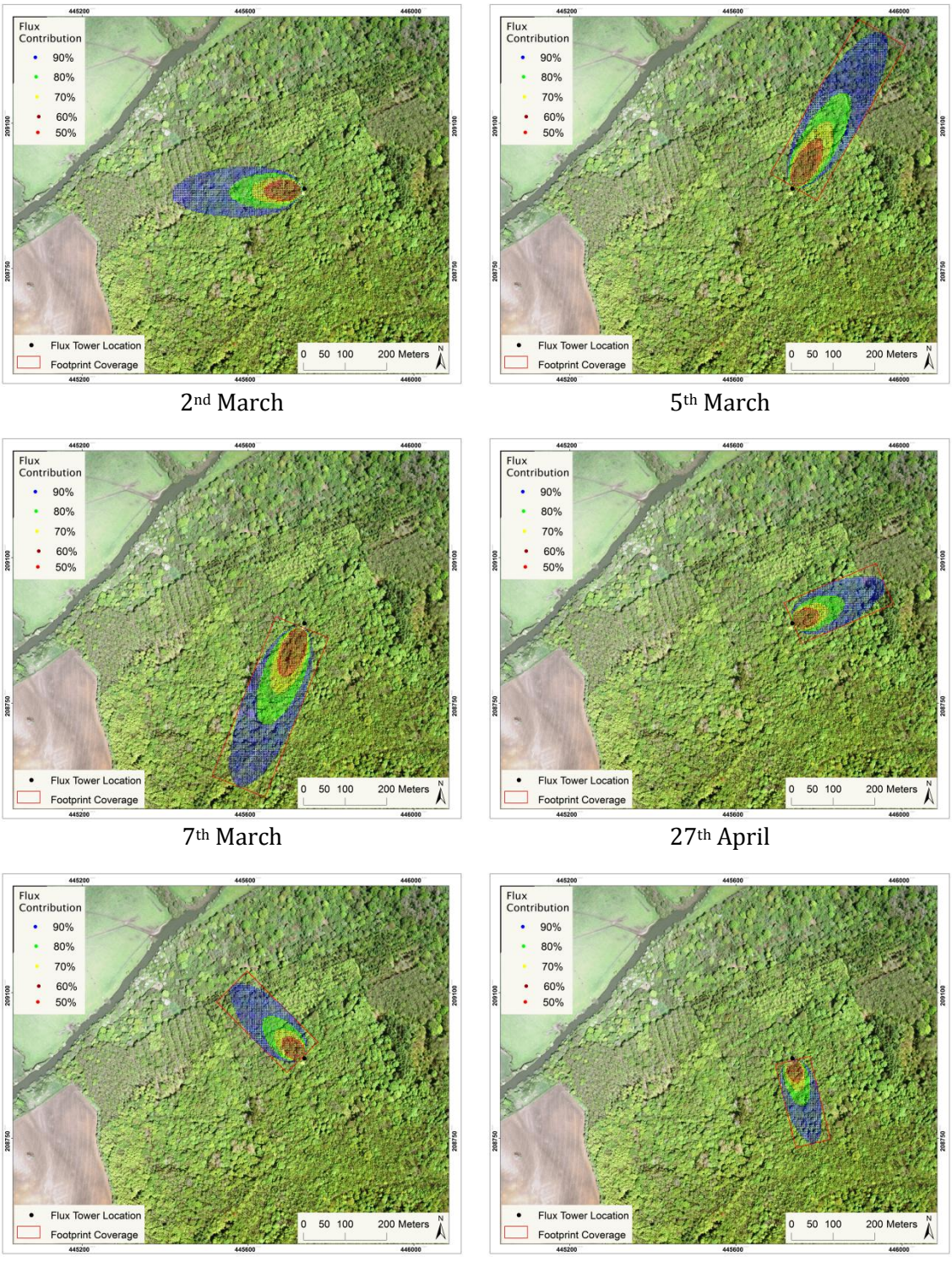

Figure 6-3 Estimated real flux tower footprints overlaid on Wytham's aerial image for six dates involving a platform-sensor overpass the gradient colours signify the source weight and distance for probability cumulative footprints (50%, 60%, 70%, 80% and 90%).

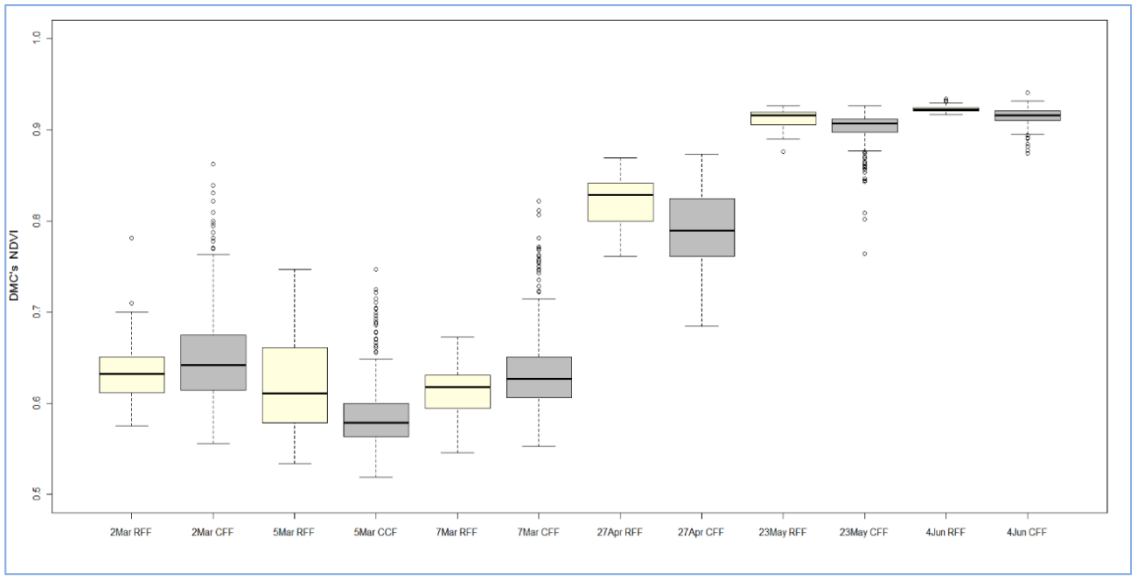

Figure 6-4 Boxplots showing DMC NDVI variation for tower-specific real flux tower footprints (RFF; white) and the long-term pattern flux tower footprint coverage (CFF; grey) over the early growing season in 2010

For example, there was a statistically significant difference in the 7th March NDVI between the tower-specific RFF *(M* = 0.6150, *SD* = 0.0266*)* and the long-term pattern circular flux tower footprint *(M* = 0.6628, *SD* = 0.0602*), t (*122*)* = -8.595, *p* = 0.00. This difference results from the interaction between the variation in NDVI in the canopy and the flux tower footprint variation due to short-term micrometeorological changes, influenced by the wind direction and strength.

Table 6-3 Paired sampled *t*-test across the Wytham's realistic and circular flux tower footprints over the early growing season in 2010, real flux tower footprint (CFF) and circular flux tower footprint (CFF)

Paired Sample		Sample Statistics		Paired Differences		t	df	Sig. (2-tailed)
		Mean	SD	Mean	SD			
2nd March	RFF	0.6359	0.0326	-0.0232	0.0749	-2.844	83	.006
	CFF	0.6592	0.0560					
5th March	RFF	0.6223	0.0490	0.0124	0.0605	2.210	115	.029
	CFF	0.6099	0.0510					
7th March	RFF	0.6150	0.0266	-0.0478	0.0617	-8.595	122	.000
	CFF	0.6628	0.0602					
27th April	RFF	0.8218	0.0265	0.0564	0.0346	12.429	57	.000
	CFF	0.7653	0.0228					
23rd May	RFF	0.9122	0.0096	0.0237	0.0255	7.433	63	.000
	CFF	0.8885	0.0236					
4th June	RFF	0.9234	0.0048	0.0172	0.0126	8.394	37	.000
	CFF	0.9061	0.0113					

The empirical prediction of the choice of support size based on the observed image data (DMC NDVI across time-specific RFF) was represented by Figure 6.

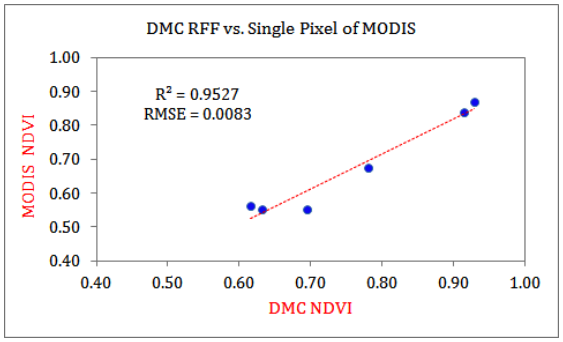

(a) Image support 1

R^2= 0.044, F (1, 4) =67.761, p=0.001

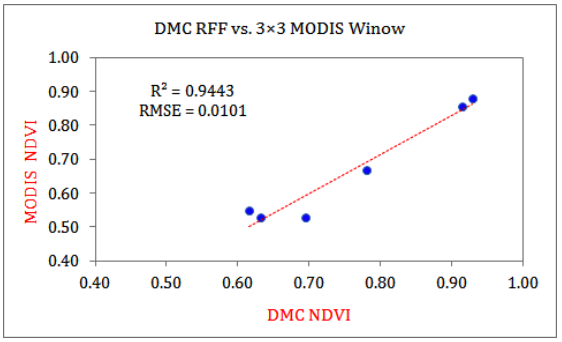

(b) Image support 2

R^2= 0.044, F (1, 4) =67.761, p=0.001

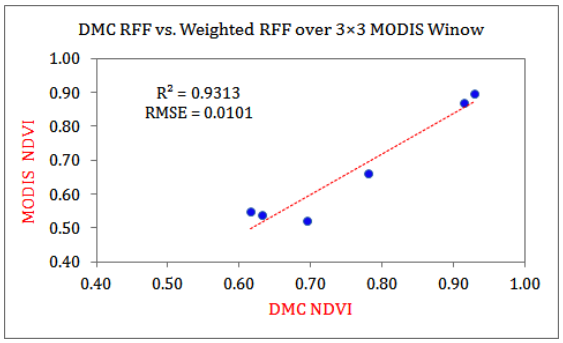

(c) Image support 3

R^2= 0.931, F (1, 4) =54.248, p=0.002

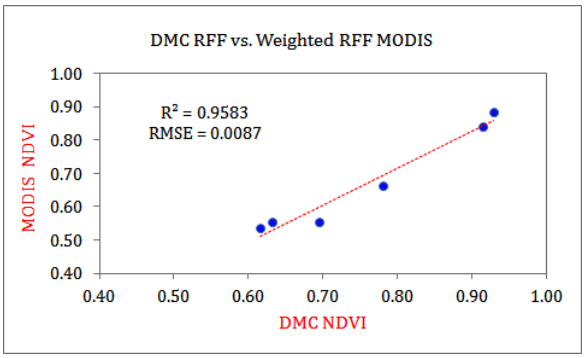

(d) Image support 4

R^2= 0.958, F (1, 4) =91.969, p=0.001

Figure 6-5 Empirical predication of different support size on the basis of the DMC NDVI

In addition, Figure 6-6 shows the effect of choice of support on the ability to predict the true flux tower value of NDVI as a proxy of CO_2 flux.

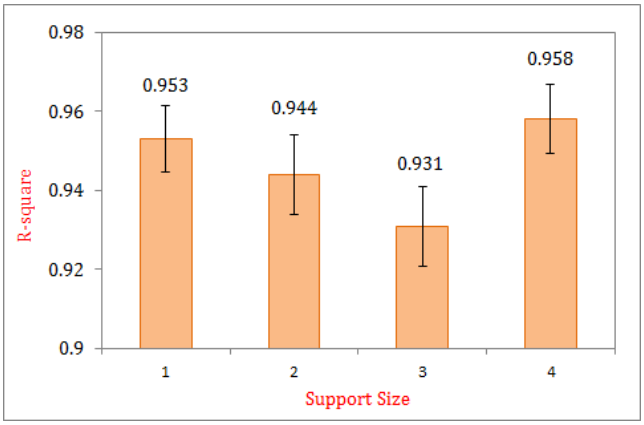

Figure 6-6 Comparison of different support size for predicting the true value of NDVI across flux tower extent, the error bars on the Y-axis show RMSE of prediction

6.3.3 Variogram Analysis

6.3.3.1 Airborne Fine Spatial Resolution NDVI_705 from AISA-Eagle

Figure 6-7 shows the omnidirectional variogram of the NDVI_705 derived from the AISA Eagle image across a buffer distance around flux tower location of 200 m and an exponential model fitted to the data based on the maximum likelihood (ML) method. The model parameters are: *"*C_0= 75×10^{-4}*"*, "C= 425×10^{-3}", and A_0= 19 m", showing that the data are spatially autocorrelated within a practical range of 57 m (Isaaks and Srivastava 1989). The NDVI_705 at this site is represented by an asymptotic exponential variogram: increasing the lag distance between two pixels (2 m × 2 m for AISA Eagle) increases the degree of dissimilarity in the NDVI_705 values defined at those locations. A Monte Carlo simulation based on the experimental variogram is presented in Figure 6-7 (left). A part of the experimental variogram lies inside the envelope simulated (dashed lines) indicating no significant spatial auto-correlation beyond the practical range at 57 m. Figure 6-7 (right) also depicts the variogram model fitted to observed data with simulated envelopes based on the model parameters such as to characterise the variability of the variogram (Ribeiro Jr and Diggle 2001).

The limits of the simulated envelopes may be defined by the minimum and maximum model parameters of influence in the principal directions (Houlding 2000). Hence, knowing the orientation of observation data with respect to the flux tower footprint criteria (in particular, upwind direction) may lead us to calculate the corresponding model parameters of influence. In this regard, directional variograms of NDVI_705 obtained along approximately 200 m transects in the principal directions 0-180°, 45-225°, 90-270°, and 135-315° were computed to investigate the spatial heterogeneity in terms of anisotropy in the variogram (Figure 6-8). The exponential model (Equation 6-9) was found to provide the best fit to the experimental variogram. The models parameters along each transect are given in Table 6-4.

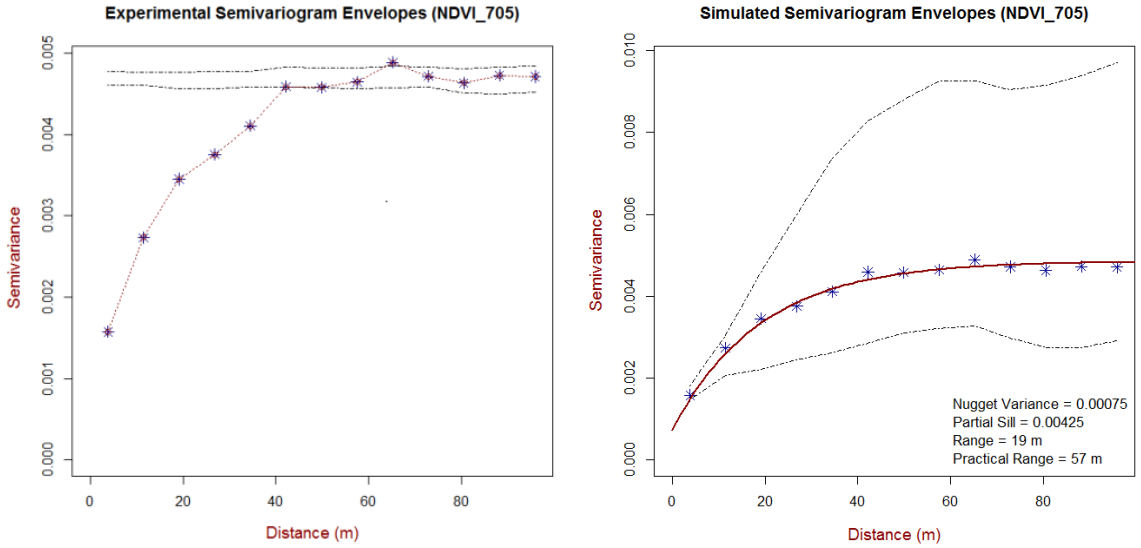

Figure 6-7 Experimental variogram of the NDVI_705 derived from the AISA Eagle image across a buffer distance-off from flux tower location at 200 m as a conventional circular flux tower footprint, with active lag distance 100 m and lag distance interval as RS spatial resolution (left); omnidirectional variogram with 99% confidence interval envelopes (dashed lines) of residuals from non-spatial auto-correlation, and (right) variogram model fitted (solid red line) with simulated envelopes (dashed lines) based on the model parameters.

Table 6-4 Directional variogram model fitted of NDVI_705 derived from AISA Eagle Image across Wytham's flux tower extent along approximately 200 m transect

Transect Direction	Nugget variance	Partial sill	Practical range (m)
0-180˚	95×10^{-4}	452×10^{-3}	49.80
45-225˚	21×10^{-3}	385×10^{-3}	79.20
90-270˚	80×10^{-4}	240×10^{-3}	35.40
135-315˚	70×10^{-4}	409×10^{-3}	52.50

As mentioned previously, spatial heterogeneity in NDVI can be described by two components including spatial variability (i.e. spatial variance for a process in two dimensions) and spatial structure at a certain scale defined by geographic extent and spatial resolution of the observed data. As shown in Figure 6-8, the variogram and the degree of spatial heterogeneity vary with direction. Accordingly, high variance was found along the 45-225° transect (sill variance at 593×10^{-3}), while low variance was found along the 90-270° transect (sill variance at 320×10^{-3}), because the former is related to the mosaic of mixed forest that includes scrub, deciduous and coniferous trees in the form of ancient, plantation and secondary woodlands.

In general, the shape of variogram provides an insight into the spatial structure of the landscape within a given extent. It is interesting that the NDVI-705 along the 45-225° transect shows a typical anisotropy behaviour with largest sill variance (593×10-3) and largest range (79.20 m). In this direction, the variogram fluctuates with increasing lag distance with two peaks, reflecting higher spatial heterogeneity than other directions. Alternatively, the 90-270° transect variogram increases smoothly and reaches comparatively the variance of the observations at the smallest range (35.40 m) compared to the other directions, indicating finer spatial structure and less pronounced spatial variation. All variograms transition smoothly from the intercept correspond to the nugget variance (Figure 6-8), resulting from short-range spatial variation within pixels rather than between them (Atkinson and Kelly 1997).

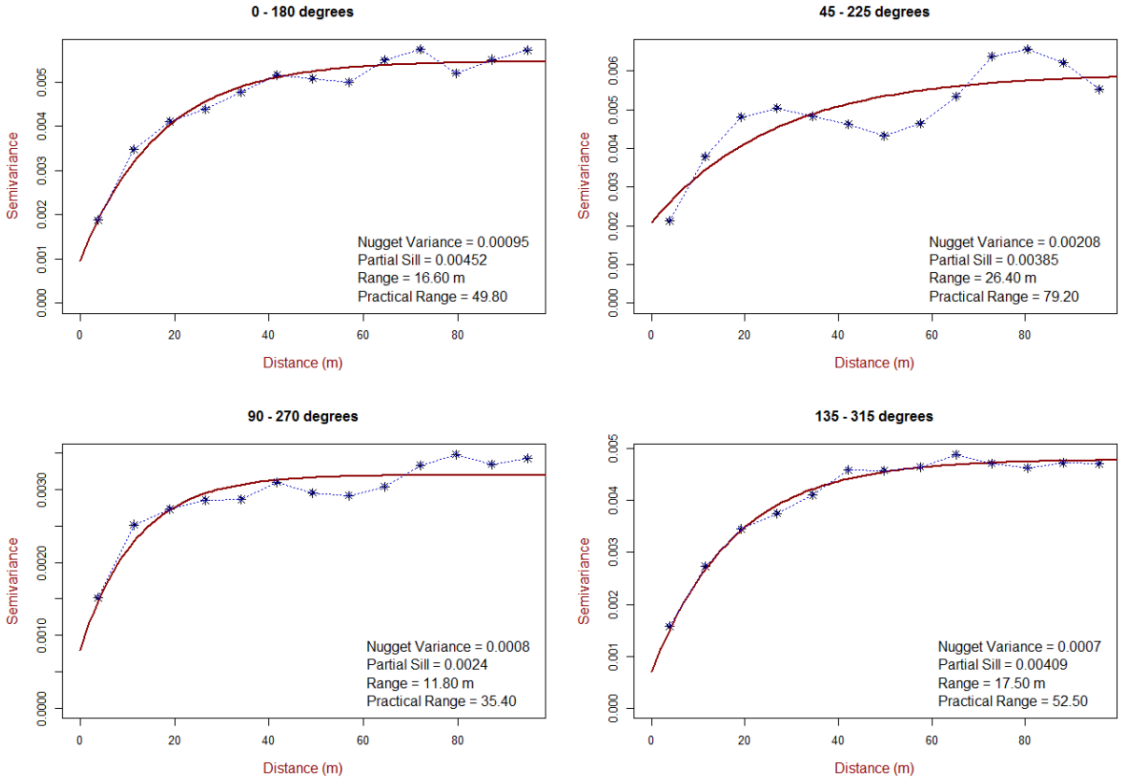

Figure 6-8 Anisotropic variogram of NDVI_705 along 200 m transects of principal directions as 0-180°, 45-225°, 90-270°, and 135-315°

6.3.3.2 Satellite High Spatial Resolution NDVI from DMC

Multi-temporal experimental variograms representing the spatial dependence in NDVI derived from DMC constellation are shown in Figure 6-9. Anisotropy was not taken into account because the observed data were obtained from the long-term pattern of the weighted flux tower footprint (i.e. RFF). Several mathematical models were fitted to the experimental variograms and the exponential model given by Equation 6-9 was found to provide the optimal fit.

The variogram shape of DMC NDVI was different among multi-temporal observations throughout the leaf-off and leaf-on conditions, reflecting that the spatial covariance in the flux tower footprint coverage varies through time according to the vegetation phenological trend. The exponential model was found to provide the optimal fit to the experimental variogram. The model fitted was defined by its parameters which include the nugget variance (i.e. assumed as

micro-scale variation), structured variance (sill), and range (Table 6-5). For example, the exponential model indicates spatial dependence up to approximately 75 m in the DMC NDVI derived for 2nd March 2010, while autocorrelation varies up to 150 m in the DMC NDVI derived for late spring through developing greenness of forest canopy (27th April, 23rd May, and 4th June). Accordingly the second null hypothesis of this investigation was accepted in terms of no spatial variation in NDVI within a certain support size at a scale smaller than the data observed (i.e. DMC pixel size at 22 m). The 99% confidence intervals using Monte Carlo simulation of experimental variogram was computed from independent random permutations of the residuals across the locations (Diggle and Ribeiro Jr. 2007; Ribeiro Jr and Diggle 2001). Accordingly, as shown in Figure 6-10, experimental variograms corresponding to the leaf-off period lie outside the envelope simulated (dashed line), indicating significant spatial autocorrelation among the model residuals upon the DMC NDVI in terms of flux tower footprint variability, while the null hypothesis of no spatial correlation confirms that the spatial dependence is statistically significant within approximately 380 m for 23rd May and 300 m for 4th June.

Table 6-5 Parameters of the fitted variogram models and spatial covariance within Wytham Woods landscape domain and tower-specific weighted flux tower footprint over early growing season in 2010

Date	Nugget variance	Sill variance	Range (m)
2 March	2.99×10^{-4}	2.39×10^{-3}	75
5 March	1.62×10^{-4}	1.29×10^{-3}	75
7 March	2.22×10^{-4}	1.77×10^{-3}	70
27 April	2.05×10^{-4}	1.64×10^{-3}	150
23 May	3.35×10^{-5}	2.68×10^{-4}	130
4 June	1.05×10^{-5}	8.42×10^{-5}	105

As shown in Figure 6-9, the degree of spatial variability (sill variance) differs relying upon phenological trend. However, inferring the CO_2 flux variability of this site using spatial variation in NDVI across the landscape may be problematic because the NDVI saturates in dense canopy cover, particularly through

developing greenness of forest canopy over summer. Therefore, the range parameter reveals spatial auto-correction and spatial structure. Although the value of spatial structure increases (spatial dependence increases during phenological green-up), the nugget variance decreases. This means that the development of greenness over the top of canopy and understory limits NDVI variation across landscape, as well as sub-pixel variation throughout the growing season. The spatial structure of NDVI during phenological green-up indicates that an EC-based CO_2 flux with a given flux tower footprint coverage restricted within the estimated range could potentially introduce a large bias in representing the landscape scale.

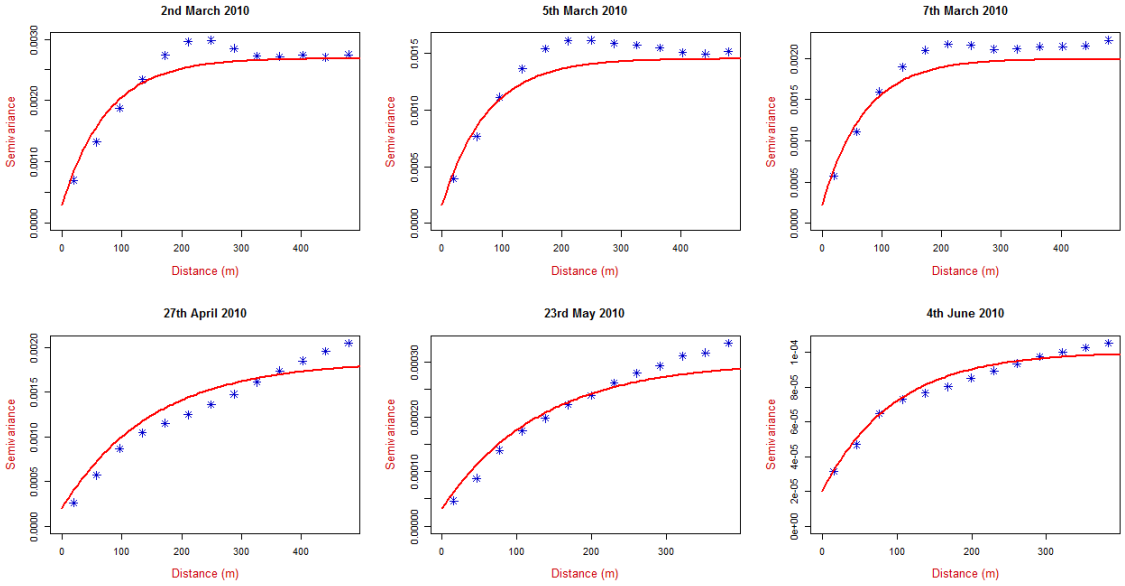

Figure 6-9 Omnidirectional variogram model fitted on experimental variogram across Wytham Woods tower-specific weighted flux tower footprint over a growing season in 2010

To test the effect of choice of image support on the ability to predict the true value of MODIS NDVI across flux tower extent, the modelled variograms were applied to compute the block-to-block spatial covariance between three different support sizes (single MODIS pixel at 1 km spatial resolution; a 3×3 window of MODIS pixels at 250 m spatial resolution; and a 3×3 window of weighted MODIS pixels at 250 m spatial resolution) and the tower-specific weighted flux tower footprint (RFF)

(Table 6-6). Finally, cross validation by the block-kriging method was performed to quantify the goodness-of-fit for variogram model and estimation bias as uncertainty in terms of the (RMSE) and the Pearson's observed-predicted correlation coefficient (COR), as given in Table 6-6, to test the third null hypothesis that there is no co-variability in NDVI between that area averaged across the coarse spatial resolution satellite sensor pixels and that weighted by the flux tower footprint criteria.

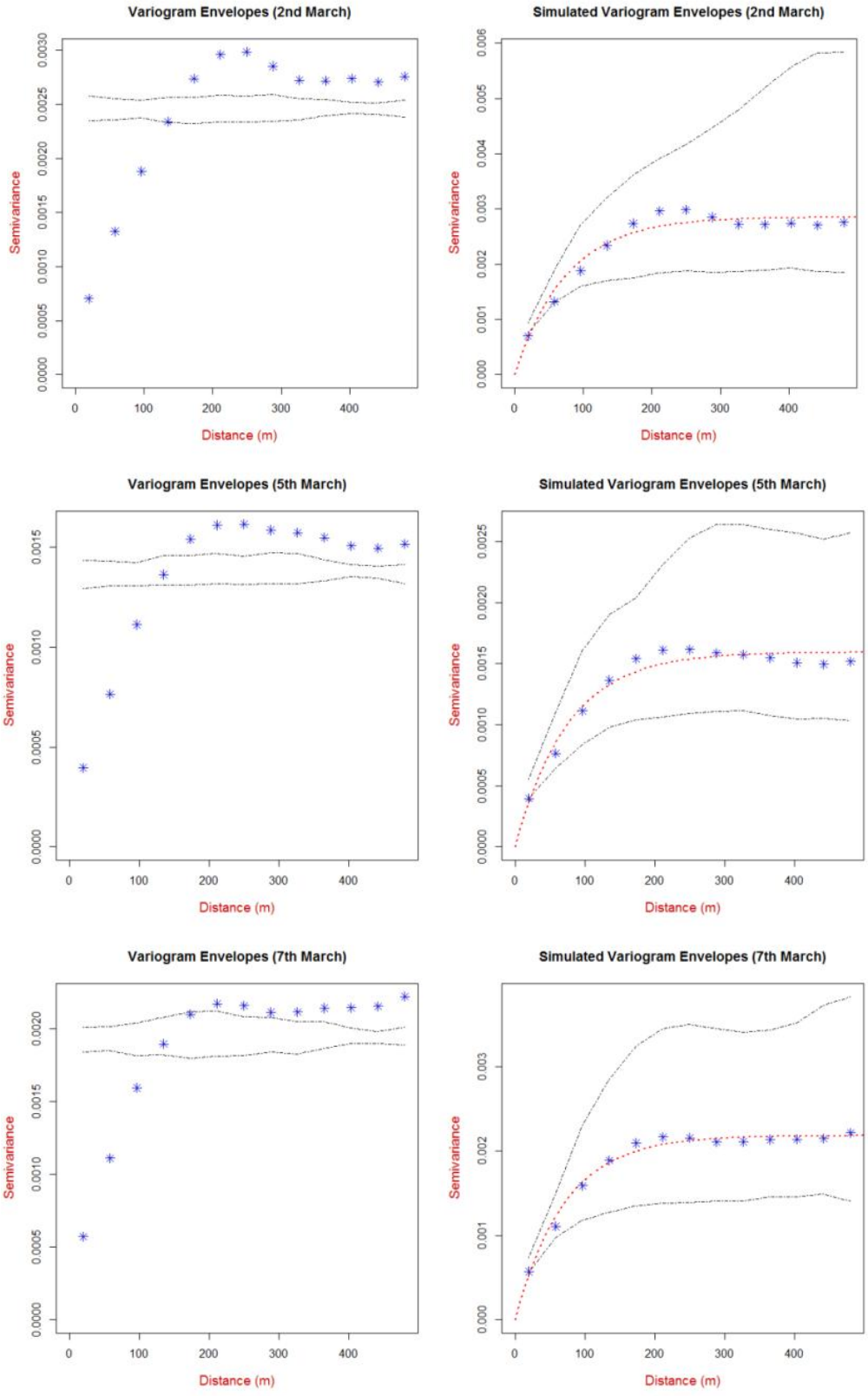
Variogram Envelopes (2nd March)
Simulated Variogram Envelopes (2nd March)
Variogram Envelopes (5th March)
Simulated Variogram Envelopes (5th March)
Variogram Envelopes (7th March)
Simulated Variogram Envelopes (7th March)
Semivariance
Distance (m)

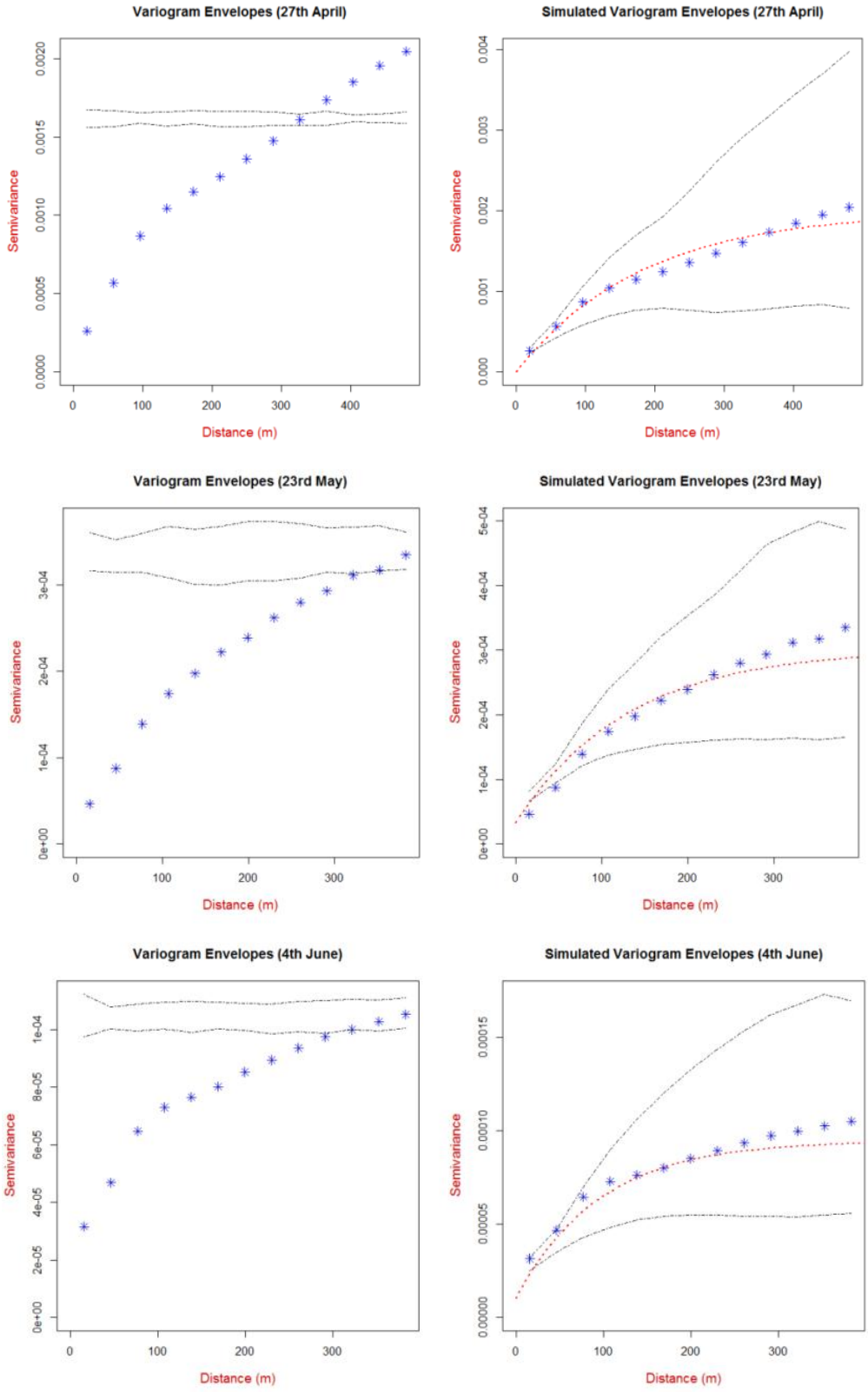

Figure 6-10 99% confidence envelopes for experimental variogram (left) and simulated variogram envelopes based on the parameters of fitted model across long-term pattern of weighted flux tower footprint over early growing season in 2010

Table 6-6 Block-to-block spatial covariance analysis and cross-validation over different support size; "V_O" refers to the spatial covariance of observed responses across time-specific weighted flux tower footprint (RFF), "V_P" is spatial covariance of responses to predicted for a set of spatial location within desired support, and "V_{OP}" is the block-to-black covariance for a set of spatial location between observed responses across tower-specific weighted flux tower footprint and responses to be predicted over Wytham Woods landscape as a 3×3 window of MODIS pixel at 250m spatial resolution and a single pixel of MODIS 1km spatial resolution

Date	Mean V_O	Mean V_P			Mean V_{OP}			RMSE			COR		
		Single MODIS	MODIS Window	MODIS over RFF	Single MODIS	MODIS Window	MODIS over RFF	Single MODIS	MODIS Window	MODIS over RFF	Single MODIS	MODIS Window	MODIS over RFF
2 Mar	1.27E-04	6.22E-05	3.77E-04	7.19E-04	7.17E-05	1.56E-04	1.49E-04	0.023	0.026	0.019	0.891	0.900	0.658
5 Mar	1.02E-04	5.00E-05	2.04E-04	2.95E-04	5.76E-05	8.42E-05	7.25E-05	0.016	0.017	0.019	0.900	0.930	0.918
7 Mar	8.36E-05	4.06E-05	2.54E-04	3.62E-04	4.66E-05	1.02E-04	8.78E-05	0.020	0.020	0.022	0.891	0.921	0.568
27 Apr	2.24E-04	1.23E-04	6.65E-04	1.02E-03	1.47E-04	4.03E-04	4.01E-04	0.012	0.012	0.012	0.951	0.924	0.917
23May	3.41E-05	1.81E-05	8.12E-05	1.38E-04	2.16E-05	4.30E-05	4.26E-05	0.007	0.005	0.006	0.936	0.774	0.685
4 June	6.63E-06	3.34E-06	1.80E-05	4.03E-05	3.93E-06	8.29E-06	8.35E-06	0.006	0.004	0.005	0.830	0.544	0.204

Single MODIS: single MODIS pixel at 1km spatial resolution

MODIS Window: average of a 3×3 window of MODIS pixel at 250 m spatial resolution across flux tower extent

MODIS over RFF: average of MODIS pixels at 250 m spatial resolution across time-specific weighted flux tower footprint

Figure 6-11 shows the theoretical assessment of the effect of choice of image support based on the spatial covariance on the ability to predict the true value of spectral index of CO_2 flux from satellite remote sensing. Accordingly, the co-variability between desired support and the RFF reveals three different phases in the growing season based on the developing canopy greenness. As canopy cover saturates by over story, co-variability between different supports sizes decreases.

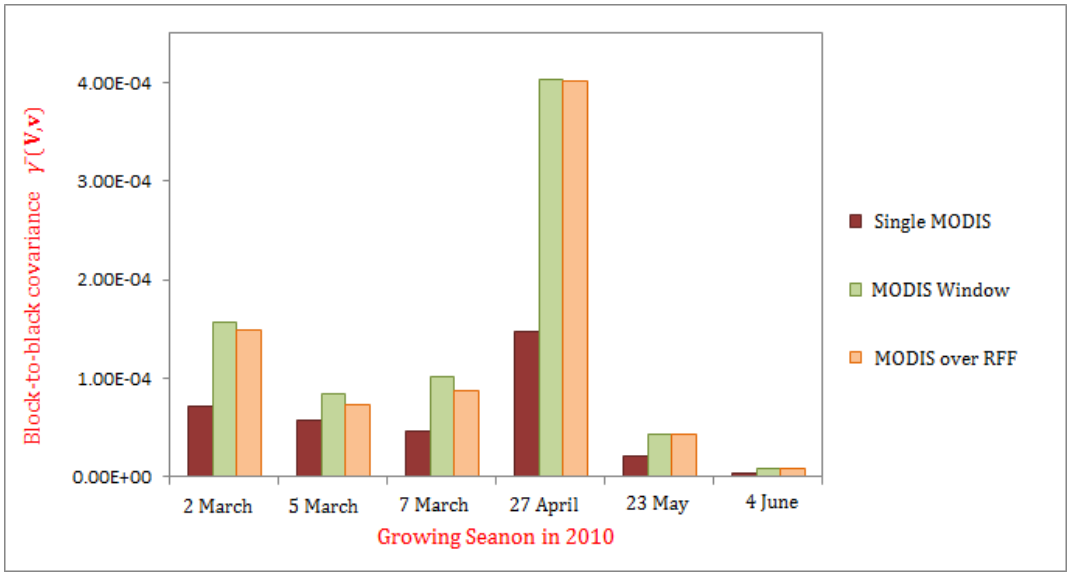

Figure 6-11 Co-variability between the desired support from MODIS imagery and the RFF

6.4 Conclusion

This chapter proposed a block-to-block spatial covariance Kriging-based geostatistical solution to test the effect of choice of image support on the ability to predict the true value of MODIS NDVI across flux tower extent for upscale from tower-based EC measurement to larger areas. The new approach is a covariate scaling. It explicitly account for the size of support, and has the characteristic of perfect coherence with the original coarse data. The proposed approach was examined using both AISA Eagle hyperspectral and MODIS images

This chapter has investigated the relevance of tower-specific EC CO_2 flux measurements in terms of spatial heterogeneity in a spectral vegetation index distribution for a temperate forest in southern England. The temporal variability was also accounted for by both incorporating tower-specific weighted flux tower footprint and coarse spatial resolution platform-sensor support size, such as DMC constellation and MODIS.

Two different vegetation indices in terms of support size, broadband NDVI and airborne narrowband red edge NDVI (NDVI-705) were used as spectral indices of CO_2 flux. The latter represents a snapshot in time and is more variable in space whereas the former is variable in both space and time depending on canopy cover and phenological trend. The spatial heterogeneity was accounted for by integrating flux tower footprint variability to NDVI obtained from both fine-resolution AISA Eagle image and multi-temporal high resolution DMC image analysis. Moreover, four different image supports from MODIS imagery were calculated to test the effect of choice of support on the ability to predict the true value of spectral vegetation index (NDVI) as a proxy of CO_2 flux across a flux tower extent. The resulting weighted flux tower footprint NDVI was compared with those average across flux tower extent as landscape scale of three by three MODIS pixels (231 m × 231 m) with the flux tower location at the centre pixel, as well as a single pixel of MODIS-1km.

The current investigation showed that there was a statistically significant difference between NDVI values across realistic flux tower footprint and flux tower extent over forested area due to time-varying flux tower footprint coverage. The semi-variogram analysis from both airborne- and satellite-based NDVI showed that the spatial variability occurred beyond a certain support size at 2 m and 22 m, respectively. Furthermore, directional semi-variogram analysis on AISA Eagle-based NDVI indicated an anisotropic distributed pattern within conventional flux tower footprint across a buffer distance-off from flux tower location at 200 m. In contrast, omnidirectional semi-variogram analysis on the multi-temporal DMC NDVI over early growing season, which conducted with realistic weighted flux tower footprint, showed that the degree of spatial variability varied among each realistic flux tower footprint. Furthermore, these results signified that spatial covariance in the realistic flux tower footprint coverage varied through time due to phenological trend. In reality, this spatial co-variability across time-varying weighted flux tower footprint can affect the prediction of NDVI across the flux tower domain based on the coarse satellite observations.

In conclusion, the variogram as a representation of spatial dependence in spectral index of CO_2 flux was introduced to assess the primary source of uncertainty association with scaling process from tower-specific flux tower footprint to coarse satellite observations.

The matching of ground data to remotely sensed satellite sensor pixels is a generic requirement in remote sensing. The matching of flux tower observations to coarse spatial resolution, global coverage satellite sensor observations is a key requirement for the global monitoring of carbon flux, which is an important component of our understanding of climate change. Advances in the ability to characterise the true time-varying flux tower footprint have opened up the possibility for improved matching of spatial supports. This chapter, based on explicit representation of the time-varying flux tower footprint, demonstrated quantitatively that prediction of flux tower measurements directly from space-

borne coarse spatial resolution imagery is challenging and leads to a low predictive ability, no matter how the imagery are manipulated.

Many schemes have been devised for scaling between coarse spatial resolution imagery and ground data such as those obtained from flux towers, the majority based on the use of intermediate spatial resolution data to upscale ground observations to the coarse pixel scale. However, these generally do not account for the true flux tower footprint. Future research will be undertaken to investigate how knowledge of the flux tower footprint can be used in combination with intermediate spatial resolution imagery to increase the accuracy with which flux tower measurements can be matched to coarse spatial resolution imagery.

7. Evaluating the Sensitivity of a Satellite-Based Light Use Efficiency (LUE) Model from MODIS using Regional CO_2 Flux Network Observations

7.1 Introduction

The final section of the pilot study (section 3.4) showed the potential of Airborne Imaging Spectrometry (AIS) to provide detailed spectral information at a fine spatial resolution and, therefore, the opportunity to derive narrowband spectral indices such as the Photochemical Reflectance Index (PRI)[1] (Gamon et al., 1992). The airborne hyperspectral data provided a rich source of information about the spectral and spatial heterogeneity of woodlands, and so had great potential spatially to act as a transfer standard addressing ecosystem function in the scaling process between tower-based EC flux measurements and coarse satellite sensor observation, but they reliable (e.g. Figure 3-21) so it was not possible to use them to create a seasonal PRI profile. The Natural Environment Research Council (NERC) Airborne Research and Survey facility (ARSF) data were also time-consuming to pre-process and the problems of cross-track illumination variation and narrow swath width made creating an accurate single image of Wytham Woods from a mosaic of flight-lines difficult or impossible.

[1]. The PRI is a normalized difference index using narrow reflectance wavebands that are influenced by the xanthophylls cycle pigment content, and represents photosynthesis efficiency.

Chapter 4 represented the sensitivity of spectral indices (i.e. NDVI and PRI) using the FLIGHT simulation under the effect of four extraneous parameters across different canopy stands in Wytham Woods and at fine spatial resolution (the UK-DMC support size). The results (i.e. simulated spectral responses of the corresponding VIs and wavebands) showed different sources of uncertainty in the solar/view geometry and atmospheric effects.

The available evidence shows that NDVI is a reliable estimator of biophysical variables related closely to photosynthesis capacity at various spatial and temporal scales over a wide range of PFTs (Tucker 1979, Sellers, Berry et al. 1992, Turner, Ritts et al. 2005, Turner, Ritts et al. 2006).

The research reported in chapter 5 has shown that NDVI can be measured accurately using data from the DMC constellation, and that this system has several important advantages over the more commonly used systems such as MODIS, such as finer spatial resolution, which means that smaller areas of uniform land cover can be sensed, and also that heterogeneous sites can be studied. This is particularly important if the aim is to compare satellite sensor observations with ground measurements, either for model calibration or for product validation purposes. In the specific example studied, the uncertainty in NDVI as a result of differences in the conditions of measurement did affect the median NDVI. However, the difference was less than that due to uncertainty in the atmospheric correction. Thus, in the case of Wytham Woods, as chapter 4 showed, it is more important to improve the representation of aerosols in the atmospheric model used than replace the generalised circular flux tower footprint with a realistic flux tower footprint.

In the following section (i.e. chapter 6) the spatial variability within the Wytham Woods site was investigated in more detail using geostatistical methods. Two different VIs in terms of support size, broadband NDVI and airborne narrowband red edge NDVI (NDVI-705) were used as spectral indices of CO_2 flux. The current results showed that there was a statistically significant difference between NDVI values across the realistic flux tower footprint (RFF) and the flux tower extent over

the forested area due to the time-varying flux tower footprint coverage. The semi-variogram analysis from both airborne- and satellite-based NDVI showed that the spatial variability occurred beyond a certain support size at 2 m and 22 m, respectively. Furthermore, these results signified that spatial covariance in the realistic flux tower footprint coverage varied through time due to the phenological trend. In reality, this spatial co-variability across the time-varying weighted flux tower footprint can affect the prediction of NDVI across the flux tower domain based on coarse satellite sensor observations. In conclusion, the variogram as a representation of spatial dependence in spectral indices of CO_2 flux was introduced to assess the primary source of uncertainty association with up-scaling from the tower-specific flux tower footprint to coarse satellite sensor observations. In summary, the AIS sensor limitations would have affected subsequent work based on flux tower footprint analysis, so attention turned to alternative sources of data.

This chapter focuses on remote sensing-based terrestrial productivity from Moderate Resolution Imaging Spectrometer (MODIS), the NASA Earth Observing System (EOS), using regional tower-based flux network observations. Both these sources offered relatively frequent temporal sampling. The UK Disaster Monitoring Constellation (UK-DMC) combined this with fine spatial resolution, while the EOS data had more spectral detail.

Data from the MODIS on the Terra and Aqua satellites are currently being used to provide spatially continuous estimates of carbon dynamics in terms of Gross Primary Production (GPP) at 1 km spatial resolution (Running et al., 2000; Running et al., 2004). The MODIS GPP algorithm (Figure 7-1) is based on the concept of LUE logic (Monteith 1972).

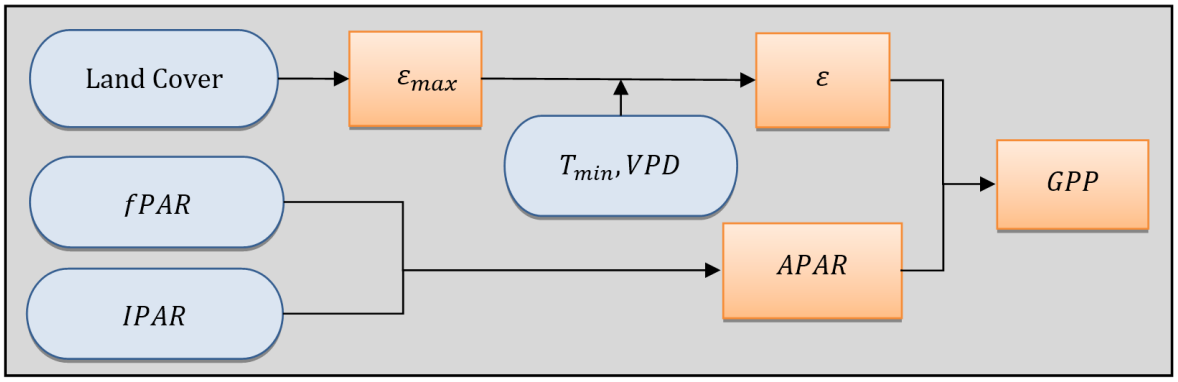

Figure 7-1 The MODIS GPP algorithm based on the concept of LUE logic

Monteith (1972) defined gross photosynthesis as a function of the Photosynthetically Active Radiation (PAR) absorbed by vegetation and the efficiency of photosynthesis, which generates the Light Use Efficiency (LUE) logic for estimating GPP from remotely sensed spectral observations. The concept suggests that GPP is linearly related to the amount of absorbed PAR and the efficiency of production as

$$GPP = \varepsilon \times fPAR \times PAR \qquad \text{Equation 7-1}$$

where ε is the realized LUE[1] of vegetation, $fPAR$ is the fraction of incident PAR that is absorbed by the canopy (Monteith, 1972; Sellers et al., 1992; Running et al., 2000; Running et al., 2004). Estimates of the fraction of PAR absorbed by vegetation (Ruimy et al., 1996) and the LUE (Gamon, 1997) play a critical role in the energy balance of ecosystems and in the estimation of the carbon budget over various spatial and temporal scales. The LUE is influenced by environmental factors and constraints, the scalars that attenuate the maximum efficiency of photosynthesis, including air temperature and water availability as

$$\varepsilon = \varepsilon_{max} \times T_s \times W_s \qquad \text{Equation 7-2}$$

where ε_{max} is the biome-specific maximum efficiency of photosynthesis, and T_s and W_s refer to air temperature and water availability, respectively.

1. The efficiency of converting $fPAR$ into fixed carbon, here referred to as LUE

Despite the consensus that current remotely sensed models provide valuable data on GPP with spatially and temporally consistent coverage, the information content of these data remains uncertain (Kim et al., 2006; Xiao et al., 2011; Chen et al., 2012). There are several sources of uncertainty associated with scaling RS-based models of GPP at various spatial and temporal scales, including sensor limitations in terms of support size defined by spatial and temporal resolution (Dungan, 2002); spatial heterogeneity of land surface properties (Atkinson and Foody, 2002; Sogachev et al., 2004; Kim et al., 2006; Chen et al., 2012; Xioa et al., 2012); pre-processing calibration (Baret, 1995; Danson, 1995; Woodcock, 2002; Liang, 2004); and structure of the model proposed and its parameterization (Dungan, 2002).

Regarding the above approach, Rahman et al. (2001) developed a method of combining spectral VIs (the basis of LUE logic) to generate spatially continuous maps of gross CO_2 exchange[1] rate. Their study, however, was conducted in a specific biome (boreal forest), and cannot be extrapolated to different biomes or across regions. In addition, results from the Hierarchical Bayesian Light Use Efficiency (HBLUE) model developed by Naithani et al. (2012), within the North America Carbon Program Science Steering Group – Pennsylvania State University, suggested that taking less than 150 days of data for estimating maximum efficiency of photosynthesis (ε_{max}) generates a large uncertainty (Figure 7-2). Then it is needed to consider both spatial and temporal variation in ecosystem function to generate seasonal PRI profiles across different stands.

1. Net Ecosystem Exchange (NEE) of CO_2

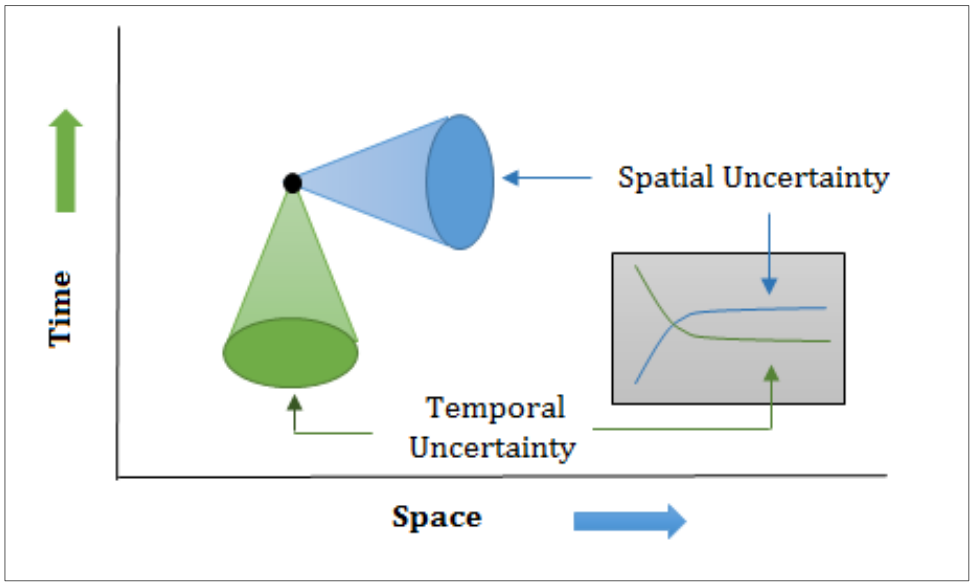

Figure 7-2 Constraining and representing uncertainty, adapted from Naithani et al., (2012).

In recent years, the integration of spatially-explicit ecosystem models, remote sensing and eddy covariance flux network observations with environmental variables has facilitated the quantification of carbon cycling dynamics across multiple spatial and temporal scales (Keane et al. 2002; Miao et al. 2011). In this regard, process-based models with the aim of simulation of carbon dynamics in forest ecosystems are increasingly being used besides other tools to predict the effects of environmental factors on forest carbon pool and productivity. Nevertheless, decision makers must be aware of the limitations of these models by uncertainty analysis to make the process-based models more applicable (Smith & Heath, 2001). Despite the importance of uncertainty issues in ecological research, sensitivity and uncertainty analyses still remain rarely used in carbon cycling models of terrestrial ecosystems (Smith & Heath 2001; Verbeeck et al. 2006).

One of the most common spectral approaches used for estimating photosynthetic efficiency at leaf and ecosystem levels is the PRI, which relates variation in the efficiency of carbon uptake to the relative level of xanthophyll cycle pigments (Gamon, et al., 1990; Gomon et al., 1992; Penuelas 1995; Gamon et al., 1997; Rahman et al., 2001; Coops et al., 2008). The PRI was originally developed to study

short-term variation in the efficiency of the photosynthesis process by detecting changes in the xanthophylls pigment (Figure 7-3). The index uses data in a narrow spectral band at 531 nm relative to a reference band that is not influenced by changes due to short-term stress events, usually located at around either 550 or 570 nm (Gamon et al., 1997).

$$PRI = (R_{531} - R_{Ref})/R_{531} - R_{Ref}) \qquad \text{Equation 7-3}$$

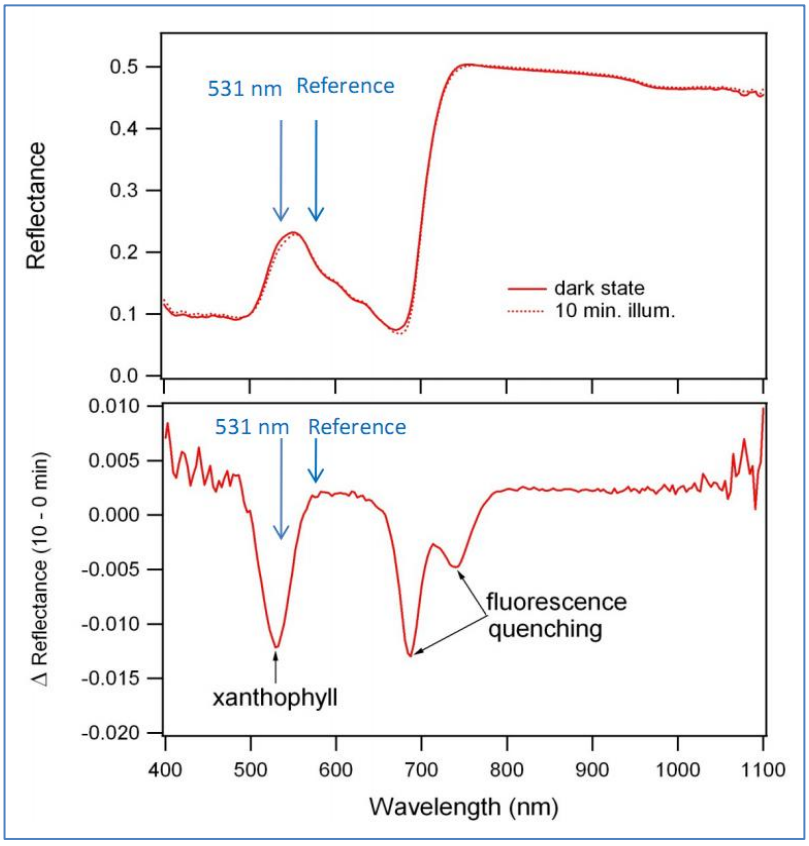

Figure 7-3 Photochemical Reflectance Index (PRI) as a spectral index of the xanthophyll cycle activity provides a measure of realized photosynthesis light-use-efficiency (LUE); Δ reflectance refers to reflectance different between time zero on dark state and time 10 (here in minute) under illumination state, adapted from Gamon (2010)

Many studies support the use of the PRI as a spectral index of LUE for various scales from leaf level (Gamon et al., 1992; Gamon et al., 1997) to stand and ecosystem level (Rahman et al., 2001; Drolet et al., 2005; Coops et al., 2008; Drolet et al., 2008; Goerner et al., 2009), but not across wide ranges in biomes. MODIS observations from Terra and Aqua provide a useful temporal resolution, a band

around 531 nm, but not the PRI reference band at 570 nm. In this respect, Doret et al. (2005) found large correlations between MODIS PRI and the LUE of a boreal deciduous forest using band 13 centred at 667 nm as the reference band, while bands 4 and 12 centred at 551 nm and 555 nm, respectively, showed no relationship with LUE. Their findings showed that PRI calculated from top of atmosphere reflectance had larger correlations than surface reflectance. However, this finding was limited by the small ranges of tower-based LUE values in the cloud-free MODIS observations.

7.2 Aim and Objectives

The overall aim of this part of research was to reduce the uncertainty in parameterizing a spectral indices-based LUE model. This could then be applied across heterogeneous landscapes in terms of PFTs, so as to estimate directly the efficiency of carbon uptake (i.e. LUE) based on satellite sensor observations. Moreover, the next objective of this research was to evaluate the sensitivity to the input parameters of a simple Diagnostic Carbon Flux Model (DCFM) developed by Xiao et al. (2011) for the estimation of net ecosystem carbon exchange (i.e. NEE of CO_2) in the Upper Midwest region of northern Wisconsin and Michigan, United States. An earlier sensitivity experiment with DCFM was carried out by Xiao et al. (2014) using an adaptive Markov chain Monte Carlo (MCMC) approach. In the current research, the sensitivity of the same input parameters was considered by local and global methods across three PFTs, including wetland mixed forest, deciduous forest and mixed forest) in the Upper Midwest region of northern Wisconsin and Michigan, USA.

In this study, furthermore, the MODIS-based PRI was based on taking band 13 as the reference band. Accurate radiometric calibrations, as well as proper correction for atmospheric scattering in the derivation of surface reflectance, appear to be critical challenges in deriving a valid PRI from satellite sensors (Gamon et al., 1997; Sims and Gamon, 2002; Hiker et al. 2009b; Drolet et al. 2005).

The specific objectives of this chapter were, thus, as follows.

- To estimate the LUE model parameters by combining regional flux network observations from tower-based instruments with data from MODIS;
- To evaluate the sensitivity of a simple Diagnostic Carbon Flux Model (DCFM) to the input parameters.
- To estimate ecosystem function (i.e. photosynthetic LUE) using a satellite-derived spectral index from MODIS data; and
- To investigate whether a MODIS-based model of LUE could be applied across a range of PFTs.

This part of the research was based on data from the Chequamegon Ecosystem Atmosphere Study (ChEAS) study site described in Chapter 2, rather than Wytham Woods, for four reasons. First, the limitations described above with the AISA Eagle data from Wytham Woods limited what would have been possible. Second, the length of the EC data record from ChEAS was much longer than that at Wytham Woods and, therefore, the conclusions are likely to be more reliable. Third, the US site had eight flux towers across a heterogeneous landscape at regional scale, each in different plant communities. Finally, the opportunity arose through the World University Network (WUN) to spend two months based at Penn State University, working with the research group that had developed a new method for up-scaling carbon fluxes and uncertainty across the northern forest eco-region.

7.3 Data Acquisition and Methodology

7.3.1 Eddy Covariance Observations

Long-term tower-based EC flux measurements (i.e. NEE of CO_2) across eight selected sites (Table 7-1) in the Upper Midwest region of northern Wisconsin and Michigan drawn from the ChEAS programme at Pennsylvania State University were used to compute CO_2 uptake rate based on the EC-LUE model. The gap-filled

half-hourly flux measurements were aggregated to daily values by considering more than 75% of the original data (Moffat et al., 2007; Xiao, et al., 2011).

Table 7-1 Location and characteristics of selected sites for EC flux observations in the ChEAS region

Site Name	Lat (N)	Lon (W)	Land Cover / PFT
Lost Creek (LC)	46.08	89.98	Wetland Mixed Forest
Park Falls / WLEF (WLEF)	45.65	90.27	Wetland Mixed Forest
Willow Creek (WC)	45.81	90.08	Deciduous Forest
Sylvania Wilderness (SW)	46.24	89.35	Mixed Forest
Wisconsin Young Jack Pine (YJP)	46.62	91.08	Mixed Forest
Wisconsin Mature Red Pine (MRP)	46.74	91.16	Mixed Forest
Wisconsin South Fork (SF)	45.92	90.13	Mixed Forest
University of Michigan Biological Station (UMBS)	45.56	84.71	Mixed Forest

7.3.2 MODIS Data Acquisition and Preparation

The MODIS vegetation index MOD13A2 (Huete et al., 2002) and surface reflectance MOD09A1 (Vermote and Vermeulen, 1999) products were obtained from NASA's Earth Observation System Data and Information System (EOSDIS) for each 8 day interval over the period 2000-2006. For each product, the quality of the data was determined using the quality assurance (QA) flags. For each flux tower site, the average values of MODIS products of 3 km by 3 km area were extracted to better represent the flux tower footprint coverage (Xiao, et al., 2011). In addition, the MODIS GPP product at a spatial resolution of 1 km (MOD17A2) (Running et al., 2004) was obtained to compare with estimated GPP from the EC-MODIS based model over the study period.

To calculate the satellite-based PRI signal, three MODIS products from both the TERRA and AQUA satellites were downloaded from NASA's EOSDIS[1] The first product, MOD/MYD021KM contains calibrated and geo-located radiance for the 36 MODIS spectral bands at a spatial resolution of 1 km (Toller et al., 2006), from which the top-of-atmosphere (TOA) reflectance signals could be computed for

1. http://reverb.echo.nasa.gov

bands 11 (centred at 531 nm) and 13 (centred at 667 nm), by a linear calibration algorithm based on the calibration coefficients (i.e. reflectance scaling and offsets) in the HDF header file. The second product, MOD/MYD03 provided the geo-location with the same spatial resolution, as well as ground elevation and the solar/view geometry (i.e. azimuth and zenith angles) of each pixel to extract the spectral information of the flux tower-pixel (Toller et al., 2006). The TOA reflectance products were corrected atmospherically to the surface reflectance using an algorithm based on an accurate radiative transfer model developed by Rahman and Dedieu (1994), Simplified Method for Atmospheric Correction (SMAC). SMAC is suitable for the atmospheric correction of large amounts of data, and takes into account the effects of gaseous absorption (i.e. ozone and water vapour), scattering by aerosols and solar/sensor geometry. In this research, MOD/MYD04, aerosol optical thicknesses (AOT) at 550 nm across the land surface at 10 km spatial resolution (Toller et al., 2006), was used t estimate aerosol scattering optical depth. Figure 7-4 shows a simplified flowchart of the procedure used to retrieve daily MODIS surface reflectance from the MODIS Level 1B product. The dataset was inspected visually to screen cloud contamination over the flux tower locations for the study sites.

7.3.3 MODIS-based Photochemical Reflectance Index (PRI)

For the cloud-free flux tower pixels corresponding to the existing EC observations PRI was calculated (Equation 4-3) using MODIS band 11 centred at 531 nm, and band 13 centred at 667 nm as the reference band (Drolet et al., 2005; Drolet et al., 2008).

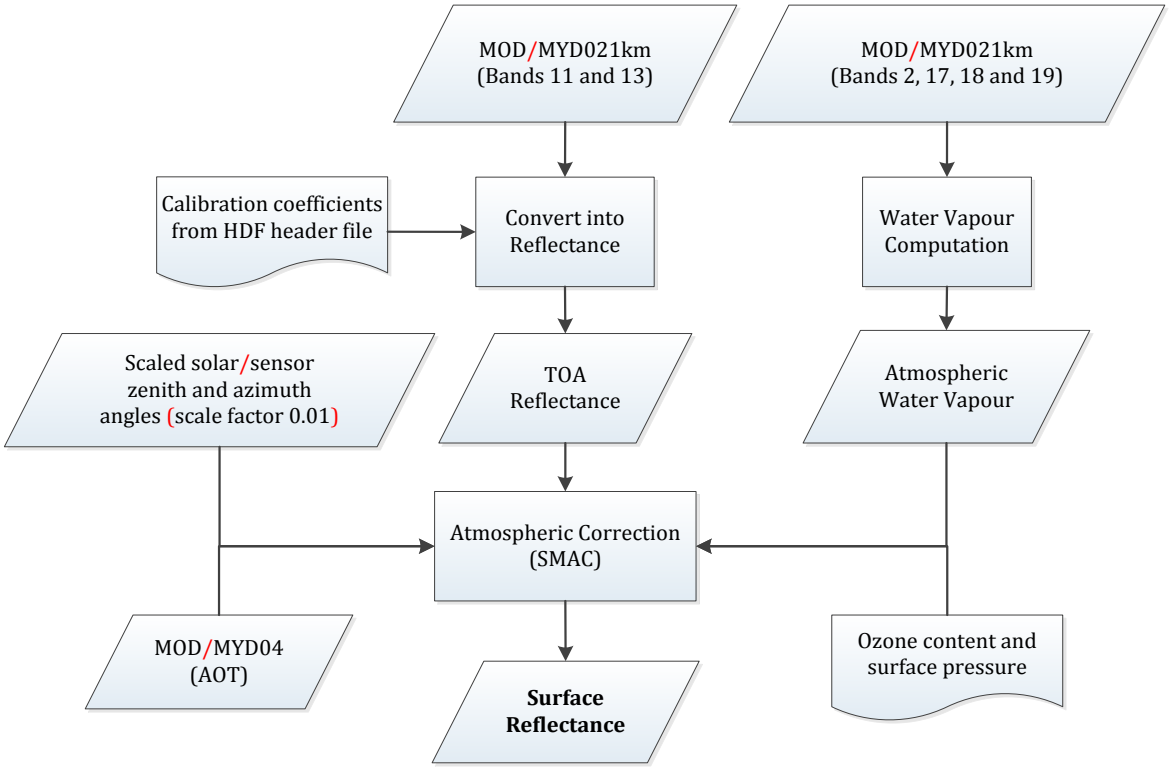

Figure 7-4 Flowchart of the procedure for retrieving daily MODIS surface reflectance from MODIS L1B

7.3.4 Description of Light Use Efficiency (LUE) Model

A simple diagnostic carbon flux (DCF) model developed by Xiao et al. (2011) was used to estimate the parameters of NEE of CO_2 particularly photosynthesis efficiency (ε) on the basis of the LUE logic, differences of gross photosynthesis or GPP and ecosystem respiration (Re):

$$NEE = -\varepsilon_{max} \times PAR \times fPAR \times W_s \times T_s + \left(R'_{ref} + \gamma \times AGB + \lambda \times GPP\right) \times e^{E_0\left(1/(T_{ref}-T_0)-1/(T-T_0)\right)}$$

Equation 7-4

where $\boldsymbol{\varepsilon_{max}}$ is the maximum light use efficiency (LUE) ($gCm^{-2}MJ^{-1}APAR$), ***PAR*** is the incident photosynthetically active radiation (MJm^{-2}) per time period (e.g., day or month), ***fPAR*** is the fraction of PAR absorbed by vegetation canopies, $\boldsymbol{W_S}$ is the water scalar, $\boldsymbol{T_S}$ is the temperature scalar, $\boldsymbol{R'_{ref}}$ is a parameter associated with the rate of respiration at the reference temperature, $\boldsymbol{T_{ref}}$ is the reference temperature,

E_0 is an activation energy parameter that determines the temperature sensitivity, and T_0 is a constant regression parameter. W_S and T_S represent the limiting effects of water availability and temperature on GPP, respectively, and both scalars vary from 0 to 1. T_{ref} is set to 10°C, and T_0 is kept constant at −46.02°C (Xiao et al.2011). Further information on the methods for model parameterization can be found in Xiao et al. (2011).

As mentioned previously, photosynthesis efficiency and its restraining factors are of crucial importance in the DCF model. In this study, the temperature scalar was used as implemented in the terrestrial ecosystem model (TEM) (Xiao et al., 2009; Xiao et al., 2011):

$$T_S = \frac{(T-T_{min})(T-T_{max})}{[(T-T_{min})(T-T_{max})]-(T-T_{opt})^2} \quad \text{Equation 7-5}$$

where T is the mean air temperature (°C), T_{min} and T_{max} are the minimum and maximum constraints for photosynthesis activity, and T_{opt} represents the optimum air temperature (°C) for carbon uptake.

The normalized difference water index (NDWI) obtained directly from MODIS was used as a proxy of water scalar (W_S) due to its high correlation with leaf water content (Jackson et al., 2004) and soil moisture (Fensholt and Sandholt, 2003) over time. The water scalar W_S was calculated using an algorithm introduced by Xiao, et al. (2004) as:

$$W_S = \frac{1+NDWI}{1+NDWI_{max}} \quad \text{Equation 7-6}$$

where $NDWI_{max}$ is the maximum NDWI for each flux tower site over the period of study. The NDWI was also calculated using band 2 (centred at 858.5 nm) and band 6 (centred at 1640 nm) of MODIS surface reflectance products.

The algorithm for parameterizing *f PAR* and photosynthesis efficiency, two key variables in the EC-LUE model, was defined as follows. On the basis of the radiative transfer model, there is a linear relationship between *f PAR* and a vegetation index (e.g. NDVI) for a large set of different ecological conditions. In this research, a

linear transformation of the MODIS derived enhanced vegetation index (EVI) was used to approximate *PAR* as:

$$fPAR = \alpha + \beta \times EVI \quad \text{Equation 7-7}$$

where $\boldsymbol{\alpha}$ and $\boldsymbol{\beta}$ are empirical constants. The EVI was obtained directly from 1 km MODIS observations (Equation 5) as the spectral index of photosynthesis capacity to avoid soil background effects, and then α and β were parameterized by the DCF model on the basis of the LUE logic.

$$EVI = 2.5 \frac{\rho_{nir} - \rho_{red}}{\rho_{nir} + (6\rho_{red} - 7.5\rho_{blue}) + 1} \quad \text{Equation 7-8}$$

where $\boldsymbol{\rho_{nir}}$, $\boldsymbol{\rho_{red}}$, and $\boldsymbol{\rho_{blue}}$ are the near-infrared, visible red and blue reflectance, respectively.

The parameters of the DCF model were estimated by the differential evolution algorithm (Price et al., 2006) using the DEoptim package (Ardia et al., 2013) implemented in the R statistical package. The resulting model parameters were used for the estimation of photosynthesis efficiency (ε) for comparing with MODIS derived light use efficiency. Finally, the MODIS PRI as a proxy of photosynthesis efficiency was compared with EC- and RS-based light use efficiency and EC/RS-based LUE estimated.

7.3.5 Sensitivity analysis

Seven parameters were selected ($\varepsilon_{max}, \alpha, \beta, R'_{ref}, \gamma, \lambda$ and E_0) for sensitivity analysis as suggested by Xiao et al. (2014). Monte Carlo analysis is a common name given to a group of methods that require repetitive sampling from a so-called Probability Density Function (PDF) to study the error propagation and the uncertainty associated with each parameter (Smith and Heath, 2001). These Monte Carlo simulations are usually merged with uncertainty analysis to draw conclusions about the behaviour of a model. The ranges and probability density function used for each parameter are given in Table (7-2). The local, one-at-a time

(OAT) and global sensitivity analysis (EFAST and Morris, 1991) were then applied to these parameters.

Among the most frequent global methods, it is possible to identify three main classes, including screening methods, regression-based methods, and variance-based methods (Confalonieri et al., 2010). Extended Fourier Amplitude Sensitivity Test explained (EFAST) earlier is a variance based method whereas the most popular screening method is the one proposed by (Morris, 1991). The method of Morris varies one-factor-at-a-time and therefore can be referred to as an OAT method, however as it attempts to explore several regions of the input space, the method can be regarded as global too (Saltelli, 2004).

This method is based on the computation of a certain number of incremental ratios (elementary effects) for each factor and on averaging them to estimate the overall factor importance on model output(s) (Campolongo et al., 2007). In Morris, each input factor is allowed to vary over $\boldsymbol{p}$ levels and $\boldsymbol{r}$ trajectories are generated randomly. Each trajectory is built in such a way that factors are varied one-at-a-time across their levels (Confalonieri et al., 2010). Along each trajectory, the so-called *elementary effect* of factor *i*, $\boldsymbol{R_i}$, is evaluated as (Confalonieri et al., 2010):

$$R_i(x_1, \dots, x_n, \Delta) = \frac{y(x_1,\dots,x_{i-1},x_i+\Delta,x_{i+1},\dots,x_n)-y(x_1,\dots,x_n)}{\Delta} \quad \text{Equation 7-9}$$

where $\boldsymbol{y(X)}$ is the output, $\boldsymbol{X} = (\boldsymbol{x_1}, \dots, \boldsymbol{x_n})$ is the n-dimensional vector of factors being studied, Δ is a value between 1/(p-1) and 1-1/(p-1), and $\boldsymbol{p}$ is the number of levels. The mean $\boldsymbol{\mu}$ and the standard deviation $\boldsymbol{\sigma}$ of the absolute values of the elementary effects over $\boldsymbol{r}$ trajectories are used as sensitivity measures to ascertain each factor's importance. The $\boldsymbol{\mu}$ measures the overall effects of a given factor on the output while σ accounts for all effects of a factor that are non-linear or due to interactions with other factors (Cariboni et al., 2007). In the Morris method, the number of model simulations (N) is equal to $N = r(k + 1)$, where $\boldsymbol{r}$ is the number of trajectories (i.e. number of randomly sampled points for each parameter) and $\boldsymbol{k}$ the number of model parameters (Morris 1991). Previous experiments

(Campolongo et al., 2007; Campolongo et al., 1999; Saltelli and Annoni, 2010; Saltelli et al., 2000) have demonstrated that the choice of p = 4 and r = 10 has produced valuable results.

In the present experiment, each factor was varied across p=4 levels, and r = 10 trajectories. The probability density function and initial values of each parameter are in Table 2. The implementation of the sensitivity analysis was conducted in SimLab Ver. 2.2.

Table 7-2 Probability Density Function (PDF) and initial values of parameters associated with each Plant Functional Type (PFT).

PFT	Parameters	Unit	PDF	Mean	SD	Min	Max
WC	ε_{max}	gCmMJ^{-1} APAR	Normal	1.399	0.509	-	-
	α	-	Normal	-0.429	0.092	-	-
	β	-	Normal	1.493	0.288	-	-
LC	ε_{max}	gCmMJ^{-1} APAR	Normal	1.204	0.388	-	-
	α	-	Normal	-0.274	0.074	-	-
	β	-	Normal	1.520	0.291	-	-
SWA	ε_{max}	gCmMJ^{-1} APAR	Normal	1.590	0.678	-	-
	α	-	Normal	-0.485	0.290	-	-
	β	-	Normal	1.513	0.286	-	-
UMBS	ε_{max}	gCmMJ^{-1} APAR	Normal	1.570	0.684	-	-
	α	-	Normal	-0.500	0.289	-	-
	β	-	Normal	1.488	2.88	-	-
For All Sites	R'_{ref}	gCm^{-2} day^{-1}	Uniform	-	-	0	20
	γ	gCm^{-2} day^{-1}	Uniform	-	-	-1	1
	λ	-	Uniform	-	-	-1	1
	E_0	°C	Uniform	-	-	0	500

7.4 Results and Discussion

7.4.1 Light Use Efficiency Model Parameters

Long-term EC flux measurements can reduce uncertainty in parameterization of the LUE model (Xiao et al., 2011; Naithani et al. 2012). Thus, the LUE model parameters were estimated using tower-based EC CO_2 flux measurements and corresponding time-series MODIS products.

Figure 7-5 shows the EC/RS-based GPP estimates versus an associated MOD17 GPP product across four flux tower sites with different PFTs (deciduous wetland forest, deciduous frost, and mixed forest). The estimated GPP values derived from the EC/RS-based LUE model were lower than the MOD17 GPP product, during the selected peak growing season due to cloud free days. At Willow Creek (Figure 7-5-a), a deciduous broadleaf forest site, the EC/RS-based GPP values had a large positive correlation (R^2=0.69) with the MOD17 GPP products. Furthermore, the EC/RS-based GPP values resulted in low RMSE values and a slope close to 1.0 implying high precision and low bias in the model. Apart from the Sylvania Wilderness (Figure 7-5-c), analysis of the performance of the EC/RS-based GPP versus the MOD17 GPP products in mixed forest sites revealed good agreement (R^2=0.63) in the University of Michigan Biological Station (Figure 7-5-d). The RMSE values were also relatively low indicating high precision of the EC/RS-based LUE model in estimating the *in situ* GPP of this PFT.

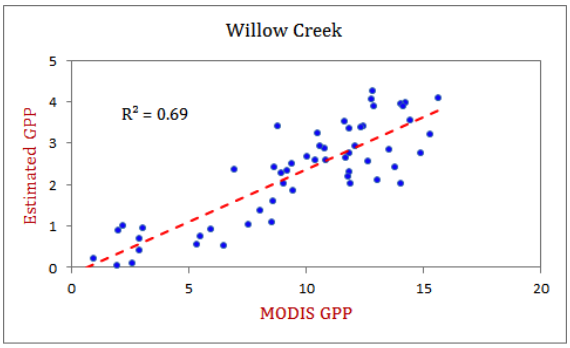

(a) EC/RS-based GPP Estimates vs MOD17 GPP, Willow Creek (deciduous forest)

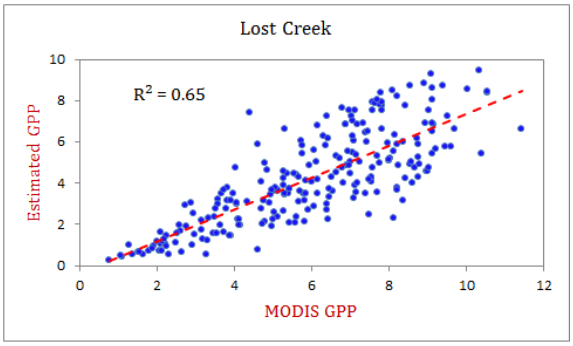

(b) EC/RS-based GPP Estimates vs MOD17 GPP, Lost Creek (deciduous wetland forest)

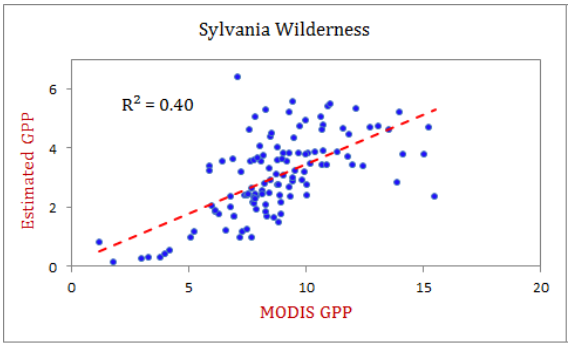

(c) EC/RS-based GPP Estimates vs MOD17 GPP, Sylvania Wilderness (mixed forest)

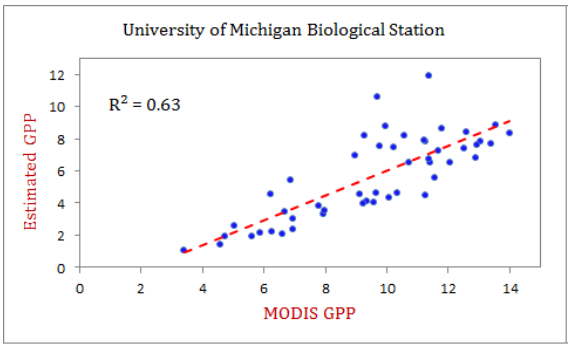

(d) EC/RS-based GPP Estimates vs MOD17 GPP, UMBS (mixed forest)

Figure 7-5 Relationship between EC/RS-based GPP estimation and corresponding MODIS GPP across four flux tower site (GPP unit: g C day-1)

According to the present findings, MODIS GPP is more representative of the deciduous forest site, for example R^2=0.69, RMSE=2.96 g C day^{-1} for Willow Creek, than mixed forest sites, for example, R^2=0.40, RMSE=6.04 g C day^{-1} for Sylvania Wilderness. Overall, the EC/RS-based GPP compared well to MOD17 GPP at each site separately across four AmeriFlux sites. This indicates that the EC/RS-based LUE model can be used as a tool to reliably estimate the values of GPP across various PFTs/biomes at regional and global scales. On the basis of this finding, the site-specific photosynthesis efficiency was computed using Equations 7-1 and 7-2 for the three sites with relatively large correlation: Willow Creek (deciduous forest), Lost Creek (deciduous wetland forest), and University of Michigan Biological Station (mixed forest).

The Pearson product-moment correlation (Table 7-3) was computed to assess the relationship between estimated parameters and MODIS products (GPP and EVI). A scatterplot summarises the results (Figure 7-6).

Table 7-3 Comparison of EC-based estimated parameters with MODIS products (p-value<0.01; N_{LC}= 235, N_{WC}=56, N_{SW}=118, N_{UMBS}= 49)

Parameters	MODIS-GPP				MODIS-EVI			
	LC	WC	SW	UMBS	LC	WC	SW	UMBS
EC-GPP	0.804	0.830	0.632	0.795	0.750	0.782	0.783	0.717
EC-ε	0.585	0.762	0.552	0.231	0.686	0.569	0.340	0.175

The correlation between photosynthesis efficiency obtained from the EC flux tower and MODIS EVI reveals a moderate-poor relationship with different coefficient of determination (R^2) with evident differences among PFTs, which indicate that the EVI is an insufficient approximation of photosynthesis efficiency.

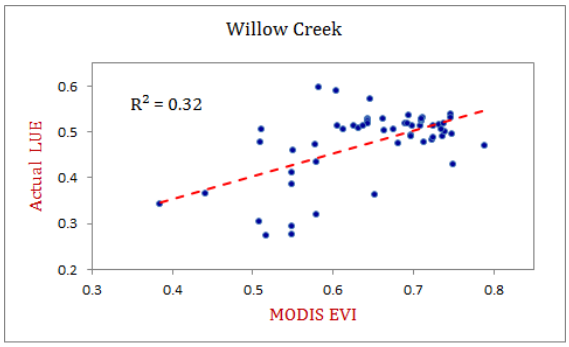

(a) EC/RS-based LUE vs MODIS EVI, Willow Creek (deciduous forest)

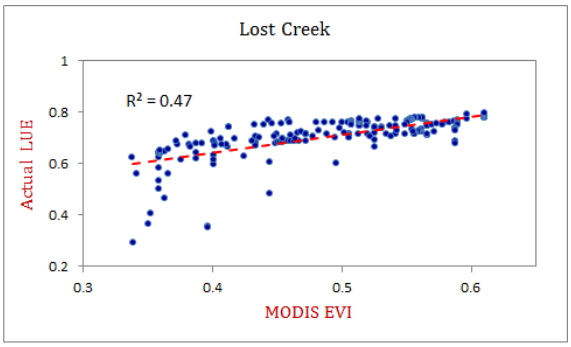

(b) EC/RS-based LUE vs MODISEVI, Lost Creek (deciduous wetland forest)

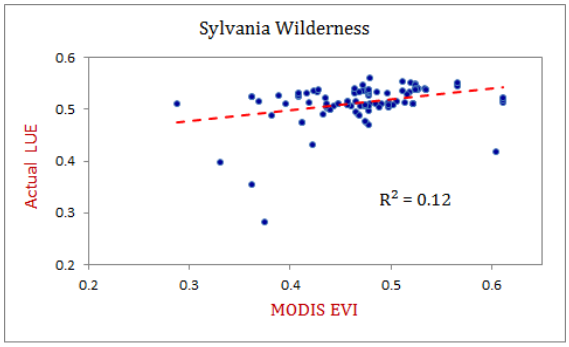

(c) EC/RS-based LUE vs MODISEVI, Sylvania Wilderness (mixed forest)

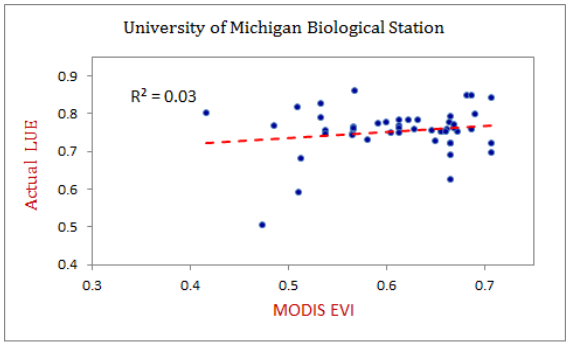

(d) EC/RS-based LUE vs MODISEVI, UMBS (mixed forest)

Figure 7-6 EC/RS-based photosynthesis efficiency (ε) estimates versus associated MODIS EVI across four flux tower site

7.4.2 Sensitivity Analysis

7.4.2.1 One-at-time sensitivity analysis

The results of OAT sensitivity analysis have been illustrated in Figure (7-7) and Figure (7-8). With respect to these figures, it can be concluded that in view of maximum light use efficiency (ε_{max}), it is the least influential parameter on the estimation of NEE. That is due to the fact that, the slope of the plot for all values within WC, SWA, and UMBS (PFTs) are roughly uniform and the same. On the contrary, the LC has been differently influenced by the above-mentioned parameter. That is to say, by 1.176 g C mMJ-1 APAR, the effect of this parameter on the NEE in this PFT has been a source, while thereafter it has changed to a sink of carbon. In addition, the role of this parameter in higher values has been more important than for lower values. The maximum Light Use Efficiency (LUE) is mainly dependent on the dominant vegetation type in each ecosystem. For the SWA and UMBS, the behaviour of this parameter is similar based on the PFTs which are mixed forest. On the other hand, the value of ε_{max} for each vegetation type is not only affected by its physiological attributes, but also the spatial scale and uniformity of vegetation coverage (Wenquan et al. 2006).

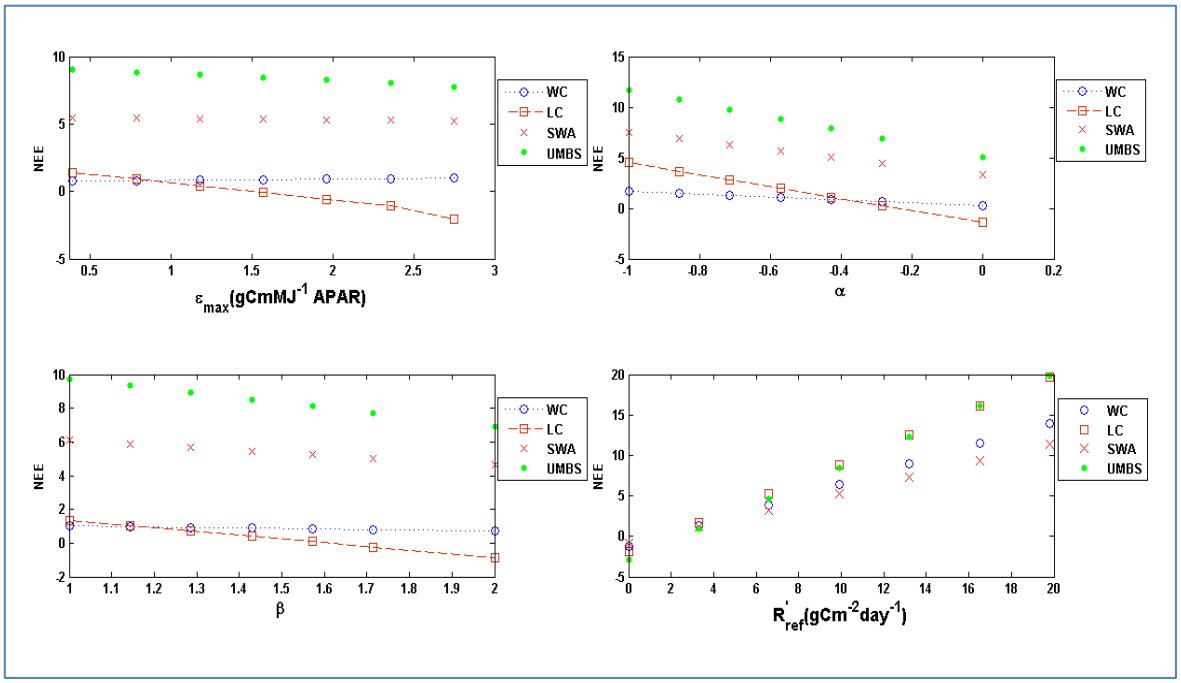

Figure 7-7 One-at-a-time sensitivity analysis for ε_{max},R'_{ref}, α *and* β associated with each PFT

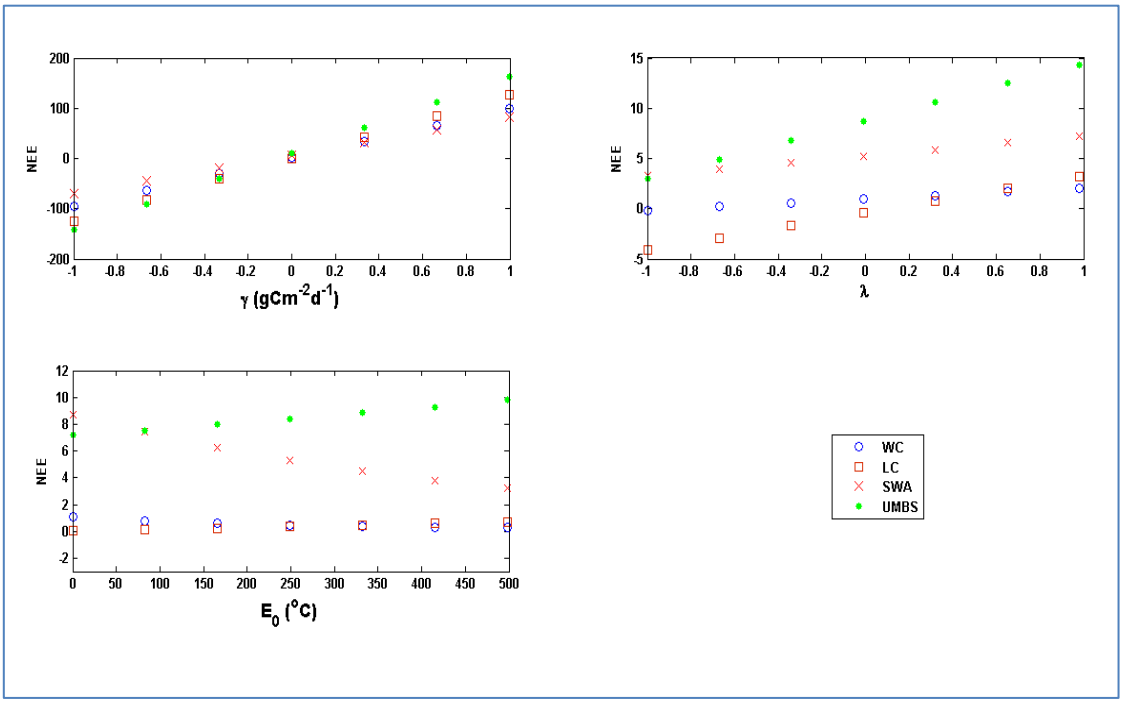

Figure 7-8 One-at-a-time sensitivity analysis for γ, E_0 and λ associated with each PFT

On the other hand, considering the α and β parameters, it can be concluded that the impact of α on NEE has been higher than that of β. The trend was nearly the same for lower and higher values of these parameters. For higher values of α and β in LC, they acted as a sink instead of a source. In addition, in this PFT, in comparison with , in β the effect of this parameter in lower values (i.e. by 1.286) was less than that of higher values. R'_{ref} next to γ are the most influential parameters on the estimation of the NEE. The behavior of R'_{ref} in WC and SWA is non-linear while for LC and UMBS it is completely linear. As respiration (i.e. g Carbon per surface area per day) increases that amount of NEE also rises accordingly, which shows that the ecosystem is going to be a source of carbon.

The results of the study also show that in LC the effect of λ for negative values acts as a sink while for positive values it becomes a source of carbon. On the other hand, the effect of λ in UMBS is more significant than for other PFTs.

Finally, the effect of E_0 in different PFTs is variable. While its effect in WC and LC has not been that important, the sensitivity of UMBS and SWA to this parameter is different. The increase of E_0 on the SWA resulted in a decrease of NEE whereas it caused an increase of NEE in UMBS. In summary, the results of the study were contradictory for the E_0 over different PFTs.

7.4.2.2 Global sensitivity analysis

First order global sensitivities(S) are the ratio of the input contribution to the output variance (Thogmartin, 2010), whereas total sensitivity indices (S_T) account for the main effects plus the contribution of interaction amongst parameters. Therefore, total sensitivity indices are always slightly larger than first-order sensitivity indices (Fieberg and Jenkins, 2005).

The resulting set of global sensitivities using the EFAST algorithm are presented in Table(7-4). Referring to this table, the differences between the main and total sensitivity indices (e.g. ΔS) are minor showing that the interaction amongst parameters is not significant. It can also be concluded from Table 3 that the sensitivity of NEE to the ε_{max}, α and β parameters in all of the PFTs was low and nearly the same. The only

exception was the sensitivity of NEE to the α parameter in SWA and UMBS which was higher to some extent (e.g. $S_{\alpha,\mathrm{SWA}} = 0.0006$ and $S_{\alpha,\mathrm{UMBS}} = 0.0004$). By contrast, the total order global sensitivities of the foregoing parameters in WC and LC were nearly the same and equal to 0.0025 and 0.0007, respectively. The S_T in SWA and UMBS were also roughly the same (e.g. 0.001) indicating that the interaction of these parameters with the other parameters does not have a significant effect on NEE in all PFTs. On the contrary, γ had the most significant impact on the resultant NEE in view of the first order and total order sensitivities. The highest first and total order sensitivities were observed in UMBS ($S_\gamma = 0.9830$ and $S_{T,\gamma} = 0.9922$) whereas the lowest sensitivities were recorded in WC ($S_\gamma = 0.7233$ and $S_{T,\gamma} = 0.9879$). This shows that in almost all of the PFTs, the key parameter in the variation of NEE was γ. For instance, in UMBS 98.3% of NEE variation was due to the direct impact of γ and almost all of its variation (e.g, 99.2%) was because of γ 's interaction with other parameters. On the other hand, λ,R'_{ref} and E_0 had an intermediate effect on NEE variation. The largest impact can be attributed to E_0 in WC, with a first order sensitivity of 0.0056. The total order global sensitivity of this parameter in this PFT was high however ($S_{T,E0} = 0.2706$) suggesting the high interaction of it with other parameters. One of the reasons for this contradiction as proposed by Thogmartin (2010) may be the high fraction of the variance explained by the interaction of the parameters (1-$\sum$S) in comparison with the other PFTs.

Table 7-4 Results of the EFAST global sensitivity method on seven parameters for each sites

PFT	WC			LC			SWA			UMBS		
Parameters	S	S_T	ΔS	S	S_T	ΔS	S	S_T	ΔS	S	S_T	ΔS
ε_{max}	2.65×10^{-6}	0.0025	0.0025	4.74×10^{-5}	0.0007	0.0007	1.76×10^{-6}	0.0009	0.0009	1.08×10^{-5}	0.0007	0.0007
α	1.33×10^{-5}	0.0025	0.0025	2.79×10^{-5}	0.0007	0.0007	0.0006	0.0016	0.001	0.0004	0.0011	0.0007
β	6.55×10^{-6}	0.0025	0.0024	6.41×10^{-5}	0.0007	0.0006	7.48×10^{-5}	0.0009	0.0008	7.17×10^{-5}	0.0007	0.0006
R'_{ref}	0.0045	0.0087	0.0042	0.0073	0.008	0.0007	0.0061	0.0074	0.0013	0.0055	0.0062	0.0007
γ	0.7233	0.9879	0.2646	0.9808	0.9914	0.0106	0.917	0.9904	0.0734	0.983	0.9922	0.0092
λ	0.0003	0.0033	0.003	0.0013	0.0023	0.001	0.001	0.0023	0.0013	0.0008	0.0018	0.001
E_0	0.0056	0.2706	0.265	0.0001	0.0091	0.009	0.0018	0.074	0.0722	0.0004	0.0081	0.0077
$1-\sum S$	0.2662			0.0104			0.0734			0.0098		

S and $\mathbf{S_T}$ are the main and total effects, respectively. **ΔS** represents the difference between main and total effects indicating integration among parameters.

The results of the application of the Morris method for each PFT are shown in Figure (7-9), which plots μ and σ for the seven input parameters. The plotted values may, thus, be examined relative to each other to see which input factor appears to be the most important. In particular, as shown in Figure 4, for WC, γ, E_0 and to some extent R'_{ref} are separated from the others because of their high mean and standard deviation values. Each input factor with a high value of the estimated mean μ also presents a high value of the estimated standard deviation (σ), highlighting that the model in this PFT is strongly non-linear and non-additive. In all of the PFTs, γ stands out from the other parameters with high mean and standard deviation, although the most nonlinear role of this parameter on NEE estimation can be seen in WC with a high level of standard deviation. This means that the elementary effects (refer to screening method) relative to this factor are significantly different from each other, i.e. the value of an elementary effect is strongly affected by the choice of the point in the input space at which it is computed (i.e. by the choice of the other factor's values). In contrast, a low σ indicates very similar values of the elementary effects, implying that the effect of this factor is almost independent of the values taken by the other factors (Saltelli, 2004).

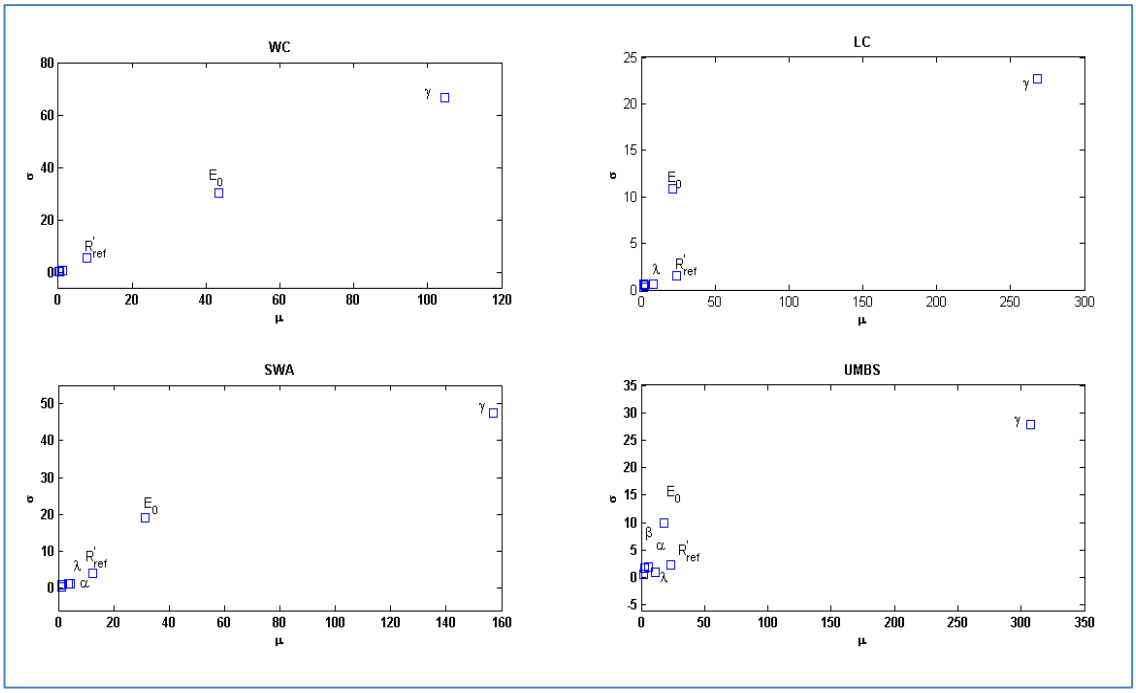

Figure 7-9 Results of Morris method, showing the scatterplot of σ versus μ for each site.

With the exception of E_0 which does not lie exactly on the diagonal of the plane but in the $\sigma > \mu$ zone, the same trend can be seen in LC. The latter parameter is highly involved in the interaction and/or curvature effects in comparison with the other ones. Moreover, in LC, α, β and ε_{max} contain small values of μ and . When factors with small values of μ are identified, these can be fixed at any value in their uncertainty distribution without any significant loss of information (Saltelli, 2004). Overall, in these two PFTs, each input factor with a high value for the estimated mean, μ, also has a high value for the estimated standard deviation, σ, or in other words, none of the parameters has a purely linear effect.

Considering SWA and UMBS, it can be seen that the trend is roughly the same. However, the nonlinearity effect of E_0 is more noticeable in UMBS. In this regard, factors can also be ranked in (decreasing) order of importance according to μ, which is a measure of the overall factor importance. Table (7-5) ranks the seven parameters according to decreasing value of the Morris measure μ. Considering this table, α, β and ε_{max} are the less important parameters.

Table 7-5 The ranking of parameters based on the results of Morris method for each site.

PFT	Parameters	μ	PFT	Parameters	μ
WC	γ	104.54	SWA	γ	157.07
	E_0	43.38		E_0	31.34
	R'_{ref}	7.70		R'_{ref}	12.31
	λ	1.30		λ	4.30
	α	0.39		α	3.58
	β	0.23		ε_{max}	1.24
	ε_{max}	0.16		β	1.07
LC	γ	267.96	UMBS	γ	307.71
	R'_{ref}	23.80		R'_{ref}	23.49
	E_0	21.14		E_0	17.93
	λ	8.13		λ	11.35
	β	2.13		α	5.63
	α	1.51		ε_{max}	2.32
	ε_{max}	1.45		β	2.06

The results confirmed that α, β and $\varepsilon_{\max}$ have little impact on the fluctuations of NEE within each PFT whereas the DCFM model is very sensitive to γ so, the estimation of this factor, in comparison with the other parameters, plays the key role in the accuracy of NEE predictions as well. Besides γ ,the other parameters to which the DCFM model is most sensitive, as obtained by the Morris method, were E_0 and R'_{ref}. These latter parameters are directly or indirectly related to temperature as R'_{ref} is a parameter associated with the rate of respiration at the reference temperature while E_0 is an activation energy parameter that determines the temperature sensitivity. This indicates the prominent role of temperature in reducing the uncertainty of the DCFM model.

In addition, except for WC, in other PFTs, interactions among the crucial eco-physiological parameters have a minor contribution to uncertainty of NEE prediction by DCFM model. The results are in agreement with those of White et al. (2000), however, they do not conform to Miao et al. (2011) who used the EFAST approach for sensitivity analysis, and suggested that the 2nd- and higher-order interactions among the 11 key eco-physiological parameters had much higher

contributions to the NEP, GPP and total carbon predictions than the 1st-order (i.e., effects of individual) parameter for the three tower sites in New Jersey Pinelands.

In previous work in the same ChEAS region, the adaptive MCMC approach of Xiao et al. (2014) led to a probability density function (PDF) for each parameter, and the spread of the variability of the PDF provided an estimate of parameter uncertainty. Although, their method (using an independent and identically distributed normal likelihood function) captures first-order uncertainty, ecosystem function and processes of some of PFTs such as woody wetlands are strongly influenced by water and temperature dynamics, and these interactions are not well represented in ecosystem models (Xiao et al., 2014) leading to a large uncertainty in NEE estimates. Our method using EFAST has obviated this problem to some extent. In addition, we used multiple PFTs to study the sensitivity of NEE predictions to input parameters. The different behaviour of parameters for each PFT was consistent with that of Xiao et al. (2014) and confirms this fact that the large within-PFT variability of some parameters indicating that it is inadequate to use one site to parameterize the parameters for a given PFT for regional applications.

A large standard deviation in annual NEE was observed over the PFTs using one-at-a time local sensitivity analysis. For some influential parameters, such as , the carbon sink and source of the PFT depends completely on the initial estimation of this parameter. For instance, if the initial value of this parameter was negative the ecosystem would act as a sink of carbon while the positive values would result in prediction of carbon release by the ecosystem indicating the key role of this parameter in NEE predictions. This phenomenon for some other parameters like λ hinges on the PFT. For example, the role of λ in LC was the same as that of γ with respect to the results of the OAT method.

Despite the widespread use of local sensitivity analysis in ecological research one of the shortcomings of this method is the lack of meaningful results for non-linear models, and its inability to detect interactions among factors (Saltelli and Annoni, 2010) since the interactions are activated only when all the factors move

simultaneously. For instance, there was a high discrepancy between the results of OAT and global sensitivity analysis using the EFAST algorithm in the study of Thogmartin (2010) on bird populations, which was attributed to the interaction amongst input parameters. In this research, however, the results of OAT and global sensitivity analysis support each other, which might be due to the negligible interaction among parameters as mentioned earlier.

In the current research, we used a uniform distribution for parameters (e.g. R'_{ref}, γ, λ and E_0) because little information was available, although the conclusions regarding uncertainty analysis depend strongly on these assigned distributions. Thus, in the future if these information gaps are filled, these distributions might change. Despite this, as long as the distribution of parameters is well identified, using Monte Carlo simulation for studying the sensitivity to and uncertainty associated with each parameter is a reasonable approach (Kremer, 1983). In addition, we believe that it is necessary to consider other sources of uncertainty in NEE predictions, such as uncertainty due to model parameters and structure which can be obviated by gathering more data, the impacts of natural or human-made disturbances on carbon storage and fluxes in different PFTs like fire, wind and habitat destruction, uncertainty resulting from temporal changes in each PFT such as maturity stage, leaf biomass and loss (especially for deciduous forests), the fraction of aboveground biomass and the effects of biomass harvest etc..

7.4.3 EC/RS Derived LUE versus MODIS PRI

Moderate resolution PRI data, such as MODIS data at 1 km spatial resolution, are sensitive to variation in atmospheric condition, Sun-sensor geometry, and canopy chlorophyll content, even across a homogeneous ecosystem (Drolet et al., 2005). Thus, a different relationship between MODIS PRI and LUE across various PFTs/biomes would be expected. Using band 13 as a reference band for computing the PRI produced a large correlation with LUE, $r\ (51) = 0.797,\ p < 0.01$, even when data from different PFTs/biomes were used (Figure 7-10).

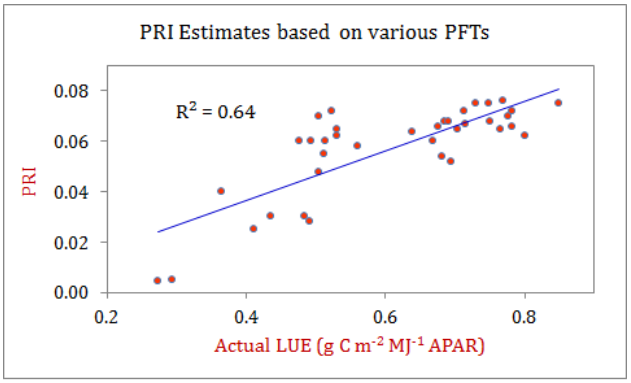

Figure 7-10 MODISPRI versus LUE derived from long-term EC flux tower measurements across three different plant functional types

The relationships with MODIS PRI were also tested for each site separately. Willow Creek, a deciduous homogeneous forest stand produced the largest correlation between MODIS PRI and LUE, *r (14) =0.840, p<0.01*, while Lost Creek with a relatively heterogeneous deciduous wetland forest stand produced a moderate correlation, *r (13) =0.736, p<0.01* (Figure 7-11).

The MODIS PRI, derived from atmospherically-corrected surface reflectance based on the band 11 centred at 531 nm as a xanthophyll-sensitive spectral band (Gamon et al., 1992) and 13 centred at 667 nm as a reference band (Drolet et al., 2005), was explored as a spectral index of photosynthesis LUE across three flux tower sites representing various PFTs/Biomes: wetland forest, deciduous forest and mixed forest. The PRI signals for Willow Creek, a relatively homogeneous deciduous forest, was significantly correlated with photosynthesis LUE measured by tower-based EC observations, Pearson correlation: *r (14) =0.840, p<0.01*(Figure 7-11-a). However, this relation for wetland and mixed forests was not statistically significant (Figure 7-11-b and –c), despite presenting similar behaviour between MODIS PRI and LUE.

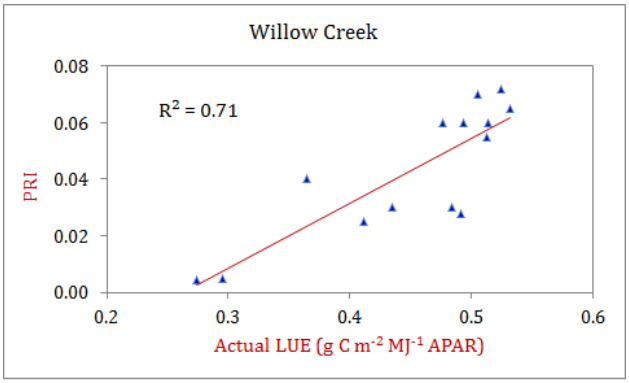

(a) Willow Creek - Pearson correlation: *r (14) =0.840, p<0.01*

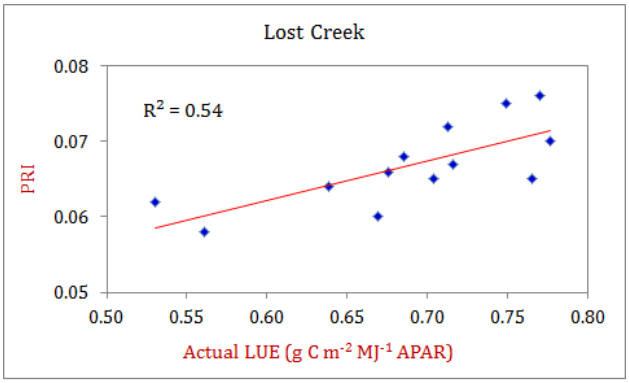

(b) Lost Creek – Pearson correlation: *r (13) =0.736, p<0.01*

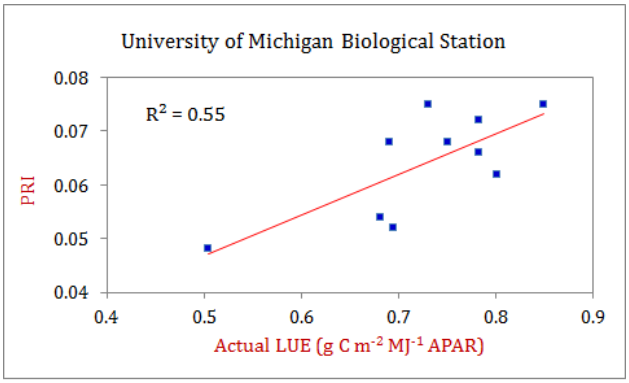

(c) University of Michigan Biological– Pearson correlation: *r (10) =0.741, p<0.05*

Figure 7-11 MODIS-PRI versus R-LUE derived from long-term EC flux tower measurements across different PFTs; (a) Willow Creek, (b) Lost Creek, (c) University of Michigan Biological Station.

7.5 Conclusion

This chapter was concerned with the sensitivity of a simple Diagnostic Carbon Flux Model (DCFM) developed to estimate the net ecosystem carbon exchange (NEE) in forest ecosystems, to seven input parameters. The results of the global sensitivity analysis demonstrated that as the differences between the first and total order sensitivity indices were negligible, interactions between model parameters appear to be relatively insignificant. Therefore, OAT sensitivity analysis for each site will produce sufficiently accurate estimates of the sensitivity of the model to input parameters. Moreover, the calculation of elementary effects will help us identify parameters with influential effects and those with a minor influence on the NEE. This information will aid researches for possible simplification and improvement of the DCFM model in the future studies. As a whole, the results of sensitivity methods, both local and global, agreed with each other. The results of this research also confirm the fact that due to the different ecological characteristics of each site (i.e. PFT), the uncertainty analysis should be based on multiple PFTs to produce reliable results.

To sum up, this study showed the potential of the Monte Carlo method and uncertainty analysis to study the behaviour of parameters in carbon cycling modelling in forest ecosystems. However, in the case of more complex methods with a larger number of parameters such as mechanistic models that require the solution of partial differential equations, the time scale and cost of running the model will be much higher. Since there are few cases of using these complex models for carbon cycling in previous studies, these methods can be regarded as a new research direction in this field to consider their pros and cons for uncertainty analysis in comparison with simple models.

Followed by the above, the results produced a large correlation between satellite-based PRI computed from surface reflectance and the EC-based LUE of a homogeneous deciduous forest. However, estimating the regional level LUE of a

heterogeneous landscape, such as Wytham Woods, from space is still an uncertain process because the required spectral index (PRI) will be affected by canopy-level variables as well as the geometry of illumination and view, as represented in chapter 4. This conclusion points to the need to combine narrowband reflectance indices (PRI) with data on the fine-scale spatial variability of forest canopies at frequent temporal intervals. This requirement for fine detail in all three sampling domains is not currently met with a single remote sensing system.

8. General Discussion and Conclusion

In this chapter, the main findings with regard to research questions are summarised and general conclusions based on the finding of the studies presented in this thesis are described, Furthermore, the strengths and limitations of the thesis are considered and suggestions for future researches are presented.

8.1 Introduction

The term "Earth System" refers to land-atmosphere interactions which comprise both the physical climate system and the biogeochemical processes (Flato 2011), along with the human systems (i.e. social and economic systems), such as the carbon cycle and its concentration in the terrestrial and oceanic ecosystems (Schimel et al. 2015).

Earth System Models (ESMs)[1] have been developed and are widely used to understand the land-atmosphere interaction and the planet's natural cycles (Flato 2011). The ESMs can be evaluated by direct continuous ecosystem observations of sensible heat, latent heat, water vapour, and CO_2 exchange (Xiao et al., 2012; Williams et al., 2009). However, uncertainty in the Earth's surface energy budget and terrestrial CO_2 fluxes can lead to variations in atmospheric carbon concentration and a dominant constraint for robust climate projections and

1- Earth System Models (ESMs) are global climate models with the added capability to explicitly represent biogeochemical processes that interact with the physical climate and so alter its response to forcing such as that associated with human-caused emissions of greenhouse gases.

ecosystem productivity estimates. Therefore, comparing observations to the ESMs requires careful consideration of the observation uncertainty and representativeness of observations for the model grid scale. Internationally synchronized experiments are increasingly important in providing a multi-model ensemble of ecosystem simulations, thereby taking advantage of some elimination of errors and allowing better quantification of uncertainty.

In recent years, the integration of spatially-explicit ecosystem models, remote sensing and eddy covariance flux network observations with environmental variables have facilitated the quantification of carbon cycling dynamics across multiple spatial and temporal scales (Miao et al. 2011). In this regard, process-based models with the aim of simulation of carbon dynamics in forest ecosystems are increasingly being used besides other tools to predict the effects of environmental factors on the forest carbon pool and forest productivity. However, despite this, decision makers must be aware of the limitations of these models by sensitivity and uncertainty analysis to make the process-based models more robust (Smith & Heath, 2001; Huntzinger et al., 2012). Despite the importance of uncertainty issues in ecological researches, sensitivity and uncertainty analyses still remain rarely used in carbon cycling models of terrestrial ecosystems (Smith & Heath, 2001; Hilker et al., 2008; Masek et al., 2015; Oijen et al.; 2017)

8.2 General Conclusion

Ecosystem primary productivity contributes to commercial and ecological services by the process of plant photosynthesis, which converts atmospheric CO_2 into biomass. In this context, accurate quantification of temporal and spatial variation in the amount of carbon fixed by the photosynthesis process and its sequestration by vegetation over large areas is important. There is a need to address the various sources of uncertainty associated with such quantification. The research addressed this need using a combination of tower-based EC flux measurements and EO data from both airborne and satellite remote sensing systems at a range of temporal and spatial scales. There are several sources of uncertainty associated with scaling

RS-based models of the ecosystem productivity at various spatial and temporal scales, including sensor limitations in terms of support size defined by spatial and temporal resolution (Dungan, 2002); spatial heterogeneity of land surface properties (Atkinson and Foody, 2002; Sogachev et al., 2004; Kim et al., 2006; Chen et al., 2012; Xioa et al., 2012); pre-processing calibration (Baret, 1995; Danson, 1995; Woodcock, 2002; Liang, 2004); and the structure of the model proposed and its parameterization (Dungan, 2002) (final chapter, i.e. to reduce the uncertainty in parameterizing a spectral indices-based LUE model). The research investigated these sources of uncertainty and error across three domains of interest: spectral, spatial and temporal.

The primary goal of this research was to demonstrate and extend a new approach to a wide range of plant functional types (PFTs) in order to provide a quantitative, model-driven assessment of uncertainties and research priorities for improved prediction of the carbon cycle and vegetation dynamics. Specifically, chapter 7 focus on uncertainty associated with model parameter choice and aim to identify the key sources of uncertainty in a sophisticated terrestrial biosphere model. In this chapter, a specific approach for improving representativeness and estimating corresponding uncertainty of tower-based observations of carbon fluxes. Tower-based observations of carbon fluxes have been increasingly used to constrain model uncertainty, because it provides reliable spatially distributed and temporally continuous observations of surface-atmosphere exchanges (Bonan et al., 2011; Baldocchi et al., 2001).

In terms of the spectral domain, the research adds to the evidence that NDVI alone is insufficient to fully characterise the primary productivity of plant canopies, specifically temperate mixed woodlands. The preliminary research in Wytham Woods, Oxfordshire, showed that the MODIS EVI was more closely related to gross primary productivity than NDVI. It also highlighted the potential of airborne imaging spectrometry (AIS) to provide information on the process of photosynthesis, through the photochemical reflectance index (PRI). One of the

significant achievements of the research was the creation of three calibrated high spatial resolution reflectance maps of Wytham Woods (Figure 4.2). This is important as it provides an example of the use of data from an airborne imaging spectrometer to create a quantitative multi-date product to underpin further biophysical research. In the present research, the multi-date reflectance map provided accurate spectra from elements of the forest canopy and background which would have been impossible to measure on the ground using a Spectroradiometer.

Technical issues and a lack of suitable data meant that further development of an approach based on AIS was not possible, even for a small site as well-studied as Wytham Woods (Table 8-1). Instead, effort was directed to understanding the potential of a PRI-like index derived from MODIS data and applied to a more suitable field site in the US.

Direct approaches regarding global prediction of the photosynthesis process from remote sensing, using PRI show promise to facilitate precise estimation of the photosynthesis process over large areas using satellite observations. Satellite sensors providing high spectral and spatial resolution hold promise to facilitate acquisition of information on the photosynthesis capacity and efficiency. Currently there is an absence of satellite sensors available with wavebands narrow enough to obtain reflectance measurements specifically in the PRI region (Hilker et al., 2008). EO1-Hyperion was the first hyperspectral sensor in space with a contiguous spectral bandwidth of 10 nm. However, being designed as a demonstration instrument, this sensor is limited in its signal to noise ratio and calibration accuracy (Datt et al., 2003; Khurshid et al., 2006; Hilker et al., 2008). The MODIS sensor provides wavebands close to the PRI region (Drolet et al., 2005; Hilker et al., 2008), however, initial results indicate that the approach at this stage does not sufficiently account for the spatial heterogeneity of the landscape. Additionally, there is a lack of algorithms available for processing the full suite of MODIS water bands over land surfaces which limits the routine application of the approach.

The large area characterization of primary production depends on comprehensive assessing and continued efforts of land surface validation, requiring coordinated scientific networking to meaningfully combine findings and results representative of a range of spatial scales. Networking approaches such as the global flux tower network have greatly improved our knowledge on interactions of ecosystem physiological responses to changing environmental conditions.

In the temporal domain, the research made use of a unique time-series of 10 multispectral images acquired during a single growing season by the DMC satellite sensors. Although these sensors lack the spectral bands necessary to compute EVI or PRI, the system as a whole has the advantage of being a constellation of several satellites. This greatly increases the frequency of imaging a specific site, which in especially important in mid-latitude areas due to the problem of cloud cover. The DMC sensor is also well-calibrated, has fine spatial resolution and a very wide swath, making it ideally suited to acquiring a high quality time series of images. In practice, a significant amount of work was required to inter-calibrate the DMC images, involving a new way to normalise the separate images. However, the end result was a calibrated, multi-date sequence of high spatial resolution NDVI images from Wytham Woods. This was a significant technical achievement and a notable contribution to research at this internationally important site.

The DMC data enabled a spatially detailed, temporal sequence of NDVI to be assembled, and from this it was possible to see how patterns of NDVI changed over time and how these interacted with the areas of the forest canopy sampled by instruments on a flux tower. Early in the growing season (leaf-off) the distribution from samples of NDVI from around the flux tower was positively skewed, but this changed as the canopy developed, until by the time the canopy was fully developed the distribution showed negative skewness.

Table 8-1 The advantage and limitation of AIS-based vegetation indices of Ecosystem function

RS-based Technique	Advantages	Limitations
AIS-based Spectral Indices of Ecosystem Function	✓ Detailed spectral information at fine spatial resolution across a heterogonous woodland ✓ Narrowband spectral indices such as PRI ✓ Addressing spatially ecosystem function in the scaling process between flux tower measurements and coarse satellite observation ✓ NDVI as a reliable estimator of biophysical variables closely related to photosynthesis capacity at various spatial and temporal scales over a wide range of plant functional types ✓ PRI as a reliable estimator of photosynthesis efficiency at leaf and stand level over a wide range of plant functional types ✓ Combining spectral vegetation indices to generate spatially continuous map of ecosystem function in a specific biome	* Snapshot in time and often affected by cloud and cloud shadows * Impossible to generate a seasonal PRI profile * Time-consuming in pre-processing and problem of cross-track illumination variation * Impossible to create an accurate single image of entire of stand forest due to narrow swath width and generating a mosaic of flight-lines * Sensitive to solar/view geometry, particularly across heterogonous canopy stand at the UK-DMC support size * Affected by differences in the conditions of measurement, particularly the atmospheric correction * Significant difference between VI values across realistic flux tower footprint and landscape level over forested area due to time-varying flux tower footprint coverage * Spatial dependence in spectral indices of ecosystem function was introduced as a primary source of uncertainty association with scaling process between flux tower measurements and coarse satellite observation * The specific biome-based spectral vegetation indices of ecosystem function cannot be extrapolated across heterogonous landscape at region scale

The Moderate Resolution Imaging Spectroradiometer (MODIS) and DMC sensors can revisit the Earth regularly at fine temporal resolution. Moreover, their swath (i.e. MODIS and DMC images) are much wider than the commercial high-resolution images such as IKONOS, QuickBird and WorldView. These advantages lead to the popular use of MODIS and DMC images in global land cover/use monitoring, carbon cycle and ecosystem productivity. However, they provide coarse spatial resolution relative to the estimating CO_2 flux.

Modelled flux tower footprints showed the uncertainty in NDVI to vary with the wind conditions (speed and direction), peaking at around 5% early in the season. Computing and investigating the RFF is important, because an accurate estimate of the RFF is crucial in linking remotely sensed data and plant spectral indices (e.g. NDVI) to the eddy covariance data measured from flux towers. It is interesting that the uncertainty due to choice of footprint is around 5%. This is comparable to the error that others have reported due to the uncertainty in atmospheric correction (specifically the parameterisation of aerosols). Thus, in the case of Wytham Woods, one might argue that it will be equally important to improve the representation of aerosols in the atmospheric model used as to replace the generalised circular flux tower footprint with a realistic flux tower footprint (RFF). However, this thesis has shown clearly that careful definition of the true flux tower footprint is possible through modelling, and so there is no reason why researchers should not take advantage of such an approach and improved footprint definitions to reduce this specific source of uncertainty associated with linking ground and image data. A fundamental challenge for model-data comparison is the scale mismatch between a small-scale, spatially non-uniform flux footprint and the typically larger-scale gridded, continuous predictions made in simulations/RS-based simulations. The flux measurement footprint typically represents a small fraction of the model grid cell in most ESMs, and the location of this fraction changes with time. Any transient bias that occurs from changes in sampled characteristics with time can bias model-data comparison. Recent analysis has shown that consideration of flux footprint for

scaling chamber emissions can significantly improve comparison of EC to chamber-scaled fluxes (Budishchev et al., 2014).

For EC fluxes, many sites have differing preferred wind magnitude and directions at daytime versus night time, making flux observations at daily scale a mix of diurnal cycle and change of flux footprint. Methods to account for this variable footprint bias could aid in removing a potentially large source of systematic uncertainty for EC flux towers.

Two main scaling approaches, process-based approach (Wang et al., 2006; Desai et al., 2008, 2010; Xiao et al., 2011) and data-driven approach, have been utilized for scaling tower-based observation of surface-atmosphere exchange in space and time, each subject to specific limitations. The process-based scaling (Wang et al., 2006; Desai et al., 2008, 2010; Xiao et al., 2011) relies on prescribed mechanistic relationships, often times based on laboratory calibrations and far-reaching assumptions, such as functional steady-state and closure of energy or water balances. Purely data-driven scaling (Xiao et al.,2014; Hutjes et al., 2010) minimizes the number of assumptions employed by inferring relationships among observations directly from the available data, but are limited in model robustness and predictive performance, in particular for discrete predictions with substantial intra-class variability (Prueger et al., 2012; Wang et al.,2006). Among many data-driven methods, machine-learning techniques, such as artificial neutral network (Sulkava et al., 2011; Papale and Valentini, 2003) and model ensemble (Jung et al., 2010), have been used to regress atmospheric fluxes against surface properties. However, due to a lack of sample size, the temporal resolution of these approaches is typically aggregated from daily to monthly timescales, and cannot provide information on the diurnal cycle. Further consideration of transient footprint bias is usually neglected in either case.

Chapter 6 investigated how the realistic flux tower footprint could be defined under different conditions and for different remote sensing systems. Two different vegetation indices in terms of support size, satellite-derived broadband NDVI and airborne narrowband red edge NDVI (NDVI-705) were used as spectral indices of

CO_2 flux. Four different image supports from MODIS imagery were defined to test the effect of choice of support on the ability to predict the true value of spectral vegetation index (NDVI). The resulting weighted flux tower footprint NDVI was compared with those averaged equally across the flux tower extent (i.e., across three by three MODIS pixels) (231 m × 231 m) with the flux tower location at the centre pixel, as well as a single 1 km pixel of MODIS.

The investigation showed that there was a statistically significant difference between NDVI values across the realistic flux tower footprint and flux tower extent over the forested area due to the time-varying flux tower footprint coverage. Variogram analysis from both airborne- and satellite-based NDVI showed that the spatial variability occurred beyond a certain support size at 2 m and 22 m, respectively. Furthermore, directional variogram of AISA Eagle-based NDVI indicated an anisotropic distributed pattern within the conventional flux tower footprint, defined as a circular buffer with 200 m radius centred on the flux tower. In contrast, omnidirectional variogram analysis on the multi-temporal DMC NDVI early in the growing season showed that the degree of spatial variability varied among each realistic flux tower footprint. These results showed that the spatial covariance in the realistic flux tower footprint coverage varied through time due to the vegetation phenological trend. This change in spatial co-variability across the time-varying weighted flux tower footprint can affect the prediction of NDVI across the flux tower domain based on coarse satellite observations.

The final part of the research conducted in the US showed a large correlation between satellite-based PRI computed from surface reflectance and EC-based LUE for a homogeneous deciduous forest. However, estimation of the regional level LUE of a heterogeneous landscape from space was uncertain because the spectral index necessary (PRI) was affected by canopy-level variables as well as the geometry of illumination and view. This conclusion points to the need to combine imaging spectrometry with data on the spatial variability of forest canopies at a fine temporal scale. This is not currently possible with a single remote sensing system

8.3 Research Finding

The research described in this thesis involved many different remote sensing platforms and sensors, from the airborne LiDAR used to characterise the forest canopy, to global-scale MODIS data used to develop and test an index of light use efficiency. Each component of the system had strengths and weaknesses in relation to the overall task, the determination of plant productivity in a mixed forest. An important conclusion is that no single system currently exists to deliver information on both plant cover (NDVI) and photosynthetic processes (PRI) at the temporal and spatial scales necessary, even when including the calibration and validation of this information using measurements from the global flux tower network, and thus provide global information on plant productivity.

Overall, the research investigated the main sources of uncertainty and error across three domains of interest: spectral, spatial and temporal. In this regard, the research conducted in:

- Quantification of regional carbon fluxes and associated uncertainty;
- Diagnosis of uncertainty as
    - calibration of remotely sensed observations;
    - sensor limitations in terms of support size defined by spatial and temporal resolution;
    - spatial representation of EC flux measurement (flux footprint)
    - spatial heterogeneity of land surface properties (role of landscape level heterogeneity/canopy patches through growing season); and
    - the structure of the model proposed and its parameterization
- Determination of the sensitivity of a number of vegetation indices in terms of optical geometry, atmospheric effects, canopy structure and soil background; and
- Characterizing observational and model uncertainty (uncertainty decline with increasing temporal coverage of flux tower measurements, while it increases with increasing spatial coverage of flux data record).

Accordingly, main finding the research are:

- Over the whole phenological trend, Wytham Woods was found to be acting as a net carbon sink.
- The MODIS EVI was found to estimate GPP slightly more accurately than NDVI.
- In addition to having fine spatial resolution, imaging spectrometry provides many spectral bands and thus allows simulation of many different remotely sensed indices, including those thought to be related to ecological processes, not just canopy state.
- The AIS data required considerable pre-processing, and the data volume would have become unmanageable for any site larger than Wytham Woods.
- Although the AIS data was felt to be unsuitable for operational use over large areas, it was uniquely suited to simulation studies and to investigating up-scaling from very small areas (a few square metres) to an area the size of a MODIS or DMC pixel.
- The optical geometry (sun and view zenith angles) effects accounted for approximately 10-20% of the variance in spectral indicators of CO_2 flux's wavelengths responses in mixed forested images collected by those sensors such as UK_DMC with 22 m pixel size.
- Soil reflectance also contributed to the observed reflectance, but only at sufficiently sparse canopy cover, particular across ancient stand in Wytham Woods.
- Leaf Area Index (LAI) can have significant effects on reflectance and should be considered. The spectral indices (NDVI and PRI) are strongly influenced by varying soil background for LAI of less than 3.
- The spectral indices (NDVI and PRI) are relatively robust to aerosol scattering.
- The DMC constellation system has several important advantages over the more commonly used systems such as MODIS as:

  - The data from DMC are of finer spatial resolution, which means that smaller areas of uniform land cover can be sensed, and also that heterogeneous sites can be studied. This is particularly important if the aim is to compare the satellite observation with ground measurements, either for model calibration or for product validation purposes.
  - The second advantage of DMC over MODIS concerns the temporal precision of the measurements. The 16-day sampling window of MODIS could become a limitation at certain times during the growing season. In the case of Wytham Woods in 2010, the DMC time-series shows an increase in NDVI between 20th and 27th April, whereas the MODIS data show no significant change between these dates.
- A time-series of DMC images were acquired and inter-calibrated, and these provided a unique insight into the seasonal changes occurring in one of the most important ecological sites in the UK (Wytham Woods).
- The DMC limitations for this task (scaling process) is the large off-nadir view angle of some pixels as a consequence of the very wide swath.
- The heterogeneity of Wytham Woods had greatest impact on the DMC data early in the season, and this highlighted the importance of understanding how the flux tower footprint varies with weather conditions.
- In Wytham Woods, as the canopy began to green-up, the precision of temporal sampling became more important. The rapid rise in NDVI in late Spring was captured effectively by DMC images one week apart, whereas in the MODIS data from the same period this was less clear.
- The geostatistical-based investigation showed that there was a statistically significant difference between NDVI values across realistic flux tower footprint and flux tower extent over forested area due to time-varying flux tower footprint coverage.

- The semi-variogram analysis from both airborne- and satellite-based NDVI showed that the spatial variability occurred beyond a certain support size at 2 m (AISA Eagle pixel size) and 22 m (DMC pixel size), respectively.
- Directional semi-variogram analysis on AISA Eagle-based NDVI indicated an anisotropic distributed pattern within conventional flux tower footprint across a buffer distance-off from flux tower location at 200 m
- Based on explicit representation of the time-varying flux tower footprint, prediction of flux tower measurements directly from space-borne coarse spatial resolution imagery is challenging and leads to a low predictive ability, no matter how the imagery are manipulated.
- Due to the different ecological characteristics of various Plant Functional Types (PFT) across heterogeneous landscape, the analysis of the uncertainty in parameterizing a spectral indices-based LUE model should be based on multiple PFTs to produce reliable results.
- The results of chapter 7 indicates a large correlation between satellite-based PRI and the EC-based LUE of a homogeneous deciduous forest. However, estimating the regional level LUE of a heterogeneous landscape, such as Wytham Woods, from space is still an uncertain process because the required spectral index (PRI) will be affected by canopy-level variables as well as the geometry of illumination and view.

- Generally, the study concludes that a combination of hypertemporal, fine spatial resolution NDVI from the DMC constellation and a PRI-like index from MODIS currently offers the best solution to uncertainty associated with scaling spectral indices of carbon fluxes.

8.4 Recommendation

This research conducted direct integration of remote sensing with flux measurements, which offers greater insights into the underlying controls on ecosystem–atmosphere fluxes than possible with either method alone. While optical sampling is readily scalable, a key focus was on proximal remote sensing explicitly designed to match the sampling scale of flux measurements as a means of understanding functional processes. Proximal sampling can also be readily linked to conventional remote sensing, providing critical validation and extrapolation of fine-scale measurements to larger regions (i.e. up-scaling). While optical methods was the primary focus, other methods (e.g., LiDAR) was also be applied to a wide range of ecological properties within the flux tower extent (i.e. flux footprint).

The research demonstrated the value of a constellation of identical satellites, as exemplified by DMC. The combination of frequent imaging at fine spatial resolution, and the choice of spectral bands optimised for vegetation (NDVI) meant that DMC was nearly perfect for the application. The main problem with DMC for this application was the lack of bands to compute PRI. Had such bands been available, the limitation would then become the accuracy of atmospheric correction and issues related to sensor view angle and illumination geometry (i.e. uncertainty due to the bidirectional reflectance distribution function).

In the absence of a PRI-capable sensor on DMC, the research demonstrated that both AIS and MODIS are credible sources of information on photosynthetic processes. AIS has a role to play as a research tool, and specifically to investigate further the geostatistical aspects of the problem discussed in the final chapter, but for operational applications it is likely that MODIS and its successors will remain the sensor of choice. Currently, the combination of DMC and MODIS appears to be the optimum sensor combination for remote sensing the productivity of woodland areas, especially where the sites are small and/or heterogeneous as in much of Europe. This conclusion may change when ESA Sentinel-2 is launched later this year, but there is some evidence that the spectral bands proposed for this sensor will not be optimal for sensing photosynthetic processes (Frampton et al., 2013). In

the longer term, satellite sensors specifically designed to measure photosynthetic processes, such as ESA's proposed Fluoresence Explorer (FLEX) may make index-based methods such as PRI redundant.

Finally, hundreds of flux tower site are currently operational as standalone projects to measure mass and energy for many different projects. However, the vast majority of these measurements may not straight-forward coupling with satellite data, and even fewer have optical sensors for validation of satellite products and up-scaling from field to regional and global scales. The scaling progress of flux tower measurements needs an integrated system to collect and process synchronized flux data from multiple towers at landscape scale in coupling with optical sensors from both tower-based and satellite observations. In other word, an integrated system are required for improved understanding of physically and physiologically induced reflectance properties of various vegetation types to facilitate modelling of GPP estimates representative of large areas. This requires the aligning flux footprints and satellite observations to precisely align optical data and flux measurements in terms of both time and scape. In this aspect, current flux towers can be augmented with optical sensors as a bridge to deliver continuous products (e.g. NDVI, PRI, etc.) from automated field spectrometers (i.e. tower-based optical sensor from the flux footprint at the same time with satellite-based sensor overpass). This integrated system may help to interpret satellite products, validate models and improve up-scaling of flux tower measurements into regional and global scales.

Bibliography

Acito, N., Gorsini, G. & Diani, M. 2002. *Proceedings of the 2002 IEEE Geoscience and Remote Sensing Symposium (IGARSS2002)*.

Adams, B., White, A. & Lenton, T. M. 2004. An analysis of some diverse approaches to modelling terrestrial net primary productivity. *Ecological Modelling,* 177**,** 353-391.

Adler-Golden, S. M., Matthew, M. W., Bernstein, L. S., Levine, R. Y., Berk, A., Richtsmeier, S. C., Acharya, P. K., Anderson, G. P., Felde, J. W., Gardner, J. A., Hoke, M. L., Jeong, L. S., Pukall, B., Ratkowski, A. J. & Burke, H.-H. K. Atmospheric correction for shortwave spectral imagery based on MODTRAN4. 1999. 61-69.

Ahl, D. E., Gower, S. T., Burrows, S. N., Shabanov, N. V., Myneni, R. B. & Knyazikhin, Y. 2006. Monitoring spring canopy phenology of a deciduous broadleaf forest using MODIS. *Remote Sensing of Environment,* 104**,** 88-95.

Ahl, D. E., Gower, S. T., Mackay, D. S., Burrows, S. N., Norman, J. M. & Diak, G. R. 2004. Heterogeneity of light use efficiency in a northern Wisconsin forest: implications for modeling net primary production with remote sensing. *Remote Sensing of Environment,* 93**,** 168-178.

Ahl, D. E., Gower, S. T., Mackay, D. S., Burrows, S. N., Norman, J. M. & Diak, G. R. 2005. The effects of aggregated land cover data on estimating NPP in northern Wisconsin. *Remote Sensing of Environment,* 97**,** 1-14.

Anonymous 2016. Peer review report 2 on "Is scale really a challenge in evapotranspiration estimation? A multi-scale study in the Heihe Oasis using thermal remote sensing and the three-temperature model". *Agricultural and Forest Meteorology,* 217, Supplement 1**,** 256.

Antonarakis, A. S., Richards, K. S. & Brasington, J. 2008. Object-based land cover classification using airborne LiDAR. *Remote Sensing of Environment,* 112**,** 2988–2998.

Ardia, D., Mullen, K., Peterson, K. & Ulrich, J. 2013. Global optimization by Differential Evolution - DEoptim: Differential Evolution Optimazation in R. *R Package version 2.2-2.*

Armitage, R. P., Ramirez, F. A., Danson, F. M. & Ogunbadewa, E. Y. 2013. Probability of cloud-free observation conditions across Great Britain estimated using MODIS cloud mask. *Remote Sensing Letters,* 4**,** 427-435.

Atkinson, P., M. 1999. Spatial Statistics. *In:* Stein, A., Van Der Meer, F. & Gorte, B. (eds.) *Spatila Statistics for Remote Sensing.* First ed. Netherland Kluwer Academic Publishers.

Atkinson, P., M. & Curran, P. J. 1995. Defining an Optimal Size of Support for Remote Sensing Investigations. *Transaction on Geoscience and Remote Sensing,* 33**,** 768-776.

Atkinson, P., M. & Jeganathan, C. 2010. Estimating the Local Small Support Semivariogram for Use in Supper-Resolution Mapping. *In:* Atkinson, P., M. & Lloyd, C. D. (eds.) *geoENV VII - Geostatistics for Environmental Application* Springer.

Atkinson, P. M. 2006. Resolution Manipulation and Sub-Pixel Mapping. *In:* De Jong, S. M. & Van Der Meer, F. D. (eds.) *Remote Sensing Image Analysis: Including the spatial Domain.* The Netherlands: Springer.

Atkinson, P. M. 2013. Downscaling in remote sensing. *International Journal of Applied Earth Observation and Geoinformation,* 22**,** 106-114.

Atkinson, P. M. & Foody, G. M. (eds.) 2002. *Uncertainty in Remote Sensing and GIS,* West Sussex, England: John Wiley and Sons Ltd.

Atkinson, P. M., Foody, G. M., Gething, P. W., Mathur, A. & Kelly, C. K. 2007. Investigating spatial structure in specific tree species in ancient semi-natural woodland using remote sensing and marked point pattern analysis. *Ecography,* 30**,** 88-104.

Atkinson, P. M. & Kelly, R. E. J. 1997. Scaling-up point snow depth data in the U.K. for comparison with SSM/I imagery. *International Journal of Remote Sensing,* 18**,** 437-443.

Atkinson, P. M. & Tate, N. J. 2000. Spatial scale Problems and Geostatistical Solution: A Review. *Professional Geographer,* 52**,** 607-623.

Atkinson, P. M., Webster, R. & Curran, P. J. 1994. Cokriging with airborne MSS imagery. *Remote Sensing of Environment,* 50**,** 335-345.

Avissar, R. & Pielke, R. A. 1989. A Parameterization of Heterogeneous Land Surfaces for Atmospheric Numerical Models and Its Impact on Regional Meteorology. *Monthly Weather Review,* 117**,** 2113-2136.

Bailey, T. C. & Gatrell, A. C. 1995. *Interactive Spatial Data Analysis* Addison Wesley Longman.

Baldocchi, D. 2008. Turner Review No. 15. Breathing of the terrestrial biosphere: lessons learned from a global network of carbon dioxide flux measurement systems. *Australian Journal of Botany,* 56**,** 1 - 26.

Baldocchi, D., Falge, E., Gu, L., Olson, R., Hollinger, D., Running, S., Anthoni, P., Bernhofer, C., Davis, K. J., Evans, R., Fuentes, J., Goldstein, A., Katul, G., Law, B., Lee, Z., Malhi, Y., Meyers, T., Munger, W. J., Oechel, W., Paw, U. K. T., Pilegaard, K., Schmid, H. P., Valentini, R., Verma, S., Vesala, T., Wilson, K. B. & Wofsy, S. 2001. FLUXNET: A New Tool to Study the Temporal and Spatial Variability of Ecosystem-Scale Carbon Dioxide, Water Vapor, and Energy Flux Densities. *Bulletin of the American Meteorological Society,* 82**,** 2415 - 2434.

Baldocchi, D. D., Hincks, B. B. & Meyers, T. P. 1988. Measuring Biosphere-Atmosphere Exchanges of Biologically Related Gases with Micrometeorological Methods. *Ecology,* 69**,** 1331-1340.

Baret, F. 1995. Use of Spectral Reflectance Variation to Retrive Canopy Biophysical Characteristics. *In:* Danson, F. M. & Plummer, S. E. (eds.) *Advances in Environmental Remote Sensing.* West Wessex, England: Jhon Wiley and Sons.

Baret, F. & Guyot, G. 1991. Potentials and limits of vegetation indices for LAI and APAR assessment. *Remote Sensing of Environment,* 35**,** 161-173.

Barilotti, A., Turco, S. & Alberti, G. 2006. LAI Determination in Forestry Ecosystems by LiDAR Data Analysis. *3D Remote Sesning in Forestry.*

Barrett, E. C. & Curtis, L. F. 1997. *Introduction to Environmental Remote Sensing,* London, Chapman and Hall.

Barrett, E. C. & Curtis, L. F. 1999. *Introduction to Environmental Remote Sensing,* Glos. UK, Stanley Thornes LtD.

Bartlett, D. S., Whiting, G. J. & Hartman, J. M. 1990. Use of vegetation indices to estimate indices to estimate intercepted solar radiation and net carbon dioxide exchange of a grass canopy. *Remote Sensing of Environment,* 30**,** 115-128.

Bell, I. E. & Baranoski, G. V. G. 2004. *IEEE Transactions on Geoscience and Remote Sensing,* 42**,** 570.

Berni, Kljun, Gorsel, V., Haverd, Leuning, Ceabello-Leblic, Held, Hopkinson & Chasmer. spatial distribution of biophysical parameters derived from hyperspectral and lidar remote sensing. Improving the constraints in land surface modelling. 34th International Symposium on Remote Sensing of Environment. April 10-15., 2011 Sydney Australia., unpaginated USB.

Berry, S., Mackey, B. & Brown, T. 2007. Potential Applications of Remotely Sensed Vegetation Greenness to Habitat Analysis and the Conservation of Dispersive Fauna. *Pacific Conservation Biology,* 13**,** 120 - 127.

Bivand, R. S., Pebesma, E. J. & Gomez-Rubio, V. 2008. *Applied Spatial Data Analysis with R,* New York, Springer.

Blackburn, G. A. & Milton, E. J. 1997. An Ecological Survey of Deciduous Woodlands using Ariborne Remote Sensing and Geographical Information Systems (GIS). *International Journal of Remote Sensing,* 18**,** 1919-1935.

Bonan, G. B. 1993. Importance of Leaf Area Index and Forest Type When Estimating Photosysnthesis in Boral Forests. *Remote Sensing of Environment,* 43**,** 303-314.

Boschetti, M., Boschetti, L., Oliveri, S., Casati, L. & Canova, I. 2007. Tree species mapping with Airborne hyper-spectral MIVIS data: the Ticino Park study case *International Journal of Remote Sensing,* 28**,** 1251-1261.

Boudreau, J., Nelson, R. F., Margolis, H. A., Beaudoin, A., Guindon, L. & Kimes, D. S. 2008. Regional aboveground forest biomass using airborne and spaceborne LiDAR in Québec. *Remote Sensing of Environment,* 112**,** 3876-3890.

Bowen, B. M., Dewat, J. M. & Chen, A. I. Stability Class Determination: A comparision for one site. Proceedings Sixth Syposium on Turbulence and Diffusion, 1983 Boston, MA. American Meteorological Society, 211 - 214.

Box, E., Holben, B. & Kalb, V. 1989. Accuracy of the AVHRR vegetation index as a predictor of biomass, primary productivity and net CO2 flux. *Vegetatio,* 80**,** 71-89.

Brook, A. & Dor, E. B. 2011. Supervised vicarious calibration (SVC) of hyperspectral remote-sensing data. *Remote Sensing of Environment,* 115**,** 1543-1555.

Bruce K. Wylie, D. a. J., Emilio Laca, Nicanor Z. Saliendra, Tagir G. Gilmanov, Bradley C. Reed, Larry L. Tieszen, Bruce B. Worstell 2003. Calibration of remotely sensed, coarse resolution NDVI to CO_2 fluxes in a sagebrush-steppe ecosystem. *Remote Sensing of Environment,* 85**,** 243-255.

Burba, G. & Anderson, D. 2010a. *A Brief Practical Guide to Eddy Covariance Flux Measurements,* USA, LI-COR Biosciences.

Burba, G. G. & Anderson, D. J. 2010b. Introduction to the Eddy Covariance Method. *General Guidelines, and Conventional Workflow.* LI-COR Biosciences.

Burgess, T. M. & Webster, R. 1980. Optimal Interpolation and Isarithmic Mapping of Soil Properties, II Block Kriging. *Journal of Soil Science,* 31**,** 33-341.

Burgheimer, J., Wilske, B., Maseyk, K., Karnieli, A., Zaady, E., Yakir, D. & Kesselmeier, J. 2006. Relationships between Normalized Difference Vegetation Index (NDVI) and carbon fluxes of biologic soil crusts assessed by ground measurements. *Journal of Arid Environments,* 64**,** 651-669.

Byrne, G. F., Crapper, P. F. & Mayo, K. K. 1980. Monitoring land-cover change by principal component analysis of multitemporal landsat data. *Remote Sensing of Environment,* 10**,** 175-184.

Cammalleri, C., Anderson, M. C., Ciraolo, G., D'urso, G., Kustas, W. P., La Loggia, G. & Minacapilli, M. 2012. Applications of a remote sensing-based two-source energy balance algorithm for mapping surface fluxes without in situ air temperature observations. *Remote Sensing of Environment,* 124**,** 502-515.

Canadell, J. G., Mooney, H. A., Baldocchi, D. D., Berry, J. A., Ehleringer, J. R., Field, C. B., Gower, S. T., Hollinger, D. Y., Hunt, J. E., Jackson, R. B., Running, S. W., Shaver, G. R., Steffen, W., Trumbore, S. E., Valentini, R. & Bond, B. Y. 2000. Carbon Metabolism of the Terrestrial Biosphere: A Multitechnique Approach for Improved Understanding. *Ecosystems,* 3**,** 115-130.

Canty, M. J. 2010. *Image Analysis, Classification, and Change Detection in Remote Sensing: With Algorithm for ENVI/IDL,* Boca Raton, CRC Press Taylor & Francis Group.

Canty, M. J. & Nielsen, A. A. 2007. Investigation of Alternative Iteration Schemes for the IR-MAD Algorithm. *Image and Signal Peocessing for Remote Sensing* [Online], 674808.

Canty, M. J. & Nielsen, A. A. 2008. Automatic radiometric normalization of multitemporal satellite imagery with the iteratively re-weighted MAD transformation. *Remote Sensing of Environment,* 112**,** 1025 - 1036.

Canty, M. J., Nielsen, A. A. & Schmidt, M. 2004. Atumatic radiometric normalizationof multitemporel satellite imagery. *Remote Sensing of Environment,* 91**,** 441 - 451.

Carlson, T. N. & Ripley, D. A. 1997. On the relation between NDVI, fractional vegetation cover, and leaf area index. *Remote Sensing of Environment,* 62**,** 241-252.

Chelle, M., Andrieu, B. & Bouatouch, K. 1998. *Visualization and Computer Graphics,* 14**,** 109.

Chen, B., Black, T., Coops, N., Hilker, T., Trofymow, J. & Morgenstern, K. 2009a. Assessing Tower Flux Footprint Climatology and Scaling Between Remotely Sensed and Eddy Covariance Measurements. *Boundary-Layer Meteorology,* 130**,** 137-167.

Chen, B., Coops, N. C., Fu, D., Margolis, H. A., Amiro, B. D., Black, T. A., Arain, M. A., Barr, A. G., Bourque, C. P. A., Flanagan, L. B., Lafleur, P. M., Mccaughey, J. H. & Wofsy, S. C. 2012. Characterizing spatial representativeness of flux tower eddy-covariance measurements across the Canadian Carbon Program Network using remote sensing and footprint analysis. *Remote Sensing of Environment,* 124**,** 742-755.

Chen, B., Ge, Q., Fu, D., Liu, G., Yu, G., Sun, X., Wang, S. & Wang, H. 2009b. Upscaling of gross ecosystem production to the landscape scale using multi-temporal Landsat images, eddy covariance measurements and a footprint model. *Biogeosciences Discussions,* 6**,** 11317 - 11345.

Chen, J. M. 2016. Peer review report 1 on "Development of a coupled carbon and water model for estimating global gross primary productivity and evapotranspiration based on eddy flux and remote sensing data". *Agricultural and Forest Meteorology,* 217, Supplement 1**,** 285-286.

Chen, J. M., Leblanc, S. G., Miller, J. R., Freemantle, J., Loechel, S. E., Walthall, C. L., Innanen, K. A. & White, H. P. 1999. Compact Airborne Spectrographic Imager (CASI) used for mapping biophysical parameters of boreal forests. *Journal of Geophysical research,* 104**,** 27945 - 27958.

Cheriyadat, A. & Bruce, L. M. 2003. *Proceedings of the 2003 IEEE Geoscience and Remote Sensing Symposium*.

Chiang, M. Y. & Hsu, L. M. 2000. *Proceedings of the 2000 Biodiversity and Preservation Symposium*.

Cho, M. A., Skidmore, A., Corsi, F., Van Wieren, S. E. & Sobhan, I. 2007. Estimation of green grass/herb biomass from airborne hyperspectral imagery using spectral indices and partial least squares regression. *International Journal of Applied Earth Observation and Geoinformation,* 9**,** 414-424.

Clark, I. 1977. Regularization of a semivariogram. *Computers & Geosciences,* 3**,** 341-346.

Clark, R. N., Swayze, G. A., Heidebrecht, K. B., Goetz, A. F. H. & Green, R. O. Comparison of Methods for Calibrating AVIRIS Data to Ground Reflectance. In Summaries of the Fourth Annual JPL Airborne Geoscience Workshop 1993 Pasadena, California. Jet Propulsion Laboratory, 35-36.

Clark, R. N., Swayze, G. A., Heidebrecht, K. B., Green, R. O. & Goetz, A. F. H. Calibration to Surface Reflectance of Terrestrial Imaging Spectrometry Data: Comparison of Methods. In Summaries of the Fifth Annual JPL Airborne Earth Science Workshop 1995 Pasadena, California. Jet Propulsion Laboratory, 41-42.

Cochrane, M. A. 2000. Using vegetation reflectance variability for species level classification of hyperspectral data. *international Journal of Remote Sensing,* 21**,** 2075-2087.

Cohen, W. B., Maiersperger, T. K., Turner, D. P., Ritts, W. D., Pflugmacher, D., Kennedy, R. E., Kirschbaum, A., Running, S. W., Costa, M. & Gower, S. T. 2006. MODIS land cover and LAI collection 4 product quality across nine sites in the western hemisphere *IEEE Transactions Geoscience and Remote Sensing* 44**,** 1843-1857.

Conese, C., Maracchi, G., Miglietta, F., Maselli, F. & Sacco, V. M. 1988. Forest classification by principal component analyses of TM data. *International Journal of Remote Sensing,* 9**,** 1597-1612.

Coops, N. C., Wulder, M. A., Duro, D. C., Han, T. & Berry, S. 2008. The development of a Canadian dynamic habitat index using multi-temporal satellite estimates of canopy light absorbance. *Ecological Indicators,* 8**,** 754-766.

Coops, N. C., Wulder, M. A. & Iwanicka, D. 2009. Demonstration of a satellite-based index to monitor habitat at continental-scales. *Ecological Indicators,* 9**,** 948-958.

Corney, P. M., Kirby, K. J., Le Duc, M. G., Smart, S. M., Mcallister, H. A. & Marrs, R. H. 2008. Changes in the field-layer of Wytham Woods - assessment of the impacts of a range of environmental factors controlling change. *Journal of Vegetation Science,* 19**,** 287-298.

Cosh, M. H. & Brutsaert, W. 2003. Microscale structural aspects of vegetation density variability. *Journal of Hydrology,* 276**,** 128-136.

Cramer, W., Bondeau, A., Woodward, F. I., Prentice, I. C., Betts, R. A., Brovkin, V., Cox, P. M., Fisher, V., Foley, J. A., Friend, A. D., Kucharik, C., Lomas, M. R., Ramankutty, N., Sitch, S., Smith, B., White, A. & Young-Molling, C. 2001. Global response of terrestrial ecosystem structure and function to CO2 and climate change: results from six dynamic global vegetation models. *Global Change Biology,* 7**,** 357-373.

Cressie, N. 1993. *Statistics for Spatial Data,* New Yourk, John Wiley & Sons.

Cressie, N. & Hawhins, D. M. 1980. Robust Estimation Of the Variogram. *Mathematical Geology,* 12.

Crowley, G. 2010. *DMC Data Product Manual* [Online]. Guildford: DMC International Imaging. Available: http://WWW.dmcii.com [Accessed 31/January/2012 2012].

Curran, P. 1980. Multispectral remote sensing of vegetation amount. *Progress in Physical Geography,* 4**,** 315-341.

Curran, P. J. 1982. Polarized visible light as an aid to vegetation classification. *Remote Sensing of Environment,* 12**,** 491-499.

Curran, P. J. 1988. The semivariogram in remote sensing: An introduction. *Remote Sensing of Environment,* 24**,** 493-507.

Curran, P. J. & Atkinson, P. M. 1998. Geostatistics and Remote Sesning. *Progress in Physical Gepgraphy,* 22**,** 61 - 78.

Curran, P. J., Dungan, J. L., Macler, B. A. & Plummer, S. E. 1991. The effect of a red leaf pigment on the relationship between red edge and chlorophyll concentration. *Remote Sensing of Environment,* 35**,** 69-76.

Curran, P. J. & Milton, E. J. 1983. The relationships between the chlorophyll concentration, LAI and reflectance of a simple vegetation canopy. *international Journal of Remote Sensing,* 4**,** 247-255.

Curran, P. J. & Williamson, H. D. 1986. Sample size for ground and remotely sensed data. *Remote Sensing of Environment,* 20**,** 31-41.

Curran, P. J., Windham, W. R. & Gholz, H. L. 1995. Exploring the Relationship Between Reflectance Red Edge and Chlorophyll Concentration in Slash Pine Leaves. *Tree Physiology,* 15**,** 203-206.

Curtis, P. S., Hanson, P. J., Bolstad, P., Barford, C., Randolph, J. C., Schimd, H. P. & Wilson, K. B. 2002. Biometric and eddy-covariance based estimates of annual carbon storage in five eastern North American deciduous forests. *Agricultural and Forest Meteorology,* 113**,** 3 - 19.

Danson, F. M. (ed.) 1995. *Developments in the Remote Sensing of Forest Canopy Structure,* West Wessex, England: John Wiley and Sons Ltd.

Danson, F. M. & Curran, P. J. 1993. Factors affecting the remotely sensed response of coniferous forest plantations. *Remote Sensing of Environment,* 43**,** 55-65.

Danson, F. M. & Rowland, C. S. 2003. Training a neural network with a canopy reflectance model to estimate crop leaf area index. *international Journal of Remote Sensing,* 24**,** 4891-4905.

Dash, J. & Curran, P. J. 2007. Evaluation of the MERIS terrestrial chlorophyll index (MTCI). *Advances in Space Research,* 39**,** 100-104.

Datt, B., Mcvicar, T. R., Van Niel, T. G., Jupp, D. L. B. & Pearlman, J. S. 2003. *IEEE Transactions on Geoscience and Remote Sensing,* 41**,** 1246.

Davi, H., Gillmann, M., Ibanez, T., Cailleret, M., Bontemps, A., Fady, B. & Lefèvre, F. 2011. Diversity of leaf unfolding dynamics among tree species: New insights from a study along an altitudinal gradient. *Agricultural and Forest Meteorology,* 151**,** 1504-1513.

Davis, K. J. The Role of the Chequamegon Ecosystem-Atmosphere Study in the U.S. Carbon Cycle Science Plan. *In:* Desai, A. R. & Smithwick, E., eds. Observing and Simulating Carbon Cycle Impacts of Forest Management and Climate Variability in Heterogenous Landscapes 27-29 June, 2012 2012 Kemp Natural Resources Station, Woodruff, WI. University of Wisconsin-Madison

De Jong, S. M., Pebesma, E. J. & Van Der Meer, F. D. 2006. Spatial Variability, Mapping Methods, Image Analysis and Pixels. *In:* De Jong, S. M. & Van Der Meer, F. D. (eds.) *Remote Sensing Image Analysis: Including the Spatial Domain.* Springer.

Deng, J. S., Wang, K., Deng, Y. H. & Qi, G. J. 2008. PCA-based land-use change detection and analysis using multitemporal and multisensor satellite data. *International Journal of Remote Sensing,* 29**,** 4823-4838.

Desai, A. R., Bolstad, P. V., Cook, B. D., Davis, K. J. & Carey, E. V. 2005. Comparing net ecosystem exchange of carbon dioxide between an old-growth and mature forest in the upper Midwest, USA. *Agricultural and Forest Meteorology,* 128**,** 33-55.

Desai, A. R., Noormets, A., Bolstad, P. V., Chen, J., Cook, B. D., Davis, K. J., Euskirchen, E. S., Gough, C., Martin, J. G., Ricciuto, D. M., Schmid, H. P., Tang, J. & Wang, W. 2008. Influence of vegetation and seasonal forcing on carbon dioxide fluxes across the Upper Midwest, USA: Implications for regional scaling. *Agricultural and Forest Meteorology,* 148**,** 288-308.

Devlin, R. M. & Baker, A. V. 1971. *Photosynthesis*.

Diggle, P. J. & Ribeiro Jr., P. J. 2007. *Model-based Geostatistics,* New York, Springer.

Dörnhöfer, K. & Oppelt, N. 2016. Remote sensing for lake research and monitoring – Recent advances. *Ecological Indicators,* 64**,** 105-122.

Drolet, G. G., Huemmrich, K. F., Hall, F. G., Middleton, E. M., Black, T. A., Barr, A. G. & Margolis, H. A. 2005. A MODIS-derived photochemical reflectance index to detect inter-annual variations in the photosynthetic light-use efficiency of a boreal deciduous forest. *Remote Sensing of Environment,* 98**,** 212-224.

Drolet, G. G., Middleton, E. M., Huemmrich, K. F., Hall, F. G., Amiro, B. D., Barr, A. G., Black, T. A., Mccaughey, J. H. & Margolis, H. A. 2008. Regional mapping of gross light-use efficiency using MODIS spectral indices. *Remote Sensing of Environment,* 112**,** 3064-3078.

Du, H., Cui, R., Zhou, G., Shi, Y., Xu, X., Fan, W. & Lü, Y. 2010. The responses of Moso bamboo (Phyllostachys heterocycla var. pubescens) forest aboveground biomass to Landsat TM spectral reflectance and NDVI. *Acta Ecologica Sinica,* 30**,** 257-263.

Dungan, J. L. 2002. Toward a Comprehensive View of Uncertainty in Remote Sensing Analysis. *In:* Foody, G. M. & Atkinson, P. M. (eds.) *Uncertainty in Remote Sensing and GIS.* West Sussex, England: John Wiley & Sons Ltd.

Duro, D. C., Coops, N. C., Wulder, M. A. & Han, T. 2007. Development of a large area biodiversity monitoring system driven by remote sensing. *Progress in Physical Geography,* 31**,** 235–260.

Eastman, J. R. & Fulk, M. 1993. Long sequence time series evaluation using standardized principal components. *Photogrametric Engineering & Remote Sensing,* 59**,** 991-996.

Edirisinghe, A., Clark, D. & Waugh, D. 2012. Spatio-temporal modelling of biomass of intensively grazed perennial dairy pastures using multispectral remote sensing. *International Journal of Applied Earth Observation and Geoinformation,* 16**,** 5-16.

Elton, C. S. & Miller, R. S. 1954. The Ecological Survey of Animal Communities: With a Practical System of Classifying Habitats by Structural Characters. *journal of Ecology,* 42**,** 460-196.

Emmerton, C. A., St. Louis, V. L., Humphreys, E. R., Gamon, J. A., Barker, J. D. & Pastorello, G. Z. 2016. Net ecosystem exchange of CO2 with rapidly changing high Arctic landscapes. *Global Change Biology,* 22**,** 1185-1200.

Erik & Økland, T. 2002. Estimating tree height and tree crown properties using airborne scanning laser in a boreal nature reserve. *Remote Sensing of Environment,* 79**,** 105-115.

Evain, S., Flexas, J. & Moya, I. 2004. A new instrument for passive remote sensing: 2. Measurement of leaf and canopy reflectance changes at 531 nm and their relationship with photosynthesis and chlorophyll fluorescence. *Remote Sensing of Environment,* 91**,** 175-185.

Farquhar, G. D. & Caemmerer, S. 1982. Modelling of Photosynthetic Response to Environmental Conditions. *In:* Lange, O. L., Nobel, P. S., Osmond, C. B. & Ziegler, H. (eds.) *Physiological Plant Ecology II.* Springer Berlin Heidelberg.

Fenn, K., Malhi, Y., Morecroft, M., Lloyd, C. & Thomas, M. 2010. Comprehensive description of the carbon cycle of an ancient temperate broadleaved woodland. *Biogeosciences Discussions,* 7**,** 3735 - 3763.

Fensholt, R. & Sandholt, I. 2003. Derivation of a shortwave infrared water stress index from MODIS near- and shortwave infrared data in a semiarid environment. *Remote Sensing of Environment,* 87**,** 111-121.

Fensholt, R., Sandholt, I. & Rasmussen, M. S. 2004. Evaluation of MODIS LAI, fAPAR and the relation between fAPAR and NDVI in a semi-arid environment using in situ measurements. *Remote Sensing of Environment,* 91**,** 490-507.

Field, C. B., Randerson, J. T. & Malmström, C. M. 1995. Global net primary production: Combining ecology and remote sensing. *Remote Sensing of Environment,* 51**,** 74-88.

Fisher, R. A. 1992. Statistical Methods for Research Workers. *In:* Kotz, S. & Johnson, N. (eds.) *Breakthroughs in Statistics.* Springer New York.

Flanagan, L. B., Cai, T., Black, T. A., Barr, A. G., Mccaughey, J. H. & Margolis, H. A. 2012. Measuring and modeling ecosystem photosynthesis and the carbon isotope composition of ecosystem-respired CO2 in three boreal coniferous forests. *Agricultural and Forest Meteorology,* 153**,** 165-176.

Flato, G. M. 2011. Earth system models: an overview. *Wiley Interdisciplinary Reviews: Climate Change,* 2**,** 783-800.

Fluxnet. 2013. *FLUXNET - Integrating Worldwide CO2, Water and Energy Flux Measurements* [Online]. Available: http://fluxnet.ornl.gov/introduction [Accessed 19/10/2013.

Foody, G. M. 2006. Sub-Pixel Methods in Remote Sensing. *In:* De Jong, S. M. & Van Der Meer, F. D. (eds.) *Remote Sensing Image Analysis: Including the Spatial Domain.* Netherlands: Springer.

Foody, G. M. 2010. Assessing the accuracy of land cover change with imperfect ground reference data. *Remote Sensing of Environment,* 114**,** 2271-2285.

Foody, G. M., Atkinson, P. M., Gething, P. W., Ravenhill, N. A. & Kelly, C. K. 2005. IDENTIFICATION OF SPECIFIC TREE SPECIES IN ANCIENT SEMI-NATURAL WOODLAND FROM DIGITAL AERIAL SENSOR IMAGERY. *Ecological Applications,* 15**,** 1233-1244.

Foody, G. M., Palubinskas, G., Lucas, R. M., Curran, P. J. & Honzak, M. 1996. Identifying terrestrial carbon sinks: Classification of successional stages in regenerating tropical forest from Landsat TM data. *Remote Sensing of Environment,* 55**,** 205-216.

Forman, R. T. 1995. *Land Mosaics: the ecology of landscape and regions,* Cambridge, Cambrdge University Press.

Forman, R. T. & Godron, M. 1986. *Landscape Ecology,* New York, Wiley and Sons Ltd.

Forzieri, G., Moser, G. & Catani, F. 2012. Assessment of hyperspectral MIVIS sensor capability for heterogeneous landscape classification. *ISPRS Journal of Photogrammetry and Remote Sensing,* 74**,** 175-184.

Franklin, S. E., Hall, R. J., Moskal, L. M., Maudie, A. J. & Lavigne, M. B. 2000. *International Journal of Remote Sensing,* 21**,** 61.

French, J. 2013. Tools for spatial data analysis. 0.5.4 ed.

Friedl, M. A., Davis, F. W., Michaelsen, J. & Moritz, M. A. 1995. Scaling and uncertainty in the relationship between the NDVI and land surface biophysical variables: An analysis using a scene simulation model and data from FIFE. *Remote Sensing of Environment,* 54**,** 233-246.

Frohn, R. C. 1998. *Remote Sensing for Landscape Ecology: New Metrcis Indicators for Monitoring, Modeling and Assessment of Ecosystems,* Florida, CRC Press LLC.

Fung, I. Y., Tucker, C. J. & Prentice, K. C. 1987. Application of Advanced Very High Resolution Radiometer vegetation index to study atmosphere-biosphere exchange of CO2. *Journal of Geophysical Research: Atmospheres,* 92**,** 2999-3015.

Gamon, J. A., Field, C. B., Bilger, W., Björkman, O., Fredeen, A. L. & Peñuelas, J. 1990. Remote sensing of the xanthophyll cycle and chlorophyll fluorescence in sunflower leaves and canopies. *Oecologia,* 85**,** 1-7.

Gamon, J. A., Field, C. B., Goulden, M. L., Griffin, K. L., Hartley, A. E., Joel, G., Peñuelas, J. & Valentini, R. 1995. Relationships Between NDVI, Canopy Structure, and Photosynthesis in Three Californian Vegetation Types. *Ecological Applications,* 5**,** 28 - 41.

Gamon, J. A., Penuelas, J. & Field, C. B. 1992. A Narrow-Waveband Spectral Index that Tracks Diurnal Changes in Phtotosynthetic Efficiency. *Remote Sensing of Environment,* 44**,** 35 - 44.

Gamon, J. A., Serrano, L. & Surfus, J. S. 1997. The Photochemical Reflectance Index: An Optical Indicator of Photosynthetic Radiation Use Efficiency across Species, Functional Types, and Nutrient Levels. *Oecologia,* 112**,** 492-501.

Gamon, J. A. & Surfus, J. S. 1999. Assessing leaf pigment content and activity with a reflectometer. *New Phytologist,* 143**,** 105-117.

Gao, B.-C., Montes, M. J., Davis, C. O. & Goetz, A. F. H. 2009. Atmospheric Correction Algorithms for Hyperspectral Remote Sensing Data of Land And Ocean. *Remote Sensing of Environment,* 113, Supplement 1**,** S17-S24.

García, M., Riaño, D., Chuvieco, E. & Danson, F. M. 2010. Estimating biomass carbon stocks for a Mediterranean forest in central Spain using LiDAR height and intensity data. *Remote Sensing of Environment,* 114**,** 816-830.

Garrigues, S., Allard, D., Baret, F. & Weiss, M. 2006. Quantifying spatial heterogeneity at the landscape scale using variogram models. *Remote Sensing of Environment,* 103**,** 81-96.

Geerling, G. W., Labrador-Garcia, M., Clevers, J. G. P. W., Ragas, A. M. J. & Smits, A. J. M. 2007. Classification of floodplain vegetation by data fusion of spectral (CASI) and LiDAR data. *International Journal of Remote Sensing,* 28**,** 4263-4284.

Gianelle, D., Vescovo, L., Marcolla, B., Manca, G. & Cescatti, A. 2008. Ecosystem carbon fluxes and canopy spectral reflectance of a mountain meadow. *International Journal of Remote Sensing,* 30**,** 435-449.

Gitay, H., Suárez, A., Watson, R. T. & Dokken, D. J. 2002. Climate change and Biodiversity. *In:* Watson, R. T. (ed.). Intercovermental Panel on Climate Change (IPCC).

Gitelson, A. & Merzlyak, M. N. 1994. Spectral Reflectance Changes Associated with Autumn Senescence of Aesculus hippocastanum L. and Acer platanoides L. Leaves. Spectral Features and Relation to Chlorophyll Estimation. *Journal of Plant Physiology,* 143**,** 286-292.

Glenn, E. P., Huete, A. R., Nagller, P. L. & Nelson, S. G. 2008. Relationship Between Remotely-sened Vegetation Indices, Canopy Attributes and Plant Physiological Processes: What Vegetation Indices Can and Cannot Tell Us About the Landscape *Sensors,* 8**,** 2136 - 2160.

Goerner, A., Reichstein, M. & Rambal, S. 2009. Tracking seasonal drought effects on ecosystem light use efficiency with satellite-based PRI in a Mediterranean forest. *Remote Sensing of Environment,* 113**,** 1101-1111.

Goerner, A., Reichstein, M., Tomelleri, E., Hanna, N., Rambal, S., Papale, D., Dragoni, D. & Schmullius, C. 2010. Remote Sensing of Ecosystem light use efficiency with MODIS-based PRI - the DOs and DON'Ts. *Biogeosciences Discussion,* 7**,** 6935 - 6969.

Goetz, S. L. 1996. *Modeling Carbon Fluxes, Net PrimaryProduction and Light Utlization in Boreal Forst Stands.* Doctor of Philosophy, Unversity of Maryland.

Gonzalez, P., Asner, G. P., Battles, J. J., Lefsky, M. A., Waring, K. M. & Palace, M. 2010. Forest carbon densities and uncertainties from Lidar, QuickBird, and field measurements in California. *Remote Sensing of Environment,* 114**,** 1561-1575.

Goovaerts, P. 1997. *Geostatistics for Natural Resources Evaluation,* Oxford, Oxford University Press.

Gower, S. T., Kucharik, C. J. & Norman, J. M. 1999. Direct and indirect estimate of leaf area index fapar and net primary production of terrestrial ecosystems. *Special Issue of EOS Remote Sensing of the Environment,* 70**,** 29-51.

Grace, J., Nichol, C., Disney, M., Lewis, P., Quaife, T. & Bowyer, P. 2007. Can we measure terrestrial photosynthesis from space directly, using spectral reflectance and fluorescence? *Global Change Biology,* 13**,** 1484-1497.

Green, A. A., Berman, M., Switzer, P. & Craig, M. D. 1988. *IEEE Transactions on Geoscience and Remote Sensing,* 26**,** 65.

Gu, Y. & Wylie, B. 2015. Downscaling 250-m MODIS Growing Season NDVI Based on Multiple-Date Landsat Images and Data Mining Approaches. *Remote Sensing,* 7**,** 3489.

Guo, J. & Trotter, C. M. 2004. Estimating photosynthetic light-use efficiency using the photochemical reflectance index: variations among species. *Functional Plant Biology,* 31**,** 255-265.

Gupta, R. K., Prasad, T. S. & Vijayan, D. 2000. Relationship between LAI and NDVI for IRS LISS and Landsat TM bands. *Advances in Space Research,* 26**,** 1047-1050.

Gupta, R. K. & Vijayan, D. 2001. *Advances in Space Research,* 28**,** 201.

Hall, D. O., Scurlock, J. M. O., Bolhar-Nordenkampe, H. R., Leegood, R. C. & Long, S. P. 1993. *Photosynthesis and Production in a Changing Environmet* London, Chapman & Hall.

Hall, F. G., Hilker, T., Coops, N. C., Lyapustin, A., Huemmrich, K. F., Middleton, E., Margolis, H., Drolet, G. & Black, T. A. 2008. Multi-angle remote sensing of forest light use efficiency by observing PRI variation with canopy shadow fraction. *Remote Sensing of Environment,* 112**,** 3201-3211.

Hall, F. G., Strebel, D. E., Nickeson, J. E. & Goetz, S. J. 1991. Radiometric Rectification: Toward a Common Radiometric Response Among Multidate, Multisensor Images. *Remote Sensing of Environment,* 35**,** 11-27.

Hardiman, B. S., Gough, C. M., Halperin, A., Hofmeister, K. L., Nave, L. E., Bohrer, G. & Curtis, P. S. 2013. Maintaining high rates of carbon storage in old forests: A mechanism linking canopy structure to forest function. *Forest Ecology and Management,* 298**,** 111-119.

Harris, A. & Dash, J. 2010. The potential of the MERIS Terrestrial Chlorophyll Index for carbon flux estimation. *Remote Sensing of Environment,* 144**,** 1856-1862.

Hassol, S. J. & Katzenberger, J. 1997. Scaling From Site-Specific Observations to Global ModelGrids. *A report on the Aspen Global Change Workshop, Elements of Change Series.* Colorado: Aspen Global Change Institute.

Hayes, D. J. & Sader, S. A. 2001. Comparison of Change-Detection TEchniques for Monitoring Tropical Forest Clearing and Vegetation Regrowth in a Time Series. *Photogrametric Engineering & Remote Sensing,* 67**,** 1067-1075.

Heinsch, F. A., Zhao, M. & Running, S. W. 2006. Evaluation of Remote Sensing Based Terrestrial Productivity from MODIS using Regional Tower Eddy Flux Network Observations. *IEEE Transaction on Geoscience and Remote Sensing,* 44**,** 1908 - 1927.

Helmer, E. H. & Ruefenacht, B. 2007. A Comparison of Radiometric Normalization Methods when Filling Cloud Gaps in Landsat Imagery. *Can. J. Remote Sensing,* 33**,** 325 - 340.

Hengle, T. 2009. *A Practical Guide to Geostatistics Mapping,* Luxembourg, Office for Official Publications of the European Communities.

Heuvelink, G. B. M., Pebesma, E. & Stein, A. 2013. Spatial statistics for mapping the environment. *International Journal of Applied Earth Observation and Geoinformation,* 22**,** 1-2.

Hilker, T., Coops, N. C., Wulder, M. A., Black, T. A. & Guy, R. D. 2008. The use of remote sensing in light use efficiency based models of gross primary production: A review of current status and future requirements. *Science of The Total Environment,* 404**,** 411-423.

Hill, M. J., Held, A. A., Leuning, R., Coops, N. C., Hughes, D. & Cleugh, H. A. 2006. MODIS spectral signals at a flux tower site: Relationships with high-resolution data, and CO2 flux and light use efficiency measurements. *Remote Sensing of Environment,* 103**,** 351-368.

Hill, R. A. & Broughton, R. K. 2009. Mapping the understorey of deciduous woodland from leaf-on and leaf-off airborne LiDAR data: A case study in lowland Britain. *ISPRS Journal of Photogrammetry and Remote Sensing,* 64**,** 223-233.

Hill, R. A. & Thomson, A. G. 2005. Mapping woodland species composition and structure using airborne spectral and LiDAR data. *International Journal of Remote Sensing,* 26**,** 3763-3779.

Hirano, A., Madden, M. & Welch, R. 2003. *Wetlands,* 23**,** 436.

Hirose, T. 2005. Development of the Monsi-Saeki Theory on Canopy Structure and Function. *Annals of Botany,* 95**,** 483-494.

Hofer, C. & Papritz, A. 2011. constrainedKriging: An R-package for customary, constrained and covariance-matching constrained point or block kriging. *Computers & Geosciences,* 37**,** 1562-1569.

Hoffer, R. H. 1978. Biological and Physiological Considerations in Applying Computer-Aided Analysis Techniqes to Remote Sensing Data. *In:* Swain, P., H & Davis, S., M. (eds.) *Remote Sensing: The Quantitative Approach.* McGraw-Hill.

Hoffman, F. O. & Gardner, R. H. 1983. Evaluation of Uncertainty in Environmental Radiological Assessment Models. *In:* Till, J. E. & Meyer, H. R. (eds.) *Radiological Assessment: a Textbook on Environmental Dose Assessment.* Washington, DC: Nuclear RegulatorybCommission.

Hommeltenberg, J., Mauder, M., Drösler, M., Heidbach, K., Werle, P. & Schmid, H. P. 2014. Ecosystem scale methane fluxes in a natural temperate bog-pine forest in southern Germany. *Agricultural and Forest Meteorology,* 198–199**,** 273-284.

Horst, T. W. & Weil, J. C. 1992. Footprint estimation for scalar flux measurements in the atmospheric boundary layer *Boundary-Layer Meteorology,* 59**,** 279 - 296.

Houborg, R., Fisher, J. B. & Skidmore, A. K. 2015. Advances in remote sensing of vegetation function and traits. *International Journal of Applied Earth Observation and Geoinformation,* 43**,** 1-6.

Houlding, S. W. 2000. *Practical Geostatistics: Modeling and Spatial Analysis,* Germany, Springer.

Huber, P. J. 2004. *Robust Statistics,* New Jersey, USA, John Wiley & Sons.

Hudak, A. T., Lefsky, M. A., Cohen, W. B. & Berterretche, M. 2002. Integration of lidar and Landsat ETM+ data for estimating and mapping forest canopy height. *Remote Sensing of Environment,* 82**,** 397-416.

Huemmrich, K. F., Gamon, J. A., Tweedie, C. E., Oberbauer, S. F., Kinoshita, G., Houston, S., Kuchy, A., Hollister, R. D., Kwon, H., Mano, M., Harazono, Y., Webber, P. J. & Oechel, W. C. 2010. Remote sensing of tundra gross ecosystem productivity and light use efficiency under varying temperature and moisture conditions. *Remote Sensing of Environment,* 114**,** 481-489.

Huemmrich, K. F. & Goward, S. N. 1997. Vegetation canopy PAR absorptance and NDVI: An assessment for ten tree species with the SAIL model. *Remote Sensing of Environment,* 61**,** 254-269.

Huete, A., Didan, K., Miura, T., Rodriguez, E. P., Gao, X. & Ferreira, L. G. 2002. Overview of the radiometric and biophysical performance of the MODIS vegetation indices. *Remote Sensing of Environment,* 83**,** 195-213.

Huete, A. R. 1988. A soil-adjusted vegetation index (SAVI). *Remote Sensing of Environment,* 25**,** 295-309.

Huete, A. R., Liu, H. Q., Batchily, K., Vanleeuwen , W. & 1997. A comparison of vegetation indices global set of TM images for EOS-MODIS. *Remote Sensing of Environment,* 59**,** 440-451.

Huntzinger, D. N., Post, W. M., Wei, Y., Michalak, A. M., West, T. O., Jacobson, A. R., Baker, I. T., Chen, J. M., Davis, K. J., Hayes, D. J., Hoffman, F. M., Jain, A. K., Liu, J., S. , Mcguire, A. D., Neilson, R. P., Chris Potter, Poulter, B., David Pricep, Raczka, B. M., Tian, H. Q., Thornton, P., Tomelleri, E., Viovy, N., Xiao, J., Yuan, W., Zeng, N., Zhao, M. & Cook, D. R. 2012. North American Carbon Program (NACP) regional interim synthesis: Terrestrial
biospheric model intercomparison. *Ecological Modelling,* 232**,** 144-157.

Hutchings, M. J., John, E. A. & Stewart, A. J. A. 2000. *The Ecological Consequences of Environmental Heterogeneity,* Cambridge Cambridge Uineversity Press.

Ichii, K., Hashimoto, H., Nemani, R. & White, M. 2005. Modeling the interannual variability and trends in gross and net primary productivity of tropical forests from 1982 to 1999. *Global and Planetary Change,* 48**,** 274-286.

Ipcc. 2001a. *Summary for policy makers: The third assessment report of working group I of the Intergovermental Panel on Climate Change* [Online]. Available: http://WWW.ipcc.ch.

Ipcc 2014. Climate Change 2014: Systhesis Report - Summary for Policymakers

Ipcc, F. 2001b. Climate change 2001: The scientific basis. *In:* Houghton, J. T., Ding, Y., Griggs, D. J., Noguer, M., Van Der Linden, P. J., Dai, X., Maskell, K. & Johnson, C. A. (eds.). Intergovernmental Panel on Climate Change (IPCC).

Isaaks, E. H. & Srivastava, R. M. 1989. *An introduction to Applied Geostatistics*, Oxford University Press.

Jackson, R. D. & Huete, A. R. 1991. Interpreting vegetation indices. *Preventive Veterinary Medician,* 11**,** 185 - 200.

Jackson, T. J., Chen, D., Cosh, M., Li, F., Anderson, M., Walthall, C., Doriaswamy, P. & Hunt, E. R. 2004. Vegetation water content mapping using Landsat data derived normalized difference water index for corn and soybeans. *Remote Sensing of Environment,* 92**,** 475-482.

Jacquemound, S. & Baret, F. 1990. *Remote Sensing of Environment,* 34**,** 75.

Jensen, J. L. R., Humes, K. S., Vierling, L. A. & Hudak, A. T. 2008. Discrete return lidar-based prediction of leaf area index in two conifer forests. *Remote Sensing of Environment,* 112**,** 3947-3957.

Jensen, J. R. 2005. *Introductory Digital Image Processing, A Remote Sensing Perspective,* USA, Pearson Prentice Hall.

Jia, X. & Richards, J. A. 1999a. *IEEE Transactions on Geoscience and Remote Sensing,* 37**,** 538.

Jia, X. & Richards, J. A. 1999b. Segmented Principal Components Transformation for Efficient Hyperspectral Remote-Sensing Image Display and Classification. *IEEE Transaction on Geoscience and Remote Sensing,* 37**,** 538-542.

Johnson, I. R. 1996. Modelling canopy photosynthesis in response to environmental conditions. *Advances in Space Research,* 18**,** 163-166.

Jones, T. G., Coops, N. C. & Sharma, T. 2010. Assessing the utility of airborne hyperspectral and LiDAR data for species distribution mapping in the coastal Pacific Northwest, Canada. *Remote Sensing of Environment,* 114**,** 2841-2852.

Jose, S. 2009. Agroforestry for ecosystem services and environmental benefits: an overview. *Agroforestry Systems,* 76**,** 1-10.

Journel, A. G. & Huijbregts, C. J. 1993. *Mining Geostatistics,* London, Academic Press Limited.

K.J., N., Davis, K. J. & Keller, K. Upscaling carbon fluxes and uncertainty across the northern forest ecoregion using Bayesian fusion of eddy covariance and remote sensing observations ForestSAT Meeting, September 11-14, 2012 2012 Oregon State University, Corvallis, OR, USA.

Katoh, M. 2004. *Journal of Forest Research,* 9**,** 7.

Kaufman, Y. J. & Tanre, D. 1992. Atmospherically resistant vegetation index (ARVI) for EOS-MODIS. *Geoscience and Remote Sensing, IEEE Transactions on,* 30**,** 261-270.

Kauth, R. J. & Thomas, G. S. The tasseled Cap - a graphic description of the spectral-temporal development of agricultural crops as seen by Landsat. Proceedings of the 3rd Symposium on Machine Processing of Remotely Sensed Data, June 29 - July 1, 1976 1976 Lafayette, Indiana. LARS, Purdue University, 41-49.

Kennedy, R. E., Cohen, W. B. & Takao, G. 1997. Empirical methods to compensate for a view-angle-dependent brightness gradient in AVIRIS imagery. *Remote Sensing of Environment,* 62**,** 277-291.

Kerry, R., Giménez, D., Oudemans, P. & Goovaerts, P. 2010. Investigating the Potential of Area-to-Area and Area-to-Point Kriging for Defining Management Zones for Precision Farming of Cranberries. *In:* Atkinson, P. M. & Lloyd, C. D. (eds.) *geoENV VII – Geostatistics for Environmental Applications.* Springer Netherlands.

Khavarian N., H. 2012. *Inter-comparision of multiple angle remotely sensed data across different spatiasl resolutions and sensors for determination of albedo.* Docor of Philosophy, University of Southampton.

Kia, S. H. & Milton, E. J. What can time series of remotely sensed measurements from a mixed broadleaf forest tell us about net ecosystem exchange? *In:* Hill, R. A. & Baines, N., eds. In, Annual Conference of the Remote Sensing and Photogrammetry Society. Earth Observation in a Changing World (RSPSoc 2011), 13-14 Sep 2011 2011 Bournemouth, GB. RSPSoc.

Kia, S. H. & Milton, E. J. 2015. Hyper-temporal remote sensing for scaling between spectral indices and flux tower measurements. *Applied Ecology and Environmental Research,* 13**,** 464-487.

Kim, J., Guo, Q., Baldocchi, D. D., Leclerc, M. Y., Xu., L. & Schmind, H. P. 2006. Upscaling Fluxes from Tower to Landscape: Overlaying Flux Footprints on High-Resolution (IKONOS) Images of Vegetation Cover. *Agriculture and Forest Meteorology,* 136**,** 132 - 146.

Kljun, N., Kormann, R., Rotach, M. W. & Meixer, F. X. 2003. Comparison of the Langrangian Footprint. *Boundary-Layer Meteorology,* 106**,** 349-355.

Korhonen, L., Korpela, I., Heiskanen, J. & Maltamo, M. 2011. Airborne discrete-return LIDAR data in the estimation of vertical canopy cover, angular canopy closure and leaf area index. *Remote Sensing of Environment,* 115**,** 1065-1080.

Kraus, K. & Pfeifer, N. 1998. Determination of terrain models in wooded areas with airborne laser scanner data. *ISPRS Journal of Photogrammetry and Remote Sensing,* 53**,** 193-203.

Kruse, F. A. Comparison of ATREM, ACORN, and FLAASH atmospheric correction using low-altitude AVIRIS data of Boulder. 13th JPL Airborne Geoscience Workshop 2004 Pasadena, CA. Jet Propulsion Lab.

Kwak, D.-A., Lee, W.-K. & Cho, H.-K. 2007. Estimation of LAI Using LiDAR Remote Sesning in Forest. *ISPRS Journal of Photogrammetry and Remote Sensing*.

Laba, M., Tsai, F., Ogurcak, D., Smith, S. & Richmond, M. E. 2005. *Photogrammetric Engineering and Remote Sensing,* 71**,** 603.

Lal, R. 2005. Forest soils and carbon sequestration. *Forest Ecology and Management,* 220**,** 242-258.

Lam, N. S.-N. & Quattrochi, D. A. 1992. On the Issues of Scale, Resolution, and Fractal Analysis in the Mapping Sciences*. *The Professional Geographer,* 44**,** 88-98.

Lambers, H., Chapin Iii, F. S. & Pons, T. L. 2008. *Plant Physiological Ecology,* New York, Springer.

Le Maire, G., Marsden, C., Nouvellon, Y., Grinand, C., Hakamada, R., Stape, J.-L. & Laclau, J.-P. 2011. MODIS NDVI time-series allow the monitoring of Eucalyptus plantation biomass. *Remote Sensing of Environment,* 115**,** 2613-2625.

Lecain, D. R., Morgan, J. A., Schuman, G. E., Reeder, J. D. & Hart, R. H. 2002. Carbon exchange and species composition of grazed pastures and exclosures in the shortgrass steppe of Colorado. *Agriculture, Ecosystems & Environment,* 93**,** 421-435.

Lee, C. & Landgrebe, D. A. 1993. *IEEE Transactions on Geoscience and Remote Sensing,* 31**,** 792.

Lee, K.-S., Cohen, W. B., Kennedy, R. E., Maiersperger, T. K. & Gower, S. T. 2004. Hyperspectral versus multispectral data for estimating leaf area index in four different biomes. *Remote Sensing of Environment,* 91**,** 508-520.

Lefsky, M. A., Cohen, W. B., Acker, S. A., Parker, G. G., Spies, T. A. & Harding, D. 1999a. Lidar Remote Sensing of the Canopy Structure and Biophysical Properties of Douglas-Fir Western Hemlock Forests. *Remote Sensing of Environment,* 70**,** 339-361.

Lefsky, M. A., Cohen, W. B., Harding, D. J., Parker, G. G., Acker, S. A. & Gower, S. T. 2002. Lidar remote sensing of above-ground biomassin three biomes. *Global Ecology and Biogeography,* 11**,** 2011.

Lefsky, M. A., Harding, D., Cohen, W. B., Parker, G. & Shugart, H. H. 1999b. Surface Lidar Remote Sensing of Basal Area and Biomass in Deciduous Forests of Eastern Maryland, USA. *Remote Sensing of Environment,* 67**,** 83-98.

Lefsky, M. A., Turner, D. P., Guzy, M. & Cohen, W. B. 2005. Combining lidar estimates of aboveground biomass and Landsat estimates of stand age for spatially extensive validation of modeled forest productivity. *Remote Sensing of Environment,* 95**,** 549-558.

Leuangthong, O., Khan, K. D. & Deutsch, V. 2008. *Solved Problems in Geostatistics* John Wiley and Sons.

Leys, C., Ley, C., Klein, O., Bernard, P. & Licata, L. 2013. Detecting outliers: Do not use standard deviation around the mean, use absolute deviation around the median. *Journal of Experimental Social Psychology,* 49**,** 764-766.

Liang, S. 2004. *Quantitative Remote Sensing of Land Surfaces,* New Jersey, John Wiley & Sons.

Lillesand, T. M., Kiefer, R. W. & Chipman, J. 2008. *Remote Sensing and Images Interpretation*, John Wiley & Sons, Inc.

Lin, J. C., Pejam, M. R., Chan, E., Wofsy, S. C., Gottlieb, E. W., Margolis, H. A. & Mccaughey, J. H. 2011. Attributing uncertainties in simulated biospheric carbon fluxes to different error sources. *Global Biogeochemical Cycles,* 25**,** n/a-n/a.

Liu, F. Y. & Chen, M. A. 2002. *Conservation Research Report No. 112*.

Liu, Z., Wang, L. & Wang, S. 2014. Comparison of Different GPP Models in China Using MODIS Image and ChinaFLUX Data. *Remote Sensing,* 6**,** 10215.

Lloyd, J. & Taylor, J. A. 1994. On the temperature dependence of soil respiration. *Functional Ecology,* 8**,** 315-323.

M. F. Ramli, D. N. P. 2006. Best band combination for landslide studies in temperate environments. *International Journal of Remote Sensing,* 27**,** 1219-1231.

Macarthur, R. H. & Macarthur, J. W. 1961. On Bird Species Diversity. *Ecology,* 42**,** 594-598.

Malhi, Y., Wood, D., Baker, T. R., Wright, J., Phillips, O. L., Cochrane, T., Meir, P., Chave, J., Almeida, S., Arroyo, L., Higuchi, N., Killeen, T. J., Laurance, S. G., Laurance, W. F., Lewis, S. L., Monteagudo, A., Neill, D. A., Vargas, P. N., Pitman, N. C. A., Quesada, C. A., Salomão, R., Silva, J. N. M., Lezama, A. T., Terborgh, J., Martínez, R. V. & Vinceti, B. 2006. The regional variation of aboveground live biomass in old-growth Amazonian forests. *Global Change Biology,* 12**,** 1107-1138.

Marceau, D. J. & Hay, G. J. 1999. Remote Sensing Contributions to the Scale Issue. *Canadian Journal of Remote Sensing,* 25**,** 357-366.

Martin, M. E., Newman, S. D., Aber, J. D. & Congalton, R. G. 1998. Determining Forest Species Composition Using High Spectral Resolution Remote Sensing Data. *Remote Sensing of Environment,* 65**,** 249-254.

Masek, J. G., Hayes, D. J., Joseph, H. M., P., H. S. & Turner, D. P. 2015. The role of remote sensing in process-scaling studies of managed forest ecosystems. *Forest Ecology and Management,* 355**,** 109-123.

Masuoka, E., Roy, D., Wolfe, R., Morisette, J., Sinno, S., Teague, M., Saleous, N., Devadiga, S., Justice, C. O. & Nickeson, J. 2011. MODIS Land Data Products: Generation, Quality Assurance and Validation. *In:* Ramachandran, B., Justice, C. O. & Abrams, M. J. (eds.) *Land Remote Sensing and Global Environmental Change: NASA's Earth Observation System and the Science of ASTER and MODIS.* New York, USA: Springer.

Mather, P. M. 2004. *Computer Processing of Remotely-Sensed Images,* West Sussex, England, John Wiley & Sins, Ltd.

Matheron, G. 1971. *The Theory of Regionalized Variables and Its Applications,* Paris, EÌcole National Superieure des Mines.

Matross, D. M., Andrews, A., Pathmathevan, M., Gerbig, C., Lin, J. C., Wofsy, S. C., Daube, B. C., Gottlieb, E. W., Chow, V. Y., Lee, J. T., Zhao, C., Bakwin, P. S., Munger, J. W. & Hollinger, D. Y. 2006. Estimating regional carbon exchange in New England and Quebec by combining atmospheric, ground-based and satellite data. *Tellus B,* 58**,** 344-358.

Matthes, J. H., Sturtevant, C., Verfaillie, J., Knox, S. & Baldocchi, D. 2014. Parsing the variability in CH4 flux at a spatially heterogeneous wetland: Integrating multiple eddy covariance towers with high-resolution flux footprint analysis. *Journal of Geophysical Research: Biogeosciences,* 119**,** 1322-1339.

Mccormick, C. M. 1999. *Photogrammetric Engineering and Remote Sensing,* 65**,** 179.

Melaas, E. K., Richardson, A. D., Friedl, M. A., Dragoni, D., Gough, C. M., Herbst, M., Montagnani, L. & Moors, E. 2013. Using FLUXNET Data to Improve Models of Springtime Vegetation Activity Onset in Forest Ecosystems. *Agricultural and Forest Meteorology,* 171–172**,** 46-56.

Metzger, S., Junkermann, W., Mauder, M., Butterbach-Bahl, K., Trancón Y Widemann, B., Neidl, F., Schäfer, K., Wieneke, S., Zheng, X. H., Schmid, H. P. & Foken, T. 2013. Spatially explicit regionalization of airborne flux measurements using environmental response functions. *Biogeosciences,* 10**,** 2193-2217.

Millennium Ecosystem Assessment 2005. Ecosystems and Human Well-being: Biodiversity Synthesis

Washington, DC: World Resources Institute.

Milton, E. J., Baret, F., Rossello, P., Anderson, E. & Rockall, E. 2011. A multistage database of field measurements and synoptic remotely sensed data to support model validation and testing in Earth observation. *Computers & Geosciences,* 37**,** 1511-1514.

Moffat, A. M., Papale, D., Reichstein, M., Hollinger, D. Y., Richardson, A. D., Barr, A. G., Beckstein, C., Braswell, B. H., Churkina, G., Desai, A. R., Falge, E., Gove, J. H., Heimann, M., Hui, D., Jarvis, A. J., Kattge, J., Noormets, A. & Stauch, V. J. 2007. Comprehensive comparison of gap-filling techniques for eddy covariance net carbon fluxes. *Agricultural and Forest Meteorology,* 147**,** 209-232.

Monteith, J. L. 1972a. SOLAR-RADIATION AND PRODUCTIVITY IN TROPICAL ECOSYSTEMS. *Journal of Applied Ecology,* 9**,** 747-766.

Monteith, J. L. 1972b. Solar Radiation and Productivity in Tropical Ecosystems. *The Journal of Applied Ecology,* 9**,** 747-766.

Monteith, J. L. & Moss, C. J. 1977. Climate and the Efficiency of Crop Production in Britain [and Discussion]. *Philosophical Transactions of the Royal Society of London. Series B, Biological Sciences,* 281**,** 277-294.

Myneni, R. B., Hoffman, S. & Knyazikhin, Y. 2002. Global products of vegetation leaf area and fraction absorbed PAR from year one of MODIS data. *Remote Sensing of Environment,* 83**,** 214-231.

Myneni, R. B. & Williams, D. L. 1994. On the relationship between FAPAR and NDVI. *Remote Sensing of Environment,* 49**,** 200-211.

Næsset, E. & Bjerknes, K.-O. 2001. Estimating tree heights and number of stems in young forest stands using airborne laser scanner data. *Remote Sensing of Environment,* 78**,** 328-340.

Næsset, E. & Gobakken, T. 2008. Estimation of above- and below-ground biomass across regions of the boreal forest zone using airborne laser. *Remote Sensing of Environment,* 112**,** 3079-3090.

Næsset, E., Gobakken, T., Solberg, S., Gregoire, T. G., Nelson, R., Ståhl, G. & Weydahl, D. 2011. Model-assisted regional forest biomass estimation using LiDAR and InSAR as auxiliary data: A case study from a boreal forest area. *Remote Sensing of Environment,* 115**,** 3599-3614.

Nakaji, T., Ide, R., Oguma, H., Saigusa, N. & Fujinuma, Y. 2007. Utility of Spectral Vegetation Index for Estimation of Gross CO2 Flux under Varied Sky Conditions. *Remote Sensing of Environment,* 109**,** 274-284.

Nasa. 2012. *NASA Terrestrial Ecology Program* [Online]. [Accessed 05 January 2012].

Network, E. C. 2010. ECN Sites: Wytham. *In:* Oxford, N. E. R. C. U. O. (ed.) *ECN Sites.*

Nichol, C. J., Huemmrich, K. F., Balck, T. A., Jarvis, P. G., Walthall, C. L., Grace, J. & Hall, F. G. 2000. Remote sensing of photosynthetic-light-use effciency of boreal forest. *Agricultural and Forest Meteorology,* 101**,** 131 - 142.

Nielsen, A. A. 2007. The Regularized Iteratively Reweighted MAD Method for Change Detection in Multi and Hyperspectral Data. *IEEE Transaction on Geoscience and Remote Sensing,* 16**,** 463 - 478.

Nielsen, A. A. & Canty, M. J. 2011. A Method for Unsupervised Change Detection and Radiometric Normalization in Multispectral Data. *34th International Symposium on Remote Sensing of Environment.* Sydney, Australia.

Nielsen, A. A., Conradsen, K. & Simpson, J. J. 1998. Multivariate Alteration detection (MAD) and MAF Post-processing in Multispectral, Bitemporal Image Data: New Approaches to Change Detection Studies.*Remote Sensing of Environment,* 64**,** 1 - 19.

Nijland, W., Addink, E. A., De Jong, S. M. & Van Der Meer, F. D. 2009. Optimizing spatial image support for quantitative mapping of natural vegetation. *Remote Sensing of Environment,* 113**,** 771-780.

Nilsen, E. B., Herfindal, I. & Linnell, J. D. C. 2005. Can intra-specific variation in carnivore home-range size be explained using remote-sensing estimates of environmental productivity? *Ecoscience* 12**,** 68 - 75

Nilsen, E. B., Pedersen, S. & Linnell, J. D. C. 2008. Can minimum convex polygon home ranges be used to draw biologically meaningful conclusions? *Ecological Research,* 23**,** 635 - 639.

O'shea, S. J., Allen, G., Fleming, Z. L., Bauguitte, S. J. B., Percival, C. J., Gallagher, M. W., Lee, J., Helfter, C. & Nemitz, E. 2014. Area fluxes of carbon dioxide, methane, and carbon monoxide derived from airborne measurements around Greater London: A case study during summer 2012. *Journal of Geophysical Research: Atmospheres,* 119**,** 4940-4952.

Ogunbadewa, E. Y. 2012. Investigating availability of cloud free images with cloud masks in relation to fatellite fevisite frequency in the Northwest of England. *Contributions to Geophysics and Geodesy,* 42**,** 63-100.

Ogutu, B. O., Dash, J. & Dawson, T. P. 2014. Evaluation of the influence of two operational fraction of absorbed photosynthetically active radiation (FAPAR) products on terrestrial ecosystem productivity modelling. *International Journal of Remote Sensing,* 35**,** 321-340.

Oijen, M. V., Cameron, D., Levy, P. E. & Preston, R. 2017. Correcting errors from spatial upscaling of nonlinear greenhouse gas

flux models. *Environmental Modelling & Software,* 94**,** 157-165.

Olofsson, P., Foody, G. M., Stehman, S. V. & Woodcock, C. E. 2013. Making better use of accuracy data in land change studies: Estimating accuracy and area and quantifying uncertainty using stratified estimation. *Remote Sensing of Environment,* 129**,** 122-131.

Park, N.-W. 2013. Spatial Downscaling of TRMM Precipitation Using Geostatistics and Fine Scale Environmental Variables. *Advances in Meteorology,* 2013**,** 9.

Paruelo, J. M. & Lauenroth, W. K. 1998. Interannual Variability of NDVI and its Relationship to Climate for North American Shrublands and Grasslands. *Journal of Biogeography,* 25**,** 721-733.

Pasquill, F. 1961. The estimation of the dispersion of windborne material. *Meteorological Magazine,* 90**,** 33 - 49.

Patenaude, G., Hill, R. A., Milne, R., Gaveau, D. L. A., Briggs, B. B. J. & Dawson, T. P. 2004. Quantifying forest above ground carbon content using LiDAR remote sensing. *Remote Sensing of Environment,* 93**,** 368-380.

Pearlman, J. S., Barry, P. S., Segal, C. C., Shepanski, J., Beiso, D. & Carman, S. L. 2003. *IEEE Transactions on Geoscience and Remote Sensing,* 41**,** 1160.

Peerbhay, K. Y., Mutanga, O. & Ismail, R. 2013. Commercial tree species discrimination using airborne AISA Eagle hyperspectral imagery and partial least squares discriminant analysis (PLS-DA) in KwaZulu–Natal, South Africa. *ISPRS Journal of Photogrammetry and Remote Sensing,* 79**,** 19-28.

Peltola, O., Hensen, A., Belelli Marchesini, L., Helfter, C., Bosveld, F. C., Van Den Bulk, W. C. M., Haapanala, S., Van Huissteden, J., Laurila, T., Lindroth, A., Nemitz, E., Röckmann, T., Vermeulen, A. T. & Mammarella, I. 2015. Studying the spatial variability of methane flux with five eddy covariance towers of varying height. *Agricultural and Forest Meteorology,* 214–215**,** 456-472.

Penuelas, J., Filella, I. & Gamon, J. A. 1995. Assessment of Photosynthetic Radiation-Use Efficiency with Spectral Reflectance. *New Phytologist,* 131**,** 291-296.

Pettorelli, N., Vik, J. O., Mysterud, A., Gaillard, J.-M., Tucker, C. J. & Stenseth, N. C. 2005. Using the satellite-derived NDVI to assess ecological responses to environmental change. *Trends in Ecology & Evolution,* 20**,** 503-510.

Plant, R. E. 2012. *Spatial Data Analysis in Ecology and Agriculture using R,* United States of America, CRC Press, Taylor & Francis Group

Potter, C. S., Randerson, J. T., Field, C. B., Matson, P. A., Vitousek, P. M., Mooney, H. A. & Klooster, S. A. 1993. Terrestrial ecosystem production: A process model based on global satellite and surface data. *Global Biogeochemical Cycles,* 7**,** 811-841.

Poveda, G. & Salazar, L. F. 2004. Annual and interannual (ENSO) variability of spatial scaling properties of a vegetation index (NDVI) in Amazonia. *Remote Sensing of Environment,* 93**,** 391-401.

Prentice, C., Heimann, M. & Sitch, S. 2000. The Carbon Balance of the Terrestrial Biosphere: Ecosystem Models and Atmospheric Observations. *Ecological Applications,* 10**,** 1553-1573.

Price, J. C. 1997. *IEEE Transactions on Geoscience and Remote Sensing,* 35**,** 1277.

Price, K., Storn, R. M. & Lampinen, J. A. 2006. *Differential Evolution: Apractical Approach to Global Optimization*, Springer.

Qi, J., Chehbouni, A., Huete, A. R., Kerr, Y. H. & Sorooshian, S. 1994. A modified soil adjusted vegetation index. *Remote Sensing of Environment,* 48**,** 119-126.

R Core Team 2013. R: A Language and Environment for Statistical Computing. 3.0.2 ed. Vienna, Austria: R Foundation for Statistical Computing.

Raffy, M. 1992. Change of scale in models of remote sensing: A general method for spatialization of models. *Remote Sensing of Environment,* 40**,** 101-112.

Rahman, A. F., Gamon, J. A., Fuentes, D. A., Roberts, D. A. & Prentiss, D. 2001. Modeling spatially distributed ecosystem flux of boreal forest using hyperspectral indices from AVIRIS imagery. *Journal of Geophysical Research,* 106**,** 33,579-33,591.

Rahman, A. F., Gamon, J. A., Sims, D. A. & Schmidts, M. 2003. Optimum pixel size for hyperspectral studies of ecosystem function in southern California chaparral and grassland. *Remote Sensing of Environment,* 84**,** 192-207.

Rahman, H. & Dedieu, G. 1994. SMAC: a simplified method for the atmospheric correction of satellite measurements in the solar spectrum. *International Journal of Remote Sensing,* 15**,** 123–143.

Ramachandran, B., Justice, C. O. & Abrams, N. J. (eds.) 2011a. *Land Remote Sensing and Global Environmental Change, NASA's Earth Observation System and the Science of ASTER and MODIS,* New York: Springer.

Ramachandran, B., Justice, C. O. & Abrams, N. J. (eds.) 2011b. *Land Remote Sensing and Global Environmental Change: NASA's Earth Observing System and the Science of ASTER and MODIS,* New York, USA: Springer.

Ranson, K. J., Daughtry, C. S. T., Biehl, L. L. & Bauer, M. E. 1985. Sun-view angle effects on reflectance factors of corn canopies. *Remote Sensing of Environment,* 18**,** 147-161.

Razak, K. A., Straatsma, M. W., Van Westen, C. J., Malet, J. P. & De Jong, S. M. 2011. Airborne laser scanning of forested landslides characterization: Terrain model quality and visualization. *Geomorphology,* 126**,** 186-200.

Remer, L. A., Kaufman, Y. J., Tanré, D., Mattoo, S., Chu, D. A., Martins, J. V., Li, R. R., Ichoku, C., Levy, R. C., Kleidman, R. G., Eck, T. F., Vermote, E. & Holben, B. N. 2005. The MODIS Aerosol Algorithm, Products, and Validation. *Journal of the Atmospheric Sciences,* 62**,** 947-973.

Ribeiro Jr, P. J. & Diggle, P. J. 2001. geoR: A Package for Geostatistical Analysis. *R-NEWS,* 1**,** 15-18.

Richards, J. A. & Jia, X. 1999. *Remote Sensing Digital Image Analysis: An Introduction, 3rd Edition*.

Richardson, A. D. & Berlyn, G. P. 2002. Changes in fliar spectral reflectance and chlorophyll fluorescence of four temperate species following branch cutting. *Tree Physiology,* 22**,** 499-506.

Richardson, A. D., Keenan, T. F., Migliavacca, M., Ryu, Y., Sonnentag, O. & Toomey, M. 2013. Climate change, phenology, and phenological control of vegetation feedbacks to the climate system. *Agricultural and Forest Meteorology,* 169**,** 156-173.

Richardson, J. J., Moskal, L. M. & Kim, S.-H. 2009. Modeling approaches to estimate effective leaf area index from aerial discrete-return LIDAR. *Agricultural and Forest Meteorology,* 149**,** 1152-1160.

Richter, R. 1996. Atmospheric correction of DAIS hyperspectral image data. *Computers & Geosciences,* 22**,** 785-793.

Richter, R. 2011. Atmospheric / Topographic Correction for Satellite Imagery. *ATCOR-2/3 User Guide.* DLR - German Aerospace Center.

Ricotta, C., Avena, G. & De Palma, A. 1999. Mapping and monitoring net primary productivity with AVHRR NDVI time-series: statistical equivalence of cumulative vegetation indices. *ISPRS Journal of Photogrammetry and Remote Sensing,* 54**,** 325-331.

Riedman, M. 2003. *Band selection using hyperspectral data from airborne and satellite sensors.* PhD, University of Southampton.

Roberts, D. A., Yamaguchi, Y. & Lyon, R. J. P. Comparison of various techniques for calibration of AIS data. In JPL Proceedings of the Second Airborn Imaging Spectrometer Data Analysis Workshop, 1986 Pasadena, CA, USA. Jet Propulsion Laboratory, 21-30.

Robertson, G. P. 1987. Geostatistics in Ecology: Interpolating With Known Variance. *Ecology,* 68**,** 744-748.

Rodwell, J. S. (ed.) 1991. *Woodlands and Scrub,* Cambridge: Cambridge University Press.

Roujean, J.-L., Leroy, M. & Deschamps, P.-Y. 1992. A bidirectional reflectance model of the Earth's surface for the correction of remote sensing data. *Journal of Geophysical Research: Atmospheres,* 97**,** 20455-20468.

Roy, D. P., Devereux, B., Grainger, B. & White, S. J. 1997. Parametric geometric correction of airborne thematic mapper imagery. *International Journal of Remote Sensing,* 18**,** 1865 - 1887.

Ruimy, A., Dedieu, G. & Saugier, B. 1996a. TURC: A diagnostic model of continental gross primary productivity and net primary productivity. *Global Biogeochemical Cycles,* 10**,** 269-285.

Ruimy, A., Kergoat, L., Field, C. B. & Saugier, B. 1996b. The use of CO2 flux measurements in models of the global terrestrial carbon budget. *Global Change Biology,* 2**,** 287-296.

Ruimy, A., Saugier, B. & Dedieu, G. 1994a. Methodology for the estimation of terrestrial net primary production from remotely sensed data. *Journal of Geophysical Research: Atmospheres,* 99**,** 5263-5283.

Ruimy, A., Saugir, B. & Dedieu, G. 1994b. Methodology for the estimation of terrestrial net primary production from remotely sensed data. *Journal of Geophysical Research,* 99**,** 5263-5284.

Running, S. W., Baldocchi, D. D., Turner, D. P., Gower, S. T., Bakwin, P. S. & Hibbard, K. A. 1999. A Global Terrestrial Monitoring Network Integrating Tower Fluxes, Flask Sampling, Ecosystem Modeling and EOS Satellite Data. *Remote Sensing of Environment,* 70**,** 108-127.

Running, S. W. & Coughlan, J. C. 1988. A general model of forest ecosystem processes for regional applications I. Hydrologic balance, canopy gas exchange and primary production processes. *Ecological Modelling,* 42**,** 125-154.

Running, S. W., Nemani, R., Glassy, J. M. & Thornton, P. E. 2000. *MODIS Vegetation Production and Net Primary Production (MOD 17)* [Online]. NASA. Available: http://modis.gsfc.nasa.gov/data/dataprod/nontech/MOD17.php [Accessed 17 January 2012 2012].

Running, S. W., Nemani, R. R., Heinsch, F. A., Zhao, M., Reeves, M. & Hashimoto, H. 2004a. A continuous satellite-derived measure of global terrestrial primary production. *BioScience,* 54**,** 547 – 560

Salas, C., Ene, L., Gregoire, T. G., Næsset, E. & Gobakken, T. 2010. Modelling tree diameter from airborne laser scanning derived variables: A comparison of spatial statistical models. *Remote Sensing of Environment,* 114**,** 1277-1285.

San, B. T. & Süzen, M. L. 2011. Evaluation of cross-track illumination in EO-1 Hyperion imagery for lithological mapping. *International Journal of Remote Sensing,* 32**,** 7873-7889.

Sannigrahi, S. 2017. Modeling terrestrial ecosystem productivity of an estuarine ecosystem in the Sundarban Biosphere Region, India using seven ecosystem models. *Ecological Modelling,* 356**,** 73-90.

Savill, P. S., Perrins, C. M., Kirby, K. J. & Fisher, N. (eds.) 2010. *Wytham Woods Oxford's Ecological Laboratory,* Oxford: Oxford University Press.

Schabenberger, O. & Gotway, C. A. 2005. *Statistical Methods for Spatial Data Analysis,* USA, Chapman and Hall/CRC Press.

Schaepman-Strub, G., Schaepman, M. E., Painter, T. H., Dangel, S. & Martonchik, J. V. 2006. Reflectance quantities in optical remote sensing—definitions and case studies. *Remote Sensing of Environment,* 103**,** 27-42.

Schimd, H. P. 1994. Source Areas for Scalars and Scalar Fluxes *Boundary-Layer Meteorology,* 67**,** 293–318.

Schimd, H. P. 2002. Footprint modeling for vegetation atmosphere exchange studies: a review and perspective. *Agricultural and Forest Meteorology,* 113**,** 159 - 183.

Schimel, D., Hibbard, K., Costa, D., Cox, P. & Leeuw, S. V. D. 2015. Analysis, Integration and Modeling of the Earth System (AIMES): Advancing the post-disciplinary understanding of coupled human–environment dynamics in the Anthropocene. *Anthropocene,* 12**,** 99-106.

Schlapfer, R. S. A. 2010. Atmospheric & Topographic Correction (ATCOR).

Schlesinger, W. H. 1997. *Biogeochemistry: Ananalysis of Global Change,* San Diego, Academic Press.

Schlesinger, W. H. & Lichter, J. 2001. Limited carbon storage in soil and litter of experimental forest plots under increased atomspheric CO2. *Academic Journal,* 411**,** 466-469.

Schmid, H. P. 1997. Experimental design for flux measurements: matching scales of observations and fluxes. *Agricultural and Forest Meteorology,* 87**,** 179 - 200.

Schmid, H. P. 2002. Footprint modeling for vegetation atmosphere exchange studies: a review and perspective. *Agricultural and Forest Meteorology,* 113**,** 159-183.

Schmid, H. P., Grimmond, C. S. B., Cropley, F., Offerle, B. & Su, H.-B. 2000. Measurements of CO2 and energy fluxes over a mixed hardwood forest in the mid-western United States. *Agricultural and Forest Meteorology,* 103**,** 357-374.

Schmid, H. P. & Lloyd, C. R. 1999. Spatial Representativeness and the Location Bias of Flux Footprints over Inhomogeneous Areas. *Agricultural and Forest Meteorology,* 93**,** 195-209.

Schott, J. R., Salvaggio, C. & Volchok, W. J. 1988a. Radiometric Scene Normalization using Pseudoinvariant Features. *Remote Sensing of Environment,* 26**,** 1-16.

Schroeder, T. A., Cohen, W. B., Song, C., Canty, M. J. & Yang, Z. 2006. Radiometric correction of multi-temporal Landsat data for characterization of early successional forest patterns in western Oregon. *Remote Sensing of Environment,* 103**,** 16 - 26.

Schubert, P., Eklundh, L., Lund, M. & Nilsson, M. 2010. Estimating northern peatland CO2 exchange from MODIS time series data. *Remote Sensing of Environment,* 114**,** 1178-1189.

Schwartz, M. D., Hanes, J. M. & Liang, L. 2013. Comparing carbon flux and high-resolution spring phenological measurements in a northern mixed forest. *Agricultural and Forest Meteorology,* 169**,** 136-147.

Schwartz, M. W., Brigham, C. A., Hoeksema, J. D., Lyons, K. G., Mills, M. H. & Van Mantgem, P. J. 2000. Linking biodiversity to ecosystem function: implications for conservation ecology. *Oecologia,* 122**,** 297-305.

Seaquist, J. W., Olsson, L. & Ardö, J. 2003. A remote sensing-based primary production model for grassland biomes. *Ecological Modelling,* 169**,** 131-155.

Sellers, P. J. 1987. Canopy reflectance, photosynthesis, and transpiration, II. The role of biophysics in the linearity of their interdependence. *Remote Sensing of Environment,* 21**,** 143-183.

Sellers, P. J., Berry, J. A., Collatz, G. J., Field, C. B. & Hall, F. G. 1992. Canopy reflectance, photosynthesis, and transpiration. III. A reanalysis using improved leaf models and a new canopy integration scheme. *Remote Sensing of Environment,* 42**,** 187-216.

Senay, G. B., Velpuri, N. M., Bohms, S., Budde, M., Young, C., Rowland, J. & Verdin, J. P. 2015. Chapter 9 - Drought Monitoring and Assessment: Remote Sensing and Modeling Approaches for the Famine Early Warning Systems Network A2 - Shroder, John F. *In:* Paron, P. & Baldassarre, G. D. (eds.) *Hydro-Meteorological Hazards, Risks and Disasters.* Boston: Elsevier.

Serbin, S. P., Dillaway, D. N., Kruger, E. L. & Townsend, P. A. 2011. Leaf optical properties reflect variation in photosynthetic metabolism and its sensitivity to temperature. *Journal of Experimental Botany*.

Sims, D. A. & Gamon, J. A. 2002. Relationships between leaf pigment content and spectral reflectance across a wide range of species, leaf structures and developmental stages. *Remote Sensing of Environment,* 81**,** 337-354.

Sims, D. A., Rahman, A. F., Cordova, V. D., El-Masri, B. Z., Baldocchi, D. D., Bolstad, P. V., Flanagan, L. B., Goldstein, A. H., Hollinger, D. Y., Misson, L., Monson, R. K., Oechel, W. C., Schmid, H. P., Wofsy, S. C. & Xu, L. 2008. A new model of gross primary productivity for North American ecosystems based solely on the enhanced vegetation index and land surface temperature from MODIS. *Remote Sensing of Environment,* 112**,** 1633-1646.

Singh, A. & Harrison, A. 1985. Standardized principal components. *International Journal of Remote Sensing,* 6**,** 883-896.

Smith, G. M. & Milton, E. J. 1999. The Use of the Empirical Line Method to Calibratemremotely Sensed Data to Reflectance. *International Journal of Remote Sensing,* 20**,** 2653 – 2662.

Smith, J. E., Heath, L. S. & Jenkins, J. C. 2003. Forest volume-to-biomass models and estimates of mass for live and standing dead trees of U.S. forests. *General Technical.* Newtown Square, PA: U.S. Department of Agriculture, Forest Service.

Soenen, S. A., Peddle, D. R., Hall, R. J., Coburn, C. A. & Hall, F. G. 2010. Estimating aboveground forest biomass from canopy reflectance model inversion in mountainous terrain. *Remote Sensing of Environment,* 114**,** 1325-1337.

Sogachev, A., Rannik, Ü. & Vesala, T. 2004. Flux footprints over complex terrain covered by heterogeneous forest. *Agricultural and Forest Meteorology,* 127**,** 143-158.

Solomon, S. D., Qin, M., Manning, Z., Chen, M., Marquis, K. B. & Averyt, M. 2007. *Climate Change 2007: The Physical Science Basis, ,* Cambridge, United Kingdom and New York, NY, USA, Cambridge University Press.

Song, C., Woodcock, C. E., Seto, K. C., Lenney, M. P. & Macomber, S. A. 2001. Classification and Change Detection Using Landsat TM Data: When and How to Correct Atmospheric Effects? *Remote Sensing of Environment,* 75**,** 230-244.

Staenz, K. 1996. *Canadian Journal of Remote Sensing,* 22**,** 248.

Starck, J. L., Murtagh, F. & Bijaoui, A. 1998. *Image Processing and Data Analysis: The Multiscale Approch,* Canbridge, Cambridge University Press.

Stein, A., Van Der Meer, F. & Gorte, B. (eds.) 1999. *Spatial Statistics for Remote Sensing,* Netherland: Kluwer Academic Publishers.

Steltzer, H. & Welker, J. M. 2006. Modeling the Effect of Photosynthetic Vegetation Properties on the NDVI-LAI Relationship. *Ecology,* 87**,** 2765-2772.

Stow, D., Hope, A., Boynton, W., Phinn, S., Walker, D. & Auerbach, N. 1998. Satellite-derived vegetation index and cover type maps for estimating carbon dioxide flux for arctic tundra regions. *Geomorphology,* 21**,** 313-327.

Street, L. E., Shaver, G. R., Williams, M. & Van Wijk, M. T. 2007. What is the relationship between changes in canopy leaf area and changes in photosynthetic CO2 flux in arctic ecosystems? *Journal of Ecology,* 95**,** 139-150.

Su, Z., Roebeling, R. A., Schulz, J., Holleman, I., Levizzani, V., Timmermans, W. J., Rott, H., Mognard-Campbell, N., De Jeu, R., Wagner, W., Rodell, M., Salama, M. S., Parodi, G. N. & Wang, L. 2011. 2.14 - Observation of Hydrological Processes Using Remote Sensing A2 - Wilderer, Peter. *Treatise on Water Science.* Oxford: Elsevier.

Tan, K., Piao, S., Peng, C. & Fang, J. 2007. Satellite-based estimation of biomass carbon stocks for northeast China's forests between 1982 and 1999. *Forest Ecology and Management,* 240**,** 114-121.

Tang, G., Beckage, B., Smith, B. & Miller, P. A. 2010. Estimating potential forest NPP, biomass and their climatic sensitivity in New England using a dynamic ecosystem model. *Ecosphere,* 1**,** 1-20.

Tanguy, M., Baille, A., González-Real, M. M., Lloyd, C., Cappelaere, B., Kergoat, L. & Cohard, J. M. 2012. A new parameterisation scheme of ground heat flux for land surface flux retrieval from remote sensing information. *Journal of Hydrology,* 454–455**,** 113-122.

Tebaldi, C. & Knutti, R. 2007. The use of the multi-model ensemble in probabilistic climate projections. *Philosophical Transactions of the Royal Society A: Mathematical, Physical and Engineering Sciences,* 365**,** 2053-2075.

Teillet, P. M. 1986. Image correction for radiometric effects in remote sensing. *International Journal of Remote Sensing,* 7**,** 1637-1651.

Thenkabail, P. S., Lyon, J. G. & Huete, A. R. (eds.) 2011. *Hyperspectral Remote Sensing of Vegetation*: CRC Press, Taylor & Francis Group.

Thomas, M. V., Malhi, Y., Fenn, K. M., Fisher, J. B., Morecroft, M. D., R., L. C., E., T. M. & D, M. D. 2010. Carbon dioxide fuxes over an ancient broadleaved deciduous woodland in southern England. *Biogeosciences Discussions,* 7**,** 3765 - 3814.

Thomas, V., Finch, D. A., Mccaughey, J. H., Noland, T., Rich, L. & Treitz, P. 2006. Spatial modelling of the fraction of photosynthetically active radiation absorbed by a boreal mixedwood forest using a lidar-hyperspectral approach. *Agricultural and Forest Meteorology,* 140**,** 287-307.

Thomas, V., Mccaughey, J. H., Treitz, P., Finch, D. A., Noland, T. & Rich, L. 2009. Spatial modelling of photosynthesis for a boreal mixedwood forest by integrating micrometeorological, lidar and hyperspectral remote sensing data. *Agricultural and Forest Meteorology,* 149**,** 639-654.

Thome, K., Palluconi, F., Takashima, T. & Masuda, K. 1998. Atmospheric Correction of ASTER. *Geoscience and Remote Sensing, IEEE Transactions on,* 36**,** 1199-1211.

Tobler, W. R. 1970. A Computer Movie Simulating Urban Growth in the Detroit Region. *Economic Geography,* 46**,** 234-240.

Toller, G. J., Xiong, J., Sun, J., Wenny, B. N., Geng, X., Kuyper, J., Angal, A., Chen, H., Madhavan, S. & Wu, A. 2013. Terra and Aqua moderate-resolution imaging spectroradiometer collection 6 level 1B algorithm Journal of Applied Remote Sensing. *Journal of Applied Remote Sensing,* 7.

Toller, G. N., Isaacman, A., Kuper, J. & Salomonson, V. 2006. MODIS Level 1B Product User's Guide for Level 1B Version 5.0.6 (Terra) and Version 5.0.7 (Aqua). Greenbelt, MD: NASA/Goddard Space Flight Center

Tsai, F., Lin, E. K. & Yoshino, K. 2007. Spectrally segmented principal component analysis of hyperspectral imagery for mapping invasive plant species. *International Journal of Remote Sensing,* 28**,** 1023-1039.

Tsai, F. & Philpot, W. 2002. *IEEE Transactions on Geoscience and Remote Sensing,* 40**,** 416.

Tso, B. & Mather, P. M. 2001. *Classification Methods for Remote Sensing Data,* London, Taylor & Francis.

Tucker, C. J. 1979. Red and photographic infrared linear combinations for monitoring vegetation. *Remote Sensing of Environment,* 8**,** 127-150.

Turner, D. B. 1964. A diffusion model for an urban area. *Journal of Applied Meteorology,* 3**,** 83 - 91.

Turner, D. P., Ritts, W. D., Cohen, W. B., Gower, S. T., Running, S. W., Zhao, M., Costa, M. H., Kirschbaum, A. A., Ham, J. M., Saleska, S. R. & Ahl, D. E. 2006a. Evaluation of MODIS NPP and GPP products across multiple biomes. *Remote Sensing of Environment,* 102**,** 282-292.

Turner, D. P., Ritts, W. D., Cohen, W. B., Maeirsperger, T. K., Gower, S. T., Kirschbaum, A. A., Running, S. W., Zhao, M., Wofsy, S. C., Dunn, A. L., Law, B. E., Campbell, J. L., Oechel, W. C., Kwon, H. J., Meyers, T. P., Small, E. E., Kurc, S. A. & Gamon, J. A. 2005. Site-level evaluation of satellite-based global terrestrial gross primary production and net primary production monitoring. *Global Change Biology,* 11**,** 666-684.

Turner, D. P., Ritts, W. D., Maosheng, Z., Kurc, S. A., Dunn, A. L., Wofsy, S. C., Small, E. E. & Running, S. W. 2006b. Assessing interannual variation in MODIS-based estimates of gross primary production *IEEE Transaction on Geoscience and Remote Sensing,* 44**,** 1899-1907.

Turner, M. G. 1990. Spatial and Temporal Analysis of Landscape Patterns. *Landscape Ecology,* 4**,** 21 - 30.

Turner, M. G., Gardner, R. H. & O'neill, R. V. 2002. *Landscape Ecology in Theory and Practice: Pattern and Process,* New York, Springer.

Uk-Ecn 2010. Site Information: Wytham. UK Environmental Change Network.

Uk-Ecn. 2012. *Site Information: Wytham* [Online]. UK Environmental Change Network. Available: http://www.ecn.ac.uk/sites/site/terr/wytham [Accessed 01 January 2012 2012].

Underwood, E., Ustin, S. & Dipietro, D. 2003. *Remote Sensing of Environment,* 86**,** 150.

Ungar, S. G., Pearlman, J. S., Mendenhall, J. A. & Reuter, D. 2003. *IEEE Transactions on Geoscience and Remote Sensing,* 41**,** 1149.

Van Der Meer, F. D. 2006. Basic Physics of Spectrometry. *In:* Van Der Meer, F. D. & De Jong, S. M. (eds.) *Imaging Spectrometry: Basic Principles and Prospective Applications.* Netherland: Springer.

Van Leeuwen, W. J. D. & Orr, B. J. 2006. Spectral vegetation indices and uncertainty: insights from a user's perspective. *Geoscience and Remote Sensing, IEEE Transactions on,* 44**,** 1931-1933.

Verma, S. B., Sellers, P. J., Walthall, C. L., Hall, F. G., Kim, J. & Goetz, S. J. 1993. Photosynthesis and stomatal conductance related to reflectance on the canopy scale. *Remote Sensing of Environment,* 44**,** 103-116.

Vermote, E. F., Vermeulen, A. & 1999. MODIS Algorithm Technical Background Document Atmospheric Correction Algorithm: Spectral Reflectances (MOD09).

Veroustraete, F., Sabbe, H. & Eerens, H. 2002. Estimation of carbon mass fluxes over Europe using the C-Fix model and Euroflux data. *Remote Sensing of Environment,* 83**,** 376-399.

Vesala, T., Kljun, N., Rannik, U., Rinne, J., Sogachez, A., Markkanen, T., Sabelfeld, K., Foken, T. & Leclerc, M. Y. 2008. Flux and concentration footprint modelling: State of the art. *Environmental Pollution,* 152**,** 653 - 666.

Vesterdal, L., Clarke, N., Sigurdsson, B. D. & Gundersen, P. Do tree species influence soil carbon stocks in temperate and boreal forests? *Forest Ecology and Management*.

Vidal, R., Ma, Y. & Piazzi, J. 2004. *Proceedings of the 2004 IEEE Conference on Computer Vision and Pattern Recognition (CVPR'04)*.

Vidal, R., Ma, Y. & Sastry, S. 2003. *Proceedings of the 2003 IEEE Conference on Computer Vision and Pattern Recognition (CVPR'03)*.

Wallace, C. S. A., Watts, J. M. & Yool, S. R. 2000. Characterizing the spatial structure of vegetation communities in the Mojave Desert using geostatistical techniques. *Computers & Geosciences,* 26**,** 397-410.

Walser, M. L. & Nodvin, S. C. 2007. Climate Change 2007 - The Physical Science Basis. *Climate Change 2007.* Cambridge: Intergovernmental Panel on Climate Change (ICPP).

Walthall, C. L., Pachepsky, Y., Dulaney, W. P., Timlin, D. J. & Daughtry, C. S. T. 2007. Exploitation of spatial information in high resolution digital imagery to map leaf area index. *Precision Agric,* 8**,** 311-321.

Wang, H., Liu, S., Wang, J., Shi, Z., Lu, L., Zeng, J., Ming, A., Tang, J. & Yu, H. 2013a. Effects of tree species mixture on soil organic carbon stocks and greenhouse gas fluxes in subtropical plantations in China. *Forest Ecology and Management,* 300**,** 4-13.

Wang, J., Brown, D. G. & Hammerling, D. 2013b. Geostatistical inverse modeling for super-resolution mapping of continuous spatial processes. *Remote Sensing of Environment,* 139**,** 205-215.

Wang, Q., Adiku, S., Tenhunen, J. & Granier, A. 2005. On the relationship of NDVI with leaf area index in a deciduous forest site. *Remote Sensing of Environment,* 94**,** 244-255.

Wang, S., Huang, K., Yan, H., Yan, H., Zhou, L., Wang, H., Zhang, J., Yan, J., Zhao, L., Wang, Y., Shi, P., Zhao, F. & Sun, L. 2015. Improving the light use efficiency model for simulating terrestrial vegetation gross primary production by the inclusion of diffuse radiation across ecosystems in China. *Ecological Complexity,* 23**,** 1-13.

Webb, A. R. 2002. *Statistical Pattern Recognition,* West Sussex, England, John Wiley & Sons.

Wilks, D. S. 2011. *Statistical Methods in Atmospheric Sciences,* Oxford, UK, Elsevier.

Williams, M. & Rastetter, E. B. 1999. Vegetation Characteristics and Primary Productivity along an Arctic Transect: Implications for Scaling-up. *Journal of Ecology,* 87**,** 885-898.

Wilson, A. K. 1997. An integrated data system for airborne remote sensing. *International Journal of Remote Sensing,* 18**,** 1889-1901.

Witharana, C., Civco, D. L. & Meyer, T. H. 2013. Evaluation of pansharpening algorithms in support of earth observation based rapid-mapping workflows. *Applied Geography,* 37**,** 63-87.

Wohlfahrt, G., Pilloni, S., Hortnagl, L. & Hammerle, A. 2010. Estimating carbon dioxide fluxes from temerate mountain grasslands using broad-band vegetation indices. *Biogeosciences,* 7**,** 683 - 694.

Woodcock, C. E. 2002. Uncertainty in Remote Sesning. *In:* Foody, G. M. & Atkinson, P. M. (eds.) *Uncertainty in Remote Sensing and GIS.* West Sussex, England: John Wilet & Sons Ltd.

Woodcock, C. E., Strahler, A. H. & Jupp, D. L. 1988. The Use of Variograms in Remote Sensing: I. Scene Models and Simulated Images. *Remote Sensing of Environment,* 25**,** 323-348.

Woolley, J. T. 1971. *Plant Physiology,* 47**,** 656.

Wu, C., Gonsamo, A., Chen, J. M., Kurz, W. A., Price, D. T., Lafleur, P. M., Jassal, R. S., Dragoni, D., Bohrer, G., Gough, C. M., Verma, S. B., Suyker, A. E. & Munger, J. W. 2012. Interannual and spatial impacts of phenological transitions, growing season length, and spring and autumn temperatures on carbon sequestration: A North America flux data synthesis. *Global and Planetary Change,* 92–93**,** 179-190.

Wu, C., Gonsamo, A., Zhang, F. & Chen, J. M. 2014. The potential of the greenness and radiation (GR) model to interpret 8-day gross primary production of vegetation. *ISPRS Journal of Photogrammetry and Remote Sensing,* 88**,** 69-79.

Wu, H. & Li, Z.-L. 2009. Scale Issues in Remote Sensing: A Review on Analysis, Processing and Modeling. *Sensors,* 9**,** 1768-1793.

Wylie, B. K., Fosnight, E. A., Gilmanov, T. G., Frank, A. B., Morgan, J. A., Haferkamp, M. R. & Meyers, T. P. 2007. Adaptive data-driven models for estimating carbon fluxes in the Northern Great Plains. *Remote Sensing of Environment,* 106**,** 399-413.

Xiao, J., Chen, J., Davis, K. J. & Reichstein, M. 2012. Advances in upscaling of eddy covariance measurements of carbon and water fluxes. *Journal of Geophysical Research: Biogeosciences,* 117**,** n/a-n/a.

Xiao, J., Davis, K. J., Urban, N. M., Keller, K. & Saliendra, N. Z. 2011a. Upscaling carbon fluxes from towers to the regional scale: Influence of parameter variability and land cover representation on regional flux estimates. *Journal of Geophysical Research: Biogeosciences,* 116**,** 1-15.

Xiao, J., Zhuang, Q., Baldocchi, D. D., Law, B. E., Richardson, A. D., Chen, J., Oren, R., Starr, G., Noormets, A., Ma, S., Verma, S. B., Wharton, S., Wofsy, S. C., Bolstad, P. V., Burns, S. P., Cook, D. R., Curtis, P. S., Drake, B. G., Falk, M., Fischer, M. L., Foster, D. R., Gu, L., Hadley, J. L., Hollinger, D. Y., Katul, G. G., Litvak, M., Martin, T. A., Matamala, R., Mcnulty, S., Meyers, T. P., Monson, R. K., Munger, J. W., Oechel, W. C., Paw U, K. T., Schmid, H. P., Scott, R. L., Sun, G., Suyker, A. E. & Torn, M. S. 2008. Estimation of net ecosystem carbon exchange for the conterminous United States by combining MODIS and AmeriFlux data. *Agricultural and Forest Meteorology,* 148**,** 1827-1847.

Xiao, J., Zhuang, Q., Law, B. E., Baldocchi, D. D., Chen, J., Richardson, A. D., Melillo, J. M., Davis, K. J., Hollinger, D. Y., Wharton, S., Oren, R., Noormets, A., Fischer, M. L., Verma, S. B., Cook, D. R., Sun, G., Mcnulty, S., Wofsy, S. C., Bolstad, P. V., Burns, S. P., Curtis, P. S., Drake, B. G., Falk, M., Foster, D. R., Gu, L., Hadley, J. L., Katul, G. G., Litvak, M., Ma, S., Martin, T. A., Matamala, R., Meyers, T. P., Monson, R. K., Munger, J. W., Oechel, W. C., Paw, U. K. T., Schmid, H. P., Scott, R. L., Starr, G., Suyker, A. E. & Torn, M. S. 2011b. Assessing net ecosystem carbon exchange of U.S. terrestrial ecosystems by integrating eddy covariance flux measurements and satellite observations. *Agricultural and Forest Meteorology,* 151**,** 60-69.

Xiao, Q., Ustin, S. L. & Mcpherson, E. G. 2004a. *International Journal of Remote Sensing,* 25**,** 5637.

Xiao, X., Boles, S., Liu, J., Zhuang, D. & Liu, M. 2002. Characterization of forest types in Northeastern China, using multi-temporal SPOT-4 VEGETATION sensor data. *Remote Sensing of Environment,* 82**,** 335-348.

Xiao, X., Hollinger, D., Aber, J., Goltz, M., Davidson, E. A., Zhang, Q. & Moore, B. 2004b. Satellite-based modeling of gross primary production in an evergreen needleleaf forest. *Remote Sensing of Environment,* 89**,** 519-534.

Xiao, X., Zhang, Q., Braswell, B., Urbanski, S., Boles, S., Wofsy, S., Moore, B. & Ojima, D. 2004c. Modeling gross primary production of temperate deciduous broadleaf forest using satellite images and climate data. *Remote Sensing of Environment,* 91**,** 256-270.

Xiao, Z. Q., Liang, S. L., Wang, J. D., Song, J. L. & Wu, X. Y. 2009. A Temporally Integrated Inversion Method for Estimating Leaf Area Index From MODIS Data. *IEEE Transactions on Geoscience and Remote Sensing, IEEE Transactions on,* 47**,** 2536–2545.

Xiaowen, L. & Strahler, A. H. 1992. Geometric-optical bidirectional reflectance modeling of the discrete crown vegetation canopy: effect of crown shape and mutual shadowing. *Geoscience and Remote Sensing, IEEE Transactions on,* 30**,** 276-292.

Xie, Y., Sha, Z. & Yu, M. 2008. Remote sensing imagery in vegetation mapping: a review. *Journal of Plant Ecology,* 1**,** 9-23.

Yan, H., Fu, Y., Xiao, X., Huang, H. Q., He, H. & Ediger, L. 2009. Modeling gross primary productivity for winter wheat–maize double cropping system using MODIS time series and CO2 eddy flux tower data. *Agriculture, Ecosystems & Environment,* 129**,** 391-400.

Yan Yuan, W. S., Wang Yidong, Wu Weixing, Wang Jingyuan, Chen Bin, Yang Fengting 2011. Assessing productivity and carbon sequestration capacity of subtropical coniferous plantations using the process model PnET-CN. *Journal of Geographical Sciences,* 21**,** 458-474.

Yang, X. & Lo, C. P. 2000. Relative Radiometric Normalization Performance for Change Detecation from Multi-Date Satellite Images *Photogrametric Engineering & Remote Sensing,* 66**,** 967-980.

Yuan, B., Kaser, L., Karl, T., Graus, M., Peischl, J., Campos, T. L., Shertz, S., Apel, E. C., Hornbrook, R. S., Hills, A., Gilman, J. B., Lerner, B. M., Warneke, C., Flocke, F. M., Ryerson, T. B., Guenther, A. B. & De Gouw, J. A. 2015a. Airborne flux measurements of methane and volatile organic compounds over the Haynesville and Marcellus shale gas production regions.

Yuan, W., Cai, W., Liu, S., Dong, W., Chen, J., Arain, M. A., Blanken, P. D., Cescatti, A., Wohlfahrt, G., Georgiadis, T., Genesio, L., Gianelle, D., Grelle, A., Kiely, G., Knohl, A., Liu, D., Marek, M. V., Merbold, L., Montagnani, L., Panferov, O., Peltoniemi, M., Rambal, S., Raschi, A., Varlagin, A. & Xia, J. 2014a. Vegetation-specific model parameters are not required for estimating gross primary production. *Ecological Modelling,* 292**,** 1-10.

Yuan, W., Cai, W., Nguy-Robertson, A. L., Fang, H., Suyker, A. E., Chen, Y., Dong, W., Liu, S. & Zhang, H. 2015b. Uncertainty in simulating gross primary production of cropland ecosystem from satellite-based models. *Agricultural and Forest Meteorology,* 207**,** 48-57.

Yuan, W., Cai, W., Xia, J., Chen, J., Liu, S., Dong, W., Merbold, L., Law, B., Arain, A., Beringer, J., Bernhofer, C., Black, A., Blanken, P. D., Cescatti, A., Chen, Y., Francois, L., Gianelle, D., Janssens, I. A., Jung, M., Kato, T., Kiely, G., Liu, D., Marcolla, B., Montagnani, L., Raschi, A., Roupsard, O., Varlagin, A. & Wohlfahrt, G. 2014b. Global comparison of light use efficiency models for simulating terrestrial vegetation gross primary production based on the LaThuile database. *Agricultural and Forest Meteorology,* 192–193**,** 108-120.

Yuan, W., Liu, S., Zhou, G., Zhou, G., Tieszen, L. L., Baldocchi, D., Bernhofer, C., Gholz, H., Goldstein, A. H., Goulden, M. L., Hollinger, D. Y., Hu, Y., Law, B. E., Stoy, P. C., Vesala, T. & Wofsy, S. C. 2007a. Deriving a light use efficiency model from eddy covariance flux data for predicting daily gross primary production across biomes. *Agricultural and Forest Meteorology,* 143**,** 189-207.

Zar, J. H. 2010. *Biostatistical Analysis,* United State of America Pearson Education International.

Zarco-Tejada, P. J., Miller, J. R., Mohammed, G. H., Noland, T. L. & Sampson, P. H. 2001. *International Journal of Applied Earth Observation and Geoinfomation,* 3**,** 321.

Zawadzki, J., Cieszewski, C. J., Zasada, M. & Lowe, R. C. 2005. Applying Geostatistics for Investigations of Forest Ecosystems Using Remote Sensing Imagery. *Silva Fennica,* 39**,** 599-617.

Zhang, L.-X., Zhou, D.-C., Fan, J.-W. & Hu, Z.-M. 2015. Comparison of four light use efficiency models for estimating terrestrial gross primary production. *Ecological Modelling,* 300**,** 30-39.

Zhang, L., Li, D., Tong, Q. & Zheng, L. 1998. Calibration of airborne imaging spectrometer data acquired from Poyang Lake area, China. 57-64.

Zhang, X.-Q., Pu, C., Zhao, X., Xue, J.-F., Zhang, R., Nie, Z.-J., Chen, F., Lal, R. & Zhang, H.-L. 2016. Tillage effects on carbon footprint and ecosystem services of climate regulation in a winter wheat–summer maize cropping system of the North China Plain. *Ecological Indicators,* 67**,** 821-829.

Zhao, J., Chen, X. & Bao, A. M. 2014. Spatial representativeness of eddy covariance measurements using footprint analysis in arid areas. *Environmental Earth Sciences,* 71**,** 1691-1697.

Zhao, K. & Popescu, S. 2009. Lidar-based mapping of leaf area index and its use for validating GLOBCARBON satellite LAI product in a temperate forest of the southern USA. *Remote Sensing of Environment,* 113**,** 1628-1645.

Zhou, Y., Zhang, L., Xiao, J., Chen, S., Kato, T. & Zhou, G. 2014. A Comparison of Satellite-Derived Vegetation Indices for Approximating Gross Primary Productivity of Grasslands. *Rangeland Ecology & Management,* 67**,** 9-18.

Appendices

Appendix I: The Most Widely Used LUE-based Models

- **Carnegie-Ames-Stanford-Approach (CASA) Model**

An enhanced light use efficiency model Carnegie-Ames-Stanford-Approach (CASA) developed by Potter et al. (1993) and Field et al. (1995). The CASA model is used to calculate monthly terrestrial net productivity based on the concept of light-use efficiency, modified by temperature and moisture stress scalars. It needs to be calibrated and validated using training data. The CASA uses a simple light use efficiency model to estimate Net Primary Productivity ($NPP = GPP - R_A$). This assumes $\boldsymbol{R_A}$ is a constant fraction of ***GPP***, but ***GPP*** occurs only during the day and $\boldsymbol{R_A}$ is continuous, so this model cannot predict ***NEE*** on diurnal timescales.

$$NPP = PAR \times fPAR \times LUE_{max} \times T_{s1} \times T_{s2} \times W_s$$

$$PAR = 0.45 \times SR$$

$$fPAR = 1.24 \times NDVI - 0.168$$

$$T_{S1} = \frac{1.1814\left(1 + e^{0.3(-T_{opt}-10+T_a)}\right)}{1 + e^{0.2(T_{opt}-10-T_a)}}$$

$$T_{s2} = 0.8 + 0.02T_{opt} - 0.0005T_{opt}^2$$

$$W_s = \frac{AET}{PET}$$

where $\boldsymbol{LUE_{max}}$ is the maximum potential LUE (gC MJ^{-1}) of a plant under optimal conditions, ***SR*** is the incoming solar radiation(MJ m^{-2}), $\boldsymbol{T_{opt}}$ (◦C) is the optimum temperature (temperature of a particular month having maximum NDVI), $\boldsymbol{T_a}$ (◦C) is the average temperature, $\boldsymbol{T_{s1}}$ denotes how the extreme high and extreme low temperature affects the maximum potential LUE, and $\boldsymbol{T_{s2}}$ signifies how the temperature above and below from the optimum affects the maximum potential LUE (Potter et al.,1993; Field et al., 1995), $\boldsymbol{W_s}$ is the surface water stress factor is

the ratio of actual evapotranspiration (AET) and potential evapotranspiration (PET) (Deyong et al., 2009). Actual and potential ET was calculated as:

$$\lambda E = R_n - H - G$$

$$\lambda Ep = \lambda E + H = R_n - G$$

where $\boldsymbol{\lambda E}$ is the actual evapotranspiration (mm) and $\boldsymbol{\lambda Ep}$ is the potential evapotranspiration (mm), $\boldsymbol{R_n}$ is the net solar radiation (MJ m^{-2}), $\boldsymbol{H}$ is the sensible heat flux (MJ m^{-2}) and $\boldsymbol{G}$ is the soil heat flux (MJ m^{-2}) respectively.

- **Eddy Covariance Light Use Efficiency (EC-LUE) Model**

The eddy covariance light use efficiency (EC-LUE) model has been widely used for timely GPP/NPP estimation across various ecoregion (Yuan et al., 2014a,b; Wang et al., 2015; Yuanet al., 2015). This model was developed by (Yuan et al., 2007) using Liebig law (Liebig, 1840) of minimum concept (as LUE is affected by the most limiting factor at any given time).

$$fPAR = a \times NDVI + b$$

In the previous study, the empirical constant $\boldsymbol{a}$ and $\boldsymbol{b}$ were defined at $\boldsymbol{1.24}$ and $\boldsymbol{-0.68}$ (Rahman, 2004; Sims et al., 2005; Yuan et al., 2007). The invariant potential LUE was derived from eddy flux measurements using nonlinear inversion and is the most important factor for GPP estimation.

$$GPP = fPAR \times PAR \times LUE_{max} \times \min(T_s, W_s)$$

$$T_s = \frac{(T_a - T_{min}) \times (T_a - T_{max})}{\left((T_a - T_{min}) \times (T_a - T_{max}) - \left(T_a - T_{opt}\right)^2\right)}$$

$$W_s = EF = \frac{LE}{LE + H} = \frac{1}{\beta + 1}$$

where $\boldsymbol{T_s}$ and $\boldsymbol{W_s}$ are the temperature and water related stress factors which vary from zero to one while smaller values denote stronger negative impact on photosynthesis efficiency. $\boldsymbol{T_a}$, $\boldsymbol{T_{min}}$, $\boldsymbol{T_{max}}$, and $\boldsymbol{T_{opt}}$ are the mean, minimum, maximum and optimum temperature (◦C), respectively. If the air temperature falls below the $\boldsymbol{T_{min}}$ and exceeds beyond the $\boldsymbol{T_{max}}$, $\boldsymbol{T_s}$ is set to be zero (Yuan et al., 2007).

The LUE_{max} for different biomes/plant functional types were retrieved from the study of Yuanet al. (2014a,b), and the details are given in the following Table. ***EF*** is the evaporation fraction, the product of latent heat flux (W/m^{-2}) and net radiation, R_n (LE + H) (W/m^{-2}).

- **Global Production Efficiency Model (GLO-PEM) Model**

Global Production Efficiency Model (GLO-PEM) developed by Prince and Goward (1995) can be used to stimulate spatiotemporal net productivity. This model has been widely used across various ecoregion for carbon flux monitoring of grassland (Zhou et al., 2014), broadleaf, deciduous and evergreen forests (Soudani et al., 2014).

$$GPP = fPAR \times PAR \times LUE_{max} \times T_s \times W_s \times VPD_s$$

Where T_s is the temperature stress factor, W_s is water surface water stress factor, and VPD_s is the atmospheric moisture stress factor.

$$VPD_s = es - ea$$

$$es = 0.6108e\frac{17.27T}{T + 237.3}$$

$$ea = es(T_a)\frac{RH_{avg}}{100}$$

where es and ea are the saturated and actual vapor pressure (kPa), T and T_a are the absolute and mean air temperature (◦C), RH_{avg} is the average relative humidity of a particular air parcel.

- **Vegetation Production Model (VPM) Model**

The Vegetation Production Model (VPM), developed by Xiao (2004), assumes that the whole leaf and forest canopies are mainly composed by both photosynthetic vegetation and non-photosynthetic vegetation. In this model, potential LUE is affected by temperature stress scalar, surface moisture stress scalar, and phenological scalar.

$$GPP = fPAR \times PAR \times LUE_{max} \times T_s \times W_s \times P_s$$

where P_s denotes the effects of water and phenological stress on the potential LUE. Land Surface Water Index (LSWI) needs to calculate the W_s factor in this model (Xiao et al., 2002; Boles et al., 2004).

$$LSWI = \frac{\rho_{NIR} - \rho_{SWIR}}{\rho_{NIR} + \rho_{SWIR}}$$

$$W_s = \frac{1 + LSWI}{1 + LSWI_{max}}$$

where ρ_{NIR} and ρ_{SWIR} are the two spectral reflectance bandwidths in the electromagnetic spectrum of Satellite Images , for example, Landsat and MODIS (Zhang et al., 2015). $LSWI_{max}$ is the maximum LSWI within the plant growing season, ranging from −1 to +1 whereas W_s value ranges from 0 to 1. P_s denotes the effects of leaf age on net photosynthesis of a canopy. On the basis of longevity of a leaves (evergreen and deciduous), P_s scalar of a 1 year old plant leaves was retrieved by

$$P_s = \frac{1 + LSWI}{2}$$

P_s is equal to one when all leaves area were fully expanded (Xiao et al., 2002; Boles at al., 2004).

- **MOD17 Model**

The MODIS GPP model is composed with biome specific LUE, land cover, atmospheric pressure deficit (VPD), temperature stress parameters, and surface moisture stress deviation. MODIS 8-day fPAR composite was used to estimate the APAR (MJ $m^{-2}year^{-1}$). Potential LUE (LUE_{max}) denotes the maximum light use efficiency by a plant in an unstressed condition. It is the product of deviation of temperature and atmospheric pressure from the optimum (◦C) that limits the plant function which could inhibit the maximum photosynthesis (Running et al., 2004).

$$GPP = fPAR \times PAR \times LUE_{max} \times T_s \times W_s$$

$$T_s = \frac{T_{min} - T_{min}}{T_{max} - T_{min}}$$

$$W_s = \frac{VPD_{min} - VPD}{VPD_{max} - VPD_{min}}$$

where $\boldsymbol{T_{min}}$ is the monthly average minimum temperature (◦C), $\boldsymbol{TMIN_{min}}$ is the monthly minimum temperature at minimum LUE condition, $\boldsymbol{T_{max}}$ is the monthly minimum temperature at maximum LUE condition, $\boldsymbol{VPD_{min}}$ is the daytime atmospheric pressure deficit at maximum LUE condition, and $\boldsymbol{VPD_{max}}$ is the daytime atmospheric pressure deficit at minimum LUE condition (Yuan et al., 2015).

- **Temperature and Greenness (TG) Model**

The Temperature and Greenness (TG) model, developed by Simset al. (2008), can be used to estimate GPP using MODIS EVI and LST. In this model, climatic variables were not considered for GPP estimation. Correlation between LST and EVI, VPD improved the model's structural performances and explained the maximum model variances. This model has been successfully applied in a wide ecosystem region in North America and has proved to be a better model than MOD17 in GPP estimation at 11 eddy covariance flux network sites (Wu et al., 2010; Sims et al., 2008). In TG model, GPP can be calculated by the product of scaled EVI and scaled LST.

$$GPP = (EVI_{scaled} \times LST_{scaled}) \times m$$

$$EVI_{scaled} = EVI - 0.1$$

$$LST_{scaled} = min\left[\left(\frac{LST}{30}\right); (2.5 - (0.05 \times LST))\right]$$

where $\boldsymbol{m}$ is the coefficient value (gC $m^{-2}year^{-1}$) used as a substitute of LUE.

- **Greenness and Radiation (GR) Model**

The Greenness and Radiation (GR) model, developed by Gitelson et al. (2006) can be used to estimate GPP based on the correlation between the spectral vegetation indices and total PAR (Wu et al., 2014).

$$GPP = (EVI \times PAR) \times m$$

where $\boldsymbol{m}$ is the empirical scalar with the unit of gC $m^{-2}year^{-1}$.

Table 1- Input Variables used in LUE Models

Variables	Values	References
ε_0	0.542-2.76	Potter, (1993); Ruimy et al. (1999); Wenquan et al. (2006); Yuan et al. (2014a,b, 2015); Prince et al. (1995); Sims et al. (2008); Gitelson et al. (2006); Xiao et al. (2004); Running et al. (2004)
T_{min}	10° C	Potter, (1993); Field (1995); Xiao et al. (2004)
T_{max}	40° C	Field (1995); Xiao et al. (2004)
T_{opt}	20° C	Aber (1992); Field (1995); Xiao et al. (2004)

Table 2 - Limiting Factors and Parameters of the LUE Models

Models	Limiting Factors	Parameters
CASA	T_{s1}, $T_{s2,}$ W_s	ε_{max}
EC-LUE	$T_{s,}$ W_s	ε_{max}
GLO-PEN	$T_{s,}$ W_s	ε_{max}, T_{min}, T_{max}, VPD_{min}, VPD_{max}
VPM	$T_{s,}$ W_s,P_s	ε_{max}
MOD17	$T_{s,}$ W_s	ε_{max}, T_{min}, T_{max}, VPD_{min}, VPD_{max}
TG	-	m, EVI_{scaled}, LST_{scaled}
GR	-	m, EVI, PAR

Appendix II: The EC-based Wind Rose and Flux Tower Footprint: Tower-based wind rose and flux tower footprint estimated across Wytham's flux tower site

The wind rose indicates the frequency with which the wind came from a particular direction[27]. For example, in Appendix II - a (i.e. 2nd March 2010) approximately 50% of the given time the wind blew from the West direction with less than $2m/s$, i.e. mean 0.875 m/s. Accordingly, using the *EdiRe Footprint Tool* concerning the particular environmental conditions, the area between the sonic anemometer mounted on the tower and 90% distance that provides 90% of the total flux was estimated as the flux tower footprint, and then plotted on an aerial image, as shown by Figure 3-11, using the *Openair R Package 0.7-0* and *ArcGIS 10.1* software.

[27]. Directional bins are 45 degrees wide.

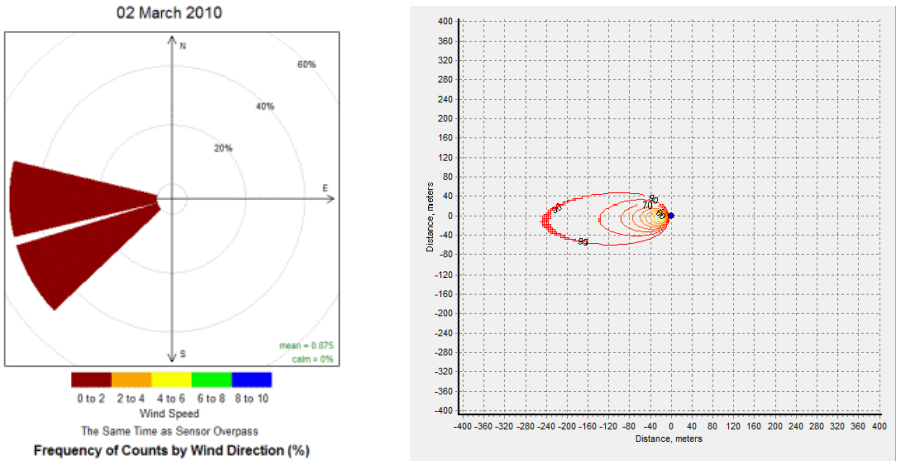

(a) 2nd March 2010, Wind Speed: <2m/s, Wind Direction: 268°, Atmospheric Stability: Moderate

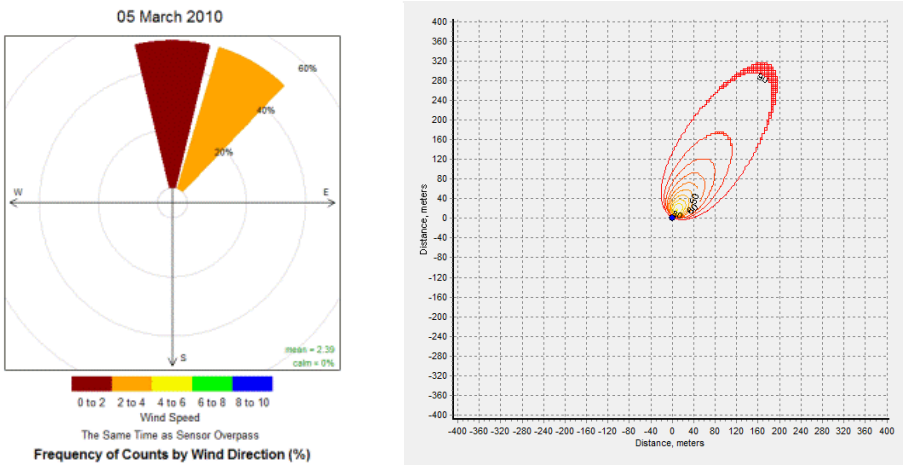

(b) 5th March 2010, Wind Speed: 2.8m/s, Wind Direction: 30°, Atmospheric Stability: Moderate

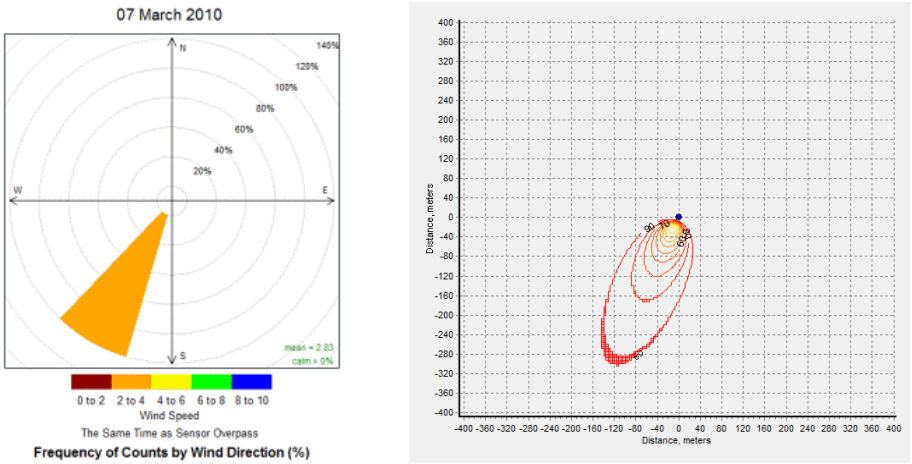

(c) 7th March 2010, Wind Speed: 2.3m/s, Wind Direction: 202°, Atmospheric Stability: Moderate

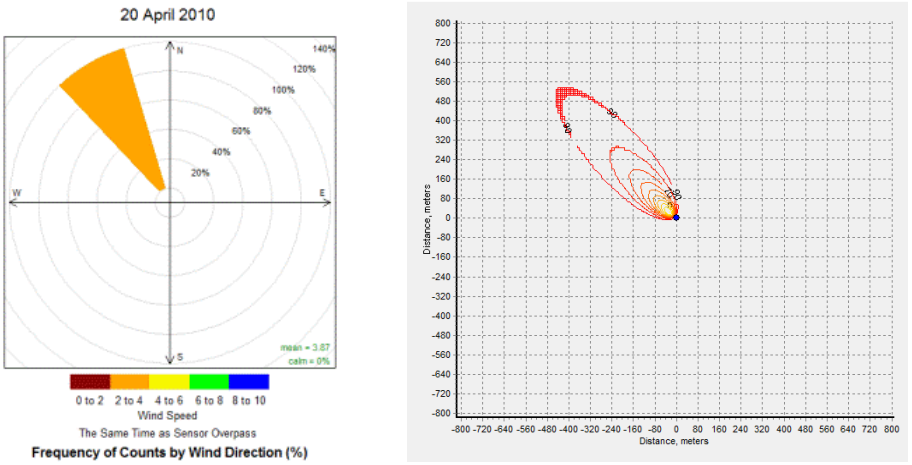

(d) 20th April 2010, Wind Speed: 3.9m/s, Wind Direction: 310°, Atmospheric Stability: Moderate

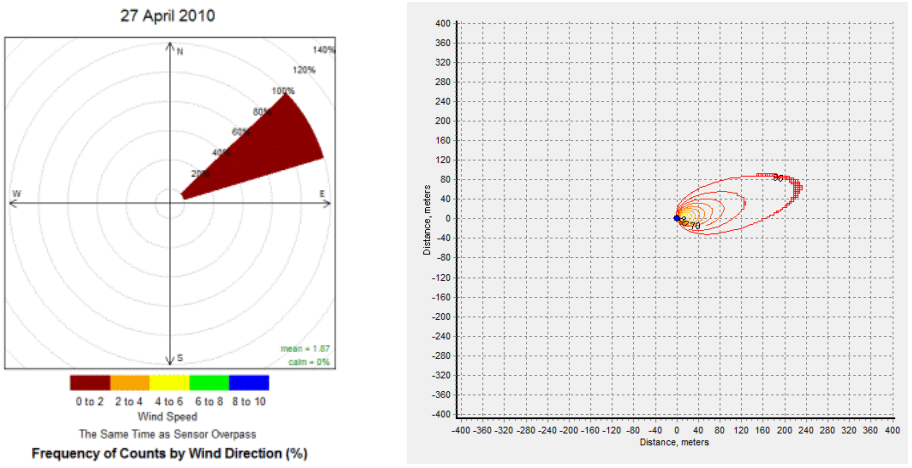

(e) 27th April 2010, Wind Speed: <2m/s, Wind Direction: 74°, Atmospheric Stability: Moderate

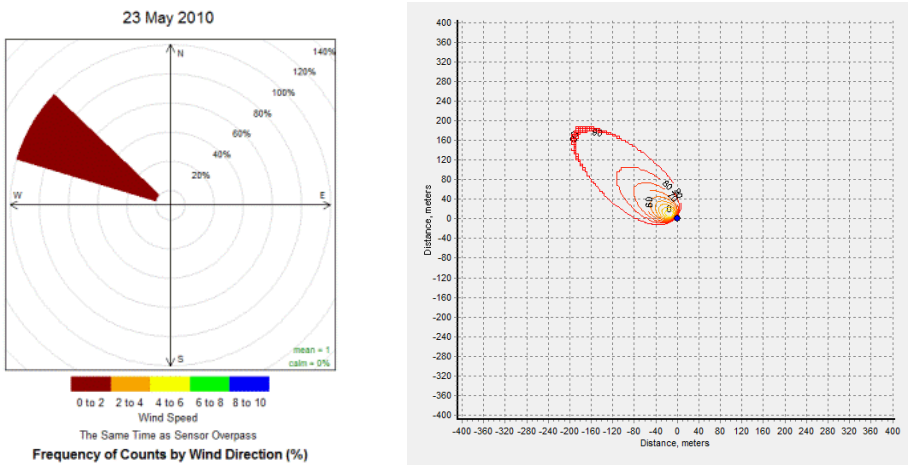

(f) 23rd May 2010, Wind Speed: <2m/s, Wind Direction: 314°, Atmospheric Stability: Moderate

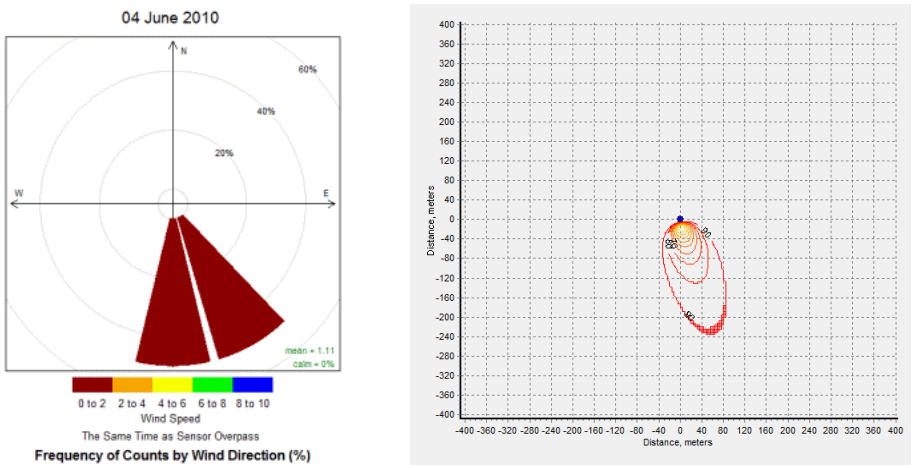

(g) 4th June 2010, Wind Speed: <2m/s, Wind Direction: 165°, Atmospheric Stability: Moderate

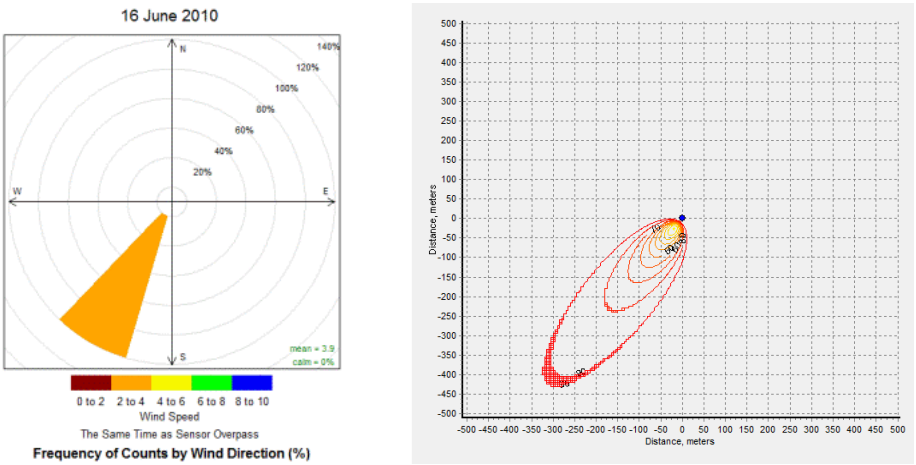

(h) 16th June 2010, Wind Speed: 3.9m/s, Wind Direction: 217°, Atmospheric Stability: Moderate